



Cardiff
Catalysis Institute

Sefydliad Catalysis
Caerdydd

**Investigation of the catalytic performance of
Palladium-based catalysts for hydrogen
production from formic acid decomposition**

Thesis submitted in accordance with the requirements of Cardiff
University for the degree of Doctor of Philosophy by

Felipe Juan Sánchez Trujillo

School of Chemistry
Cardiff University
2018

Supervisor
Dr. Nikolaos Dimitratos

ANNEX 1:

Specimen layout for Declaration/Statements page to be included in a thesis.

DECLARATION

This work has not been submitted in substance for any other degree or award at this or any other university or place of learning, nor is being submitted concurrently in candidature for any degree or other award.

Signed.....(candidate) Date.....

STATEMENT 1

This thesis is being submitted in partial fulfillment of the requirements for the degree of(insert MCh, MD, MPhil, PhD etc, as appropriate)

Signed.....(candidate) Date.....

STATEMENT 2

This thesis is the result of my own independent work/investigation, except where otherwise stated, and the thesis has not been edited by a third party beyond what is permitted by Cardiff University's Policy on the Use of Third Party Editors by Research Degree Students. Other sources are acknowledged by explicit references. The views expressed are my own.

Signed.....(candidate) Date.....

STATEMENT 3

I hereby give consent for my thesis, if accepted, to be available online in the University's Open Access repository and for inter-library loan, and for the title and summary to be made available to outside organisations.

Signed.....(candidate) Date.....

STATEMENT 4: PREVIOUSLY APPROVED BAR ON ACCESS

I hereby give consent for my thesis, if accepted, to be available online in the University's Open Access repository and for inter-library loans **after expiry of a bar on access previously approved by the Academic Standards & Quality Committee.**

Signed.....(candidate) Date.....

ABSTRACT

The objective of this work is to present formic acid as a suitable compound to be used in a hydrogen economy. Catalytic decomposition of formic acid at mild conditions is evaluated as a model reaction for hydrogen generation, making emphasis on the productivity, reusability of the catalysts, and quantification of concomitant CO evolved from the reaction. Characterisation of the fresh and used catalysts is performed to study the activity/structure relationship and investigate the possible reasons for its deactivation. Computational calculations are used to support experimental data and correlate productivity and CO evolution with the elementary steps of the reaction and the most common surfaces of the catalyst. Synthesis of materials with different surface properties and preparation methods is a fundamental part of this work.

In **Chapter 3**, a commercial Pd/C catalyst is used as a reference to establish the reaction conditions that lead to a kinetically limited reaction. Reusability tests and subsequent characterisation of the used catalyst in conjunction with computational studies are performed to investigate its stability. Continuous flow experiments are carried out as a preliminary test to improve the reusability. Following the identification of the main parameters and characteristics of the catalysts involved in formic acid decomposition, in **Chapter 4**, materials with different properties (graphitisation degree and acid/base surface functionalisation) are synthesised by two preparation methods (sol-immobilisation and impregnation) using carbon nanofibers as supports. Once the optimal preparation method is identified, a set of parameters are modified in **Chapter 5** to investigate the effects it has on the structure and morphology of the catalysts. Besides this optimisation, two supports (activated charcoal and titania) are investigated and an initial study of bimetallic catalysts and its properties is explored. **Chapter 6** presents the main consequences of these results and a set of possibilities to continue this research.

Table of Contents

1.	INTRODUCTION	1
1.1.	Background	1
1.1.1.	Energy demand, supply and fossil fuels.....	1
1.1.2.	Alternative energy sources	1
1.1.3.	Hydrogen: the fuel of the future.....	3
1.1.4.	Fuel cell systems	4
1.1.4.1.	Types of fuel cells.....	5
1.1.5.	Hydrogen production processes	9
1.1.5.1.	Steam reforming	11
1.1.5.2.	Hydrocarbon partial oxidation.....	13
1.1.5.3.	Coal gasification	15
1.1.5.4.	Other methods: electrolysis.....	17
1.1.6.	Drawbacks.....	19
1.1.7.	Alternative solutions	19
1.2.	Catalysis.....	21
1.2.1.	Types of catalysis	22
1.2.1.1.	Bio-catalysis.....	22
1.2.1.2.	Homogeneous catalysis	23
1.2.1.3.	Heterogeneous catalysis	24
1.2.2.	Preparation of catalysts (supported metal nanoparticles).....	28
1.2.2.1.	Sol-immobilisation (SI)	29
1.2.2.2.	Impregnation (IMP).....	31
1.2.3.	Liquid-phase chemical hydrogen storage systems	32
1.2.4.	Formic acid.....	33
1.2.4.1.	Natural sources of formic acid	34
1.2.4.2.	Commercial production of formic acid	34
1.2.4.3.	Formic acid decomposition.....	35
1.2.5.	Homogeneous catalytic decomposition of formic acid	36
1.2.6.	Heterogeneous catalytic decomposition of formic acid.....	38
1.3.	Aims of the study	46
1.4.	References.....	47
2.	EXPERIMENTAL, METHODS AND CHARACTERISATION	51
2.1.	Catalyst preparation.....	53

2.1.1.	Commercial Pd supported on activated carbon	53
2.1.2.	Pd nanoparticles supported on carbon nanofibers	54
2.1.2.1.	CNFs functionalisation	55
2.1.2.2.	Preparation of the Pd/CNF by sol-immobilisation (SI).....	56
2.1.2.3.	Preparation of the Pd/CNF by impregnation (IMP)	56
2.1.3.	Pd and bimetallic Au-Pd nanoparticles supported on carbon and titania using sol-immobilisation.....	57
2.1.4.	UV-Vis analysis of colloids	59
2.1.4.1.	UV-Vis set up	60
2.2.	Catalysts testing	61
2.2.1.	Inductively Coupled Plasma Mass Spectrometry (ICP-MS).....	66
2.2.2.	Quantification of metal.....	67
2.2.3.	Microwave Plasma Atomic Emission Spectroscopy (MP-AES).....	68
2.2.4.	Quantification of metal.....	69
2.3.	Analysis of reactants and products.....	69
2.3.1.	High-Performance Liquid Chromatography	70
2.3.1.1.	Quantification of reactants and products.....	72
2.3.2.	Gas analyses	74
2.3.2.1.	Mass Spectrometry	74
2.3.2.1.1.	Quantification of reactants and products.....	75
2.3.2.2.	Gas Chromatography	77
2.3.2.2.1.	Quantification of products.....	78
2.4.	Recyclability tests.....	80
2.5.	Catalyst characterisation	81
2.5.1.	X-ray Diffraction (XRD)	81
2.5.2.	X-ray photoelectron spectroscopy (XPS)	83
2.5.3.	Electron Microscopy	86
2.5.3.1.	Transmission Electron Microscopy (TEM).....	86
2.5.3.2.	Scanning Electron Microscopy-Energy Dispersive X-Ray spectroscopy.....	88
2.5.4.	Raman Spectroscopy.....	90
2.5.5.	Ammonia -Temperature Programmed Desorption (NH ₃ -TPD).....	92
2.5.6.	Brunauer, Emmett and Teller (BET) method surface area	93
2.5.7.	Thermogravimetric Analysis – Mass spectroscopy (TGA-MS)	95
2.6.	Density Functional Theory (DFT) studies	96
2.6.1.	Supercomputer used.....	98
2.7.	References.....	98

3. LIQUID-PHASE FORMIC ACID DECOMPOSITION STUDY USING A COMMERCIAL PALLADIUM-BASED CATALYST	101
3.1. Introduction	101
3.2. Results and discussion	101
3.2.1. Reaction conditions optimisation for additive-free liquid-phase formic acid decomposition	103
3.2.2. Reusability tests of 5 wt. % Pd/C	109
3.2.3. Analysis of evolved gases	111
3.2.4. Catalyst Characterisation	113
3.2.4.1. X-ray Diffraction	113
3.2.4.2. X-ray photoelectron spectroscopy.....	115
3.2.4.3. Transmission Electron Microscopy (TEM).....	120
3.2.4.4. Scanning Electron Microscopy-Energy Dispersive X-Ray spectroscopy.....	121
3.2.4.5. Brunauer, Emmett and Teller (BET) method surface area	123
3.2.4.6. Thermogravimetric Analysis - Mass spectrometry (TGA-MS)	123
3.2.5. Continuous flow set up	126
3.2.6. Kinetic Isotope Effect (KIE).....	128
3.2.7. DFT studies	130
3.2.8. Effect of calcination on catalyst activity	142
3.3. Conclusions	147
3.4. References.....	149
4. CATALYTIC INVESTIGATION OF SUPPORTED PD NANOPARTICLES ON FUNCTIONALISED CARBON NANOFIBERS: EFFECT OF FUNCTIONALISATION, HEAT TREATMENT AND PREPARATION METHOD	151
4.1. Introduction	151
4.2. Results and discussion	153
4.2.1. Initial catalytic activity screening of the Pd/CNF series catalysts for liquid-phase formic acid decomposition.....	153
4.2.2. Reaction conditions optimisation for additive-free liquid-phase formic acid decomposition	159
4.2.3. Reusability tests	162
4.2.4. Analysis of evolved gases.....	164
4.2.5. Catalyst Characterisation	165
4.2.5.1. X-ray Diffraction	165
4.2.5.2. X-ray photoelectron spectroscopy (XPS)	169
4.2.5.3. Raman	177
4.2.5.4. Transmission Electron Microscopy (TEM).....	180

4.2.5.5.	Scanning Electron Microscopy-Energy Dispersive X-Ray spectroscopy.....	188
4.2.5.6.	3D Tomography.....	190
4.2.5.7.	Ammonia -Temperature Programmed Desorption (NH ₃ -TPD).....	192
4.2.5.8.	Brunauer, Emmett and Teller (BET) method surface area	193
4.3.	Conclusions	194
4.4.	References.....	196
5.	INVESTIGATION OF SUPPORTED Pd-BASED COLLOIDAL NANOPARTICLES IN THE LIQUID PHASE DECOMPOSITION OF FORMIC ACID: EFFECT OF STABILISER, METAL LOADING, SUPPORT, AND BIMETALLICS RATIO	197
5.1.	Introduction	197
5.2.	Results and discussion	197
5.2.1.	Catalytic activity screening of the as synthesised Pd catalysts for liquid-phase formic acid decomposition: effect of PVA	198
5.2.1.1.	Catalyst Characterisation	200
5.2.2.	Reusability tests	205
5.2.3.	Effect of Pd loading on Pd/AC catalysts	207
5.2.4.	Characterisation and catalytic performance of Au _x Pd _y /TiO ₂ for liquid-phase formic acid decomposition	210
5.2.4.1.	Catalyst Characterisation	213
5.3.	Conclusions	219
5.4.	References.....	220
6.	CONCLUSIONS AND RECOMMENDED FUTURE WORK	222
6.1.	Conclusions	222
6.2.	Recommended future work.....	225
6.3.	References.....	228

PUBLICATIONS

ACKNOWLEDGEMENTS

1. INTRODUCTION

1.1. Background

1.1.1. Energy demand, supply and fossil fuels

Energy plays a unique and key role in our 21st-century society. Without conversion or transportation of energy, no activity of any kind could take place. Continuous and sufficient supply of energy is essential in order to keep and improve our standards of living. The IEA (International Energy Agency) estimated that in 2014, the total world energy consumption was 9425 Mtoe (Million Tonnes of Oil Equivalent).¹ Current United Nations predictions estimate that the world population is expected to reach 8.5 billion around 2040² and consequently, the total world energy consumption is expected to increase by 28 % in 2040 according to the IEA recent projections³.

So far, our civilisation has been deeply reliant on fossil fuels. In fact, in 2015, fossil fuels accounted for approximately 78.4 % of the global energy production.⁴ This strong dependence has led to significant economic and environmental consequences. From an economic point of view, gross production of energy from fossil fuels is concentrated in some determined areas governed by political factors, arising unstable prices. Moreover, from an environmental point of view, fossil fuels combustion constitutes the main reason for global warming. In summary, current energy production situation has led to three main areas of concern, namely depletion of fossil fuels, global warming and increasing energy costs.

Coal and oil are expected to reach the demand peak in 2020 due to increased uptake of renewables and natural gas,⁵ and both crude oil and natural gas production are estimated to reach a theoretical depletion near 2060-2070,⁶ while remaining forms of fossil fuels will do it approximately by the year 2100.⁷

1.1.2. Alternative energy sources

The installation of a sustainable energy supply chain is one of the greatest challenges to be addressed in this century.^{8,9} Regarding this matter, attention on alternative high energy fuels has been implemented during the last years, in addition to continue developing other renewable energy sources such as biomass, solar, wind or geothermal. As of 2015, renewable

energy provided approximately 19.3 % of global final energy consumption.⁴ Worldwide investments in renewable technologies amounted to US\$286 billion in 2015, with heavy investments in wind, hydro, solar and biofuels in countries such as China and the United States.⁴

Hydroelectric power is produced from moving water. The amount of energy that this moving water could produce is determined by the change in elevation (or fall) from one point to another and the volume of the water flow. In 2015, 54.3 % of the electricity generated by renewable sources was produced by hydroelectric power (Figure 1).⁴ Wind turbines are used to produce electricity generated by the movement of air. Typically, these turbines generate from 600 kW to 5 MW. Nearly a quarter of the electricity generated by renewable sources was produced by wind energy. Solar energy is a broad concept which is usually divided into passive solar or active solar depending on the way they capture, convert and distribute solar energy. Passive refers to the orientation of a building towards the Sun or the selection of materials according to thermal mass or light dispersing properties. On the other hand, active solar technologies refer to the conversion of sunlight into electricity using either photovoltaics (PV) or concentrated solar power (CSP). Solar energy accounts for approximately 15.3 % of the total energy produced from renewable sources. Biomass usually refers to plants or plant-derived materials (specifically called lignocellulosic biomass). Biomass can be used directly via combustion producing heat or indirectly converting it to several forms of biofuel such as ethanol and biodiesel. Geothermal energy is produced from thermal energy generated and stored in the Earth. It is originated from the formation of the planet and from radioactive decay of minerals. The difference in temperature between the core of the planet and the surface is the source of a continuous conduction of heat from the core to the surface.⁴

Nuclear energy, accounting for 2.3 % of the total world energy consumption, is also considered as an alternative to fossil fuel-based energy production mainly due to its high energy output. However, recent accidents such as the one that occurred in Fukushima, Japan, are a factual proof and reminder of the risks related to the use of nuclear power plants including incidents during operating procedures and disposal of harmful radioactive waste, negatively affecting its expansion at least in the near future.¹⁰

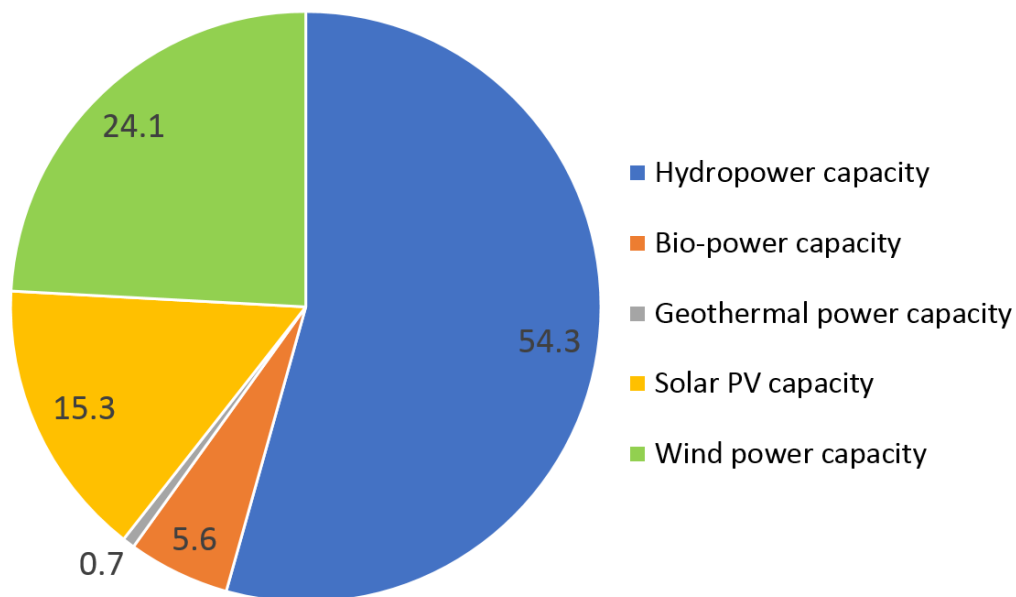


Figure 1. Worldwide renewable power capacity.

Renewable energy sources have enough potential to meet future energy needs. If properly implemented, this energy from renewable resources presents crucial advantages including unlimited and secure sustainable supply, positive impact in the environment and human health helping to mitigate climate change, and great geographical dispersion of sources ensuring price stability. Nevertheless, despite these advantages, some renewable energy sources like wind are intermittent and it is difficult to accumulate the electricity generated in order to be used in a different moment, *i.e.* electricity produced by solar photovoltaic systems to be used during the night. In order to overcome these disadvantages, hydrogen is seen as a renewable energy source that can be generated, transported to the locations where it is needed and stored until it is used.

1.1.3. Hydrogen: the fuel of the future

Hydrogen is the tenth most abundant element on Earth's crust with a 0.14 % in mass¹¹, however, it is mainly present bonded to other atoms, particularly water, hydrocarbons, carbonates and other organic compounds. Thus, energy is needed in order to break those bonds. For this reason, hydrogen is considered an energy vector instead of a direct energy source.¹² Interest in hydrogen as energy vector has increased significantly in the last few years either as vehicle fuel or as energy carrier used in fuel cells to generate electricity.¹³ Hydrogen

can play an important role since it can be used to accumulate, transport and use this energy when convenient.

The key of this material lies in the fact that in fuel cells, combustion (reaction of hydrogen with oxygen) only produces water, this being a harmless process for the environment.¹⁴ Moreover, hydrogen presents the highest energy content per mass unit compared to other fuels. The energy density of hydrogen is 120 kJ g^{-1} which is approximately three times the energy density of petrol (Table 1).¹⁵⁻¹⁷

Table 1. Heating values of some common fuels.

Fuel	Net calorific value (kJ/g)
Hydrogen	120.0
Petrol	44.2
Diesel	42.9
Crude oil	43.1
Coal	25.8
Natural gas	45.9
Methane	50.1
Ethanol	26.8
Methanol	19.9

Hydrogen is the most versatile fuel since it can be converted into electricity through electrochemical processes or to heat either through catalytic combustion or through several chemical reactions.¹⁸ Hence, energy systems powered by hydrogen seem to be an attractive alternative to current fossil fuel-based energy systems.

1.1.4. Fuel cell systems

Fuel cells are electrochemical devices that transform the chemical energy of a fuel such as hydrogen, methanol or natural gas into electrical energy when reacting with oxygen in the presence of a catalyst. Comparing with conventional combustion engines, fuel cells present a

higher fuel conversion and electrical efficiency with less toxic emissions.^{8,19} These factors and the low noise levels, lower greenhouse gas emissions, and high fuel utilisation rates, have converted, in the last few years, fuel cells to an attractive alternative for portable devices and transport with significant long-term economic and environmental benefits.²⁰⁻²³ On the other hand, the high cost, lifetime issues and, more importantly, the availability of economically profitable hydrogen generation, transportation and storage technologies are the main drawbacks that limit the commercialisation of fuel cells.^{19,23} Current research is focused on solving these issues.

1.1.4.1. Types of fuel cells

Currently, there are five main fuel cells available on the market:

- Proton exchange membrane fuel cells (PEMFCs)
- Alkaline fuel cells (AFCs)
- Phosphoric acid fuel cells (PAFCs)
- Molten-carbonate fuel cells (MCFCs)
- Solid oxide fuel cells (SOFCs)

Proton exchange membrane fuel cells (PEMFCs) can use either hydrogen or alcohol (e.g., ethanol, methanol) as a fuel. Hydrogen PEMFCs consume hydrogen and oxygen and produce water, heat and electricity, reaching an efficiency of up to 60 % and operating temperatures up to 150 °C. A direct methanol fuel cell (DMFC) consumes methanol in water and oxygen and produces water, heat and electricity with an efficiency of up to 40 % and operating temperatures up to 80 °C. In both cases, the fuel is fed to the anode where it is ionised to form protons (H^+) and electrons (e^-). Protons (H^+) can cross an electrolyte located between the electrodes while electrons (e^-) are forced to pass through the electrically conductive material and subsequently power the connected load (Figure 2). At the cathode side, oxygen is reduced with protons from the anode producing water. PEMFCs are currently being developed for transport applications, and stationary and portable applications as well.¹⁹

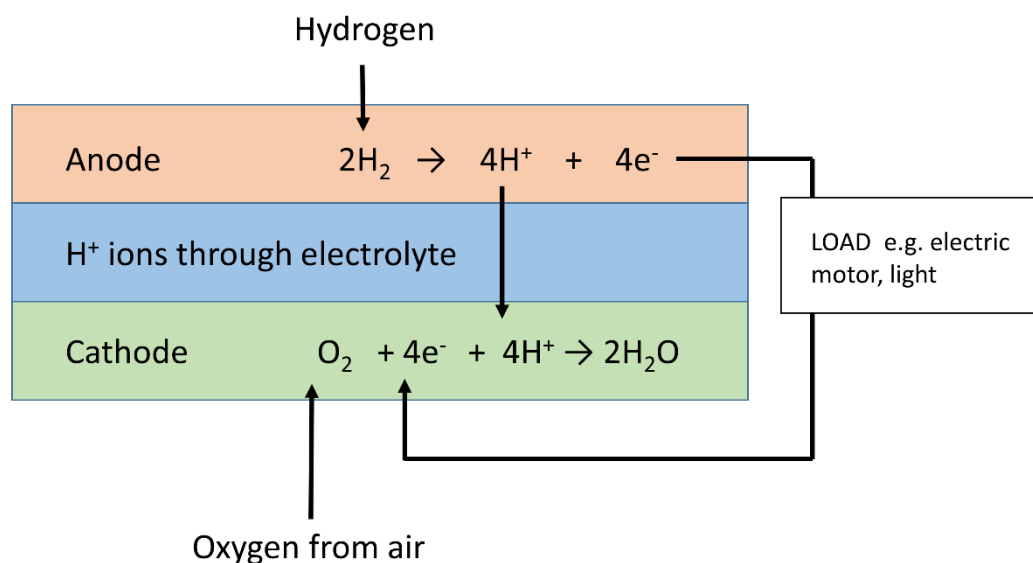


Figure 2. Schematic of a proton exchange membrane fuel cell.

PEMFCs were developed initially for military and spacecraft applications in the 1960s but was abandoned in the 1970s due to poor durability and high cost issues. Nowadays, PEMFC technology has been extended to a broad range of applications, with the potential to power a portfolio of devices and services such as mobile phones, laptops, cars, buses or houses. For large-scale manufacturing and full commercialisation of this technology, cost and durability are still the two major barriers. For example, Pt or Pt-based catalysts like Pt-Co are the only catalysts used to drive the electrochemical reactions and this element comprises a large portion of the PEMFC cost due to its high price and limited supply. Moreover, one of the major limitations on PEMFC durability is catalyst stability. Thus, developing high-performance, low-cost, and highly durable catalysts is the number one priority for PEMFC research.

Alkaline fuel cells (AFCs) are the most developed fuel cells. AFCs consume hydrogen and pure oxygen and produce water, heat and electricity at an operating temperature below 80 °C and reaching efficiencies of up to 70 %. The overall reaction is the same as in PEMFCs, however, the reactions at each electrode are different (Figure 3). At the anode, hydroxyl (OH^-) ions react with hydrogen, releasing energy and electrons and producing water, while at the cathode, oxygen reacts with electrons and water forming new OH^- ions.^{19,20}

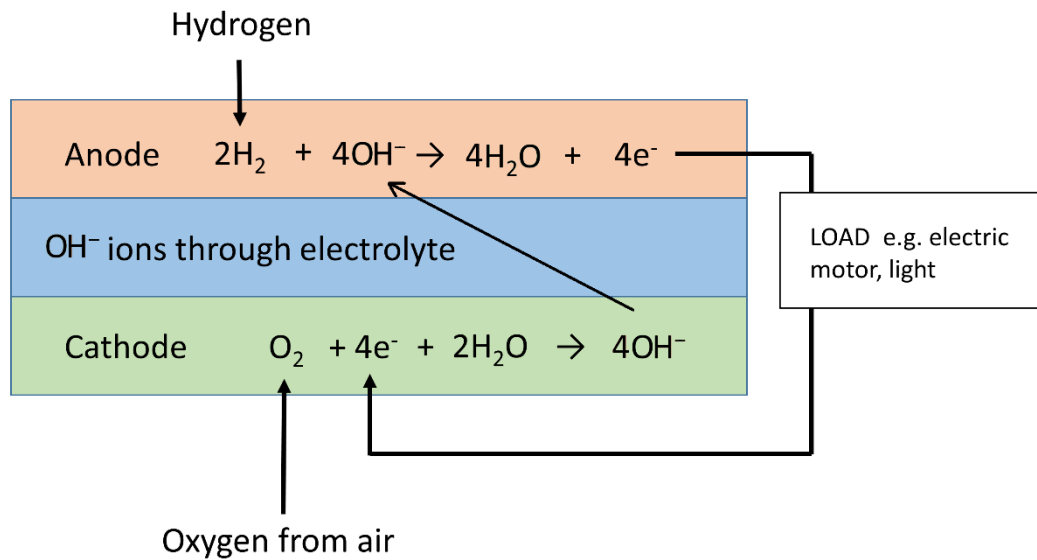


Figure 3. Schematic of an alkaline fuel cell.

Phosphoric acid fuel cells (PAFCs) consume hydrogen and oxygen and produce water, heat and electricity reaching an efficiency of up to 50%. The reactions occurring in both anode and cathode are the same as in PEMFCs (Figure 2). However, unlike the membrane in the PEMFCs, PAFCs make use of concentrated phosphoric acid (100%) as electrolyte to conduct protons. Phosphoric acid is considered as an electrolyte for fuel cells due to properties such as thermal and electrochemical stability, low volatility and being tolerant to CO₂ in the fuel. PAFC stacks are usually maintained above 42 °C which is the freezing point of phosphoric acid. This technology has reached the level of maturity where developers are focused on producing commercial capacity and prototype installations and furthermore, cell components are manufactured in large quantities. Even though it is still an expensive technology to be economically profitable compared with alternative power generation systems, the high power quality and reliability has led these systems to be used in power applications such as banks, hospitals, and computing facilities.^{19,20}

Molten-carbonate fuel cells (MCFCs) operate using a molten mixture of alkali metal carbonates, usually lithium and either potassium or sodium carbonates as electrolyte and at temperatures of up to 650 °C.¹⁹ At this temperature, the alkali carbonates form a highly conductive molten salt, being carbonate ions (CO₃²⁻) the ionic conductors. Besides oxygen, carbon dioxide needs to be supplied to the cathode and it is converted into carbonate ions.

At the anode, the carbonate ions are converted back into CO_2 and therefore, there is a net transfer of CO_2 from cathode to anode (Figure 4).

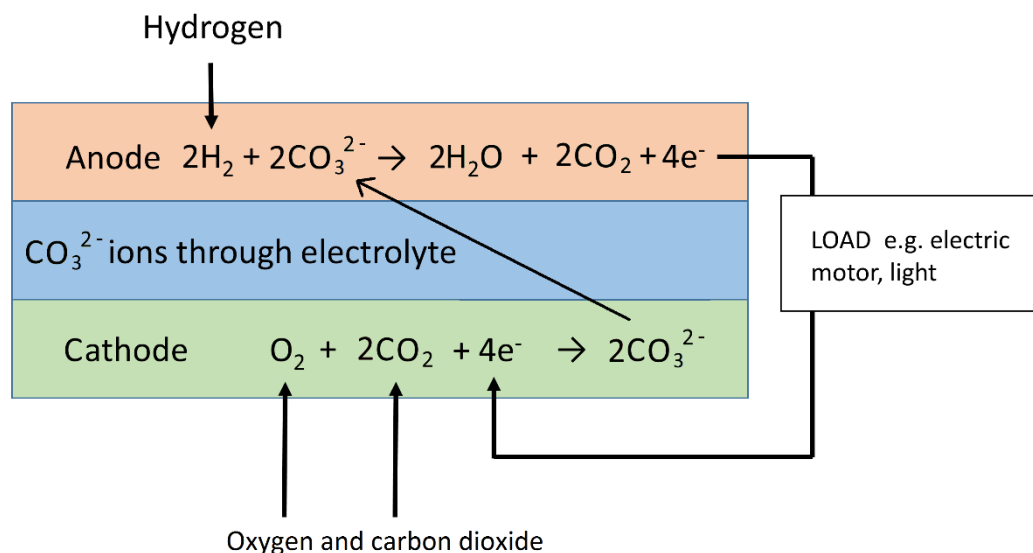


Figure 4. Schematic of a molten-carbonate fuel cell.

Contrary to PEMFCs and PAFCs, noble metals are not required. In MCFCs, nickel (anode) and nickel oxide (cathode) are used as catalysts to promote the two electrochemical reactions. Due to the high operating temperature, higher overall system efficiencies are usually achieved, and it also has greater flexibility in the use of available fuels. On the other hand, corrosion stability and lifespan of cell components play an important role, particularly in the aggressive environment of the molten carbonate electrolyte. MCFCs were initially developed for natural gas and coal-based power plants for electrical utility, industrial, and military applications.²⁰

Solid oxide fuel cells (SOFCs) operate usually between 700 and 1000 °C with efficiencies of up to 60 %. As well as in the MCFC, a negatively charged ion, O^{2-} in this case, is transferred from the cathode to the anode (Figure 5). The electrolyte is typically zirconia doped with 8 to 10 mole % yttria (Y_2O_3). This electrolyte becomes a conductor of oxygen ions at the operating temperatures. This range of temperatures presents challenges for both construction materials and durability. This electrolyte reduces the complexity of the system to only two phases (gas and solid).

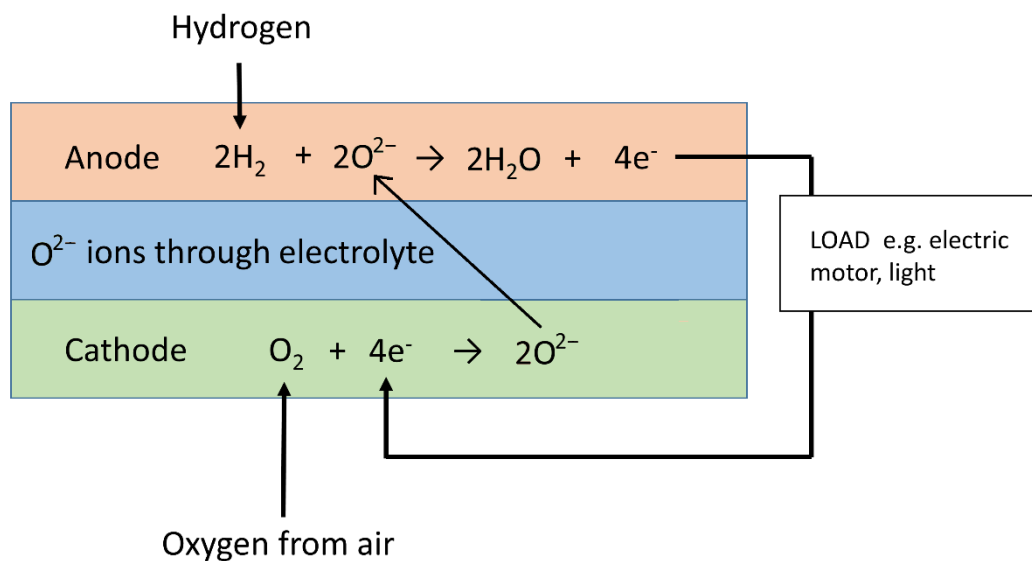


Figure 5. Schematic of a solid oxide fuel cell.

The anode is usually a mixture of zirconia and a metal, usually nickel, due to its high electronic conductivity and stability under chemically reducing conditions. Cathodes are electronically conducting oxides or mixed electronically conducting and ion-conducting ceramics being strontium-doped lanthanum manganite the most common cathode material.²⁰

In all these types of fuel cells, hydrogen is the key element that when fed into the system alongside oxygen, it is converted into electricity and water. Nevertheless, hydrogen does not occur naturally as a gaseous fuel, and for practical fuel cell systems, it usually has to be generated from whatever fuel source is locally available. Hence, economically profitable hydrogen generation is currently the challenge to solve. The next section deals with hydrogen production technologies currently used and possible future approaches.

1.1.5. Hydrogen production processes

The clean nature of hydrogen mainly depends on the raw material, in particular, its origin and the processes followed to obtain it. Nevertheless, currently 96 % of the annual mass production of hydrogen proceeds from fossil fuels, particularly, natural gas since, compared with other fossil fuels, it is less expensive, safer and easier to store, presents a less

environmentally-damaging combustion and it is expected to be fully available for at least 60 years more.²⁴

Nowadays, several processes are employed to produce economically profitable hydrogen:

- Steam reforming
- Partial oxidation of refinery oil
- Coal gasification
- Others: electrolysis, biological methods

Approximately half of the currently produced hydrogen comes from steam reforming of natural gas. Partial oxidation of refinery oil accounts for 30 %, coal gasification for 18 % and the remaining technologies such as water electrolysis just 4 % (Figure 6).²⁵

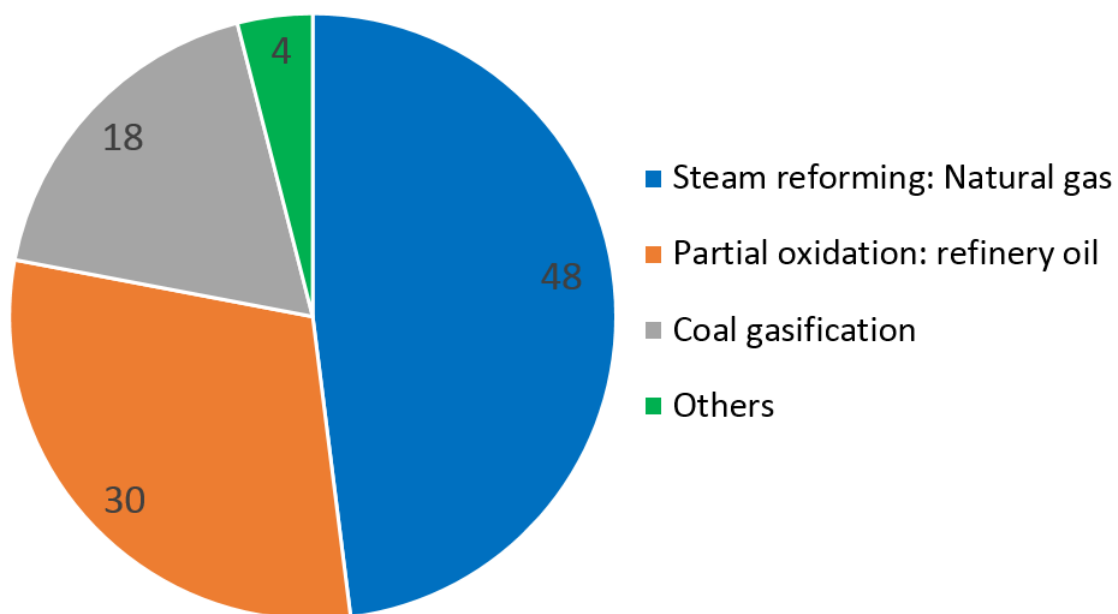


Figure 6. Worldwide hydrogen production processes.

Considering this, it is recognisable that these technologies are non-environmentally friendly, non-sustainable, expensive and/or energy intensive. A brief description of these methods is presented below.

1.1.5.1. Steam reforming

It is one of the most widespread and cheapest hydrogen production processes since it presents high efficiencies and low, both operational and production costs. In this process, hydrogen is produced by the conversion of natural gas (CH₄) or hydrocarbon into H₂ and CO₂ in presence of H₂O vapour (steam). See figure 7 for a scheme of the process.

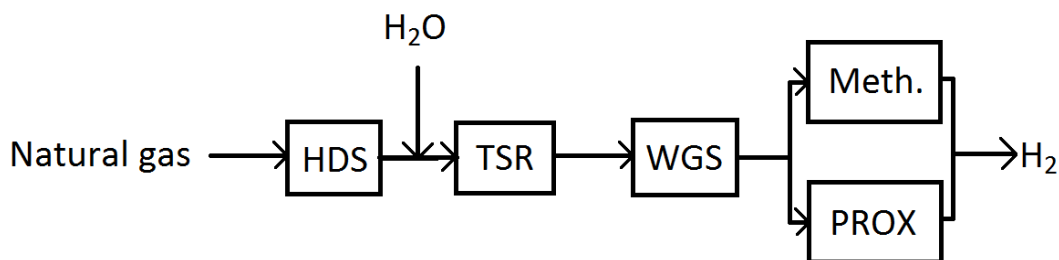
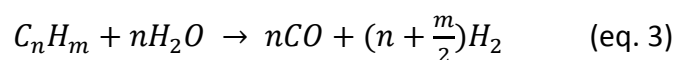


Figure 7. Schematic of the steam reforming process.

First, the feedstock is subjected to a hydrodesulphurisation (HDS) process. Typically, natural gas contains organic sulphur compounds mostly in the form of hydrogen sulphide. It has to be removed before any further fuel processing can be carried out since deactivation of the steam reforming catalysts can occur.²⁰ H₂S is absorbed onto a bed of zinc oxide (sometimes promoted with Cu) or active carbon, forming zinc sulphide according to the reaction:

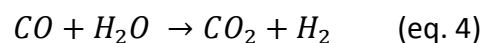


Next step is the so-called steam reforming reaction (SR) and takes place in a tubular reformer (TSR). In this step, either methane or another hydrocarbon reacts with steam, producing syngas (eq. 2 and 3). Common inlet temperatures are 450–650 °C and the product gas leaves the reformer at 850–950 °C.²⁶



The catalysts used are classified into two types: nonprecious metal (typically nickel) and precious metals (typically platinum or rhodium), both from Group VIII elements. Typically, the reforming reactions are catalysed by Ni-based materials in which the Ni species are deposited onto ceramic supports composed of alumina and/or alumina and magnesium spinels. The tubular reformer typically operates at such temperatures that sintering of the nickel catalyst is promoted, resulting in growth of the nickel particles and consequently, a decrease in nickel surface area and thus, activity. Besides high temperature, the severe conditions in a tubular reformer involve partial pressures close to 30 bar, consequently, the support should be able to withstand the severe conditions in a tubular reformer without losing strength.

In the third step, the product is fed into the catalytic converter, where CO reacts with steam converting it into carbon dioxide and hydrogen by water-gas shift (WGS) reaction (eq. 4).



WGS can be classified as high-temperature shift (HTS) or low-temperature shift (LTS). HTS operates in the temperature range from 300 to 500 °C. Typical commercial HTS catalyst is composed of Fe₂O₃, Cr₂O₃ and MgO, being chromium crucial to stabilise the iron oxide and prevent sintering. LTS, on the other hand, is carried out at 210–230 °C. Typically, a commercial catalyst for LTS is composed of CuO, ZnO and Cr₂O₃ containing 2 wt. % MnO and MgO and 5 wt. % Al₂O₃. Being CuO the active catalytic species, ZnO provides structural support as well as prevents the poisoning of copper by sulphur and, Al₂O₃ prevents dispersion and pellet shrinkage.²⁷

Even though WGS reaction does occur at the same time as steam reforming, at the high temperatures needed for hydrogen generation, the equilibrium point of the reaction tends to be displaced to the left of the equation and CO concentration can only be reduced to 1 % of the feed. Therefore, since most PEM fuel cells need CO concentration below 10-20 ppm, further processing will be required to remove it either by preferential oxidation (PROX) or methanation (Meth.). In the former case, CO reacts with oxygen from air reducing CO concentration to approximately 10 ppm, however, oxygen undesired combustion of hydrogen takes place to some degree as well. In methanation, CO is converted to methane through hydrogenation. In this case, control of the conditions inside the reactor is crucial in order to

minimise unnecessary consumption of hydrogen. Preferential oxidation is the technology currently used.²⁸

In case there is no ready source of steam, it may be replaced by carbon dioxide as reactant. This reaction is known as dry reforming, or CO₂ reforming (eq. 5). Dry reforming of methane (DRM) can be used to convert greenhouse gases (CH₄ and CO₂) into valuable fuel rich syngas. In this process, carbon dioxide is used to reform methane to obtain syngas (H₂ and CO):



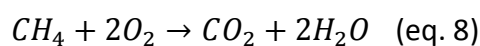
Sometimes, a hybrid approach where both steam and CO₂ are used is called mixed reforming. Both dry and mixed reforming present energy and environmental advantages compared with traditional steam reforming. Nickel is again used as catalyst but deactivation due to carbon formation and nickel sintering can be particularly severe, and better catalysts are required. H:C atom ratio in the feedstock material is a crucial factor in determining the overall efficiency. With a higher ratio, less carbon dioxide is formed and, in the case of methane, the thermal efficiency of hydrogen generation by steam reforming is approximately 70–85 %. Nowadays, tubular reformers are designed for capacities of up to 300 000 N m³ h⁻¹ of hydrogen or synthesis gas.^{26,28}

Usually, building and production costs are proportionally related to the number of tubes and size in general. For small and mid-size capacities steam reforming may be the optimum choice but for very large-scale production, partial oxidation processes become more economical because the economy of scale of the oxygen plant is more favourable.

1.1.5.2. Hydrocarbon partial oxidation

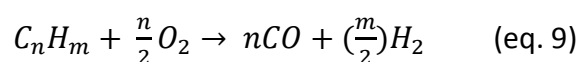
30 % of the worldwide production of hydrogen is carried out by means of partial oxidation as an alternative to steam reforming. In this process, the hydrocarbon is subjected to a partial combustion with pure O₂ gas in a combustion chamber producing an effluent of H₂O and CO. Typically, the feed consists of heavy oil fractions, but methane or biogas can be used as well. It can be classified as partial oxidation (POX) and catalytic partial oxidation (CPOX) depending on whether a catalyst is used or not.

Partial oxidation is a noncatalytic process. The raw material is gasified in the presence of oxygen and fed into the reactor where the process takes place at pressures in the 3–8 MPa range and temperatures typically comprised between 1300–1500 °C. Compared with steam reforming, more CO is produced which is further converted to CO₂ and H₂ through the water gas shift reaction.²⁸ Partial oxidation of methane is a highly exothermic reaction so, even though the operating temperature is very high, this process consumes, in general, less energy than the steam reforming process.²⁹



As advantages over the catalytic process, the removal of sulphurous elements from the feed is not necessary and with such high temperature, heavier petroleum fractions such as diesel and residual fractions can be handled. On the other hand, it is not suitable for low scale plants and the high temperatures employed derives into a difficult control of the reaction.

Catalytic partial oxidation makes use of a catalyst to drive the reaction lowering the operating temperature to 700–1000 °C.²⁸ In the case of natural gas, the catalysts are typically based on Ni or Rh. Nickel promotes the formation of syngas, and the Ni species with oxidation number ≥ 2 promote the total combustion of methane.³⁰ However, nickel tends to form coke and the cost of Rh has increased significantly. Due to the exothermic nature of the reactions, control of temperature is hard.

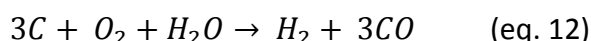
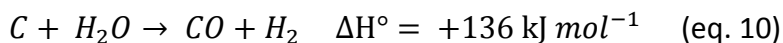


Compared with steam reforming, partial oxidation produces less hydrogen per molecule of methane which means that partial oxidation is less efficient than steam reforming. Typically, the thermal efficiency of partial oxidation with methane lies in the range 60–75 %. On the other hand, steam is not required, largely simplifying a generally very complex system. Hence, it may be considered where system simplicity is more important than high efficiency such as in small-scale cogeneration plants.^{20,28,31}

The stability of the catalysts used in steam reforming and partial oxidation is of crucial importance. Poisoning by impurities, mainly sulphur, and coke formation are, as observed, the major challenges. Catalysts deactivation can be improved with the addition of catalyst promoters as well as the choice of catalyst support. Catalyst promoters are usually metals added to the Ni catalyst forming an alloy. Some of these catalyst promoters are Co, Cu, Sn, Pt, Pd, Mn, Rh, Ru and Au. An important improvement of the hydrogen production with Ni catalysts and decrease of carbon deposition has been observed.³⁰

1.1.5.3. Coal gasification

Coal gasification is an old technology used during the 19th and the first half of the 20th century to produce the so-called “town gas” (a mixture of mainly hydrogen and carbon oxides, organic liquids such as tars and phenolics, and a residual coke). In gasification, coal reacts with steam and oxygen (or air) at high temperatures to partially oxidise coal into gaseous products (eq. 10, 11 and 12). The type of coal, temperature and pressure of the reaction, and the relative amounts of steam or oxygen injected are the key parameters driving the relative proportion of products.³²



Coal gasification systems are classified into (Figure 8):

- Moving bed
- Fluidised bed
- Entrained bed

Moving-bed gasifiers are used for low temperature process (450–650 °C). Feedstock moves in a countercurrent flow with the gasification air. The outlet is a gas mixture of methane and ethane from devolatilisation of the coal alongside a hydrocarbon liquid stream containing naphtha, tars, oils, and phenolic liquids.

Entrained-bed gasifiers operate at high temperature (1100–1500 °C) and pressures of approximately 4 MPa and a co-current flow between feedstock and an oxidising agent. Residence times are short and so, high temperatures and small fuel particles are needed. O₂ is preferable instead of air since NO_x gases are formed at this temperature.³³ The outlet gas stream is mainly composed of hydrogen, carbon monoxide, and carbon dioxide, almost no devolatilised products and liquid hydrocarbons in a much lower concentration as well.

Fluidised-bed gasifier operates in between the two previous reactor types in both composition and temperature (925–1050 °C). Gasification takes place in a fluidised bed in bubbling mode or circulating mode promoting heat and mass transfer.²⁰

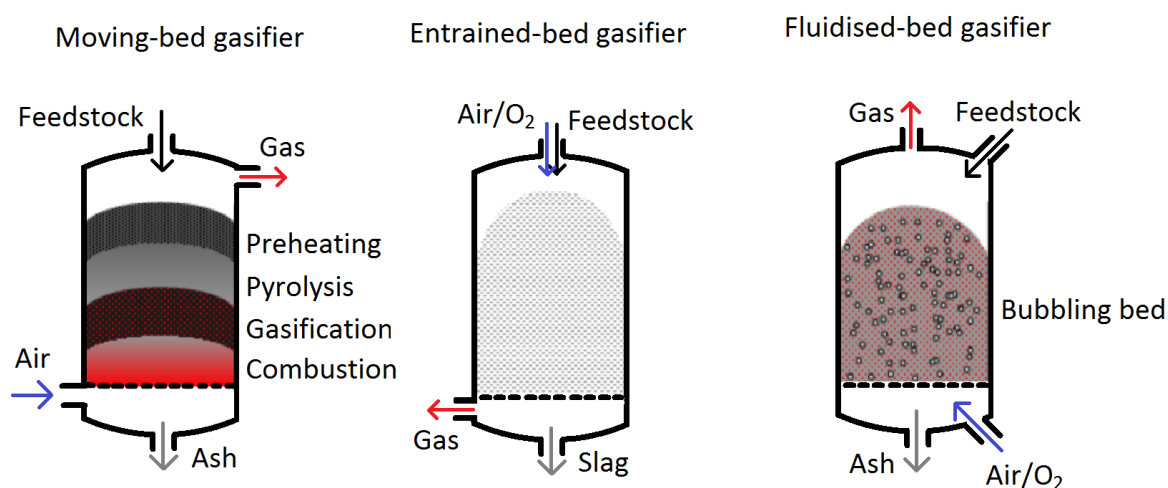


Figure 8. Scheme of gasifiers employed in coal gasification.

In all these systems, the heat required for gasification is provided by the partial oxidation of the coal. These gasification processes are mostly non-catalytic although, catalytic coal gasification has been investigated as well. During the last 30-40 years, in-depth research has been carried out for a large portion of the periodic system for the catalysis of coal and carbon gasification. Alkali, alkaline earth and transition metals have been the most investigated, although noble metals, lanthanides and actinides have also been studied,^{34–36} although the complexity of the systems and differences in setups investigated does not allow a meaningful comparison, and therefore, much agreement in the election of the optimum catalyst has not been reached yet.³² Commercialisation of catalytic coal gasification in the next years will

depend on further improvements in the control of catalyst dispersion, catalyst–support interaction and catalytic activity.

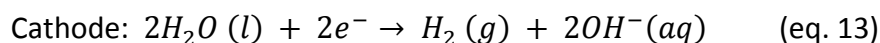
Gasifier product gases contain in all cases contaminants that need to be removed before feeding fuel cells. Since syngas is also a product of coal gasification, further conversion of CO to CO₂ through the water gas shift reaction is required. Further processing of the raw gasifier product gases can be carried out in order to increase the methane content or alter the hydrogen/carbon monoxide ratio to generate high-purity hydrogen.³²

Gasification processes normally suffer from low heat efficiency (of the order of 35–50 %) since moisture must also be vapourised.^{25,28}

Currently, this method is more expensive than steam reforming and partial oxidation because of the gasifier and the need of O₂ for the reaction process. However, since oxygen separation unit is cost-prohibitive for small-scale plants, air may be used in the gasifiers although this results in a significant dilution of the product and formation of NO_x. Furthermore, the use of coal is regarded as a cause of greenhouse gas emissions to a larger extent than other fuels. Hence, these plants need to be associated with carbon dioxide capture schemes.³⁷

1.1.5.4. Other methods: electrolysis

Among other methods electrolysis of water is by far the most used at the moment, reaching approximately 4 % of the current hydrogen worldwide production methods.^{25,28} It comprises the splitting of the chemical bonds of water molecule into hydrogen and oxygen by a direct current passing through two electrodes in a water solution according to the equations:



Typically, platinum is used as electrodes and sulphuric acid as the electrolyte, which does not corrode the electrodes, although, for industrial use, stainless steel or nickel-based electrodes are used in a potassium hydroxide solution at a temperature range of 60–80 °C.³⁸

It presents several advantages when compared with hydrogen production from fossil fuels. Water electrolysis produces very high purity hydrogen, it is an ecological process since no

greenhouse gases are produced, and the oxygen has further industrial applications, however, on the other hand, electrolysis is a very energy intensive technology.

Energetic efficiency of the electrolysis of water may reach 85 % when efficiency is the key of the process,²⁵ although, for commercial applications, where other parameters also play important roles, it is typically in the range 50–75 %.²⁸

Technologies searching for an increase in efficiency are focused on high-temperature and high-pressure electrolysis. In the former method, 800–1000 °C is reached, but, since part of the energy is applied to the system in form of heat instead of electricity, in general terms, this tends to be cheaper than ambient temperature for large-scale production. In case residual heat from another process is provided, efficiency is largely improved. At that temperature, consumption of hydrogen is approximately 5 KWh/m³. The latter method makes use of pressures in the range 120–350 bar. Compression of water requires less energy than hydrogen, thus, the necessity of a hydrogen compressor is eliminated and efficiency improved.³⁹ Normal or high-pressure electrolysis plants typically operate at 70-90 °C, consume 4-5 KWh/m³ of hydrogen and provide a cell voltage of 1.85-2.05 V. In these plants, a purity of hydrogen of 99.8 % or more is obtained.

As observed, electricity consumption is the main drawback of this technology. Then, only in regions with a large amount of electricity provided from renewable sources (waterfalls, hydroelectricity, solar or wind energy), this technology is profitable,³⁸ explaining this, the low percentage of hydrogen produced by this method.

A summary of the current technologies commercially used to produce hydrogen along with their feedstock and thermal efficiencies is presented in table 2.

Table 2. Hydrogen production technologies summary.

Technology	Feedstock	Thermal efficiency (%)
Steam reforming	Methane	70-85
Partial oxidation	Methane	60-75
Coal gasification	Coal	35-50
Electrolysis	Water + electricity	50–75 (Commercial)

1.1.6. Drawbacks

Despite the potentials of using hydrogen, besides the concerns over hydrogen industrial production, its widespread utilisation as a major energy carrier is currently limited by the capacity limitations of hydrogen storage technologies and by the safety issues related with its storage and transportation under mild conditions, which makes public acceptance difficult.⁴⁰ These safety risks include the very high flammability: in air, flammability limits are 4.0 and 77.0 % in volume at atmospheric pressure, and in oxygen, the upper limit increases up to 94 %.²⁰ Another drawback towards hydrogen economy to be faced is the energy intensive requirements in order to change its state conditions (pressure, temperature, phase) since traditional physical storage methods make use of high-pressure gas cylinders of up to 800 bar.⁴¹ Moreover, the significant weight and volume requirements are very different from those of currently used fuels. Energy per mass of hydrogen is higher than for most other fuels, however, its energy by volume is much lower than liquid fuels like gasoline. As an example, 1 kg of hydrogen at 15 bar occupies 800 litres, explaining the high pressure needed to store it. Furthermore, the energy required to transport hydrogen through pipelines of the same pipe diameter and pressure drop for natural gas is 20-30 % higher per unit of delivered energy. This means that energy transmission capacity for hydrogen is approximately 20-30 % lower than the UK annual average calorific value of 39.5 MJ/m³ for natural gas.⁴² Consequently, long distances H₂ transportation may not be economically viable.⁴³ In order to solve these problems, during the last two decades, great scientific effort has been made. Current research is exploring new methods to produce hydrogen *in situ* and store it under more favourable temperatures and pressures and focus on a sustainable, environmentally friendly source. Nevertheless, these technologies are mainly addressed for small-scale portable devices in comparison with large-scale hydrogen production commercially available techniques. In the next section, these current technologies will be overviewed.

1.1.7. Alternative solutions

Current most promising technologies to produce hydrogen *in situ* include the development of solid materials in which hydrogen is adsorbed into a porous network (physisorption), and materials whose decomposition process generates hydrogen (chemical hydrogen storage systems). These methods represent a potential route towards the development of sustainable

energy production processes. In the former method, examples of porous network are zeolites,⁴⁴ metal-organic frameworks (MOFs),⁴⁵ various carbon materials⁴⁴ and conventional organic polymers.⁴⁶ Regarding chemical hydrogen storage systems, firstly, due to several advantages as stability and safety, much attention was paid to solid-state hydrogen storage materials.⁴⁷ Possible solid phase systems include metal and non-metal hydrides,⁴⁸ amines,⁴⁹ amides,⁵⁰ ammonia-like complexes.⁵¹ However, despite these features, it presents important drawbacks as the high temperature necessary to desorb hydrogen or the slow hydrogen release kinetics. Due to this, liquid-phase hydrogen storage materials as N-ethylperhydrocarbazole,⁵² alcohols⁵³ or formic acid have been recently investigated. A more in-depth literature review will be presented later in this chapter. Figure 9 presents a scheme with the possible materials available to produce or store hydrogen.

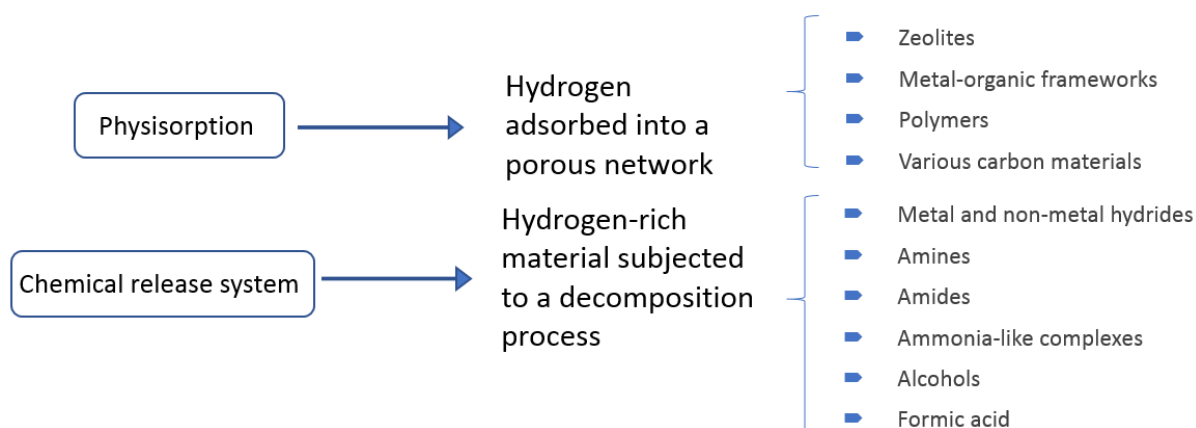


Figure 9. Scheme of possible materials used to produce or store hydrogen.

An overview of the general background and context has been introduced. At this point, a summary with the available compounds that release hydrogen has been presented, however, in order to get a more in-depth review of the mechanisms and reaction conditions that lead to hydrogen generation, a general introduction of catalysis will be provided in the next section.

1.2. Catalysis

According to IUPAC, a catalyst is “a substance that increases the rate of a reaction without modifying the overall standard Gibbs energy change in the reaction; the process is called catalysis. The catalyst is both a reactant and product of the reaction”.⁵⁴ In other words, the main function of the catalyst is to provide an alternative reaction pathway in which the total activation energy is lower compared with the non-catalytic reaction path facilitating to reach equilibrium without being consumed. Nevertheless, the catalyst does not change the thermodynamics of the reaction or the equilibrium position.⁵⁵ In industry and biology, most of the chemical reactions involve the use of catalysts or enzymes, in fact, approximately 85-90 % of materials are produced using catalysis at least in one stage.^{55,56} Actually, catalysts are not only used in chemical production but also in environmental remediation, and energy-related processes. Catalysis plays a crucial role when used in industry since it can make the process more effective economically and/or environmentally friendly.

Catalysts bond to the reactants and permit these to be converted into a product which then detaches from the catalyst without being altered, as observed in figure 10. In fact, the catalytic reaction is a cycle where the catalyst participates and is recovered in its original form.

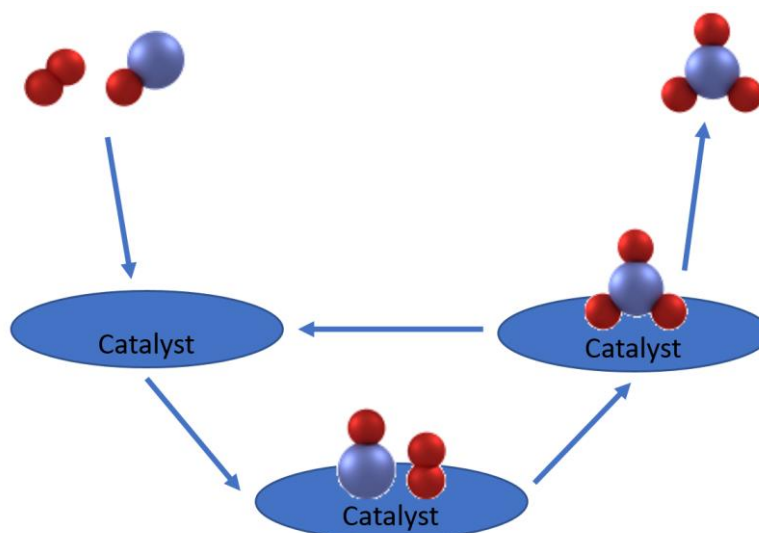


Figure 10. Scheme with the sequence of elementary steps in a catalytic reaction.

An energy diagram to explain how the catalyst accelerates the reaction will be presented in the heterogeneous catalysts section, however, the principle of the mechanism is the same for

all types of catalysts: the reactants form bonds with the catalyst in a spontaneous reaction. The formation of this complex is exothermic, and the energy of the system is lowered. The next step is the reaction between the reactants while still bound to the catalyst. There is an activation energy barrier, although it is significantly lower than that for the non-catalysed reaction. In the last step, the products detach from the catalyst in an endothermic step. The types of catalysts are introduced in the next section.

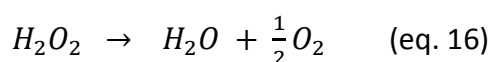
1.2.1. Types of catalysis

It is possible to differentiate among three main types of catalysis: heterogeneous, homogeneous, and bio-catalysis. In the next paragraphs, these types will be explained.

1.2.1.1. Bio-catalysis

Bio-catalysts are also named enzymes. These are large proteins that bind to the substrate through a cleft surrounded by a layer of amino acid residues. Considered to be a natural process, an enzyme is the reaction catalyst in a living cell. Enzymes permit biological reactions to occur such as the breakdown of molecules, build-up of proteins and DNA, and the storage of energy in sugars. As advantages: enzymes are extremely efficient, they can catalyse 1000 cycles per second or more in some cases, and highly selective catalysts since the shapes of both substrate and enzyme must match (Figure 11). On the other hand, enzymes are very sensitive to temperature changes. A certain increment in temperature can increase the rate at which the reaction occurs although, an increase above a certain limit can denature the proteins, this is, the breakage of the weak bonds that hold the active site in its right configuration.⁵⁷ Nature has developed organisms with proteins able to resist very high temperature, the so-called thermophiles. These are organisms that live in environments at a very high temperature such as in geothermal springs. These organisms have enzymes designed to optimally function at these conditions without denaturing.

As an example of a reaction catalysed by enzymes, one of the most representative is the decomposition of hydrogen peroxide into water and oxygen by the enzyme catalase:



This reaction can take place at a rate of up to 10^7 hydrogen peroxide molecules per second.⁵⁶

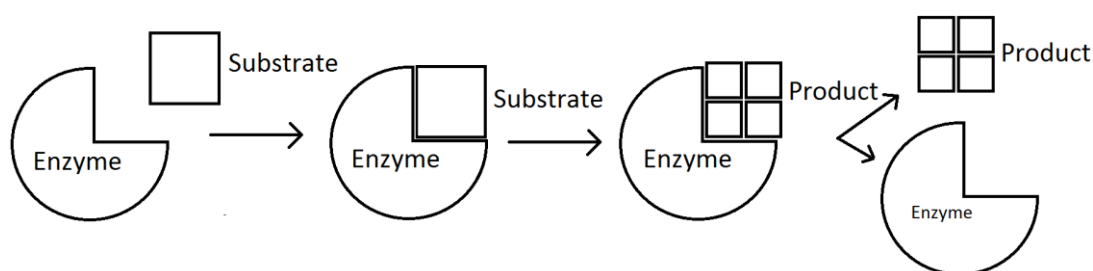


Figure 11. Schematic representation of an enzyme-catalysed reaction.

1.2.1.2. Homogeneous catalysis

In homogeneous catalysis, reagents, products and catalyst are in the same phase, most often liquid phase. The most used homogeneous catalysts are the organometallic complexes although other systems are used as well, such as acid and base catalysts in ester hydrolysis, Lewis acids in Diels-Alder reactions or porphyrin complexes in epoxidations and hydroxylations. Organometallic catalysts consist of the central metal surrounded by organic (and inorganic) ligands. Organometallic catalysts can be easily modified by changing the ligand environment. This way, the same metal can produce a variety of products from one single substrate only by changing the ligands around the metal centre as observed in figure 12. For instance, when using nickel(0) as catalyst precursor, all-trans-trimer is the product however, when allylnickel(II) complexes are used, the product is a polymer.⁵⁸

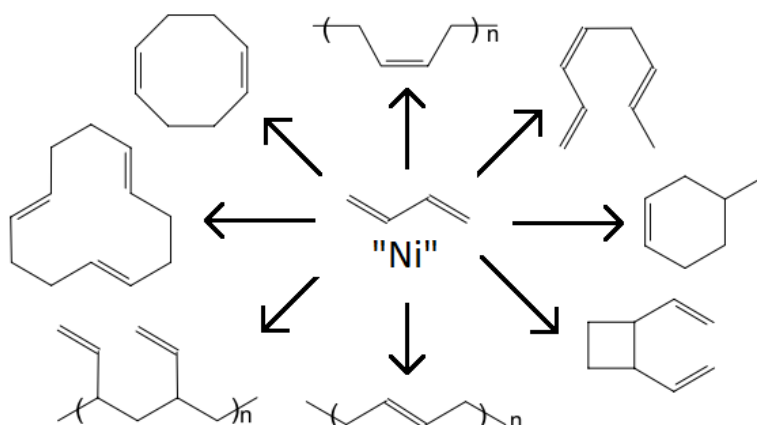
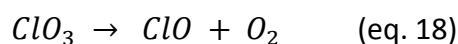


Figure 12. Effect of ligands in the nickel catalysed reaction of butadiene.

A well-known example of homogeneous catalysts is the decomposition of ozone in the atmosphere via reaction with chlorine atoms:



Chlorine, in this case, acts as a catalyst promoting the rate of decomposition of ozone.

The main advantages lie on the high selectivity reached and high utilisation since almost all the active sites of the catalyst are reachable and furthermore, single sites may be available, facilitating the study of the mechanistic aspects of the reaction. Moreover, homogeneous catalysis does not suffer from pressure drop as some applications in heterogeneous catalysts do, and deep mechanistic understanding of the multiphase processes on surfaces is therefore not needed. On the other hand, recovery and separation of products and catalyst after usage and the possibility of contamination of the products by the catalyst are major disadvantages in homogeneous catalysis.^{57,58} However, the challenge of solving the problem of separation of reactants, catalyst, and products is principally solved by three facts:

- Use of chemical and spectroscopic characterisation, usually NMR for organometallic complexes;
- Reaction kinetics are related to each metal atom;
- Catalysts are designed for special purposes according to known principles.⁵⁹

1.2.1.3. Heterogeneous catalysis

Heterogeneous catalysts are the workhorses of the chemical and petrochemical industry. In heterogeneous catalysis, both catalyst and reaction mixture are present in a different phase, being the catalyst usually in solid phase and reagents and products in liquid or gas phase. Without considering the diffusion steps, heterogeneous catalysis is mainly composed of three stages (i) the reagent is temporarily adsorbed into the active site of the catalyst surface, (ii) where the reaction takes place and subsequently, (iii) the product is desorbed from the catalyst due to the weak bond with the surface (Figure 13).

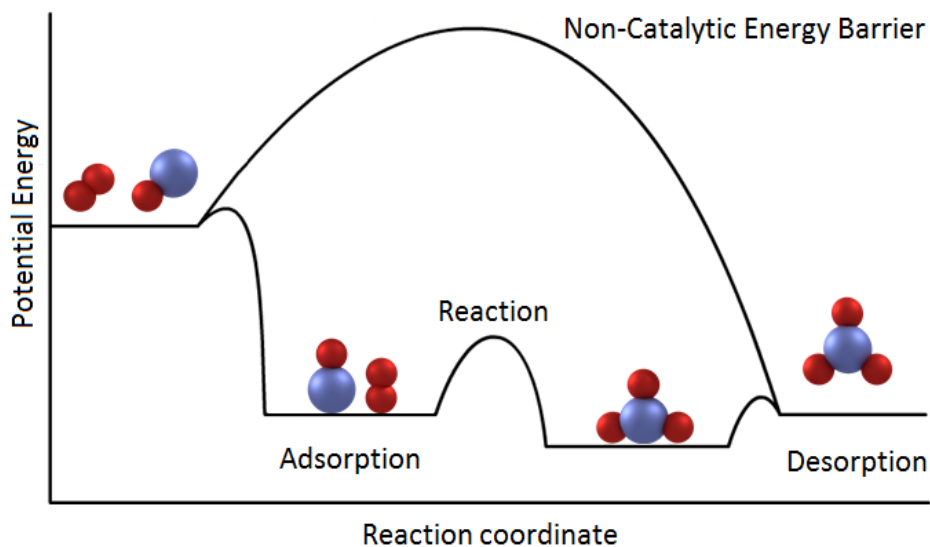


Figure 13. Mechanism of heterogeneous catalysis.

Heterogeneous catalysts can be classified as:

- Unsupported (bulk) catalysts
- Supported catalysts
- Coated catalysts

In some cases, **unsupported heterogeneous catalysts** need to be used, particularly when the support can cause side reactions or product retention by absorption. Examples of these catalysts are metal oxides, metals and metal alloys, carbides or nitrides. Metal oxides make up a large and important class of catalytically active materials. Examples such as NiO, or perovskite (CaTiO_3) are used respectively in semiconductors field and in fuel cells or as catalysts for combustion. Metal gauzes or grids are mainly used as catalysts in strongly exothermic reactions requiring catalyst beds of small height. Some examples are Ag grids used in the dehydrogenation of methane, and Pt-Rh grids in ammonia oxidation in the nitric acid process. Carbides and nitrides of transition metals usually adopt crystal structures in which C and N atoms occupy interstitial positions. These compounds present unique properties similar to ceramic materials in terms of melting point and hardness although with the electronic and magnetic properties of metals. Carbides and nitrides are excellent catalysts in hydrogenation catalysts or in hydrazine decomposition.

Supported catalysts play an important role in many industrial processes. Highly active, selective and stable supported heterogeneous catalysts are crucial for an economically profitable industry. In order to use the often expensive materials in an economical way, the solution is to increase the effective surface area of a valuable catalytic material by supporting it on an inert material or metal oxide maximising surface area and therefore the contact between reagent and active sites. Hence, an efficient, stable and cost-effective support is greatly important since it allows effective use and recycling of the expensive catalyst.

Metals and metal oxides are the most common supported catalysts. Metals usually present high surface free energies and thus, particles tend to grow, reducing the surface areas. Thus, metals are dispersed on high surface area supports as previously explained, with two objectives:

- Stabilising the nanoparticles under reaction conditions due to the metal – support interaction which modifies the electronic properties of the particles compared with the bulk metal;
- Forming small particles which expose high numbers of low-coordinate surface metal atoms (particle size effect).

Both electronic and size effects strongly influence the catalytic activity.⁶⁰

Besides monometallic supported catalysts, bimetallic catalysts are extensively used. These contain two different metals, typically, one active and one inactive which dilutes the active metal, or several active metals in the form of nanoparticle or nanooxide which are necessary to perform a specific reaction. This way, the selectivity of the process can be easily optimised; activity, stability and protection against poisoning may be enhanced; and furthermore, the total cost of the catalyst may be reduced. For example, in the Cu – Ni alloys, Cu is enriched at the surface since the surface free energy of copper is lower than that of nickel and so, the ratio number of available active sites and mass is higher for the alloy compared with bulk Cu.⁶¹

Supported metal nanoparticles are of great importance due to their unique physical and chemical properties and various methods of preparation which will be introduced in the next section. Supported noble metals nanoparticles are largely used in the industry even though the high cost makes some processes prohibitive. Therefore, preparation methods play a crucial role in order to disperse the metals and reduce particle size. These methods have been deeply investigated to synthesise metal nanoparticles with tailored size, shape and

composition followed by their assembly and activation on support materials helping us to identify and minimise main drawbacks of traditional synthetic methodologies.^{62–67}

Noble metals such as Pd, Pt, Rh or non-noble metals as Fe, Co, Ni, Ru supported on active carbon, carbon nanofibers, TiO₂, Al₂O₃ or SiO₂ find applications on hydrogenation and dehydrogenation reactions which is the focus of this Thesis; Au is active for low-temperature CO oxidation and Ag on Al₂O₃ is normally used in ethene epoxidation.

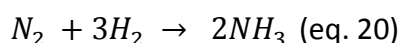
Coated catalysts are catalytically active layers applied on inert structured surfaces. The active layers are made of supported or bulk catalysts. The use of coated catalysts has recently become increasingly popular and one of the most typical examples are the monolithic honeycombs for environmental applications.

Once introduced the main types of heterogeneous catalysts, advantages, disadvantages and more in-depth applications will be studied.

Among the main advantages of heterogeneous catalysts are the facile separation from reactant and products; elimination of corrosion problems and liquid waste treatments; and wide range of operating conditions. On the contrary, disadvantages lie on the possible mass transfer limitations of reactants and products that can limit the efficiency of the catalyst; agglomeration of nanoparticles which is crucial for the stability and reusability (long-term performance) of the catalyst; possible loss of metal from the support due to leaching; and in some industrial processes, pressure drop is also an issue.

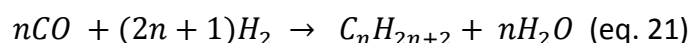
Therefore, exploration of economical methods to prepare highly reactive, stable, scalable and recyclable heterogeneous catalysts remains an important issue in the catalysis research field. More specifically, as a rule of thumb, small particle size, highly dispersed and stable nanocatalysts should be the main objectives.

Ammonia and Fischer-Tropsch synthesis are typical examples of heterogeneous catalysts largely used on an industrial scale. Ammonia synthesis by the Haber-Bosch process is among the most common applications of heterogeneous catalysis. In this method, nitrogen and hydrogen are fed over four beds of catalyst at approximately 400 °C and 15 MPa reacting according to the equation:



The most common catalyst used is iron promoted with K_2O , CaO , SiO_2 , and Al_2O_3 . Besides iron, only ruthenium-based catalysts are found to be useful for this reaction, although thousands of systems have been studied. Ruthenium is a more active catalyst and allows lower operating pressures, although it is more expensive.⁶⁰ Nowadays, the Haber-Bosch process produces approximately 450 million tonnes of nitrogen fertilizer per year, mainly in the form of ammonia, ammonium nitrate, and urea.

Fischer-Tropsch synthesis (FTS) is another example of worldwide commercial use of heterogeneous catalysts. This process is used to produce hydrocarbon chains from synthesis gas usually following the next equation:



Industrial reactors are operated at 220 – 240 °C and 2 – 4 MPa. Typically, metals like iron, cobalt, and ruthenium can be used as catalysts being iron and cobalt the most used due to the price of ruthenium. Iron is active for the water-gas shift reaction that allows the use of carbon-dioxide-containing syngas, however, iron presents kinetic inhibition by water. On the other hand, cobalt catalysts are active at lower reaction temperatures and present an extended durability of up to five years compared to about six months for iron, with the disadvantage that cobalt is more expensive than iron.⁶⁰

1.2.2. Preparation of catalysts (supported metal nanoparticles)

As previously commented, preparation methods, among other factors, strongly influence the properties of the nanoparticles, thus, a good knowledge of the process is essential.

Nanoparticles in the diameter range 1-10 nm were predicted by physicists to present electronic structures different from those of bulk metal due to quantum size effects. This occurs when the de Broglie wavelength of the valence electrons is of the same order as the size of the particle itself.⁶⁸ Therefore, particle size, interparticle distance, and shape of the nanoparticles strongly affect the physical properties of these particles. Thus, tailoring the preparation of supported metal nanoparticles is of crucial importance in catalysis.⁶⁹⁻⁷¹ Besides the preparation method, the selection of the right support plays an important role as well since by modifying the metal-support interaction, physicochemical features such as

dispersion, surface area and pore diameter of the support and metal particle size can be altered.^{72,73}

Often, catalysts are synthesised in batch reactors on a small scale. In many cases, scale-up of the process is needed, however, increasing the volume of the reactor or reagent concentrations may lead to mass and thermal transport inhomogeneities resulting in catalysts with significant variations between batches. Continuous flow methods in some cases solve these issues. The main advantages of using continuous flow methods reside on the improved heat and mass transfer leading to better uniformity; faster heating and cooling due to the reduced reaction volume and so, requires less energy input; and the possibility of automation.⁷⁴ In terms of research, usually a small amount of catalyst is enough to produce the necessary data, in that case, batch reactors present an advantage over continuous flow reactors since the set-up costs are initially less expensive and more importantly in research, linking with the previous paragraph, each batch can be easily tailored according to the catalyst physicochemical requirements.

Metal nanoparticles can be prepared either by “top down” or “bottom up” approaches. In “top down” procedures, bulk metals are systematically broken down by physical methods to generate nanoparticles of desired dimensions. On the contrary, in the “bottom up” approach, the formation of nanoparticles lies in the growth of clusters of several metal atoms. It involves a chemical reduction in two steps: nucleation and subsequent growth. The advantage of the “top down” method is the production of a large amount of nanocrystals however, uniformity of the nanoparticles and the control of the particle size is very complex.^{75,76} Therefore, the “bottom up” approach is the most used method for size- and shape-controlled nanoparticles syntheses. Within this approach, the main difference between the preparation techniques resides on how the metal is introduced and dispersed on the support. Some of the most important and the methods used in this Thesis are sol-immobilisation, impregnation, and solid grinding.

1.2.2.1. Sol-immobilisation (SI)

The immobilisation of pre-formed metallic sols finds applications in many industries since it provides a great control of the particle size distribution. This method immobilises the nanoparticles present in a colloidal suspension on a support by using stabiliser ligands and a

reducing agent. Typically, this preparation method follows these steps: (1) an aqueous solution of the metal salt precursor with a stabiliser ligand is prepared, (2) then the reducing agent is added, (3) the support is supplied to the mixture, (4) the stabiliser is removed by washing the catalyst with water, and (5) the catalyst is dried. In Chapter 2, a more in-depth explanation and step by step graphical representation of the process followed in this Thesis will be provided.

Reduction of the metal precursor is typically performed by chemical reduction (with NaBH_4 or alcohol) but electrochemical, thermal decomposition or photoreduction is used in the literature as well. The colloidal solution is immediately formed upon reduction of the metal precursor.

The role of the stabiliser is to prevent the nanoparticles from aggregation. In some cases, it may not be necessary since metal colloids are stable over long periods, however, the use of a ligand is essential in order to obtain a uniform and controlled particle size. Three stabilisation methods have been developed:

- Increasing the surface potential and/or charge density by adsorption of surface active long-chain ions (e.g., citrate).
- Reducing Van der Waals forces by adsorption of relatively rigid hydrophilic macromolecules (e.g., dextrin, starch) enhancing the interaction with the solvent.
- Steric stabilisation: high molecular weight molecules such as polymers are adsorbed in the nanoparticles (e.g., PVA).

Figure 14 presents a graphical representation of electrostatic and steric stabilisation.

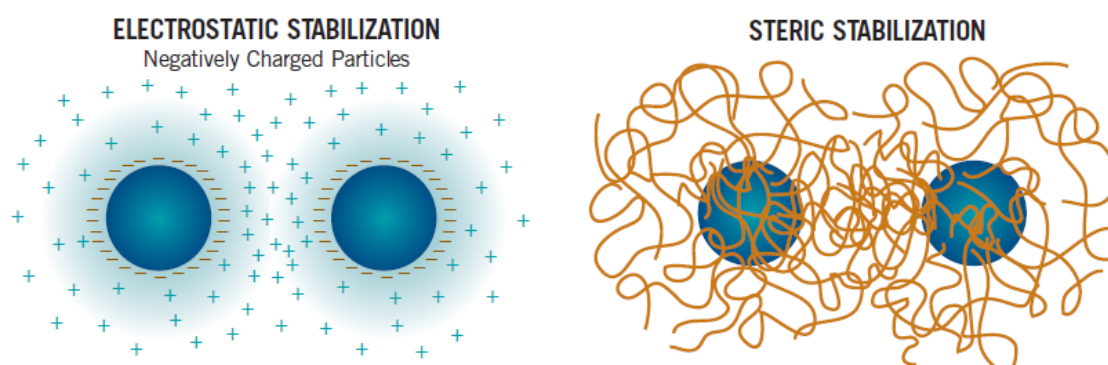


Figure 14. Electrostatic and steric stabilisation methods scheme.⁷⁷

The advantages of sol-immobilisation method lie on the fact that particle size distribution can be controlled by modifying the preparation parameters and therefore, metal nanoparticles can be synthesised with a narrow particle size distribution and with a specific morphology.⁷² Easy control of shape and composition is also achieved and furthermore, since the metal is already reduced, generally no subsequent catalyst reduction is needed.⁷⁸ Usually, a highly dispersed metal catalyst is obtained. The main disadvantages lie on the challenges when scaling-up, the requirement of removal of impurities introduced by the reducing agent or ligand and the limitation of the number of supports since for instance, SiO_2 and Al_2O_3 cannot be used due to the high dependency on the iso-electric point (IEP) of the support.^{79,80}

1.2.2.2. Impregnation (IMP)

Impregnation is the simplest and most widely used method in industry to prepare supported metal catalysts. This method makes use of the characteristic pore volume of each support. The addition to the support of this exact volume of the solution containing the catalyst precursor will fill the pores by capillarity. This is the so-called incipient wetness impregnation. In case an excess of solution is used, the method is named wetness impregnation, and instead of capillary action process, the driving force for the precursor to entering the support is diffusion. As in incipient wetness impregnation, the volume of solution added is the exact amount to fill the pores, this maximizes the loading of active components in the pore matrix of the catalyst support. The system is then allowed to dry and heat treated under air to decompose any undesired salts and volatiles, and reduced in hydrogen into the supported metal catalyst.⁸¹ This reduction step can be instead chemically performed with a reducing agent after adding the support and before washing.

The maximum loading is limited by the solubility of the precursor in the solution. The characteristics of the particles are strictly linked to the drying and calcination conditions and on the type of support.⁷⁹ The hydrophobic or hydrophilic character of the support plays an important role when choosing the solvent. In hydrophobic supports, the capillary pressure becomes negative and an external pressure is necessary in order to force the liquid into the pores. In this case, a less polar solvent such as ethanol is typically used, although precursor solubility is usually lower.⁸²

The simplicity of the preparation method has made impregnation attractive for industrial scale purposes. The advantages of this technique lie on the higher metal content that is possible to support and that there is no necessity of preformed nanoparticles. On the other hand, the particle size can reach a large value and it may result in a broad distribution of metal particle size and uneven element composition. Sintering during thermal treatment can take place as well, which can lead to poor catalytic activity and quick deactivation of the catalyst.

1.2.3. Liquid-phase chemical hydrogen storage systems

As commented in section 1.1.7, decomposition of hydrogen containing liquid-phase compounds may be the most plausible solution in the development of a hydrogen economy. Homogeneous and heterogeneous catalysis has been extensively used in the decomposition of liquid hydrogen carrier systems (table 3), for instance, sodium and lithium borohydrides, as well as ammonia borane, have been widely studied since it provides a safe and low-cost route to produce hydrogen.^{51-53,83} Ammonia decomposition has been also studied at temperatures below 500 K showing a significant reduction in activation energy when using carbon nanotube catalysts promoted with cesium.⁸⁴ One of the most promising solutions consists of the utilisation of hydrous hydrazine as reagent.⁸⁵ It presents the unique advantage that N₂ is the only by-product for the complete decomposition.⁸⁶

Methanol is another suitable material to store and handle hydrogen. Different thermochemical methods can be used in order to produce hydrogen from methanol. Methanol steam reforming is a well-known process which has attracted attention in energy generation using indirect methanol fuel cells. It takes place at medium temperatures (200 - 300 °C) however, the distribution of products is too wide preventing a higher growing.⁵³ Beller *et al.* studied the dehydrogenation of methanol using ruthenium pincer complexes in methanolic sodium hydroxide,⁸⁷ achieving a TOF of 4719 h⁻¹, showing a higher selectivity and reaction rates⁸⁸ if compared with the previous methods and mainly producing hydrogen and carbon dioxide in the form of carbonate.

Other alcohols like ethanol have also been studied as hydrogen carriers. Ethanol is a non-toxic fuel, inexpensive and moreover, in countries like USA and Brazil, the infrastructure required for ethanol production and distribution is already established since ethanol is currently distributed. Those factors have made ethanol an economically and environmentally attractive

fuel. Back in the 1970s, several studies were carried out in the dehydrogenation of ethanol among other alcohols using homogeneous catalysts. The decomposition of ethanol by rhodium–tin chloride catalysts in acidic media was firstly studied by Charman *et al.*⁸⁹ Beller *et al.* also described the dehydrogenation of ethanol to ethyl acetate and acetaldehyde using a ruthenium pincer complex producing an initial TOF of 1483 h⁻¹.⁹⁰

Table 3. Physical characteristics of liquid-phase chemical storage.

Liquid chemical storage	Density at room temperature (g/cm ⁻³)	Hydrogen content (wt. %)	Ref.
Sodium borohydride	1.07	10.8	91
Lithium borohydride	0.67	18.4	92
Ammonia borane	0.74	19.6	91
Ammonia	0.73	17.6	92
Hydrous Hydrazine	1.02	12.5	92
Hydrazine borane	0.78	15.4	91
Methanol	0.79	12.5	92
Ethanol	0.79	13.0	93
Formic acid	1.22	4.4	94

1.2.4. Formic acid

For several advantages compared with the previous materials, formic acid seems to be one of the most adequate compounds to be used in a hydrogen economy environment. Formic acid is a major product formed during biomass processing. It has been reported as a safe and convenient hydrogen storage material. It contains a volumetric hydrogen content of 4.4 wt. % of hydrogen, however, although it is relatively low compared with other hydrogen carriers systems, its high density produces a volumetric capacity of 53.4 g H₂/L at standard temperature and pressure which makes this system suitable for automobile and portable applications.⁹⁴ Furthermore, formic acid is in liquid state at room temperature, highly stable, environmentally benign, non-toxic and its decomposition produces mainly gaseous products: H₂/CO₂.⁹⁵ According to the U.S. Department of Energy, formic acid is one of the most

promising hydrogen storage materials and its volumetric capacity surpasses that of most other storage materials today.¹² Hence, an effective and controlled release of hydrogen via selective decomposition of formic acid to CO₂ and H₂ is a desirable approach.

1.2.4.1. Natural sources of formic acid

Formic acid naturally occurs in honey, fruits, leaves of some urticant plants and in the venom of bites and stings of ants and bees. It is found too in the product of photooxidation of alkanes and alkenes.^{96,97} Formic acid is an intermediary human metabolite: typically, methanol, introduced in the organism by the peels of apples or by decomposition of aspartame from sugar-free drinks among other sources, is oxidised in the liver to formaldehyde which is further oxidised into formic acid and then to formate which is excreted.⁹⁸

1.2.4.2. Commercial production of formic acid

Commercial production of formic acid has substantially increased in the past decades, reaching 950 000 tonnes/annum in 2014.⁹⁹

These commercial methods of production include:

- Hydrolysis of methyl formate. This is the currently dominant process. Approximately 80 % of the installed capacity is based on this process.⁹⁹ It is split into two stages: in the first stage, methanol is carbonylated with carbon monoxide; in the second stage, methyl formate is hydrolysed to formic acid and methanol. The methanol resulting from this process is returned to the first stage.

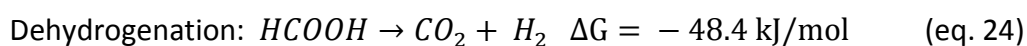


- The other current production method involves the formation of the free acid from its salts. It accounts for approximately 20 % of the total production of formic acid.⁹⁹ Sodium formate or calcium formate reacts with sulphuric, nitric or phosphoric acid. Due to the high cost of reactant formates, this production method is not economically profitable nowadays.

- Formic acid is also a by-product in the production of acetic acid by liquid-phase oxidation of naphtha or butane although, nowadays acetic acid is produced from carbonylation of methanol, in which formic acid is not formed.
- Formic acid is also a by-product in the conversion of cellulose to γ -Valerolactone (GVL). C6-sugars, water and mineral acids (sulphuric or hydrochloric acid) react producing formic acid, levulinic acid and the mineral acid used as a reactant.
- The production of formic acid by hydrolysis of formamide was of high importance several decades ago when about one third of the world production was obtained by this method,¹⁰⁰ however, since the consumption of ammonia (mainly used in the fertilisers industry and also as precursor of nitrogenous compounds and cleaner) and sulphuric acid (also used in the fertilisers and chemical industry) has increased, this process has become economically inferior compared with hydrolysis of methyl formate.
- Carbon dioxide hydrogenation in alcohol can produce formic acid in an almost water-free environment.
- Biomass conversion under mild conditions is the most sustainable method to produce formic acid, it means that the carbon neutral hydrogen storage cycle can be completed.¹⁰¹ It uses polyoxometalates as oxygen-source catalysts.¹⁰² Typically, Keggin-type polyoxometalates of the series $[H_{3+n}PV_nMo_{12-n}O_{40}]$ has been extensively used, and the Lindqvist-type catalyst $K_5V_3W_3O_{19}$ has recently presented promising results.^{103,104}

1.2.4.3. Formic acid decomposition

Formic acid decomposition occurs by two different pathways: dehydrogenation (1) and dehydration (2). Dehydration usually is promoted by heating and acidity. Selective dehydrogenation is indispensable for the production of ultrapure H_2 without undesirable dehydration since toxic CO contamination produced by the latter pathway is not tolerated by fuel cells and also reduces the activity of Pd catalysts.



The proposed cycle can be closed when CO_2 evolved during dehydrogenation of formic acid is reduced with an external supply of low purity H_2 (Figure 15).¹⁰⁵

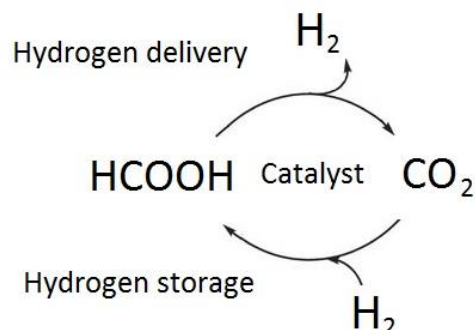


Figure 15. Formic acid/carbon dioxide cycle for hydrogen storage.

Formic acid has been intensely investigated for hydrogen generation by either homogeneous or heterogeneous catalytic decomposition approaches. There are reports of effective decomposition of formic acid using homogeneous catalysts at ambient temperatures and, recently, the catalytic efficiency has been significantly improved.^{106,107} In the next section, some of these most representative homogeneous and heterogeneous systems are introduced.

1.2.5. Homogeneous catalytic decomposition of formic acid

Previous studies have reported the utilisation of homogeneous catalysts to decompose formic acid at ambient temperatures and pressures (Table 4). Mild conditions are of key importance since fuel cells are expected to supply energy to portable devices with low heat management profile. Focusing only on the main important results at mild conditions, Fukuzumi *et al.* reported a TOF of 426 h^{-1} at room temperature, using a heterodinuclear iridium-ruthenium complex $[\text{Ir}(\text{Cp}^*)(\text{H}_2\text{O})(\text{bpm})\text{Ru}(\text{bpy})_2]^{4+}$ in presence of sodium formate.¹⁰⁸ However, they reached a higher TOF of 1880 h^{-1} when they prepared a cyclometalated organoiridium complex $[\text{Ir}(\text{Cp}^*)(\text{pba})(\text{H}_2\text{O})]^+$ based on 4-(1H-pyrazol-1-yl)benzoic acid (pba) in a potassium formate system.¹⁰⁹ At slightly higher temperature, $40 \text{ }^\circ\text{C}$, Beller *et al.* studied several homogeneous catalysts in the presence of amines. An initial TOF of 3630 h^{-1} was reached

using a ruthenium phosphine catalyst $\text{RuBr}_3 \cdot x\text{H}_2\text{O}/3\text{PPh}_3$ in a $5\text{HCOOH}-2\text{Net}_3$ mixture,¹¹⁰ while, with $[\text{RuCl}_2(\text{PPh}_3)_3]$ and dimethylformamide, a TOF of 2688 h^{-1} was reached.¹⁰⁷

Table 4. Homogeneous catalysts for the decomposition of formic acid at mild conditions.

Catalyst	T (°C)	TOF (h ⁻¹)	Ref.
$[\text{Ir}(\text{Cp}^*)(\text{H}_2\text{O})(\text{bpm})\text{Ru}(\text{bpy})_2]^{4+}$	25	426	108
$[\text{Ir}(\text{Cp}^*)(\text{pba})(\text{H}_2\text{O})]^+$	25	1880	109
$\text{RuBr}_3 \cdot x\text{H}_2\text{O}/3\text{PPh}_3$	40	3630	110
$[\text{RuCl}_2(\text{PPh}_3)_3]$	40	2688	107
$[\text{RuCl}_2(\text{benzene})]_2/6\text{dppe}$	40	900	111
$[\text{Ir}(\text{Cp}^*)(\text{H}_2\text{O})(\text{dhbpy})]^{2+}$	60	3100	112
$\text{AlH}(\text{bip})(\text{THF})$	90	14000	112
$\text{AlH}(\text{bip})(\text{THF})$	65	5200	113
$\text{Fe}(\text{BF}_4)_2 \cdot 6\text{H}_2\text{O}/2\text{PP}_3$	80	5390	114

Beller *et al.* made a remarkable discovery when they found that the hydrogen generation from formic acid using ruthenium-based catalysts could be improved by the utilisation of visible light and proposed the mechanism shown in figure 16.¹¹⁵

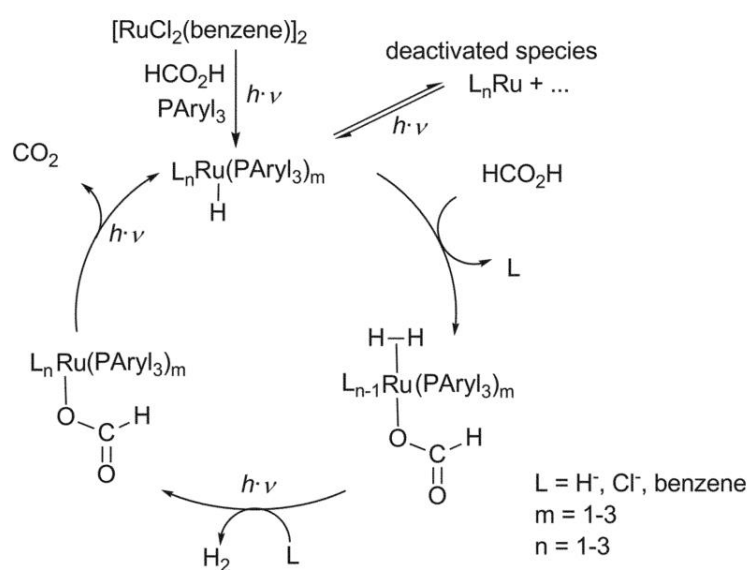


Figure 16. Proposed mechanism for the Ru-catalysed decomposition of formic acid with a $[\text{RuCl}_2(\text{benzene})]_2/\text{PARyl}_3$ catalyst.¹⁰⁶

According to their investigations, visible light irradiation activates the ruthenium precursor $\text{RuCl}_2(\text{benzene})_2$ which gives an aryl phosphine-ligated ruthenium hydride complex. At the same time, benzene ligand is cleaved under light irradiation. Formic acid subsequently is added to the complex and a dihydrogen formate ruthenium complex is formed. Subsequent eliminations of dihydrogen and carbon dioxide reform the initial ruthenium hydride phosphine complex. Additionally, irradiation prevents the catalyst from being deactivated. Simply by switching on and off the light source, it allows or stops the hydrogen generation from formic acid.¹⁰⁶

They showed promising results in terms of catalyst stability and selectivity to H_2 and CO_2 while significantly improving the catalytic efficiency however, the separation of the catalyst from the reaction mixture, in several cases harsh reaction conditions, moderate selectivity and the need for organic solvents/additives prevent formic acid decomposition using homogeneous catalysts from scaling-up for industrial applications.^{116,117} An alternative and attractive approach is the utilisation of heterogeneous catalysts that can achieve high catalytic activity (high turnover frequency - TOF) and utilisation of high substrate to metal molar ratio at low temperature and with high selectivity towards hydrogen.^{12,118}

1.2.6. Heterogeneous catalytic decomposition of formic acid

Heterogeneous gas-phase formic acid decomposition to hydrogen and carbon dioxide was first reported by Sabatier in 1912.¹¹⁹ Since then, both gas and liquid-phase catalytic decomposition of formic acid has been thoroughly studied in literature with monometallic and multimetallic systems.

Initially, studies were mainly performed in gas phase using metals¹²⁰ or metal oxides,¹²¹ however, gas-phase catalytic decomposition of formic acid requires either an inert carrier gas to dilute formic acid below its saturated vapour pressure or an increment of the temperature to at least 100 °C.¹²² At this temperature, using 1 wt. % Pd/C, Bulushev *et al.* reached a TOF of 255 h^{-1} ,¹²³ although due to these drawbacks and low selectivity obtained, these factors limit the utilisation of gas-phase formic acid decomposition for fuel cells applications. As previously commented, in order to utilise hydrogen in a fuel cell in portable devices, it is necessary to develop heterogeneous catalysts for liquid-phase formic acid decomposition under mild conditions.

Heterogeneous catalysts used in liquid-phase formic acid decomposition are mainly supported mono-/bi-/trimetallic nanoparticles with usually Pd as the principal metal component.

Starting with monometallic systems, Jiang and co-workers synthesised *in situ* Pd/C in presence of citric acid used as a dispersion agent to prevent aggregation of nanoparticles. This catalyst presented an average particle size of 2.8 nm and displayed a TOF of 64 h⁻¹ after 160 min at 25 °C. In comparison, the catalyst synthesised in absence of citric acid reached an average particle size of 11.2 nm and a TOF of 16 h⁻¹. It is clear that this difference in activity is related to the formation of smaller particles with higher accessibility of the surface of the nanoparticles prepared in presence of citric acid compared with those prepared with another dispersing agent such as polyvinyl pyrrolidone or ascorbic acid. They obtained a promising reusability of the catalyst after two runs, however, after the fourth run the catalyst seriously lost its activity.¹²⁴ Chan *et al.* studied the performance of Pd/C toward formic acid decomposition at temperatures between 21 °C and 60 °C, and using formic acid concentrations between 1.33 and 5.33 M showing that the order of reaction to formic acid decreases with the increase of temperature from 0.51 to 0.37. At 30 °C, an initial TOF of 48 h⁻¹ is reported which is lower than previous studies however, they confirmed that HCOOH decomposition on Pd is a size-dependent reaction and more importantly, found an optimal particle size distribution in the range 1.8-3.5 nm.¹²⁵ Nevertheless, even if promising results, the majority of Pd/C catalysts deactivate quickly due to the poisoning intermediates, resulting in its failure in applications.¹²³ Recent research has shown how to overcome this challenge by using a solution of formic acid and sodium formate of 9:1 volumetric ratio respectively and Pd/C reaching a TOF of 228.3 h⁻¹ at 30 °C after two hours.¹²⁶ Furthermore, the mechanism proposed for the decomposition of sodium formate does not produce CO, unlike the decomposition of pure formic acid under certain conditions.

Using this same solution of formic acid and sodium formate of 9:1 volumetric ratio with Pd nanoparticles deposited on a resin, a high TOF of 820 h⁻¹ at 75 °C with a CO evolution lower than 5 ppm was achieved by Yamashita and co-workers. In this work, they reported the use of a basic resin bearing -N(CH₃)₂ functional groups within its macroreticular structure as an efficient organic support for the active formic acid:sodium formate decomposition with Pd nanoparticles with an average particle size of 1.7 nm. Figure 17 displays the proposed scheme

for the reaction pathway on the surface of Pd nanoparticles within the basic resin showing the participation of the Pd–formate species as a reaction intermediate. Surface properties of these resins such as the hydrophilic/ hydrophobic characteristics and the easy introduction of functional groups, besides the fact that resins stabilise highly dispersed metal nanoparticles, have made these materials very attractive from the catalyst design point of view.¹²⁷ However, a lower temperature would be preferable for fuel cell applications since low heat management is required.

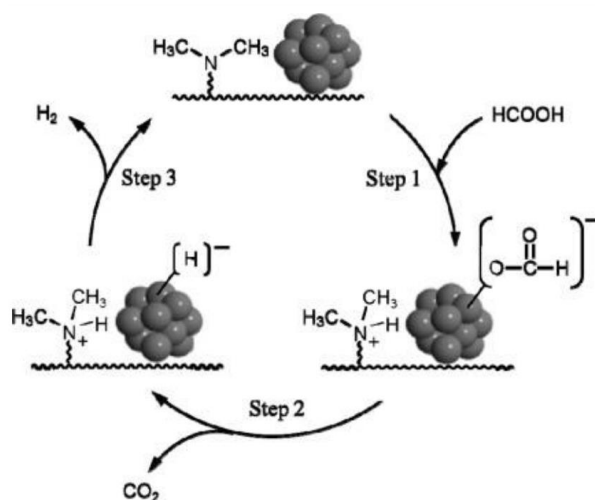


Figure 17. Proposed reaction pathway for formic acid decomposition using Pd supported on the basic resin.¹²⁷

Besides Pd, other noble metals have been used in literature such as Au or Pt. An important discovery was made by Ojeda and Iglesia. They reported that the active sites are not located on TEM-visible clusters but on the smaller Au domains such as isolated Au atoms and conclude that the activity of the gold catalyst supported over Al_2O_3 was much higher than that of Pt, likely due to the size of these gold domains. In this work, they have also investigated the mechanism of reaction on the $\text{Au}/\text{Al}_2\text{O}_3$ and $\text{Pt}/\text{Al}_2\text{O}_3$ using kinetic isotope effect (KIE – explained in Chapter 2). The exclusive formation of HD using both HCOOD and DCOOH indicates that the absorbed H atoms from $-\text{OH}$ and $-\text{CH}$ bond recombine together, and desorption is an irreversible step. KIE values ($r_{\text{H}}/r_{\text{D}}$, this means, the ratio between the reaction rate when using HCOOH and the reaction rate when using the isotope) for HCOOD were 1.1 and 1.6 for Pt and Au respectively, where for DCOOH KIE were 1.7 and 2.5 and finally for DCOOD were KIE are 2.1 and 4.7. These values suggest the dissociation of O-H as a first step,

almost thermodynamic in the case of Pt. The H adsorption is followed by the reaction between H atom and C-H bond of formates to form hydrogen and carbon dioxide and less than 10 ppm of carbon monoxide making it suitable for fuel cell applications.¹²⁸ Cao and co-workers reported for the first time the formic acid-amine mixture dehydrogenation using Au sub-nanoclusters (~1.8 nm) dispersed on ZrO₂. The reaction proceeded efficiently and selectively, reaching a high TOF of 1590 h⁻¹ at 50 °C.¹²⁹ In this study, the authors foresee a new generation of advanced nanocatalysts produced by tuning the Au clusters at the subnano level.

Regarding bimetallic systems, as previously explained, either both metals are active, or one metal is active and one inactive, diluting the active metal. When optimised, bimetallic catalysts typically improve the activity and selectivity of the process and may reduce the total cost of the catalyst. The first reported study on the formic acid decomposition by bimetallic catalyst was published back in 1957 using Pd-Au alloy wires as catalytic materials.¹³⁰ Since then, activity, selectivity and reusability have been greatly improved. Sun *et al.* compared the formic acid decomposition using monometallic Pd/C, Au/C and bimetallic alloys with different Au-Pd atomic compositions. They obtained the highest activity with an alloy C-Au₄₁Pd₅₉ catalyst with an average particle size of 4 nm, reaching an initial TOF of 230 h⁻¹ at 50 °C with an apparent activation energy as low as 28 kJ/mol. The monometallic counterparts presented a much lower activity, being the TOF for Pd/C, 30 h⁻¹ and, for Au/C, 80 h⁻¹, all under the same conditions (Figure 18).¹³¹

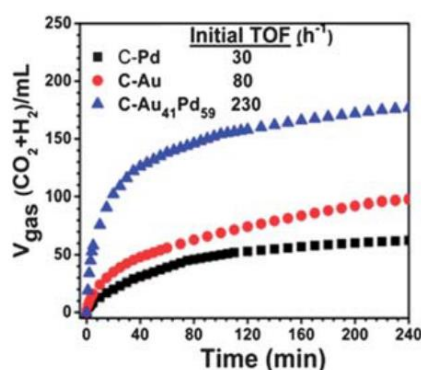


Figure 18. Gas evolution vs. time for Pd, Au and bimetallic catalysts.¹³¹

This result shows that bimetallic nanoparticles can promote the catalytic activity and selectivity for formic acid dehydrogenation compared to the monometallic species. Since the catalytic activities are dependent on the catalyst surfaces, these can be modified by adding a different metal or changing the morphology. They explained this enhancement by the fact that an alloy of Au and Pd can moderate the formic acid adsorption and activation during the reaction.

Xing and co-workers reported the development of Pd–Au and Pd–Ag alloys supported on carbon to overcome the poisoning and stability issued on monometallic Pd analogues. These bimetallic particles generated high purity hydrogen production from the decomposition of formic acid at low temperatures. They found that alloying Pd with Cu, Ag or Au, adsorption of CO on Pd is inhibited and consequently the reaction is not affected since the active sites are free. Thus, the concomitant CO poisoning is removed. The authors also reported that the activities of Pd–Au/C and Pd–Ag/C can be enhanced by co-deposition with CeO₂ due to the oxidation of CO by cationic palladium species produced by CeO₂, or the fact that formic acid may decompose by a more efficient route due to the presence of CeO₂(H₂O)_x on the Pd surface.¹³²

Tsang *et al.* developed Ag-Pd core-shell nanoparticles (Ag particle size 8 nm) with the thinnest continuous Pd shell (Figure 19) and supported on carbon-based materials obtaining a TOF (based on the surface Pd site over the Ag core-Pd shell) of 125 h⁻¹ at 20 °C and 252 h⁻¹ at 50 °C with a reported activation energy of 30 kJ mol⁻¹, one of the lowest reported in the literature at the moment of publication.

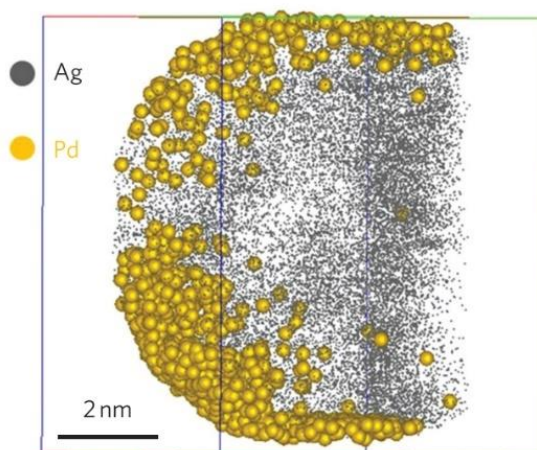


Figure 19. Topographical view of Ag core (grey) Pd shell (yellow) particle.¹³³

They explained this higher activity of the core-shell structure relating it to a larger promoting effect of the core metal than in the case of the alloy structure. When increasing the temperature above 50 °C, CO was detected in concentrations not desirable for fuel cells, above 20 ppm due to the poisoning of the catalysts. Pure Pd and Ag/Pd alloy are studied and a higher TOF was produced with the alloy, nevertheless, the poorer volume of hydrogen produced prevents this catalyst to be cost-effectively used.¹³³

Sun and co-workers reported a composition-controlled synthesis of monodisperse 2.2 nm highly active and durable Ag-Pd NPs. They studied the composition-dependent catalysis and found that the Ag₄₂Pd₅₈ NPs have the highest activity of those studied in their research with an initial TOF of 382 h⁻¹ and an apparent activation energy of 22 ± 1 kJ mol⁻¹.¹³⁴

Cheng *et al.* reported that MIL-101, a metal-organic framework, loaded with Ag-Pd alloy with an average particle size of 2.7 nm, resulted in 100 % selectivity for hydrogen generation from formic acid solution with TOF of 848 h⁻¹ at 80 °C.¹³⁵

Recently, Zahmakiran *et al.* reported an easy and reproducible synthesis method to produce well-dispersed bimetallic Pd-MnO_x nanoparticles with an average particle size of 4.6 nm, supported on 3-aminopropyl functionalised silica (Pd-MnO_x/SiO₂-NH₂). This catalyst presents a very high activity (TOF = 1300 h⁻¹ at 50 °C) at high conversion (> 99 %) and selectivity (> 99 %). These reported values are among the best heterogeneous catalysts reported in the additive-free dehydrogenation of formic acid under mild conditions. Furthermore, Pd-MnO_x/SiO₂-NH₂ catalyst retained ca. 80 % of its initial activity after the fourth run with complete conversion of formic acid to hydrogen and carbon dioxide. This is one of the most promising research and can be a milestone towards an efficient and profitable hydrogen economy.¹³⁶

Regarding these high TOF values, Xu and co-workers synthesised stable Pd nanoparticles on nanoporous carbon MSC-30 and produced a formic acid decomposition with a TOF of 2623 h⁻¹ at 50 °C and 750 h⁻¹ at 25 °C, without undesired CO formation. This performance has been related to the small particles size (2.3 ± 0.4 nm) obtained adding NaOH before the reduction step in the deposition method and to the confinement of the NPs inside the porous structure of the carbon support. The activity of the Pd/MSC-30 is higher than the one exhibited by other Pd on porous C with similar particle size, thus stronger metal-support interaction is present in the case of MSC-30.¹³⁷

Reduced graphene oxide (rGO) has been used as a single-layer carbon substrate to anchor metal nanoparticles. Graphene has become a promising candidate as a substrate due to several properties like the high theoretical surface area ($2600 \text{ m}^2/\text{g}$) and conductivity, and low cost among others. This unusual surface area produces a great dispersion which, moreover, added to the strong metal-support interaction, make these catalysts resistant to aggregation. Yan *et al.* reported a facile method to synthesise AgPd nanoparticles with an average particle size of about 6 nm, assembled on reduced graphene oxide achieving a maximum TOF of 105 h^{-1} for the formic acid decomposition using $\text{Ag}_{0.1}\text{Pd}_{0.9}/\text{rGO}$ at $25 \text{ }^\circ\text{C}$ and reaching a 100 % selectivity towards hydrogen. They reported that oxygen-containing functionalities in GO such as carboxylic ($-\text{COOH}$), carbonyl ($-\text{CO}$), and hydroxyl ($-\text{OH}$) groups, are necessary for anchoring metal ions and to help with the control of the sizes and distribution of the metal nanoparticles on the rGO during the synthesis process.¹³⁸

As well as noble metals, there are studies reporting heterogeneous catalysts composed by first-row transition metals. Being those resistant to acid corrosion when alloying with noble metals,¹³⁹ cheaper and generally more easily available, are a good alternative to noble metals. A trimetallic $\text{Co}_{0.30}\text{Au}_{0.35}\text{Pd}_{0.35}$ nanocatalyst prepared by Yan and co-workers reported an initial TOF of 80 h^{-1} at $25 \text{ }^\circ\text{C}$ which is an improved catalytic activity compared with the monometallic and bimetallic counterparts being this attributed to its special composition and surface electronic state in the alloy structure.¹⁴⁰ The same group also prepared $\text{Ni}_{0.40}\text{Au}_{0.15}\text{Pd}_{0.45}/\text{C}$ but obtaining a low TOF of 12 h^{-1} at $25 \text{ }^\circ\text{C}$.¹⁴¹ Zhang and co-workers, after further study of those transition metals, found that in some cases, Ni was eroded by H^+ resulting in the loss of activity, however, a possible solution to this problem could be the construction of a core-shell nanostructure, where the transition metal is the core, improving, therefore, the activity and stability of the catalyst.¹⁴²

Other examples of bimetallic and trimetallic Pd-based catalysts are e.g. PdCo ,¹⁴³ PdCu ,¹⁴⁴ AuPdAg ,¹⁴⁵ CoAgPd ,¹⁴⁶ which have been recently reported showing that the enhancement in the catalytic performance is mainly due to electronic and geometric effects.

Table 5 presents several heterogeneous catalysts for formic acid decomposition under mild conditions.

Table 5. Supported metal nanoparticles for catalytic formic acid decomposition at mild conditions.

Catalyst	T (°C)	Reagent	TOF (h ⁻¹)		Activation Energy (kJ mol ⁻¹)	Ref.
			Initial	2 h		
Pd/C	21	FA (1.33 M)	18	15 ^a	53.7	125
	30		48	28 ^a		
Pd/C (citric acid)	25	FA		64 ^b		124
Pd/C	30	FA:SF 1:9		228.3		126
Pd/C	50	FA (1 M)	30			131
Au/C	50	FA (1 M)	80			
Au/ZrO ₂	50	FA	1590			129
Au ₄₁ Pd ₅₉ /C	50	FA (1 M)	230		28 ± 2	131
	20			125 ^c		
Ag@Pd (1:1)	35	FA		156 ^c	30	133
	50			252 ^c		
Ag/Pd alloy (1:1)	20			144 ^c		133
Ag ₄₂ Pd ₅₈	50	FA (1 M)	382		22 ± 1	134
	20			140		
Pd-MnO _x /SiO ₂ -NH ₂	50	FA (0.265 M)	1300		61.9	136
	25			105		
Co _{0.30} Au _{0.35} Pd _{0.35}	25	FA	80			140
Ni _{0.40} Au _{0.15} Pd _{0.45} /C	25	FA	12			141

FA: Formic acid, SF: Sodium formate

^b TOF values calculated after 160 min.^a TOF values calculated after 50 min.^c TOF values calculated based on the surface metal sites.

As presented, in the last years, research efforts have led to an improvement on the experimental conditions, although for practical applications in portable electric devices, there are still limitations on component cost, catalyst deactivation, regeneration of by-products and control of the reaction kinetics, which current research tries to overcome.

1.3. Aims of the study

As addressed in the literature review, further studies are needed to improve and optimise the reaction conditions in which formic acid decomposition is performed besides improving long-term catalytic performance. The effect of the number of metals present in the catalyst, nature of the support and catalyst preparation method play a crucial role in catalytic performance. The application of these catalysts is a promising and challenging topic in heterogeneous catalysis.

Therefore, the main objectives of this study are to:

- Study first the effect of reaction parameters on the catalytic activity and selectivity to hydrogen from formic acid decomposition. By modifying parameters such as temperature, mass of catalyst, stirring speed and concentration of formic acid, optimal conditions at which the reaction is kinetically limited can be found (Chapters 3 and 4).
- Study the mechanism of the reaction making use of the four isotopes of formic acid. This way, it is possible to elucidate the most plausible pathway for formic decomposition, and, by means of computational studies, find the optimal structure to maximise selectivity towards hydrogen (Chapter 3).
- Synthesise Pd-containing catalysts with several supports and study its role in the catalytic activity and selectivity of the reaction. By using different supports such as carbon, functionalised carbon nanofibers and titania, the understanding of the metal-support interaction is facilitated (Chapters 4 and 5).
- Comparison of preparation methods as colloidal and impregnation methods provide crucial information necessary to optimise the process towards a profitable hydrogen production from formic acid decomposition (particle size, oxidation state, metal surface coverage, impurities, effect of ligand). The optimisation of these preparation methods is of great interest and will be studied by varying a set of parameters to investigate the effects these have on the structure and morphology of the as-synthesised catalysts (Chapters 4 and 5).
- Synthesise active Pd-containing monometallic and bimetallic catalysts according to the requirements observed for the decomposition of formic acid under mild

conditions and deeply characterise them in order to investigate activity-structure relationships (Chapter 5).

1.4. References

- 1 International Energy Agency (IEA), *Key World Energy Statistics 2016*, 2016.
- 2 United Nations, *World Population To 2300*, 2004, vol. 18.
- 3 U.S. Energy Information Administration, *International Energy Outlook 2017*, 2017, vol. IEO2017.
- 4 REN21, *Renewables 2017: global status report*, 2017, vol. 72.
- 5 L. Sussams and J. Leaton, *Expect the Unexpected; the disruptive Power of low carbon technology*, 2017.
- 6 D. L. Klass, *A critical assessment of renewable energy usage in the USA*, 2003, vol. 31.
- 7 R. C. Saxena, D. K. Adhikari and H. B. Goyal, *Renew. Sustain. Energy Rev.*, 2009, **13**, 167–178.
- 8 Y. Ren, G. H. Chia and Z. Gao, *Nano Today*, 2013, **8**, 577–597.
- 9 A. Afif, N. Radenahmad, Q. Cheok, S. Shams, J. H. Kim and A. K. Azad, *Renew. Sustain. Energy Rev.*, 2016, **60**, 822–835.
- 10 Yukiya Amano, *The Fukushima Daiichi Accident Report by the Director General*, 2015.
- 11 F. Michael, *Recent estimates of the abundances of the elements in the earth's crust*, 1953.
- 12 M. Grasemann and G. Laurenczy, *Energy Environ. Sci.*, 2012, **5**, 8171–8181.
- 13 S. Sharma and S. K. Ghoshal, *Renew. Sustain. Energy Rev.*, 2015, **43**, 1151–1158.
- 14 R. J. Gorte, S. Park and J. M. Vohs, *Nature*, 2000, **404**, 265–267.
- 15 J. H. Lee, J. Cho, M. Jeon, M. Ridwan, H. S. Park, S. H. Choi, S. W. Nam, J. Han, T. H. Lim, H. C. Ham and C. W. Yoon, *J. Mater. Chem. A*, 2016, **4**, 1–7.
- 16 I. Staffel, *The Energy and Fuel Data Sheet*, 2011.
- 17 Y. Demirel, *Energy. Production, Conversion, Storage, Conservation, and Coupling*, 2016.
- 18 T. N. Veziroğlu and S. Şahin, *Energy Convers. Manag.*, 2008, **49**, 1820–1831.
- 19 K. Kendall and B. G. Pollet, *Hydrogen and fuel cells in transport*, Elsevier Ltd., 2012, vol. 4.
- 20 J. Larminie and A. Dicks, *Fuel cell systems explained*, 2003.
- 21 H. W. Wu, *Appl. Energy*, 2016, **165**, 81–106.
- 22 A. Ugurlu and S. Oztuna, *Int. J. Hydrogen Energy*, 2015, **40**, 11178–11188.
- 23 A. Baroutaji, J. G. Carton, M. Sajjia and A. G. Olabi, *Ref. Modul. Mater. Sci. Mater. Eng.*, 2016, 1–11.
- 24 W. Stanek, A. Valero and G. Calvo, *Thermodynamics for Sustainable Management of Natural Resources*, Springer International Publishing, 2017.
- 25 International Energy Agency (IEA), *IEA Energy Technol. essentials*, 2007, 3–6.
- 26 J. R. Rostrup-Nielsen, in *Handbook of Heterogeneous Catalysis*, 2008, pp. 2882–2905.
- 27 K.-O. Hinrichsen, K. Kochloefl and M. Muhler, *Water Gas Shift and COS Removal*, 2004.
- 28 C. M. Kalamaras and A. M. Efstathiou, *Conf. Pap. Energy*, 2013, **2013**, 9.
- 29 S.-B. Kim, Y.-K. Kim, Y.-S. Lim, M.-S. Kim and H.-S. Hahm, *Korean J. Chem. Eng.*, 2003, **20**, 1023–1025.
- 30 S. Sengodan, R. Lan, J. Humphreys, D. Du, W. Xu, H. Wang and S. Tao, *Renew. Sustain. Energy Rev.*, 2018, **82**, 761–780.
- 31 J. R. Rostrup-Nielsen, *Catal. Rev. - Sci. Eng.*, 2004, **46**, 247–270.
- 32 L. R. Radovic, *Catalysis in Coal and Carbon Gasification*, 2004.
- 33 F. Sánchez, D. Motta and N. Dimitratos, *Appl. Petrochemical Res.*, 2016, **6**, 269–277.
- 34 W. L. Holstein and M. Boudart, *Fuel*, 1983, **62**, 162–165.
- 35 D. W. McKee, *Fuel*, 1983, **62**, 170–175.
- 36 S. Sampath, N. K. Kulkarni, M. S. Subramanian and N. C. Jayadevan, *Carbon N. Y.*, 1988, **26**, 129–

- 137.
- 37 L. Zhu, L. Li, Z. Zhang, H. Chen, L. Zhang and F. Wang, *Chem. Eng. Technol.*, 2016, **39**, 1912–1920.
- 38 E. Zoulias, E. Varkarakis, N. Lymberopoulos, C. N. Christodoulou and G. N. Karagiorgis, *TCJST*, 2004, **4**, 41–71.
- 39 R. Abouatallah, R. Wang and N. I. Joos, *High or differential pressure electrolysis cell*, 2017.
- 40 S. Z. Baykara, *Int. J. Hydrogen Energy*, 2005, **30**, 545–553.
- 41 A. Züttel, *Mater. Today*, 2003, **6**, 24–33.
- 42 P. E. Dodds and S. Demoullin, *Int. J. Hydrogen Energy*, 2013, **38**, 7189–7200.
- 43 K. Takahashi, *Encycl. Life Support Syst.*, II.
- 44 Z. Yang, Y. Xia and R. Mokaya, *J. Am. Chem. Soc.*, 2007, **129**, 1673–1679.
- 45 H. Dai, B. Xia, L. Wen, C. Du, J. Su, W. Luo and G. Cheng, *Appl. Catal. B Environ.*, 2015, **165**, 57–62.
- 46 H. Furukawa and O. M. Yaghi, *J. Am. Chem. Soc.*, 2009, **131**, 8875–8883.
- 47 B. Bogdanović and M. Schwickardi, *J. Alloys Compd.*, 1997, **253–254**, 1–9.
- 48 J. Graetz, *Chem. Soc. Rev.*, 2009, **38**, 73–82.
- 49 J. Shen, L. Yang, K. Hu, W. Luo and G. Cheng, *Int. J. Hydrogen Energy*, 2015, **40**, 1062–1070.
- 50 Y. Nakamori, G. Kitahara, A. Ninomiya, M. Aoki, T. Noritake, S. Towata and S. Orimo, *Mater. Trans.*, 2005, **46**, 2093–2097.
- 51 Z. H. Lu, H. L. Jiang, M. Yadav, K. Aranishi and Q. Xu, *J. Mater. Chem.*, 2012, **22**, 5065–5071.
- 52 Z. Wang, I. Tonks, J. Belli and C. M. Jensen, *J. Organomet. Chem.*, 2009, **694**, 2854–2857.
- 53 A. Iulianelli, P. Ribeirinha, A. Mendes and A. Basile, *Renew. Sustain. Energy Rev.*, 2014, **29**, 355–368.
- 54 IUPAC, *Compend. Chem. Terminol. Gold B.*, 2014, 1670.
- 55 G. C. Bond, *Heterogeneous Catalysis: Principles and Applications. 2nd Ed*, Clarendon Press, 1987.
- 56 I. Chorkendorff and J. W. Niemantsverdriet, *Catalyst Characterization*, 2007.
- 57 I. Chorkendorff and J. W. Niemantsverdriet, *Concepts of Modern Catalysis and Kinetics*, John Wiley & Sons, 2005.
- 58 P. W. N. M. van Leeuwen, *Homogeneous Catalysis Understanding Art*, 2004, vol. 30.
- 59 B. Cornils and W. A. Herrmann, *J. Catal.*, 2003, **216**, 23–31.
- 60 H. Knözinger and K. Kochloefl, *Heterogeneous catalysis and solid catalysts*, 2009, vol. 1.
- 61 W. M. H. Sachtler and R. Jongepier, *J. Catal.*, 1965, **4**, 665–671.
- 62 C. Della Pina, E. Falletta, L. Prati and M. Rossi, *Chem. Soc. Rev.*, 2008, **37**, 2077–2095.
- 63 A. Roucoux, J. Schulz and H. Patin, *Chem. Rev.*, 2002, **102**, 3757–3778.
- 64 M. C. Daniel and D. Astruc, *Chem. Rev.*, 2004, **104**, 293–346.
- 65 M. Sankar, N. Dimitratos, P. J. Miedzziak, P. P. Wells, C. J. Kiely and G. J. Hutchings, *Chem. Soc. Rev.*, 2012, **41**, 8099–8139.
- 66 L. Prati and A. Villa, *Acc. Chem. Res.*, 2014, **47**, 855–863.
- 67 M. Brust, M. Walker, D. Bethell, D. J. Schiffrin and R. Whyman, *Chem. Commun.*, 1994, 801–802.
- 68 M. C. M. Daniel and D. Astruc, *Chem. Rev.*, 2004, **104**, 293–346.
- 69 N. Dimitratos, A. Villa, L. Prati, C. Hammond, C. E. Chan-Thaw, J. Cookson and P. T. Bishop, *Appl. Catal. A Gen.*, 2016, **514**, 267–275.
- 70 S. M. Rogers, C. R. A. Catlow, C. E. Chan-Thaw, A. Chutia, N. Jian, R. E. Palmer, M. Perdjon, A. Thetford, N. Dimitratos, A. Villa and P. P. Wells, *ACS Catal.*, 2017, **7**, 2266–2274.
- 71 S. M. Rogers, C. R. A. Catlow, C. E. Chan-Thaw, D. Gianolio, E. K. Gibson, A. L. Gould, N. Jian, A. J. Logsdail, R. E. Palmer, L. Prati, N. Dimitratos, A. Villa and P. P. Wells, *ACS Catal.*, 2015, **5**, 4377–4384.
- 72 N. Dimitratos, C. Hammond, C. J. Kiely and G. J. Hutchings, *Appl. Petrochemical Res.*, 2014, **4**, 85–94.

- 73 N. Dimitratos, A. Villa, L. Prati, C. Hammond, C. E. Chan-Thaw, J. Cookson and P. T. Bishop, *Appl. Catal. A Gen.*, 2016, **514**, 267–275.
- 74 E. J. Roberts, S. E. Habas, L. Wang, D. A. Ruddy, E. A. White, F. G. Baddour, M. B. Griffin, J. A. Schaidle, N. Malmstadt and R. L. Brutchey, *ACS Sustain. Chem. Eng.*, 2017, **5**, 632–639.
- 75 C.-J. Jia and F. Schüth, *Phys. Chem. Chem. Phys.*, 2011, **13**, 2457–2487.
- 76 P. Zhao, N. Li and D. Astruc, *Coord. Chem. Rev.*, 2013, **257**, 638–665.
- 77 M. Mitchnick, *Drug Dev. Serv. Tech. Br.*, 2009, 1.
- 78 Z. Wei, J. Sun, Y. Li, A. K. Datye and Y. Wang, *Chem. Soc. Rev.*, 2012, 7994–8008.
- 79 L. Prati and A. Villa, *Catalysts*, 2012, **2**, 24–37.
- 80 A. Villa, D. Wang, G. M. Veith, F. Vindigni and L. Prati, *Catal. Sci. Technol.*, 2013, **3**, 3036–3041.
- 81 J. W. Niemantsverdriet, *Spectroscopy in Catalysis*, Wiley-VCH Verlag GmbH & Co. KGaA, Weinheim, 2007.
- 82 P. Munnik, P. E. De Jongh and K. P. De Jong, *Chem. Rev.*, 2015, **115**, 6687–6718.
- 83 S. C. Amendola, S. L. Sharp-Goldman, M. S. Janjua, M. T. Kelly, P. J. Petillo and M. Binder, *J. Power Sources*, 2000, **85**, 186–189.
- 84 A. K. Hill and L. Torrente-Murciano, *Int. J. Hydrogen Energy*, 2014, **39**, 7646–7654.
- 85 S. S. Tafreshi, A. Roldan and N. H. de Leeuw, *Faraday Discuss.*, 2017, **197**, 41–57.
- 86 L. He, Y. Huang, X. Y. Liu, L. Li, A. Wang, X. Wang, C. Y. Mou and T. Zhang, *Appl. Catal. B Environ.*, 2014, **147**, 779–788.
- 87 M. Nielsen, E. Alberico, W. Baumann, H.-J. Drexler, H. Junge, S. Gladiali and M. Beller, *Nature*, 2013, **495**, 85–89.
- 88 L.-C. Yang, T. Ishida, T. Yamakawa and S. Shinoda, *J. Mol. Catal. A Chem.*, 1996, **108**, 87–93.
- 89 H. B. Charman, *J. Chem. Soc. Phys. Org.*, 1970, 584–587.
- 90 M. Nielsen, A. Kammer, D. Cozzula, H. Junge, S. Gladiali and M. Beller, *Angew. Chemie - Int. Ed.*, 2011, **50**, 9593–9597.
- 91 M. Yadav and Q. Xu, *Energy Environ. Sci.*, 2012, 9698–9725.
- 92 U. B. Demirci and P. Miele, *Energy Environ. Sci.*, 2011, **4**, 3334–3341.
- 93 M. Trincado, D. Banerjee and H. Grützmacher, *Energy Environ. Sci.*, 2014, **7**, 2464–2503.
- 94 J. Eppinger and K.-W. Huang, *ACS Energy Lett.*, 2017, **2**, 188–195.
- 95 F. Joó, *ChemSusChem*, 2008, **1**, 805–808.
- 96 D. R. Hoffman, *Curr. Opin. Allergy Clin. Immunol.*, 2010, **10**, 342–346.
- 97 I. G. Kavouras, N. Mihalopoulos and E. G. Stephanou, *Nature*, 1998, **372**, 683–686.
- 98 B. A. Magnuson, G. A. Burdock, J. Doull, R. M. Kroes, G. M. Marsh, M. W. Pariza, P. S. Spencer, W. J. Waddell, R. Walker and G. M. Williams, *Crit. Rev. Toxicol.*, 2007, **37**, 629–727.
- 99 J. Hietala, A. Vuori, P. Johnsson, I. Pollari, W. Reutemann and H. Kieczka, *Ullmann's Encyclopedia of Industrial Chemistry*, Wiley-VCH Verlag GmbH & Co. KGaA, Weinheim, 2016.
- 100 W. Reutemann and H. Kieczka, *Ullmann's Encycl. Ind. Chem.*
- 101 J. F. Hull, Y. Himeda, W.-H. Wang, B. Hashiguchi, R. Periana, D. J. Szalda, J. T. Muckerman and E. Fujita, *Nat. Chem.*, 2012, **4**, 383–388.
- 102 J. Albert, R. Wölfel, A. Bösmann and P. Wasserscheid, *Energy Environ. Sci.*, 2012, **5**, 7956–7962.
- 103 B. B. Sarma and R. Neumann, *Nat. Commun.*, 2014, **5**, 1–6.
- 104 J. Albert, *Faraday Discuss.*, 2017, **202**, 99–109.
- 105 A. Roldan, N. Hollingsworth, A. Roffey, H.-U. Islam, J. B. M. Goodall, C. R. A. Catlow, J. A. Darr, W. Bras, G. Sankar, K. B. Holt, G. Hogarth and N. H. de Leeuw, *Chem. Commun.*, 2015, **51**, 7501–7504.
- 106 B. Loges, A. Boddien, F. Gärtner, H. Junge and M. Beller, *Top. Catal.*, 2010, **53**, 902–914.
- 107 B. Loges, A. Boddien, H. Junge and M. Beller, *Angew. Chemie - Int. Ed.*, 2008, **47**, 3962–3965.
- 108 S. Fukuzumi, T. Kobayashi and T. Suenobu, *J. Am. Chem. Soc.*, 2010, **132**, 1496–1497.
- 109 Y. Maenaka, T. Suenobu and S. Fukuzumi, *Energy Environ. Sci.*, 2012, **5**, 7360.
- 110 A. Boddien, B. Loges, H. Junge and M. Beller, *ChemSusChem*, 2008, **1**, 751–758.
- 111 A. Boddien, B. Loges, H. Junge, F. Gärtner, J. R. Noyes and M. Beller, *Adv. Synth. Catal.*, 2009,

- 351**, 2517–2520.
- 112 Y. Himeda, *Green Chem.*, 2009, **11**, 2018.
- 113 T. W. Myers and L. A. Berben, *Chem. Sci.*, 2014, **5**, 2771–2777.
- 114 A. Boddien, D. Mellmann, F. Gärtner, R. Jackstell, H. Junge, P. J. Dyson, G. Laurenczy, R. Ludwig and M. Beller, *Science (80-.)*, 2011, **333**, 1733–1737.
- 115 B. Loges, A. Boddien, H. Junge, J. R. Noyes, W. Baumann and M. Beller, *Chem. Commun. (Camb.)*, 2009, 4185–4187.
- 116 C. Fellay, P. J. Dyson and G. Laurenczy, *Angew. Chemie - Int. Ed.*, 2008, **47**, 3966–3968.
- 117 D. J. Morris, G. J. Clarkson and M. Wills, *Organometallics*, 2009, **28**, 4133–4140.
- 118 A. Boddien and H. Junge, *Nat. Nanotechnol.*, 2011, **6**, 265–266.
- 119 A. Mailhe and P. Sabatier, *Comptes Rendus Chim.*, 1911, **152**, 1212.
- 120 K. Hirota, K. Kuwate and Y. Nakai, *Bull. Chem. Soc. Jpn.*, 1958, **31**, 861–864.
- 121 M. Bowker, E. Rowbotham, F. M. Leibsle and S. Haq, *Surf. Sci.*, 1996, **349**, 97–110.
- 122 F. Solymosi, Á. Koós, N. Liliom and I. Ugrai, *J. Catal.*, 2011, **279**, 213–219.
- 123 D. A. Bulushev, S. Beloshapkin and J. R. H. Ross, *Catal. Today*, 2010, **154**, 7–12.
- 124 Z.-L. Wang, J.-M. Yan, H.-L. Wang, Y. Ping and Q. Jiang, *Sci. Rep.*, 2012, **2**, 598–604.
- 125 C. Hu, J. K. Pulleri, S. W. Ting and K. Y. Chan, *Int. J. Hydrogen Energy*, 2014, **39**, 381–390.
- 126 X. Wang, G. W. Qi, C. H. Tan, Y. P. Li, J. Guo, X. J. Pang and S. Y. Zhang, *Int. J. Hydrogen Energy*, 2014, **39**, 837–843.
- 127 K. Mori, M. Dojo and H. Yamashita, *ACS Catal.*, 2013, **3**, 1114–1119.
- 128 M. Ojeda and E. Iglesia, *Angew. Chemie - Int. Ed.*, 2009, **48**, 4800–4803.
- 129 Q. Y. Bi, X. L. Du, Y. M. Liu, Y. Cao, H. Y. He and K. N. Fan, *J. Am. Chem. Soc.*, 2012, **134**, 8926–8933.
- 130 D. D. Eley and P. Luetic, *Trans. Faraday Soc.*, 1957, **53**, 1483–1487.
- 131 Ö. Metin, X. Sun and S. Sun, *Nanoscale*, 2013, **5**, 910–912.
- 132 X. Zhou, Y. Huang, W. Xing, C. Liu, J. Liao and T. Lu, *Chem. Commun. (Camb.)*, 2008, 3540–3542.
- 133 K. Tedsree, T. Li, S. Jones, C. W. A. Chan, K. M. K. Yu, P. a J. Bagot, E. a Marquis, G. D. W. Smith and S. C. E. Tsang, *Nat. Nanotechnol.*, 2011, **6**, 302–307.
- 134 S. Zhang, O. Metin, D. Su and S. Sun, *Angew. Chemie - Int. Ed.*, 2013, **52**, 3681–3684.
- 135 H. Dai, N. Cao, L. Yang, J. Su, W. Luo and G. Cheng, *J. Mater. Chem. A*, 2014, **2**, 11060–11064.
- 136 A. Bulut, M. Yurderi, Y. Karatas, M. Zahmakiran, H. Kivrak, M. Gulcan and M. Kaya, *Appl. Catal. B Environ.*, 2015, **164**, 324–333.
- 137 Q.-L. Zhu, N. Tsumori and Q. Xu, *Chem. Sci.*, 2014, **5**, 195–199.
- 138 Y. Ping, J.-M. Yan, Z.-L. Wang, H.-L. Wang and Q. Jiang, *J. Mater. Chem. A*, 2013, **1**, 12188.
- 139 S. F. Ho, A. Mendoza-Garcia, S. Guo, K. He, D. Su, S. Liu, O. Metin and S. Sun, *Nano Lett.*, 2012, **12**, 1102–1106.
- 140 Z. L. Wang, J. M. Yan, Y. Ping, H. L. Wang, W. T. Zheng and Q. Jiang, *Angew. Chemie - Int. Ed.*, 2013, **52**, 4406–4409.
- 141 Z. L. Wang, Y. Ping, J. M. Yan, H. L. Wang and Q. Jiang, *Int. J. Hydrogen Energy*, 2014, **39**, 4850–4856.
- 142 Y. Qin, J. Wang, F. Meng, L. Wang and X. Zhang, *Chem. Commun. (Camb.)*, 2013, **49**, 10028–30.
- 143 Y. L. Qin, Y. C. Liu, F. Liang and L. M. Wang, *ChemSusChem*, 2015, **8**, 260–263.
- 144 K. Mori, H. Tanaka, M. Dojo, K. Yoshizawa and H. Yamashita, *Chem. - A Eur. J.*, 2015, **21**, 12085–12092.
- 145 S. Li, Y. Ping, J.-M. Yan, H.-L. Wang, M. Wu and Q. Jiang, *J. Mater. Chem. A*, 2015, **3**, 14535–14538.
- 146 L. Yang, W. Luo and G. Cheng, *Int. J. Hydrogen Energy*, 2016, **41**, 439–446.

2. EXPERIMENTAL, METHODS AND CHARACTERISATION

This chapter describes the materials and techniques used for catalyst preparation and experimental conditions used for catalyst testing and analysis of the products. The basic principles of the characterisation techniques used are presented as well. A list of abbreviations and equations and all the chemicals used (Table 6) is presented subsequently.

Abbreviations

C: carbon

AC: activated charcoal

CNF: carbon nanofiber

PS: Pyrolytically stripped

LHT: low-heat treated

HHT: high-heat treated

SI: sol-immobilisation

IMP: impregnation

PVA: Polyvinyl alcohol

HPLC: High-Performance Liquid Chromatography

Equations

Conversion (x_a):

$$x_a = \frac{\text{Concentration}_{\text{substrate initial}} - \text{Concentration}_{\text{substrate final}}}{\text{Concentration}_{\text{substrate initial}}} \quad (\text{eq. 1})$$

Turnover frequency number (TOF):

$$TOF = \frac{\text{moles}_{\text{substrate converted}}}{\text{moles}_{\text{metal}} \cdot \text{time}} \quad (\text{eq. 2})$$

The remaining equations used in this Thesis will be appropriately presented during the discussion for an in-depth explanation.

Table 6. List of chemicals used throughout this Thesis.

Name	Formula	Company	Purity	Use
Pyrolytically stripped carbon nanofiber	CNFs PR24-PS	Applied Sciences Inc	N/A	Catalyst support
Low-heat treated carbon nanofiber	CNFs PR24-LHT	Applied Sciences Inc	N/A	Catalyst support
High-heat treated carbon nanofiber	CNFs PR24-HHT	Applied Sciences Inc	N/A	Catalyst support
Carbon Charcoal, Wood	C	Fischer Scientific (C/4010/60)	N/A	Catalyst support
Titanium (IV) oxide	TiO ₂ (Aeroxide, P25)	Fisher scientific (10646903)	≥99.5 %	Catalyst support
Sodium tetrachloropalladate (II)	Na ₂ PdCl ₄ ·2H ₂ O	Sigma-Aldrich (379808)	99.99 %	Metal precursor
Potassium tetrachloropalladate (II)	K ₂ PdCl ₄	Alfa Aesar (11885)	99.99 %	Metal precursor
Hydrogen tetrachloroaurate (III) hydrate	HAuCl ₄ ·H ₂ O	Alfa Aesar (12325)	99.9 %	Metal precursor
Polyvinyl alcohol (Mw 9,000 -10,000)	[C ₂ H ₄ O] _n	Sigma-Aldrich (360627)	80 % hydrolised	Stabiliser ligand
Sodium borohydride	NaBH ₄	Sigma-Aldrich (480886)	99.99 %	Reducing agent
Sulphuric acid	H ₂ SO ₄	Sigma-Aldrich (258105)	95 – 98 %	pH corrector
Palladium on activated carbon	5 wt. % Pd/C	Sigma-Aldrich (205680)	N/A	Commercial catalyst

Formic Acid	HCOOH	Sigma-Aldrich (F0507)	≥95 %	Reagent
Formic Acid-d	HCOOD	Sigma-Aldrich (489441)	95 %	Reagent
Formic d-Acid	DCOOH	Sigma-Aldrich (485705)	95 %	Reagent
Formic Acid-d ₂	DCOOD	Sigma-Aldrich (426229)	95 %	Reagent
Succinic acid	C ₄ H ₆ O ₄	Sigma-Aldrich 797987	≥99 %	Calibration standard for HPLC
Phosphoric acid	H ₃ PO ₄	Sigma-Aldrich (695017)	≥85 %	Solvent acidifier for HPLC
Nitric acid	HNO ₃	Sigma-Aldrich (7697372)	70 %	Support preparation

2.1. Catalyst preparation

The catalyst preparation method is crucial since it affects the morphology and structure of the catalysts and subsequently its final activity. It is also of great importance to the reproducibility of the preparation method in order to produce reliable catalysts. Two preparation techniques have been used in this research: sol-immobilisation (2.1.2.2) and impregnation (2.1.2.3).

2.1.1. Commercial Pd supported on activated carbon

5 wt. % Palladium on activated carbon is a widely used commercial catalyst utilised here as a reference and starting point for the optimisation of reaction conditions and to get a more in-depth knowledge of the reaction mechanism through the kinetic isotope studies which will be presented in subsequent sections. In the brief introduction to continuous flow reaction in Chapter 3, this catalyst was chosen due to the promising results obtained throughout the chapter as will be explained. No pre-treatment was necessary prior to catalytic testing.

2.1.2. Pd nanoparticles supported on carbon nanofibers

In the last years, carbon nanofibers (CNFs) and carbon nanotubes (CNTs) have received much attention and have been successfully used in a broad range of important catalytic applications such as hydrogen generation,^{1,2} alcohol oxidation,^{3,4} and nitrite reduction,⁵ and also find applicability in industry where it is used to increase thermal and electrical conductivity^{6,7} or improve mechanical properties.⁸ Carbon nanofibers (CNFs) were used as support in Chapter 4 of this Thesis. CNFs consist of tubular fibers with an average diameter of 80 ± 30 nm and a specific surface area of around $50 \text{ m}^2/\text{g}$. Schlögl and co-workers carried out a detailed characterisation of these materials.⁹ CNFs present several advantages compared with other supports such as:

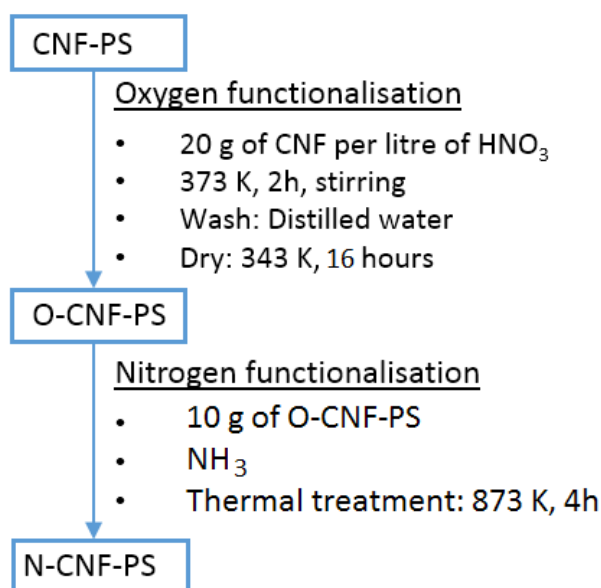
- The ability to tailor the microstructures of CNFs by selecting the growing techniques.
- High degree of control of the surface chemistry by surface modification (acidic and basic properties) using chemical and thermal treatments.
- Unlike activated charcoal (AC), where there is a certain degree of inaccessible active sites, the resistance of inner pore diffusion may be relieved by the almost completely exposed surface of the CNFs.
- The presence of specific metal-support interactions that may enhance the catalytic activity and selectivity.²

Three different grades have been used in this study: (1) pyrolytically stripped (PS-CNF), (2) low-heat treated (LHT-CNF) and (3) high-heat treated (HHT-CNF). PS grade carbon nanofiber is produced by pyrolytically stripping the fiber in order to remove polyaromatic hydrocarbons covering the outer fiber surface. LHT grade carbon nanofiber is produced by treating the fiber at $1500 \text{ }^\circ\text{C}$ which carbonises any chemically vapour deposited carbon from the surface of the fiber. HHT grade is produced by treating the fiber at $3000 \text{ }^\circ\text{C}$ converting the fiber to a fully graphitised form.¹⁰ This range of heat treatments permits the study of the graphitisation degree. Moreover, two different functionalisations were used. Pyrolytically stripped CNF was functionalised with either nitrogen or oxygen to modify the surface chemical properties by varying the acidity/basicity of the support and therefore, change the support-metal interaction.

2.1.2.1. CNFs functionalisation

The introduction of heteroatoms such as N and O in this research but also P or S has been reported to modify acidity/basicity and hydrophobicity/hydrophilicity and enhance metal-support interactions.^{11,12} Oxygen and Nitrogen-containing nanofibers (O-CNF-PS and N-CNF-PS) were carried out according to the reported procedures.^{12,13} Scheme 1 represents the experimental conditions for the functionalisation of these CNFs:

- O-containing CNFs: the pristine support (CNF-PS) was treated with concentrated nitric acid (20 g of CNF per litre of HNO₃) at 373 K under continuous stirring. After 2 h, the solution was rinsed with distilled water and dried at 343 K for 16 hours.
- N-containing CNFs: the previously formed O-containing CNFs (10 g for each batch) are thermally treated with pure NH₃ (amination) at 873 K for 4 h.



Scheme 1. Schematic representation of a two-step functionalisation process performed over carbon nanofibers (CNFs). PS: pyrolytically stripped.

At this point in the preparation method, 5 different carbon nanofibers are present: CNF-PS, CNF-LHT, CNF-HHT, O-CNF-PS and N-CNF-PS. Once the carbon nanofibers were ready, two preparation methods namely sol-immobilisation and impregnation were used to support the Pd nanoparticles.

2.1.2.2. Preparation of the Pd/CNF by sol-immobilisation (SI)

As explained in Chapter 1, sol-immobilisation method provides a great control of the particle size distribution and final particle morphology of the catalyst. Its simplicity but at the same time versatility has led to an extensive study.¹⁴⁻²¹ In the sol-immobilisation method, an aqueous solution of the metal precursor with a stabiliser ligand and a reducing agent is prepared, and then, the support is added. After a certain period of time, the mixture is washed with water and dried. Scheme 2 shows a graphical representation of the sol-immobilisation method used in this Thesis. A solution of 100 ml of H₂O with Na₂PdCl₄·2H₂O (Pd: 0.094 mmol) and freshly prepared 1wt. % PVA solution was prepared (PVA/Pd (wt/wt) = 0.25). After 3 minutes, a freshly made aqueous solution of 0.1 M NaBH₄ was added (NaBH₄/Pd (mol/mol) = 8) to the yellow-brown solution under vigorous magnetic stirring. The brown Pd⁰ sol was immediately formed and an UV-visible spectrum of the palladium sol was recorded for ensuring the complete reduction of Pd^{II}. Within a few minutes from its generation, the suspension was acidified at pH 2 by adding 2-3 drops of sulphuric acid, the support was added and left under vigorous stirring for 1 hour. The catalyst was filtered and washed with 1 litre of deionised water to ensure the removal of the material arising from the reduction treatment. The sample was dried at 80 °C for two hours. The amount of support (0.99 g) was calculated to obtain a final metal loading of 1 wt %. The obtained catalysts were labelled as Pd_{SI}/CNF-HHT, Pd_{SI}/CNF-LHT, Pd_{SI}/CNF-PS, Pd_{SI}/N-CNF-PS, Pd_{SI}/O-CNF-PS.

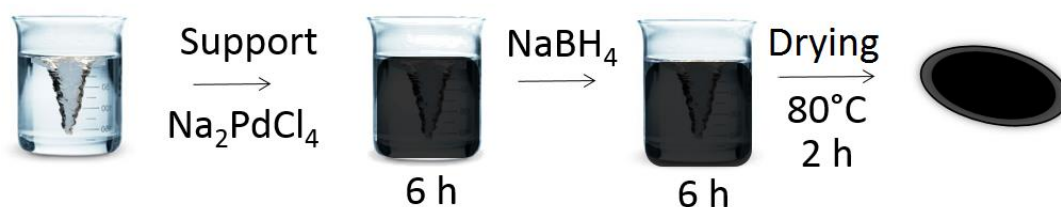


Scheme 2. Schematic representation of the sol-immobilisation process used in this Thesis.

2.1.2.3. Preparation of the Pd/CNF by impregnation (IMP)

Impregnation is the most widely used preparation method due to its easy operation and inexpensiveness. In this Thesis, specifically, wetness impregnation was used. In this method, a solution of the metal precursor with a larger volume than the pore volume of the support is poured onto the support, then the metal is chemically reduced, washed and the resultant

catalyst, dried. Scheme 3 shows a graphical representation of the impregnation method used in this Thesis. A solution of $\text{Na}_2\text{PdCl}_4 \cdot 2\text{H}_2\text{O}$ (Pd: 0.094 mmol) in 100 mL of H_2O was added to the support and stirred vigorously for six hours. Then, a freshly prepared aqueous solution of NaBH_4 (0.1 M, NaBH_4/Pd (mol/mol) = 8) was added and stirred for six more hours. The catalyst was filtered and washed with 1 litre of deionised. The samples were dried at 80°C for two hours. The amount of support (0.99 g) was calculated to obtain a final metal loading of 1 wt %. The obtained catalysts were labelled $\text{Pd}_{\text{IMP}}/\text{CNF-HHT}$, $\text{Pd}_{\text{IMP}}/\text{CNF-LHT}$, $\text{Pd}_{\text{IMP}}/\text{CNF-PS}$, $\text{Pd}_{\text{IMP}}/\text{N-CNF-PS}$, $\text{Pd}_{\text{IMP}}/\text{O-CNF-PS}$.



Scheme 3. Schematic representation of the impregnation process used in this Thesis.

2.1.3. Pd and bimetallic Au-Pd nanoparticles supported on carbon and titania using sol-immobilisation

Once completed the optimisation of the reaction parameters using Pd nanoparticles on carbon and carbon nanofibers, studied the effect of graphitisation degree of the support, acid and basic functionalities and two preparation methods, a series of catalysts were prepared using the sol-immobilisation technique as the preferred method. These results will be presented in Chapter 5. The first part of this chapter is the optimisation of parameters involved in the preparation, using sol-immobilisation, of Pd nanoparticles supported on active charcoal (AC). The effect of the stabiliser ligand and total metal loading was studied on the electronic and morphologic structure and the activity of the catalyst. Then, a comparison of active charcoal and titania P-25 (TiO_2) is presented. Titania P-25 consists of 18 % anatase and 82 % rutile. Besides the available comparison between these two supports, further spectroscopic characterisation could be carried out in terms of CO-DRIFTS and FTIR in the catalysts supported on TiO_2 . Finally, in the last part of the chapter, a comparison of the catalytic performance of monometallic Pd and Au and bimetallic Au-Pd catalysts is presented.

Table 7 displays the properties of the as-synthesised catalysts and parameters used during the sol-immobilisation preparation method.

Table 7. Synthesis parameters for Pd-based nanoparticles on activated charcoal and TiO₂.

Catalyst	Support	Pd (wt. %)	Au (wt. %)	Wt. % total metal	PVA/M weight ratio	NaBH₄/M molar ratio
Pd/AC-0	AC	1	0	1	0	5
Pd/AC-0.05	AC	1	0	1	0.05	5
Pd/AC-0.1	AC	1	0	1	0.1	5
Pd/AC-0.2	AC	1	0	1	0.2	5
Pd/AC-0.3	AC	1	0	1	0.3	5
Pd/AC-0.65	AC	1	0	1	0.65	5
Pd/AC-1.2	AC	1	0	1	1.2	5
Pd/AC-0.65N	AC	1	0	1	0.65	10
0.2-Pd/AC-0.3	AC	0.2	0	0.2	0.3	5
0.5-Pd/AC-0.3	AC	0.5	0	0.5	0.3	5
0.7Pd/AC-0.3	AC	0.7	0	0.7	0.3	5
1.2-Pd/AC-0.3	AC	1.2	0	1.2	0.3	5
Pd/TiO ₂ -0.65	TiO ₂	1	0	1	0.65	5
Pd/TiO ₂ -0.65N	TiO ₂	1	0	1	0.65	10
Pd/TiO ₂ -0.3N	TiO ₂	1	0	1	0.3	10
Au/TiO ₂	TiO ₂	0	1	1	0.3	10
Au ₁ Pd ₃ -TiO ₂	TiO ₂	0.75	0.25	1	0.3	10
Au ₁ Pd ₁ -TiO ₂	TiO ₂	0.5	0.5	1	0.3	10
Au ₃ Pd ₁ -TiO ₂	TiO ₂	0.25	0.75	1	0.3	10

For the first part of Chapter 5, a solution of 400 ml of H₂O with K₂PdCl₄ (varying concentration of metal precursor to optimising the total metal loading) and freshly prepared 1wt. % PVA solution (PVA/Pd varying weight ratio to optimise the ligand effect) was prepared. Table 7 displays the parameters used. After 3 minutes, a freshly made aqueous solution of 0.1 M

NaBH₄ was added to the solution under vigorous magnetic stirring. The brown Pd⁰ sol was immediately formed and a UV-visible spectrum of the palladium sol was recorded for ensuring the complete reduction of Pd^{II}. Within a few minutes from its generation, the suspension was acidified at pH 2 by adding 2-3 drops of sulphuric acid, the support (activated charcoal) was added and left under vigorous stirring for 1 hour. The catalyst was filtered and washed with 1 litre of deionised water. The sample was dried at 110 °C for 16 hours. The amount of support was calculated to obtain a final metal loading of 1 wt. %.

For the preparation of the monometallic Pd and Au catalysts supported on titania (instead of active charcoal), the previous procedure was followed step by step with the exceptions of the precursor (HAuCl₄ for preparation of Au catalyst) and the support. Finally, in the case of the bimetallic catalysts, the preparation of the metal precursor solution is the only modification of the procedure: instead of adding only one metal precursor, three different Au-Pd molar ratios were used 1:3, 1:1 and 3:1, therefore, three different combinations of the metal precursors were used to study the effect of molar ratio.

2.1.4. UV-Vis analysis of colloids

As previously commented, UV/vis spectroscopy analysis was performed to ensure the complete reduction of the metal precursor. Ultraviolet-visible spectroscopy technique makes use of light in the visible and ultraviolet spectral region which is passed through the sample to be analysed. It is based on the ability of a molecule to adsorb a photon, exciting at least one electron to a higher energy orbital.

The instrument actually measures the intensity of light passing through the sample (*I*) and compares it to the intensity of light emitted by the source (*I*₀). The ratio is called transmittance; however, it is usually expressed as absorbance. The Beer-Lambert equation relates the absorbance of the solution with the concentration of the absorbing species and the path length (eq. 3). Consequently, for a fixed path length, UV-Vis spectroscopy determines the concentration of the absorbant in a solution.

$$A = \epsilon \cdot b \cdot C \quad (\text{eq. 3})$$

where ϵ is the molar attenuation coefficient; b , the path length through the sample; and C , the molar concentration of the analysed solution.

Figure 20 displays a representation of a double beam UV-Vis spectrophotometer. The light source provides a beam with an accurate wavelength in the range of UV-visible, it is passed through a monochromator, followed by the sample cell, and the transmitted light reaches the detector which transforms the photons in electrical signal monitored by a computer.

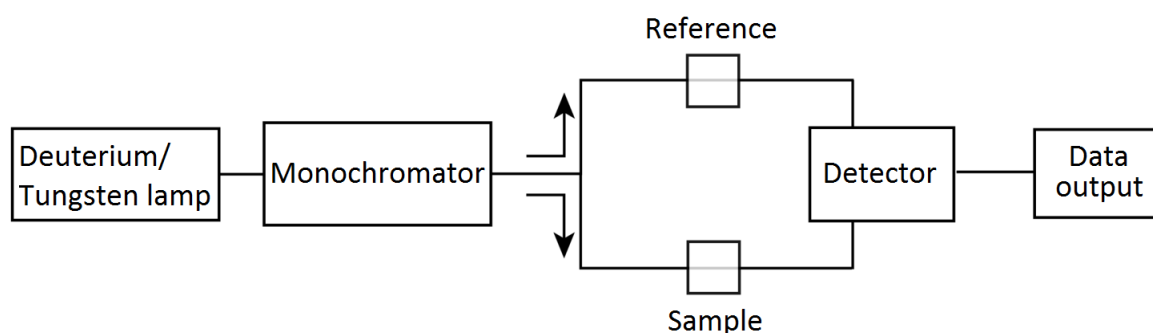


Figure 20. Simplified UV-vis diagram.

In this work, a single beam spectrophotometer was used. In this case, there is only one single beam passed from the light source to the detector. This means that both reference and sample are analysed in series and the data is stored in the computer for subsequent analysis. UV-Vis has been used in this work to ensure the reduction of the metal precursor by the colour change and identify if possible the surface plasmon resonance (SPR) absorption typically exhibited by noble metal nanoparticles. These resonances are attributed to the collective oscillation of the free conduction electrons induced by the interaction with electromagnetic radiation.^{22,23}

2.1.4.1. UV-Vis set up

UV/vis spectroscopic analyses were performed in a 1 cm² quartz cuvette using *in-situ* AvaSoft UV-Vis Spectrometry as displayed in figure 21. The solution is placed in the quartz cuvette, then set in the holder which is set at stable room temperature and the UV-vis spectra (200-900 nm) of the colloids sol recorded. A set of graphs will be provided in Chapter 5 along with the results.



Figure 21. (Up-left) AvaLight-DH-S deuterium halogen source, (up-right) AvaSpec-ULS2048XL EVO spectrometer and (bottom) CUV-UV/VIS-TC temperature controlled cuvette holder.

2.2. Catalysts testing

Typically, formic acid decomposition was performed in a batch reactor. Figure 22 shows a representative scheme and a photograph of the actual set up used. A batch reactor was used since it can provide a set of kinetic data in an accurate and reproducible way.

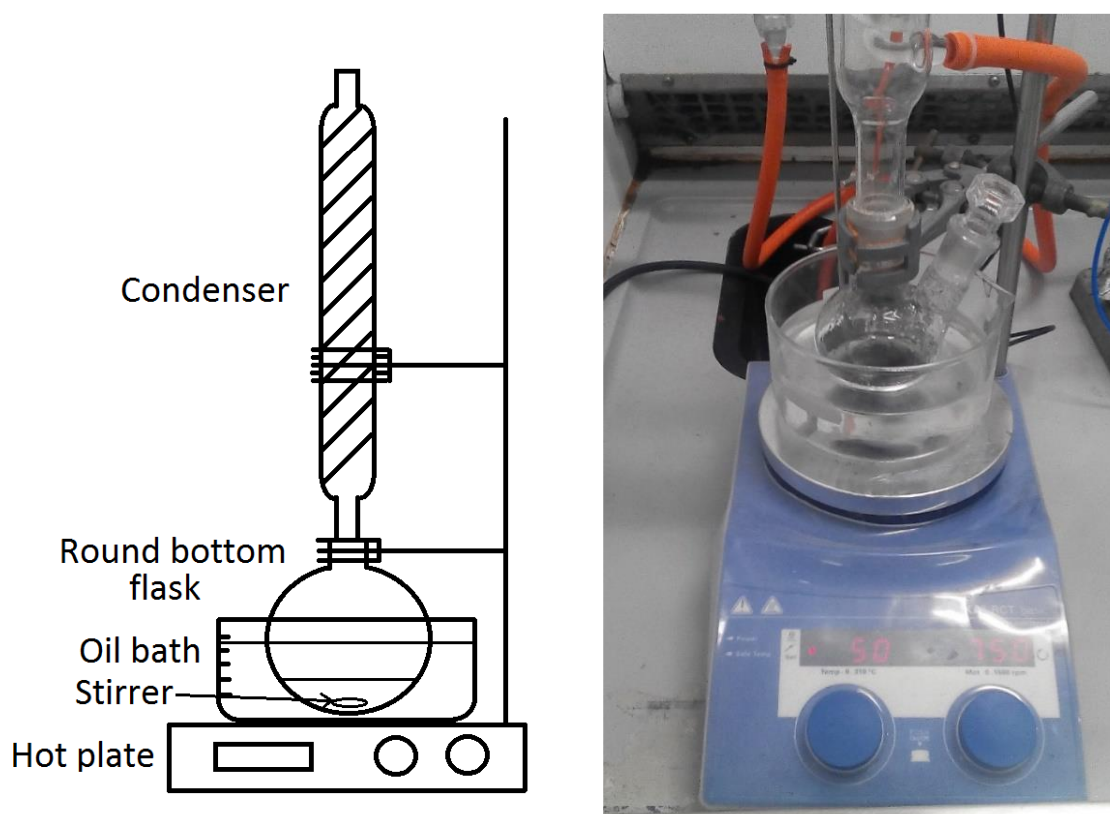


Figure 22. Diagram of the batch reactor set up and an actual photograph of the system.

For the batch reaction, formic acid decomposition was conducted in a two-necked 100 ml round-bottom flask placed in an oil bath with a reflux condenser and a magnetic stirrer at a pre-set temperature. In normal conditions, 10 ml of aqueous HCOOH solution (0.5 M) was placed in the reactor and stabilised at 30 °C. A low heat management profile is a key requirement for portable devices carrying fuel cells, therefore, the reference temperature at which catalyst activity is measured must be close to room temperature. In this case, it is slightly higher in order to grant reproducibility. A concentration of formic acid of 0.5 M was chosen due to two factors. The first reason is due to the literature: this concentration is commonly used and, by selecting it, it facilitates the comparison between different systems. The second factor is that in preliminary experiments with the commercial catalyst under these conditions, a substrate:metal molar ratio of 2000:1, would reach total formic acid conversion in approximately 1 hour, which allows performing several reactions per day without compromising reproducibility. The selection of this substrate:metal molar ratio will be explained in Chapter 3.

Once the temperature was reached, the desired amount of the catalyst was added, and the reaction was initiated by stirring. Samples from the reaction batch were withdrawn periodically and analysed by means of HPLC so as to follow the reaction progress. Each reaction was carried out a minimum of two times in order to ensure the reproducibility of data. Once averaged the value for a certain experiment, error bars are calculated applying the differences with the real values.

TOF (turnover frequency: moles of reactant converted per mole of metal per time) was calculated for the initial 5 minutes for a suitable comparison of reaction rates on different catalysts. Based on the conversion obtained by HPLC, the amount of gas evolved can be simply calculated using the general gases equation:

$$p V = n R T \quad (\text{eq. 4})$$

and subsequently, the initial rate, this is the total gas volume produced within the first 5 minutes.

An approximation of the reaction order was estimated representing the rate of gas formation vs the concentration of formic acid and fitting to a power-law model equation:

$$r = k C^n \quad (\text{eq. 5})$$

where r is the reaction rate, k is the kinetic coefficient, C is the initial formic acid concentration and n is the reaction order.

Kinetic Isotope Effect (KIE) was performed to help to elucidate first the rate-determining step and thus, the most probable pathway followed by the reaction (either formate or carboxylic decomposition, as will be deeply explained later in this Thesis). This kinetic test consists in the use of different deuterium substituted substrates, such as HCOOD, DCOOH and DCOOD (Figure 23), in order to distinguish the reaction pathway.

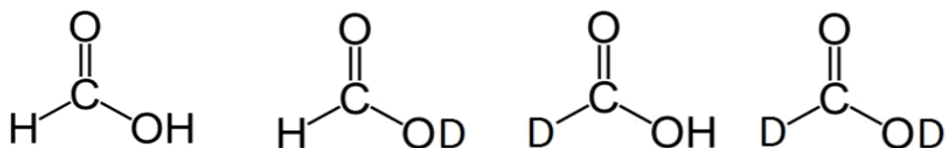


Figure 23. Isotopologues of formic acid used for kinetic isotope experiments.

By using the isotope series of formic acid, different rates will be observed due to the nature of the C-H and C-D bonds. This means, breaking a C-H or C-D bond have different energy requirements since heavier isotopologues have lower velocity/mobility and increased stability thus, the rate will be modified and probably, a pathway for formic acid decomposition can be identified. As explained in the previous chapter, KIE values are the ratio between the reaction rate when HCOOH is used and the reaction rate when an isotopologue is used. In case KIE value for HCOOD is close to 1 and larger for DCOOH, it means that HCOOH dissociation is kinetically relevant. On the contrary, KIE value close to 1 for DCOOH but not for HCOOD is due to limitation by the formate decomposition. And, in case KIE values are approximately 1 for both HCOOD and DCOOH, hydrogen desorption both from HCOOD and DCOOH is the rate determining step.²⁴

At this point, the reaction was largely studied using the commercial 5 wt. % Pd/C and a slight modification to the catalyst would be helpful to study its catalytic behaviour. In most cases, the last step in catalysts preparation is calcination.¹⁴ This process removes impurities present on the catalyst surface and stabilises the structure, however, it can greatly affect particle size. Two different heat treatments were performed: at 200 and 250 °C. Catalyst activity was investigated afterwards at the optimised reaction conditions.

Besides formic acid dehydrogenation being performed in batch reactor, continuous flow reactor was also investigated as an introduction and initial overview of the behaviour of the reaction under these conditions. Figure 24 shows the schematic diagram of the continuous flow setup.

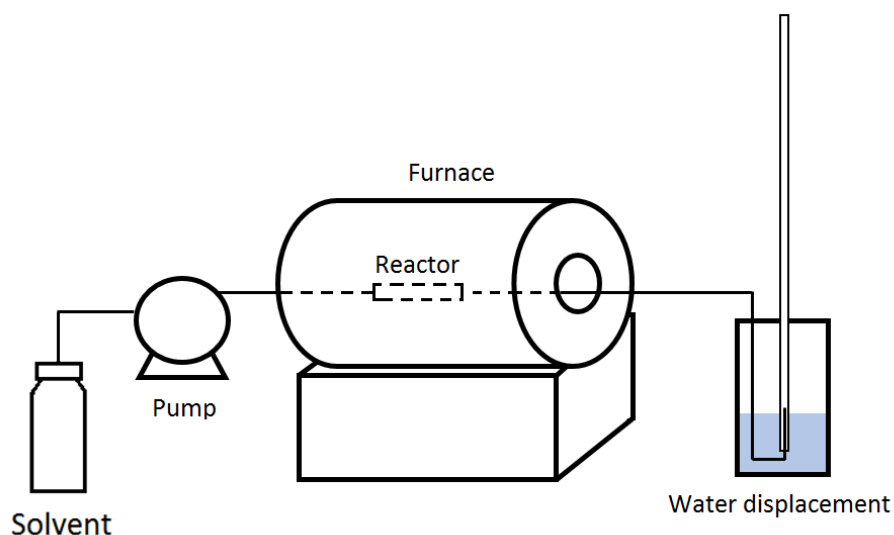


Figure 24. Diagram of continuous flow setup.

In continuous flow set up, the reactor temperature was monitored by the furnace and kept steady at 30 °C on the surface of the reactor. In a typical test, approximately 0.1 g of the commercial Pd/C catalyst was packed by glass wool in the middle section of the reactor. Once the reaction temperature was reached, a solution of 0.5 M formic acid was pumped into the reactor at 0.05 ml/min. The gas produced was collected according to the water displacement method as explained in subsequent sections. After a specific amount of time, the volume of gas produced was annotated in order to calculate reaction rate and so, conversion according to the next equation:

$$x_a = \frac{P_{atm} \cdot V_{gas}}{2 \cdot R \cdot T \cdot C_0 \cdot F_0} \quad (\text{eq. 6})$$

where P_{atm} is the atmospheric pressure, V_{gas} is the generated gas rate, R is the universal gas constant, T is the room temperature, C_0 is the inlet concentration of formic acid, and F_0 is the flow rate of formic acid solution. At the conditions of the experiment, the ideal gas law can be used since the deviation between real and ideal gas is typically small.

By using a continuous flow set up, a reusability test was performed with very promising results as it will be presented in Chapter 3. Reusability, actually, is a key parameter in catalysis. These experiments were performed in batch reactor for the most representative catalysts

synthesised throughout this Thesis and the details of these experiments will be presented later in this chapter. One of the factors preventing long-term reusability is the leaching of metal into the solution. In order to analyse the amount of metal present in the solution after the formic acid decomposition, two techniques were employed: Microwave Plasma Atomic Emission Spectroscopy (MP-AES) and Inductively Coupled Plasma Mass Spectrometry (ICP-MS) was performed. In Chapter 3, MP-AES was the selected technique since a series of samples were required to be analysed and it is a cost effective and very quick method while, in Chapter 4, more sensitivity and lower detection limit were the objectives; in that case, ICP-MS was more suitable.

2.2.1. Inductively Coupled Plasma Mass Spectrometry (ICP-MS)

An inductively coupled plasma is a plasma ionised by inductively heating the gas using an electromagnetic coil reaching temperatures in the range 8000 - 10000 K. At this temperature, the gas contains enough concentration of ions and electrons to make it electrically conductive. All chemical bonds are broken, thus, the data acquired from a plasma ion source corresponds to the total content of an element in the sample. Plasma used in spectrochemical analysis are electrically neutral, each positive charge is balanced by a free electron.²⁵

Figure 25 presents a scheme of the main parts comprising an ICP equipment.

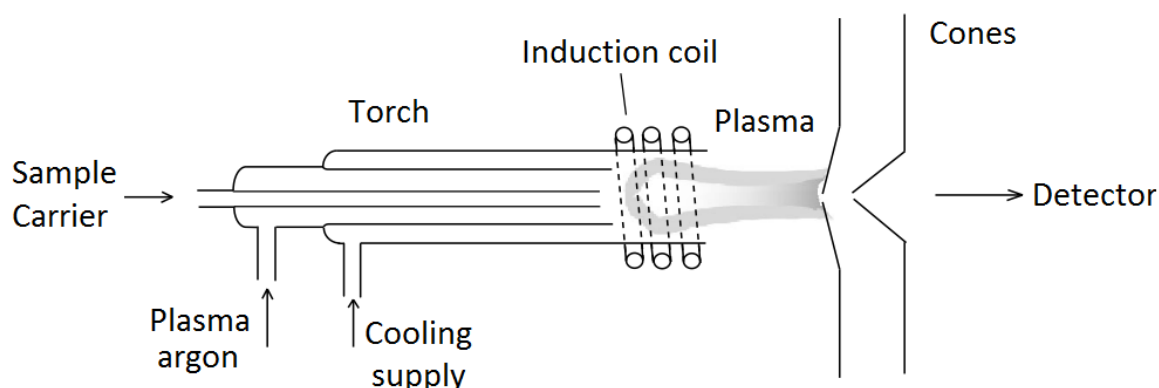


Figure 25. Diagram of the ion source and interface in ICP instrument.

First, a torch made of three concentric quartz tubes is placed inside an induction coil supplied with a radio-frequency electric current. Argon gas is introduced between the two outermost tubes and an electric spark introduces into the gas stream the free electrons which interact with the radiofrequency magnetic field and accelerates them first in one direction, then the other, as the field changes at high frequency. These accelerated electrons collide with argon atoms causing the release of another electron which is also accelerated by the magnetic field. This process stops once the rate of release of electrons is balanced by the rate of recombination of electrons with argon ions. The sample to be analysed is introduced in the central channel. ICP can analyse all gases, liquids and solids, however, their introduction into the system is different for each one of them. Gas-phase is the easiest method since it does not require any preparation. Solids, typically, must be digested and dissolved to obtain a homogeneous sample. For this purpose, laser ablation is used, which is ideally suited for microsampling on surfaces and in-depth profile analysis. Liquids are nebulised which is an easy method and by far the most used sample introduction technique, and the one used in this Thesis.²⁶ Coupling ICP into mass spectrometry, the ions are extracted through a series of cones into the mass spectrometer where the ions are separated on the basis of their mass-to-charge ratio as will be explained in a subsequent section.

2.2.2. Quantification of metal

Elemental analysis using ICP-MS of the filtered solution after reusability tests were performed to quantify the leaching of Pd from the catalysts. The analysis was performed in an Agilent 7900 ICP-MS with full calibration for Pd (1mg/l, 0.1mg/l, 0.01mg/l, 0.001mg/l and blank) prepared with certified standards from Waters. A photograph of the system is displayed in figure 26.



Figure 26. Agilent 7900 ICP-MS.

Response factors and calibration curve for Pd is presented in figure 27.

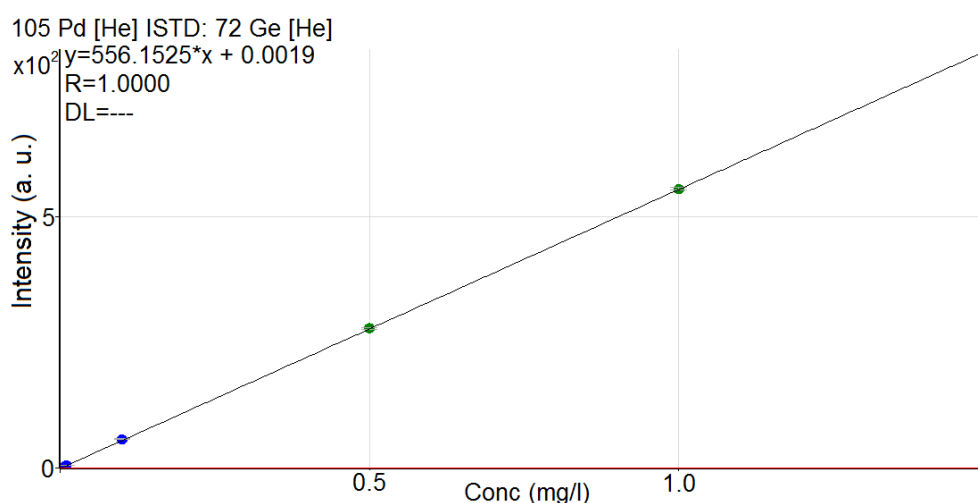


Figure 27. Calibration curve and response factor for Pd in Agilent 7900 ICP-MS.

2.2.3. Microwave Plasma Atomic Emission Spectroscopy (MP-AES)

The basic principles of this technique are very similar to the one in ICP with the exception that, in this case, it has microwave-induced nitrogen plasma as an excitation source. It uses a microwave excitation assembly to create a concentrated axial magnetic field around the torch. The microwave energy produces a toroidal plasma at approximately 5000 K with a cooler central channel where the liquid samples are introduced.²⁷ The plasma based on nitrogen and the non-requirement of argon gas is translated as a significant reduction in

operating and infrastructure costs, although in detriment of a lower sensitivity and so, higher detectability limits.

Instead of Mass spectrometry, microwave plasma typically uses Atomic emission spectroscopy (AES) as detection method. The plasma excites atoms and ions from the sample which emit electromagnetic radiation. This technique makes use of this electromagnetic radiation and analyses the wavelength and intensity. The wavelength of the atomic spectral line is characteristic of a particular element while the intensity of the emitted light is proportional to the number of atoms of the element and therefore, the concentration.

2.2.4. Quantification of metal

Elemental analysis using MP-AES of the filtered solutions after reusability tests were performed to quantify the leaching of Pd from the catalysts. The analysis was performed in an Agilent 4100 MP-AES with full calibration for Pd (5mg/l, 1mg/l and 0.1mg/l). A photograph of the system is displayed in figure 28.



Figure 28. Agilent 4100 MP-AES.

2.3. Analysis of reactants and products

HPLC (high-performance liquid chromatography) was used to calculate the concentration of formic acid and thus the conversion of formic acid during reaction progress. Liquid samples of the reaction mixture were withdrawn after 5, 15, 30, 60 and 120 minutes, added succinic acid as external standard, diluted 1:100 with deionised water, and injected into the HPLC. The

gaseous products (H_2 and CO_2) were analysed by GC (Gas Chromatography) and MS (Mass Spectrometry).

2.3.1. High-Performance Liquid Chromatography

HPLC is a technique used to separate, identify, and quantify the components in a mixture. HPLC instruments are typically composed of a mobile phase reservoir, high-pressure pump, injector, oven, column and detector (Figure 29).

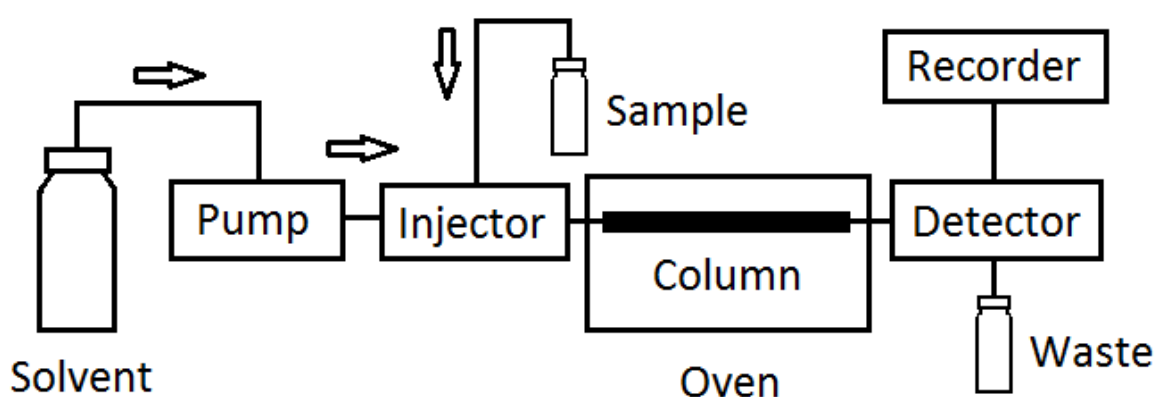


Figure 29. Diagram of an HPLC system.

In this technique, a liquid solvent (the mobile phase) is pressurised in a pump and mixed in the injector with the sample to be analysed. This mixture is pumped through a chromatographic column filled with a solid adsorbent material (stationary phase) that separates each component depending on the degree of interaction with the adsorbent material which causes different retention times (t_r) which is the time at which a specific analyte elutes, this is, to leave the column. This time depends on the chemical nature of the component, on the composition of the mobile phase and the nature of the stationary phase (column). This causes different flow rates for the different components and therefore, producing its separation. The adsorbent is typically a granular material made of solid particles such as silica, polymers, etc. The signal produced by the detector is proportional to the amount of sample component leaving the column which means that HPLC is also used for quantitative analysis of the sample components.

As a brief explanation, separation of the components is achieved by either polarity, electrical charge or molecular size.

- Separations based on polarity are divided into normal and reversed phase. Normal phase chromatography makes use of a polar stationary phase and non-polar mobile phase. In this case, the analyte is retained due to the interaction of its polar functional groups with the polar groups on the surface of the stationary phase. The least polar compound in the analyte elutes first, followed by other compounds in order of their increasing polarity. On the contrary, reversed phase uses a non-polar stationary phase and oppositely, an aqueous, moderately polar mobile phase. In this case, the most polar compound in the analyte elutes first.
- Separations based on electrical charge (Ion-Exchange Chromatography) is due to the attraction between the analyte ions and an opposite charge present in the stationary phase. This way, solute ions with the same charge of the stationary phase are quickly eluted while the ions with opposite charge are retained in the column.
- Separations based on size (Size-Exclusion Chromatography) separates particles on the basis of molecular size. In this technique, the stationary phase is made of inert particles with small pores densely packed. Through these small pores, only the smallest molecules of the analytes can pass. These molecules, therefore, will penetrate more into the pores and will take longer to elute while larger molecules can only penetrate pores of a certain size or may be totally excluded from the pores and pass only between the particles, eluting very quickly.

HPLC detectors can be classified as universal or selective. Universal detectors measure physical properties common to all analytes by measuring differences in the mobile phase with and without the sample. Universal detectors respond to all analytes; however, sensitivity is very limited. One of the typically used is the refractive index detector. On the other hand, selective detectors respond to a physical or chemical property unique to a specific analyte. The most common example is the UV detector, which response to analytes that absorb UV light at a specific wavelength. Other analyte specific detectors include fluorescence, conductivity, and electrochemical.²⁸

2.3.1.1. Quantification of reactants and products

HPLC model Agilent 1220 Infinity LC using a column (reversed phase) MetaCarb 87H 250 x 4.6 mm, Agilent, at 60 °C and a flow rate of 0.4 mL min⁻¹. A photograph of the system is displayed in figure 30.



Figure 30. HPLC Agilent 1220 Infinity LC.

The instrument is equipped with a Variable Wavelength (VW) detector pre-set at 210 nm. The eluent was an aqueous solution of phosphoric acid (0.1 wt. %). Succinic acid was used as external standard for the quantification of the concentration formic acid remaining in the reagent solution. Seven formic acid solutions were made in order to perform the calibration. Table 8 displays the concentration and areas obtained during the calibration of the instrument and its response factor and calibration curve is presented in figure 31.

Table 8. Concentration and areas obtained during the calibration of the HPLC.

Formic acid concentration (M)	Area FA	Succinic acid concentration (M)	Area SA
0.512	605.5	0.202	371.2
0.411	496.8	0.201	373.8
0.307	396.7	0.199	382.6
0.207	249.9	0.202	370.1
0.102	129.8	0.207	385.5
0.051	67.2	0.202	368.6
0.010	17	0.206	388.6

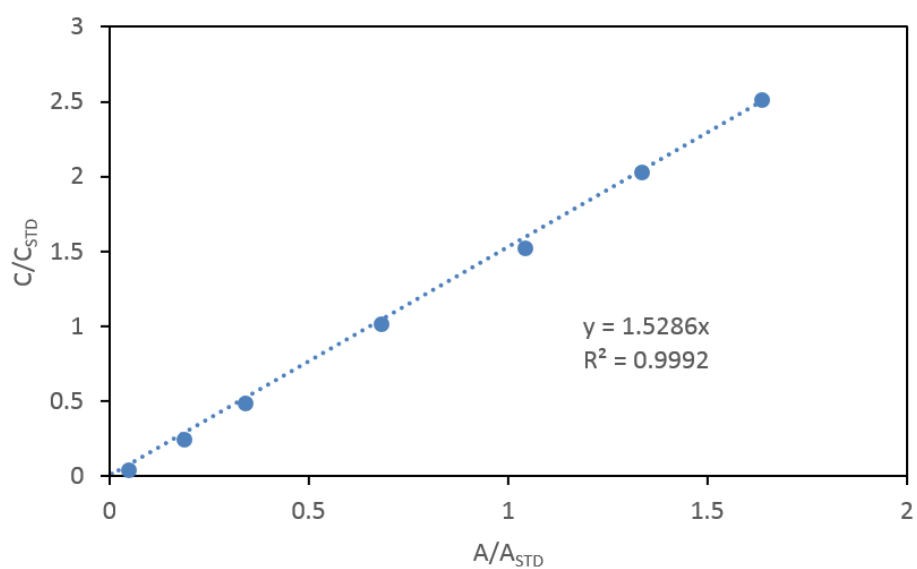


Figure 31. Calibration curve and response factor of the HPLC calibration for formic acid.

A representative chromatogram of the initial stage of a typical formic acid decomposition is displayed in figure 32.

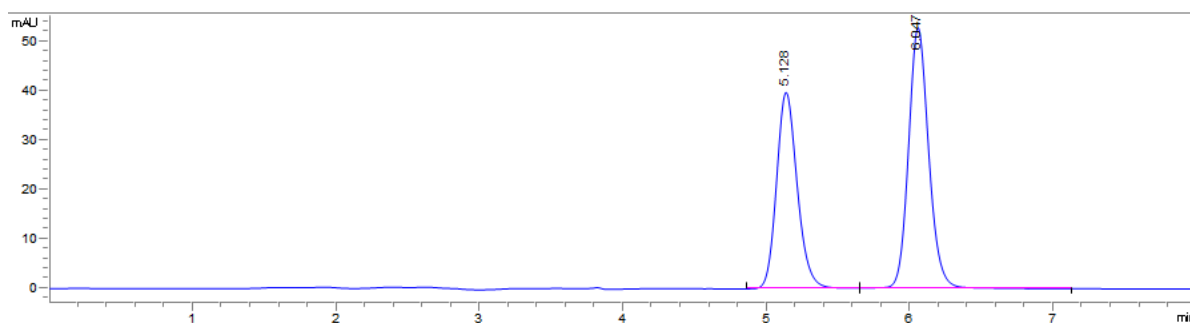


Figure 32. Representative chromatogram of formic acid decomposition before the start of the reaction. The peak at $t_r = 6.047$ min is assigned to formic acid and the peak at $t_r = 5.128$ min, to succinic acid.

2.3.2. Gas analyses

Gas evolved from formic acid decomposition was collected using a gas burette as in the water displacement method (Figure 33). Analysis of these produced gases was performed by means of Mass Spectrometry (MS), for the detection and quantification of hydrogen, and Gas Chromatography (GC), for the detection and quantification of carbon monoxide and carbon dioxide. The instruments were previously calibrated using commercial standards: three cylinders were purchased from BOC gases with concentrations of H_2 and CO_2 of 2, 5 and 10 %.

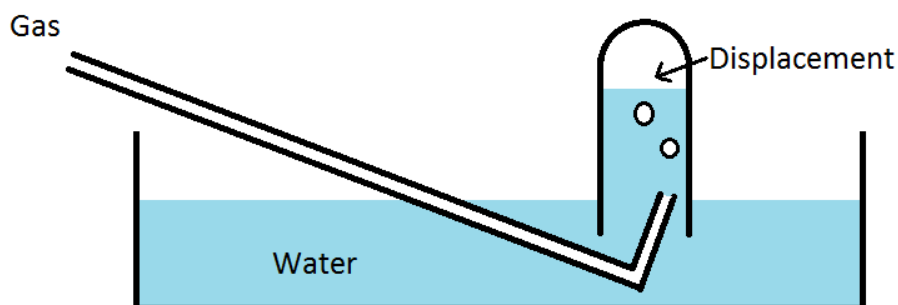


Figure 33. Graphical representation of the water displacement method used to collect gas evolved.

2.3.2.1. Mass Spectrometry

Mass spectrometry (MS) is an analytical technique used to detect, identify and quantify molecules according to their mass-to-charge (m/z) ratio (Figure 34). Typically, the sample is normally ionised to cations by bombarding it with a high energy beam of electrons. Some of

the produced ions may also fragment into smaller cations and neutral fragments. The separation of the cations is achieved by accelerating the ions in a beam which is bent by a magnetic field in an arc whose radius is inversely proportional to the mass of each ion, therefore, the strength of the magnetic field will produce the focusing on the detector of only the ions with a selected mass. Those lighter ions will be deflected more, and the opposite for heavier ions. Since the strength of the magnetic field can be modified, ions of different mass can be progressively focused. The detector is typically an electron multiplier. The resulting spectra display the relative abundance of the detected ions as a function of the mass-to-charge ratio and then, the sample may be identified by comparing the identified masses with known masses.

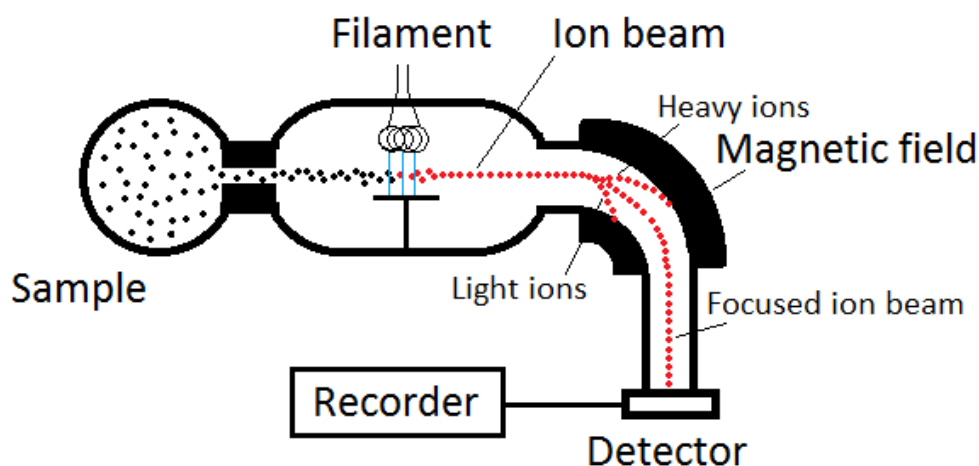


Figure 34. Diagram of a Mass Spectrometry system.

2.3.2.1.1. Quantification of reactants and products

Gas samples were analysed on-line by mass spectrometer Hiden analytical atmospheric gas analysis-quadrupole gas analyser (QGA) equipped with a quartz inert capillary with a consumption rate of 0.8 ml/min and Faraday electron multiplier detector capable of detecting concentrations of species in the range 0.1 ppm to 100 %. QGA Professional Software was used to quantify the partial pressures as a function of the m/z ratio. A representative spectra of the analysis of the evolved gases is displayed in figure 35.

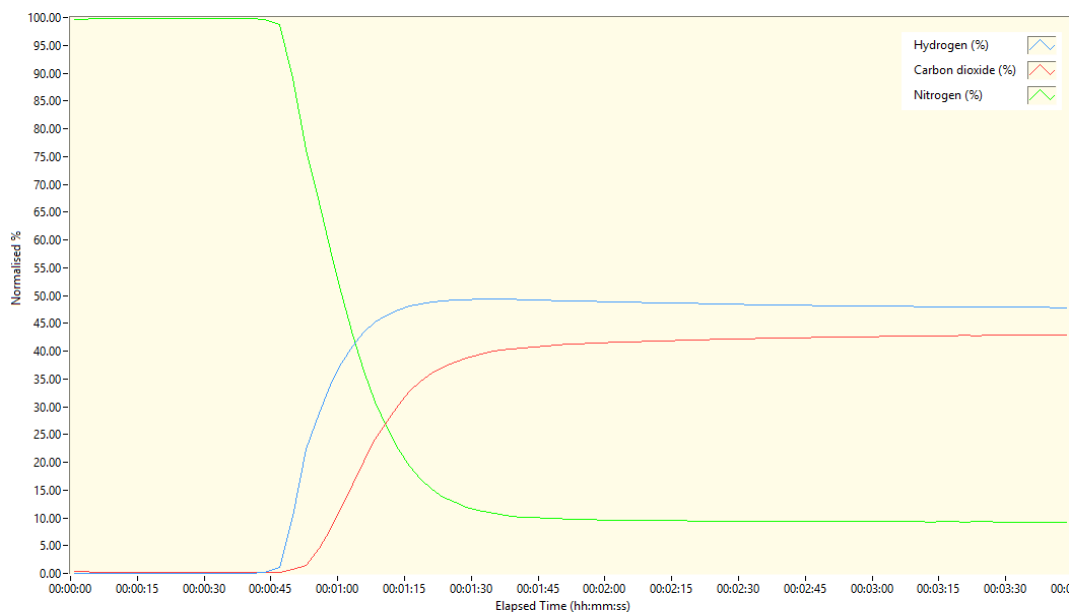


Figure 35. Time on-line of concentration of the evolved gases: hydrogen and carbon dioxide.

A photograph of the system used is displayed in figure 36.



Figure 36. Hiden analytical QGA.

No calibration curve is necessary to calculate since the injection of the three calibration standards modify internal sensitivity parameters.

Carbon dioxide can be directly analysed by means of MS, however, since carbon monoxide concentration was expected to be in the ppm range and carbon dioxide was approximately 40-50 % of the sample, fragmentations of carbon dioxide at $m/z = 28$ could interfere altering the values obtained for the concentration of carbon monoxide. Furthermore, nitrogen has a

$m/z = 28$ which would again overestimate the concentration of CO. Therefore, a GC was used in order to avoid this issue and obtain an accurate value for the carbon monoxide concentration since it is a crucial parameter for fuel cells.

2.3.2.2. Gas Chromatography

Gas Chromatography (GC) is a technique used to analyse gas mixtures by separating the component gases. The sample to be analysed is injected into the GC, eluted by a carrier gas (mobile phase) and heated to vaporisation before being injected into a chromatographic column (with the stationary phase inside). The components of the mixture are separated depending on the strength of their interactions with the stationary phase, it means, different affinities for this stationary phase will be translated into different retention times (t_r). Once a certain component leaves the column, it is detected and appears as a peak in the chromatogram. The concentration of the component can be quantified by measuring the area under the peak since it is proportional to the amount of the component present.

Even though GCs can be complex systems, all GCs are composed of an injector port, a carrier gas, column, oven, detectors and data recorder as shown in figure 37.

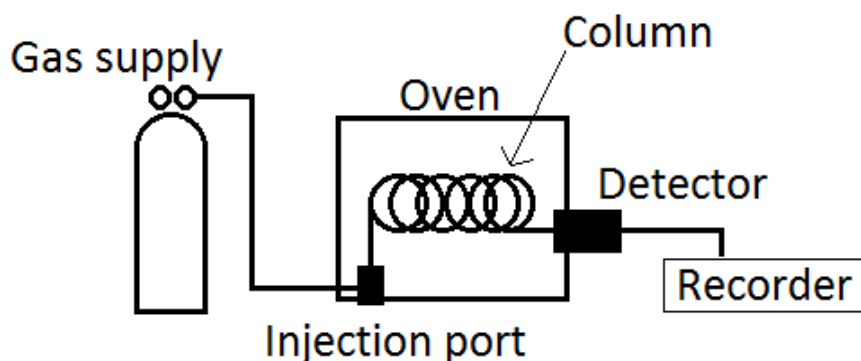


Figure 37. Diagram of a Gas Chromatography system.

The two most common detectors used with GC are thermal conductivity detectors (TCDs) and flame ionisation detectors (FIDs). TCD detects chemicals according to changes in the thermal conductivity between a reference flow of carrier gas and the column effluent. Once a component leaves the column, the TCD detector will display a change in thermal conductivity

as a difference in voltage. On the other hand, FID detectors burn the components in a flame of hydrogen between two electrodes which results in the formation of ions. These ions are attracted to a collector plate, where their impact generates a current which is detected and quantified. This current is proportional to the amount and type of ions. Whilst TCD is a non-destructive technique, FID is a destructive technique. Furthermore, FID can only be used with compounds that can be pyrolysed in a hydrogen-air flame and so, it is suitable for hydrocarbons but less sensitive to oxygen-containing compounds and completely insensitive to compounds which cannot be ionised by the flame such as H₂O, CO or CO₂. On the other hand, TCD can detect any molecule with a thermal conductivity different from the carrier gas, however, less sensitive than FID.

2.3.2.2.1. Quantification of products

CO and CO₂ were quantified using a Varian 450-GC fitted with a CP-Sil 5CB capillary column (50 m length, 0.32 mm diameter, carrier gas: He), a methanator unit at working temperature of 350 °C that converts CO_x to CH₄ through hydrogenation with a hydrogen flow of 20 ml/min and 300 ml/min of air. The oven is set up at 100 °C. It is equipped with both FID and TCD detectors with a detection limit of CO below 5 ppm. A photograph of the system is displayed in figure 38.



Figure 38. Varian 450-GC.

Table 9 displays the concentrations and areas obtained during the calibration of the GC. Response factor and calibration curve for carbon dioxide are presented in figure 39. Note that

both carbon monoxide and carbon dioxide share the same response factor in the methanator thus, carbon monoxide calibration is not required.

Table 9. Concentration and areas obtained for the calibration of the GC.

Concentration of carbon dioxide (%)	Area
2.03	10960
2.03	11001
5.02	27022
5.02	27030
10.23	55993
10.23	55749

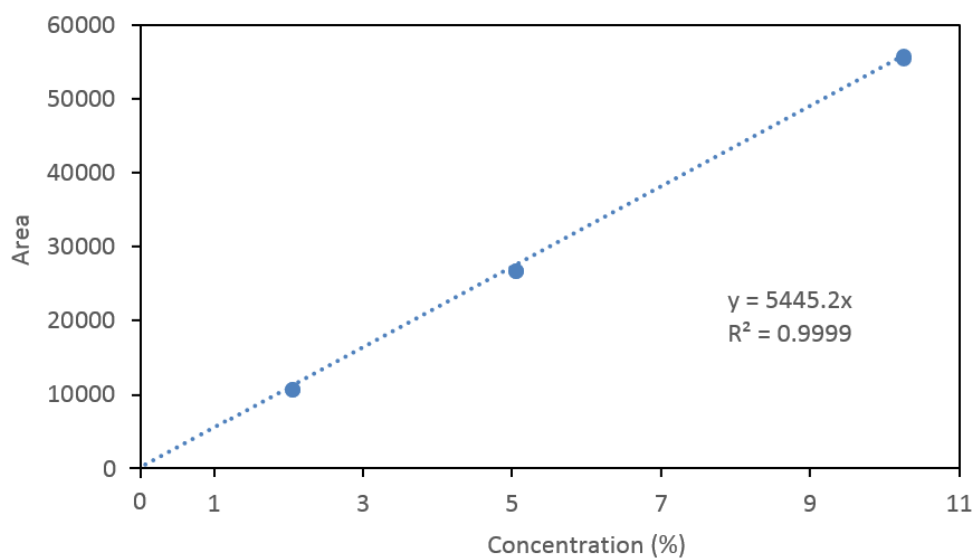


Figure 39. Calibration curve and response factor of Varian 450-GC.

A representative chromatogram of the analysis of carbon dioxide and carbon monoxide in Varian 450-GC is displayed in figure 40.

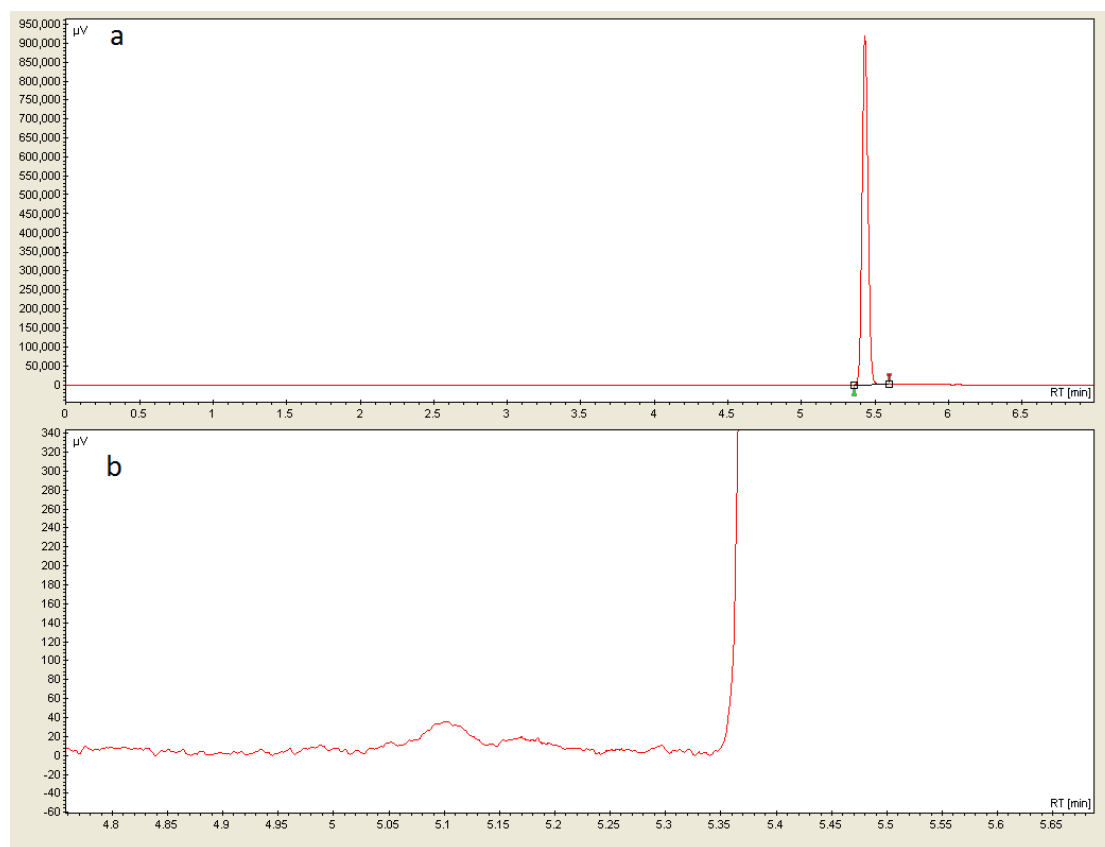


Figure 40. a) Representative chromatogram obtained using the GC Varian 450. Note the visibility of the peak of CO_2 at $t_r=5.45\text{min}$, b) Zoom of figure 40a to observe the peak at $t_r=5.1\text{min}$ attributed to CO .

2.4. Recyclability tests

The recyclability tests were performed at $30\text{ }^\circ\text{C}$ using an aqueous solution of HCOOH (0.5 M). According to the available mass of catalyst and loading, two different methods were performed to study the reusability capacity of the catalysts. In Chapter 3, the activity of a commercial 5 wt. % Pd supported on activated carbon will be studied. Since its loading is 5 wt. % and a large amount is available, the next procedure was followed: a typical formic acid decomposition was performed with a large excess of catalyst (ca. 100 mg). Once the reaction was finished, the catalyst was isolated from the reaction solution by filtration and then dried at ambient temperature for 18h. From the dried catalyst, 5.3 mg was taken to perform a standard reaction to study the activity in the second cycle and the remaining large amount of catalyst (ca. 85-90 mg) was used in the decomposition of formic acid as well. This cycle was repeated for 5 times. A large amount of catalyst was used since during recovery of the filtrated catalyst, a significant amount remained in the filter paper. On the other hand, in

Chapter 4, approximately 1-2 g of a series of catalysts with 1 wt. % loading was synthesised. This makes the previous method unsuitable, so a different technique was developed: after a typical experiment of 2 hours, the reaction was stopped, a liquid sample from the reaction mixture was collected and analysed by HPLC and the conversion of HCOOH was calculated. Based on the amount of HCCOH consumed, the necessary amount of pure formic acid to reach the initial concentration of 0.5 M was calculated and added into the reactor. The reaction was started again by initiating the stirring. This cycle was repeated for 5 times as well. ICP-MS (Inductively Coupled Plasma Mass Spectrometry) of the filtered solution after reusability tests were performed in order to quantify the leaching of Pd from the catalysts.

Since deactivation of the catalyst in continuous flow could not be avoided, an easy method for its reactivation was developed as well. Once the reaction rate decreased to 10-20 % of the original one, the catalyst was easily reactivated by switching off the pump, opening the outlet of the reactor to allow desorbed species to leave and increasing the temperature of the furnace to 180 °C. This temperature was selected according to experimental results showing a significantly low reactivation for lower temperatures. Approximately 1.5 hours was enough period of time to allow absorbed species on the active sites to desorb and exit the reactor, achieving a high degree of reactivation.

2.5. Catalyst characterisation

2.5.1. X-ray Diffraction (XRD)

X-Ray diffraction is a non-destructive crystallographic technique used to determine the crystal structure of a material and the compounds present by means of the diffraction pattern. The target compound is exposed to x-ray radiation which is scattered in all directions and therefore cancelled by destructive interference. However, when the beam strikes with a certain angle, it will produce constructive interference, generating a measurable signal (Figure 41). This produces a pattern which provides structural information about the sample. The pattern is plotted in a diffractogram which displays the intensity of the diffracted X-rays against the angle (2θ) at which constructive interference of x-rays is produced. This pattern can be used as a fingerprint of a crystalline phase and by comparing with available databases, identify the compounds present in the sample and its structural properties.

The angles in which X-rays are scattered constructively are given by Bragg's Law:²⁹

$$2d\sin\theta = n\lambda \quad (\text{eq. 7})$$

where d is the spacing between planes of the crystal structure, θ is the angle of the beam, n is an integer, and λ is the wavelength of the incident radiation.

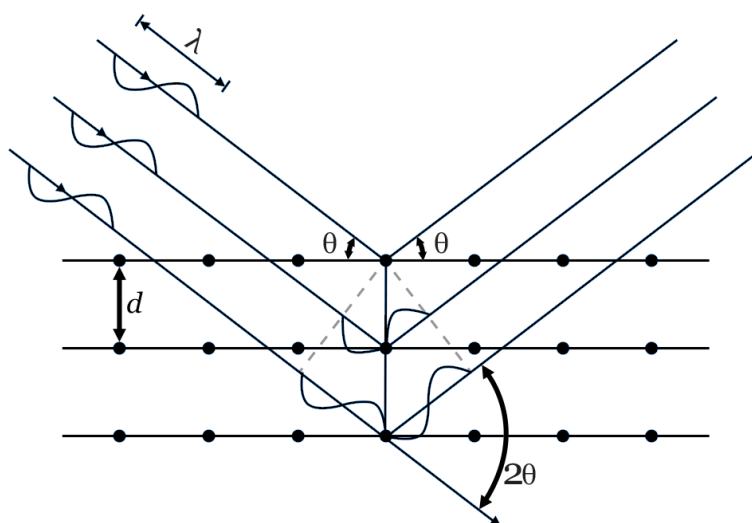


Figure 41. Diagram to illustrate Bragg's equation.

A unit cell is the smallest group of particles that constitute the repeating pattern in a lattice. A unit cell is composed of three translations and three angles. This is named lattice or unit cell parameters. Crystals are made of three-dimensional lattices. The repetitive translation of the unit cell along its principal axes builds the entire crystal lattice. Miller indices, hkl , define sets of equally spaced and parallel lattice planes.³⁰

The crystallite size of a crystal in the form of powder can be calculated by means of the Scherrer equation which relates the size of nano-scale particles in a solid with the broadening of the peak in a diffraction pattern according to the following equation:

$$D = \frac{K \cdot \lambda}{\beta \cdot \cos \theta} \quad (\text{eq. 8})$$

where D is the crystallite size, λ the wavelength of the radiation, β the FWHM (Full Width at Half Maximum) of the peak in 2θ , K a correction factor related to crystallite shape usually taken as 0.9, and θ the angle of the beam. Crystallite size can be calculated easily in this way, however, the applicability of this technique is subjected to compounds with a certain range crystal structure, this is when particle size is higher than 5 nm due to the extensive broadening that small particles create in the XRD pattern.

X-Ray diffraction (XRD) data were collected at ambient temperature with PANanalytical X'PertPRO X-ray diffractometer using the Cu K_{α} radiation ($\lambda = 0.154098$ nm) and operated at 40 kV and 40 mA. X-ray diffraction patterns were typically recorded in the range 10 - 80° 2θ at a step size of 0.017° . Samples were mounted on sample holders. A photograph of the system is displayed in figure 42.



Figure 42. PANalytical X'PertPRO X-ray diffractometer.

2.5.2. X-ray photoelectron spectroscopy (XPS)

XPS is a surface sensitive characterisation technique which provides information on the elemental composition and the oxidation state of its elements. In this technique, the sample surface is irradiated with monochromatic X-Rays under ultra-high vacuum and the emitted photoelectrons from the core energy levels of atoms are measured. This technique is surface sensitive since the electrons are emitted from a maximum depth of approximately 5 nm. From the measured kinetic energy of these photoelectrons it is possible to determine the binding energy of the atoms according to the equation:

$$E_{kinetic} = h\nu - E_{binding} - \Phi \quad (\text{eq. 9})$$

Where h is Planck's constant, ν is the frequency of the exciting radiation, and Φ is the work function of the spectrometer which is the difference between the vacuum energy level and the Fermi energy level (Figure 43).

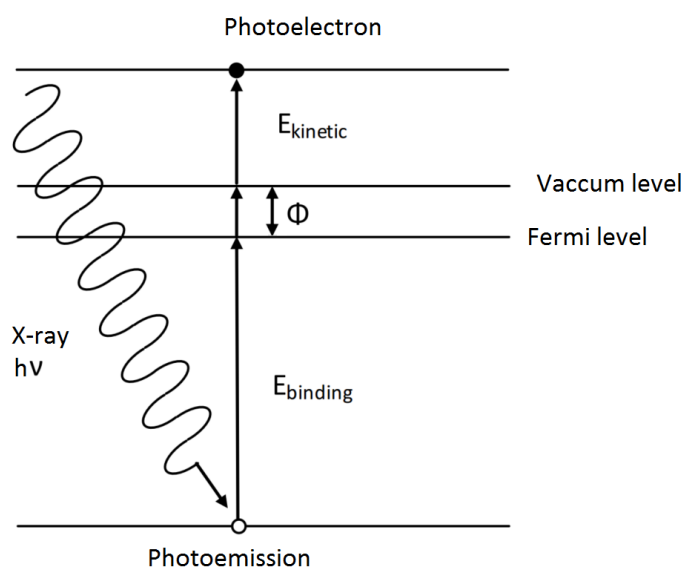


Figure 43. Diagram to illustrate photoemission.

XPS spectra is usually a plot of the intensity of the photoelectrons (i.e. number of electron counts) versus binding energy. The peaks appearing at certain binding energy allow the identification of the species present on the surface of the sample since there is a characteristic binding energy associated with each core atomic orbital. This makes XPS one of the most commonly used techniques in catalyst characterisation.

Photoelectron peaks are labelled according to the quantum numbers of the level from which the electrons are emitted, i.e. for Pd, the most common peaks are the Pd 3d. Quantum number n is an integer ≥ 1 , and the total momentum is $j = l + s$ where the orbital momentum l is 0,1,2,3... (denoted as s,p,d,f...) and, when $l \geq 1$, the spin momentum s is either $+1/2$ or $-1/2$. As a consequence, each level has two sublevels leading to the presence of a doublet in the spectrum.²⁹ Thus, the Pd 3d level gives two photoemission peaks, $3d_{5/2}$ (with $j = 2 + 1/2$) and $3d_{3/2}$ (with $j = 2 - 1/2$).

X-ray photoelectron spectroscopy (XPS) was performed on a Thermo Scientific K-alpha+ spectrometer. Samples were analysed using a monochromatic Al X-ray source operating at 72 W (6 mA x 12 kV), with the signal averaged over an oval-shaped area of approximately 600 x 400 microns. Data was recorded at pass energies of 150 eV for survey scans and 40 eV for high-resolution scan with a 1eV and 0.1 eV step size respectively. Charge neutralisation of the sample was achieved using a combination of both low energy electrons and argon ions (less than 1 eV) which gave a C(1s) binding energy for adventitious carbon of 284.8 eV. The envelopes were fitted after subtraction of a Shirley background³¹ using CasaXPS (v2.3.17 PR1.1) using Scofield sensitivity factors and an energy exponent of -0.6. For analysis of Pd²⁺/Pd⁰ species, as previously commented, the Pd 3d region presents two doublets (3d_{5/2} and 3d_{3/2}). The second peak of each doublet was constrained to have a 10 % more full width at half maximum (FWHM), an area of 2/3 of the first peak and a position 5.26 eV higher, as this is typical of the Pd 3d doublet. In the case of Au, it presents two doublets as well (4f_{7/2} and 4f_{5/2}). The second peak was constrained to have the same full width at half maximum (FWHM), an area of 3/4 of the first peak and a position 3.7 eV higher, as this is typical of the Au 4f doublet. A photograph of the system used is displayed in figure 44.



Figure 44. Thermo Scientific K-alpha+ spectrometer.

2.5.3. Electron Microscopy

Optical microscopy is not useful to see the surface of a catalyst due to the long wavelength of visible light, being not capable of detecting features smaller than about 1 μm . Therefore, electron microscopy was developed. Nowadays this technique is crucial in catalysis since it can reach magnifications on the order of one million times and resolutions of approximately 0.1 nm and due to the small wavelength of electrons of less than an Angstrom.²⁹ Electron Microscopy is a technique used to determine the size, shape and compositions of nanoparticles in heterogeneous catalysis. It can also provide information about the internal structure of the particles by analysing how the electron is diffracted. Electron Microscopy comprehends a wide series of techniques depending on the type of electrons it analyses (Figure 45). In this work, Transmission Electron Microscopy and Scanning Electron Microscopy have been used.

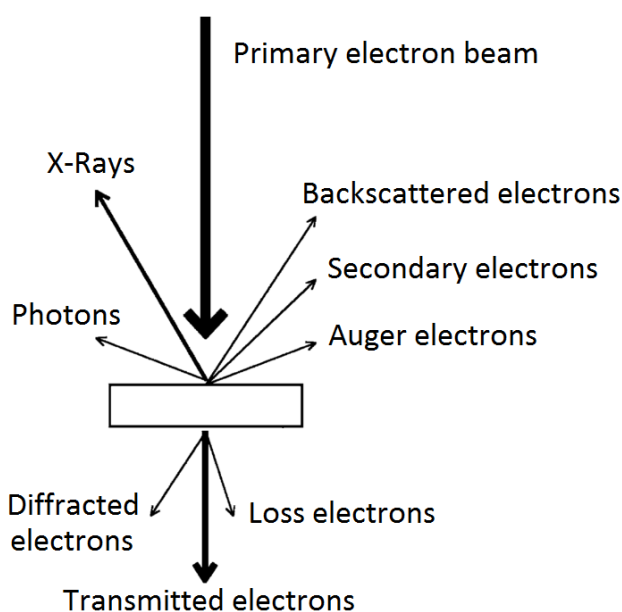


Figure 45. Interaction between the primary electron beam and the sample in an electron microscope.

2.5.3.1. Transmission Electron Microscopy (TEM)

In Transmission Electron Microscopy a gun emits a primary electron beam of high energy and high intensity that passes through a condenser to produce parallel rays that impact on the sample (Figure 46). Depending on the sample thickness and density, a fraction of the electrons

pass through the sample without suffering energy loss, these are the so-called transmitted electrons. These electrons create a two-dimensional projection of the sample mass, which is subsequently magnified by electromagnetic lenses and hit a fluorescent screen where the bright-field image is formed. Transmission Electron Microscopy also makes use of diffracted electrons to form the dark-field image. When the particles are favourably oriented towards the beam, these electrons are diffracted providing crystallographic information.²⁹

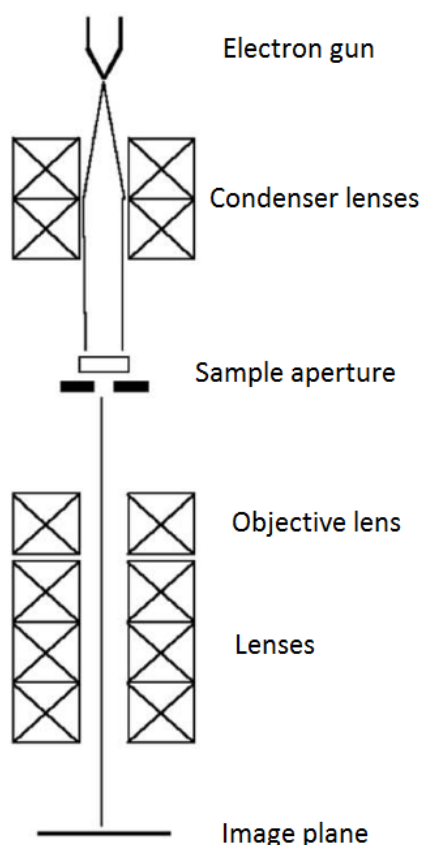


Figure 46. Schematic set-up of a transmission electron microscope.

In this work, Particle size distributions and mean particle size were obtained by means of Transmission Electron Microscopy using a JEOL JEM 2100 TEM operating at 200 keV. Samples for examination were prepared by dispersing the catalyst in high purity ethanol. A drop of the suspension was allowed to evaporate on a holey carbon film supported by a 300-mesh copper TEM grid. Samples were subjected to bright-field diffraction contrast imaging experiments. Mean particle sizes and particle size distributions were determined by measuring the size of over 200 particles from different areas.

For the samples supported on carbon nanofibers, it was of great interest to identify where the particles were mainly located, either on the inner wall of the nanofiber or outside. This could explain differences in catalyst activity since nanoparticles inside the inner wall may be detrimental for the performance of the catalyst and thus, identify a preparation method as preferable over the other. With this objective, 3D tomography was performed. This technique makes use of a special TEM holder able to rotate in its main axis direction providing a series of tilted images. When sequencing this series of images, it is easy to observe the actual location of the nanoparticle on the nanofiber. A photograph of the TEM system is displayed in figure 47.



Figure 47. JEOL JEM 2100 Electron Microscope.

2.5.3.2. Scanning Electron Microscopy-Energy Dispersive X-Ray spectroscopy

Scanning electron microscopy (SEM) provides information about the macroscopic morphology of the catalyst and when used in combination with energy dispersive X-ray spectroscopy (EDX), the chemical composition. In Scanning Electron Microscopy, the electron beam is generated by a metallic filament (typically tungsten due to the high melting point) by passing a voltage through it under vacuum and detecting the yield of either secondary or backscattered electrons as a function of the position of the primary beam (Figure 48).

Secondary electrons have low energy and originate from the surface of the sample. These electrons are collected, amplified, and fired at a scintillator that emits flashes of light into a photomultiplier. This generates an amplified signal which is displayed as an intensity distribution pattern. The intensity of the signal is based on the number of electrons detected. Therefore, contrast is caused by the orientation: when the surface directly faces the detector, more electrons are collected, and it appears brighter than parts of the surface with their normal pointing away from the detector.

Backscattered electrons, on the other hand, come from deeper regions, are of much higher energy, and carry the information on the composition of the sample since heavier atoms backscatter electrons more strongly and appear brighter in the image.

As observed, the main difference between SEM and TEM is that in SEM, contrast is produced due to the topology and composition of the surface and with a resolution in the range 1-10 nm. Whereas in TEM, the electron beam creates a two-dimensional image of the mass it encounters and is of subnanometer resolution.

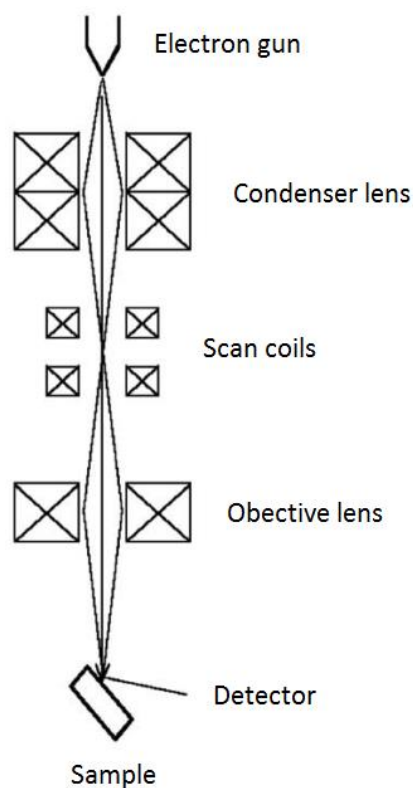


Figure 48. Schematic set-up of a scanning electron microscope.

When coupling SEM with an energy-dispersive X-ray spectroscope (EDX) detector, elemental composition can be analysed. This detector is a solid-state device consisting of lithium-doped silicon that absorbs the energy of incoming X-rays by ionisation and converts them in electrons which dissipates its kinetic energy by creating electron-hole pairs in the semiconductor. Hence, by measuring the pulse height of the current, which is proportional to the number of electron-hole pairs, the kinetic energy of the photoelectron is known and hence the energy of the incident X-ray photon which is unique to each element. Even though, atoms with similar atomic structure cannot always be resolved since the X-ray lines can be too closely spaced.²⁹

The number of X-rays emitted at certain energy value is proportional to the relative amount of the emitting atoms, therefore, the relative elemental composition can be assessed.

Selected sample powders were also dispersed on an Al-stub and examined in a Hitachi TM3030PLUS SEM equipped with a Quantax70 energy-dispersive X-ray spectroscope (EDX). A photograph of the system is displayed in figure 49.



Figure 49. Hitachi TM3030PLUS Electron Microscope.

2.5.4. Raman Spectroscopy

Raman Spectroscopy uses the inelastic scattering of photons, which modify their energy by exciting vibrations in the sample. In this technique, a monochromatic light impacts a sample

and the frequency of the scattered photons is measured. Three cases can be observed depending on the vibrational energy levels involved (Figure 50).

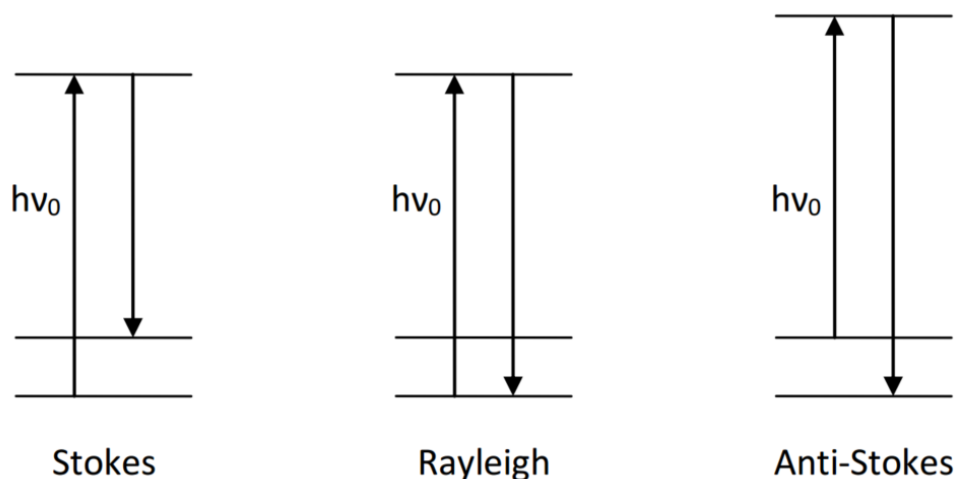


Figure 50. Diagram of types of scattering.

Most of the photons undergo Rayleigh scattering. This is an elastic scattering since no energy is exchanged between the molecule and the photon, the molecule decays to the ground state after the excitement. However, when the excited molecule decays to a different level of the original one, inelastic scattering is produced. It is called Stokes when the molecule decays to the first vibrational level and the opposite, anti-Stokes, when an already vibrationally excited molecule is brought to an unstable level to subsequently decay to the ground state. This changes in energy are translated to variations in frequency that corresponds to differences in energy between the vibrational energy levels of the sample. Consequently, this technique is used for identification of the bond vibrations and so, structure determination.

Raman spectroscopy was performed with a Renishaw inVia Raman microscope for analysing the graphitisation degree of the carbon nanofibers. Bare supports, fresh and used catalysts were analysed. Typically, a sample of approximately 0.01 g was placed on a metal slide inside the spectrometer. The powder was analysed under an IR class laser (514 nm) with a laser intensity of 50 %. The sample was scanned at an attenuation time of 22 seconds and 10 scans were performed to give a spectrum. A photograph of the system is displayed in figure 51.



Figure 51. Renishaw inVia Raman microscope.

2.5.5. Ammonia -Temperature Programmed Desorption (NH₃-TPD)

In Temperature-programmed (TP) techniques, a chemical reaction is monitored while the temperature increases with time. Temperature Programmed Desorption (TPD), Temperature Programmed Reduction (TPR) and Temperature Programmed Oxidation (TPO) are the most common thermo-analytical techniques used in heterogeneous catalyst characterisation. In NH₃-TPD, which is the technique used in this work, an adsorbate (NH₃) passes through the sample under well-defined conditions, followed by the heating of the sample in an inert atmosphere. This increase in temperature is enough to break the adsorption energies of the previously adsorbed species and therefore, the molecules desorb from the surface. The inert gas carries the desorbed molecules to a thermal conductivity detector where they are quantified.

This technique is useful to study properties of the surface of a catalyst such as the presence of acid-basic sites. In this Thesis, this technique has been used qualitatively in the carbon nanofiber functionalised samples with acid and basic sites to get an overview of the acidic strength of these sites. This means, lower temperature desorption corresponds to weak acid sites while higher temperature desorption, to strong acid sites.

However, Brønsted and Lewis acids cannot be distinguished using this method. For this purpose, pyridine FT-IR would be necessary where Brønsted and Lewis acids present different peaks, but this technique is not suitable for these catalysts since Beer's equation would not

be followed due to the presence of carbon as a support.³² Giordano *et al.* managed to successfully analyse concentrations of carbon in the range 0.03 – 0.15 % by this method.³³

NH₃-TPD was carried out using a Quantachrome ChemBET TPR/TPD chemisorption analyser with a TCD, following a method comprising four main steps. During the pre-treatment step, 50 mg of sample is heated at 15 °C/min up to 130°C during 1 h in a flow of 100 ml/min of pure He; followed by adsorption of ammonia at room temperature for 20 min to ensure saturation and subsequently the physisorbed ammonia is removed at 100 °C (1h, 15 °C/min) with pure He. The last step is the desorption of chemisorbed ammonia by heating up to 800°C (at 10°C/min) in He, monitoring the desorption with a Thermal Conductivity Detector (TCD) at attenuation 1 and current 180 mV. A photograph of the system is displayed in figure 52.



Figure 52. Quantachrome ChemBET TPR/TPD chemisorption analyser.

2.5.6. Brunauer, Emmett and Teller (BET) method surface area

Surface area is one of the main parameters in catalyst science since it has great importance in the catalyst activity. Gas adsorption can be used for the characterisation of surface area and porosity in nanoporous materials. It consists of the physical adsorption of an inert gas at its condensation temperature on the material. Typically, liquid nitrogen is used since the

temperature can be reached by immersing the sample and furthermore, it is abundant and inexpensive. The most common method to determine the surface area is that developed by Brunauer–Emmett–Teller (BET). The BET equation is derived from the Langmuir model for monolayer molecular adsorption and it can be used to estimate the surface area with several assumptions such as a) the gas molecules adsorb in layers on a solid; b) the interaction between each adsorption layer is negligible; and c) the Langmuir theory can be applied to each layer. The isotherm obtained is a function of the volume of gas adsorbed against the relative pressure according to the equation:

$$\frac{1}{v \left[\left(\frac{p}{p_0} \right) - 1 \right]} = \frac{c-1}{v_m c} \left(\frac{p}{p_0} \right) + \frac{1}{v_m c} \quad (\text{eq. 10})$$

where p and p_0 are the equilibrium and saturation pressures of adsorbates at the temperature of adsorption, v is the adsorbed gas quantity, v_m is the monolayer volume of the adsorbate, and c is the BET constant.

Note that this equation is only valid for partial pressure range p/p_0 from 0.05 to 0.35, where the BET plot is linear. From a graphical representation, v_m can be calculated and therefore, the BET specific surface area. The amount of N_2 adsorbed that forms a monolayer is measured at low temperature as a function of N_2 pressure and the surface area can be calculated with the equation:

$$A_s = (v_m / 22414) \cdot N_A \cdot \sigma \quad (\text{eq. 11})$$

where N_A is the Avogadro number and σ , the area covered by one nitrogen molecule (0.162 nm²).^{30,34}

BET surface area was determined from the N_2 adsorption-desorption at liquid nitrogen at 77 K using a Quantachrome NOVA 2200e instrument. Samples were outgassed for 3 h under vacuum at 227 °C. The total surface area was determined using the BET (Brunauer–Emmett–Teller) equation and the multi-point method. Total pore volume was taken from the total volume of adsorbate at $p/p_0 = 0.99$. A photograph of the system is displayed in figure 53.



Figure 53. Quantachrome NOVA 2200e instrument.

2.5.7. Thermogravimetric Analysis – Mass spectroscopy (TGA-MS)

Thermogravimetric is a technique which measures the weight loss of material as a function of temperature. A specific and accurate mass of the sample is located into a crucible and heated to temperatures whereupon certain components decompose and are swept by the carrier gas into the mass spectrometer. Large changes in mass for a short period of time suggests a phase change within the sample. Typically, the results are plotted as percentage loss of the total sample weight against temperature. Weight losses give information to identify the species lost during the course of the temperature ramp however, this information is not conclusive. With the help of mass spectroscopy, providing certain knowledge about the sample composition, components decomposed can be identified. In this work, TGA was used to determine the components adsorbed onto the catalyst surface during the reaction in continuous flow.

Hyphenated TGA and mass spectrometry was run on a Pyris 1 TGA, linked to a Perkin Elmer Frontier followed by a Clarus 580 GC-MS, using a TL-9000 interface. The TL-9000 was set to continuously sample 70 ml/min of effluent gas. TGA was performed under helium, from 30-700 °C (at 10 °C/min). The GC-MS was set up to negate the GC column, with the effluent

gas analysed by MS. For all specified TGA runs, a blank run was first carried out with these results subtracted from the relevant data to remove buoyancy effects. A photograph of the system is displayed in figure 54.



Figure 54. Pyris 1 TGA, Perkin Elmer Frontier and Clarus 580 GC-MS.

2.6. Density Functional Theory (DFT) studies

Once kinetic isotope effect was studied and the most probable pathway to decompose formic acid using Pd was found, DFT calculations were performed to support the results obtained with kinetic isotope study and going further, find the potential energy of each elementary step leading to formic acid decomposition. Once the potential energy diagram was determined, it was possible to elucidate the most optimal structure of Pd, this is, the one which leads towards the highest hydrogen selectivity and identifies the structure which could lead to a higher concentration of CO in the evolved gas. Transition states and frequencies were calculated as well.

Periodic plane-wave DFT calculations were performed using the Vienna ab-initio simulation package (VASP),^{35,36} the Perdew–Burke–Ernzerhof functional revised for solids³⁷ and kinetic energy of 500 eV to expand the plane-waves of the Kohn-Sham valence states.³⁸ The inner electrons were represented by the projector-augmented wave (PAW) pseudopotentials also considering non-spherical contributions from the gradient corrections.³⁹ All the calculations include the long-range dispersion correction approach by Grimme (D3),^{40,41} which is an

improvement on pure DFT when considering large polarisable atoms.⁴²⁻⁴⁷ A self-consistent aqueous implicit solvation model was included.^{48,49} The optimisation thresholds were 10^{-5} eV and 0.03 eV/Å for electronic and ionic relaxation, respectively. The Brillouin zone was sampled by Γ -centred k-point mesh generated through a Monkhorst-Pack grid of $5 \times 5 \times 1$ K-points, which ensures the electronic and ionic convergence.⁵⁰ In order to improve the convergence of the Brillouin-zone integrations, the partial occupancies were determined using the first order Methfessel-Paxton method corrections smearing with a set width for all calculations of 0.2 eV. Open shell calculations were tested leading to close shell results.

The Pd bulk lattice parameter is 3.893 Å⁵¹ which is in very good agreement to the one resulting from our cell optimisation (3.836 Å). Low-Miller index surfaces were modelled and, due to crystal symmetry, the number of surfaces was reduced to the $\{111\}$, $\{011\}$ (consisting of the equivalent (011), (101), and (110) faces), and $\{001\}$ (which includes the equivalent (001), (010), and (100) faces). These surfaces were simulated by a slab model containing 5 atomic layers, the two uppermost layers were relaxed without symmetry restrictions, and the bottom ones were frozen at the bulk lattice parameter. The slab contains 45 atoms per unit cell exposing an area of 66.217 , 93.645 and 66.217 Å² for (111), (011) and (001) respectively. A vacuum width of 15 Å was added between vertically repeated slabs, to avoid the interaction between them.

Binding energy (E_B) of surface intermediates is defined as the difference between the combined system and the isolated species according to the following equation:

$$E_{Bx} = E_{slab+x} - E_{slab} - E_x \quad (\text{eq. 12})$$

where E_{slab+x} , E_{slab} and E_x are the total energies of the adsorbate-substrate system, the clean slab and the gas-phase intermediate x , respectively. Reaction energy (E_R) of each step is calculated as the total energy difference between the final state (product(s)) and the initial state (reactant(s)). Thus, negative values of E_B and E_R indicates favourable adsorption and reaction respectively.

For each elementary step, the path has been discretised by a total of six images including both initial and final states. Each path has been determined by considering the most stable initial

and final states. Transition states (TS) were verified by calculating the corresponding vibrational frequencies and identifying a single negative curvature mode.

A more detailed study of the reaction kinetics of elementary reaction steps was done by microkinetic modelling. In microkinetic modelling, the reaction mechanism proposed and the molecular properties of reactants and intermediates are used in simulations of the reaction at the macroscopic level. In order to build a reliable microkinetic model, it is necessary to investigate all the relevant processes involved, such as adsorption, desorption, and surface reactions. For this purpose, activation barriers and the corresponding vibrational frequencies of the initial, transition and final states were used to compute forward and backward rate constants for the elementary reaction steps. A comprehensive reaction network for the catalytic reaction was built as will be presented in the next chapter.

2.6.1. Supercomputer used

DFT studies have been performed using the computational facilities of the Advanced Research Computing at Cardiff (ARCCA) Division which provides the support to develop research using computing services for the University, particularly through the Raven supercomputing cluster. VESTA software was used as 3D visualisation program of structural models.⁵²

2.7. References

- 1 M. P. Lazaro, E. Garcia-Bordeje, D. Sebastian, M. J. Lazaro and R. Moliner, *Catal. Today*, 2008, **138**, 203–209.
- 2 P. Li, Y. L. Huang, D. Chen, J. Zhu, T. J. Zhao and X. G. Zhou, *Catal. Commun.*, 2009, **10**, 815–818.
- 3 A. Villa, D. Wang, N. Dimitratos, D. Su, V. Trevisan and L. Prati, *Catal. Today*, 2010, **150**, 8–15.
- 4 A. Villa, D. Wang, P. Spontoni, R. Arrigo, D. Su and L. Prati, *Catal. Today*, 2010, **157**, 89–93.
- 5 J. K. Chinthajjala, A. Villa, D. S. Su, B. L. Mojet and L. Lefferts, *Catal. Today*, 2012, **183**, 119–123.
- 6 J. B. Baek, C. B. Lyons and L. S. Tan, *Macromolecules*, 2004, **37**, 8278–8285.
- 7 R. D. Patton, C. U. Pittman, L. Wang and J. R. Hill, *Compos. Part A Appl. Sci. Manuf.*, 1999, **30**, 1081–1091.
- 8 I. C. Finegan, G. G. Tibbetts, D. G. Glasgow, J.-M. Ting and M. L. Lake, *J. Mater. Sci.*, 2003, **38**, 3485–3490.
- 9 J.-P. Tessonnier, D. Rosenthal, T. W. Hansen, C. Hess, M. E. Schuster, R. Blume, F. Girgsdies, N. Pfänder, O. Timpe, D. S. Su and R. Schlögl, *Carbon N. Y.*, 2009, **47**, 1779–1798.
- 10 Pyrograf Products Inc, <http://pyrografproducts.com/nanofiber.html>, Accessed: 2018-01-16.
- 11 S. Campisi, F. Sanchez Trujillo, D. Motta, T. Davies, N. Dimitratos and A. Villa, *C*, 2018, **4**, 9.
- 12 R. Arrigo, S. Wrabetz, M. E. Schuster, D. Wang, A. Villa, D. Rosenthal, F. Girgsdies, G. Weinberg, L. Prati, R. Schlögl and D. S. Su, *Phys. Chem. Chem. Phys.*, 2012, **14**, 10523–10532.
- 13 L. Prati, A. Villa, C. E. Chan-Thaw, R. Arrigo, D. Wang and D. S. Su, *Faraday Discuss.*, 2011, **152**,

- 353–365.
- 14 L. Prati and A. Villa, *Catalysts*, 2012, **2**, 24–37.
- 15 N. Dimitratos, C. Hammond, C. J. Kiely and G. J. Hutchings, *Appl. Petrochemical Res.*, 2014, **4**, 85–94.
- 16 F. Porta, L. Prati, M. Rossi, S. Coluccia and G. Martra, *Catal. Today*, 2000, **61**, 165–172.
- 17 C.-J. Jia and F. Schüth, *Phys. Chem. Chem. Phys.*, 2011, **13**, 2457–2487.
- 18 M. Sankar, N. Dimitratos, P. J. Miedziak, P. P. Wells, C. J. Kiely and G. J. Hutchings, *Chem. Soc. Rev.*, 2012, **41**, 8099–8139.
- 19 A. Villa, D. Wang, G. M. Veith, F. Vindigni and L. Prati, *Catal. Sci. Technol.*, 2013, **3**, 3036–3041.
- 20 Y. Zhao, L. Jia, J. A. Medrano, J. R. H. Ross and L. Lefferts, *ACS Catal.*, 2013, **3**, 2341–2352.
- 21 N. Dimitratos, A. Villa, L. Prati, C. Hammond, C. E. Chan-Thaw, J. Cookson and P. T. Bishop, *Appl. Catal. A Gen.*, 2016, **514**, 267–275.
- 22 S. Link and M. A. El-Sayed, *J. Phys. Chem. B*, 1999, **103**, 4212.
- 23 J. M. Sanz, D. Ortiz, R. Alcaraz De La Osa, J. M. Saiz, F. González, A. S. Brown, M. Losurdo, H. O. Everitt and F. Moreno, *J. Phys. Chem. C*, 2013, **117**, 19606–19615.
- 24 M. Ojeda and E. Iglesia, *Angew. Chemie - Int. Ed.*, 2009, **48**, 4800–4803.
- 25 L. Balcaen, E. Bolea-Fernandez, M. Resano and F. Vanhaecke, *Anal. Chim. Acta*, 2015, **894**, 7–19.
- 26 A. T. Cawley and U. Flenker, *J. Mass Spectrom.*, 2008, **43**, 854–864.
- 27 C. T. Kamala, V. Balaram, V. Dharmendra, K. S. V. Subramanyam and A. Krishnaiah, *Environ. Monit. Assess.*, 2014, **186**, 7097–7113.
- 28 M. Swartz, *J. Liq. Chromatogr. Relat. Technol.*, 2010, **33**, 1130–1150.
- 29 J. W. Niemantsverdriet, *Spectroscopy in Catalysis*, Wiley-VCH Verlag GmbH & Co. KGaA, Weinheim, 2007.
- 30 M. Che and J. Védrine, *Characterization of solid materials and heterogeneous catalysts. From structure to surface reactivity*, 2012.
- 31 D. A. Shirley, *Phys. Rev. B*, 1972, **5**, 4709–4714.
- 32 G. V. A. Martins, G. Berlier, C. Bisio, S. Coluccia, H. O. Pastore and L. Marchese, *J. Phys. Chem. C*, 2008, **112**, 7193–7200.
- 33 F. Rositani, P. L. Antonucci, M. Minutoli, N. Giordano and A. Villari, *Carbon N. Y.*, 1987, **25**, 325–332.
- 34 S. Partyka, F. O. Rouquerol and J. Rouquerol, *J. Colloid Interface Sci.*, 1979, **68**, 21–31.
- 35 G. Kresse and J. Hafner, *Phys. Rev. B*, 1993, **47**, 558–561.
- 36 G. Kresse and J. Furthmüller, *Comput. Mater. Sci.*, 1996, **6**, 15–50.
- 37 J. Perdew, A. Ruzsinszky, G. Csonka, O. Vydrov, G. Scuseria, L. Constantin, X. Zhou and K. Burke, *Phys. Rev. Lett.*, 2008, **100**, 136406.
- 38 N. D. Mermin, *Phys. Rev.*, 1965, **137**, 1441–1443.
- 39 G. Kresse, *Phys. Rev. B*, 1999, **59**, 1758–1775.
- 40 S. Grimme, *J. Comput. Chem.*, 2006, **27**, 1787–1799.
- 41 S. Grimme, J. Antony, S. Ehrlich and H. Krieg, *J. Chem. Phys.*, 2010, **132**, 154104.
- 42 S. Irrera, A. Roldan, G. Portalone, N. H. De Leeuw and N. H. De Leeuw, *J. Phys. Chem. C*, 2013, **117**, 3949–3957.
- 43 N. Y. Dzade, A. Roldan and N. H. De Leeuw, *J. Chem. Phys.*, 2013, **139**, 124708.
- 44 S. S. Tafreshi, A. Roldan, N. Y. Dzade and N. H. De Leeuw, *Surf. Sci.*, 2014, **622**, 1–8.
- 45 S. Haider, A. Roldan and N. H. De Leeuw, *J. Phys. Chem. C*, 2014, **118**, 1958–1967.
- 46 N. Dzade, A. Roldan and N. de Leeuw, *Minerals*, 2014, **4**, 89–115.
- 47 F. Zhang, J. D. Gale, B. P. Uberuaga, C. R. Stanek and N. A. Marks, *Phys. Rev. B - Condens. Matter Mater. Phys.*, 2013, **88**, 1–7.
- 48 K. Mathew and R. G. Hennig, *eprint arXiv:1601.03346*, 2016, 1–6.
- 49 K. Mathew, R. Sundararaman, K. Letchworth-Weaver, T. A. Arias and R. G. Hennig, *J. Chem. Phys.*, 2014, **140**, 1–9.

- 50 J. D. Pack and H. J. Monkhorst, *Phys. Rev. B*, 1976, **13**, 5188–5192.
- 51 H. W. King and F. D. Manchester, *J. Phys. F Met. Phys.*, 1978, **8**, 15–26.
- 52 K. Momma and F. Izumi, *J. Appl. Crystallogr.*, 2011, **44**, 1272–1276.

3. LIQUID-PHASE FORMIC ACID DECOMPOSITION STUDY USING A COMMERCIAL PALLADIUM-BASED CATALYST

3.1. Introduction

The aim of this chapter is to study liquid-phase formic acid decomposition as a model reaction for hydrogen generation. A commercial 5 wt. % Pd/C catalyst was selected as a reference and necessary starting point for optimisation of reaction conditions and determination of diffusion/kinetic regime. The catalytic performance of the 5 wt. % Pd/C catalyst for the additive-free liquid-phase formic acid decomposition was systematically studied in a batch reactor by varying a set of reaction parameters, such as substrate/metal molar ratio, stirrer speed, reaction temperature and concentration of formic acid in order to optimise the main reaction parameters. Besides batch reactor, a very initial stage investigation of liquid-phase formic acid decomposition in continuous flow was also performed focusing on deactivation and regeneration protocols. Reusability tests were performed to determine the long-term stability after the reaction in both batch and continuous flow.

Fresh and used catalysts were thoroughly characterised by means of X-ray diffraction (XRD), X-ray photoelectron spectroscopy (XPS), transmission electron microscopy (TEM), scanning electron microscopy (SEM) with energy dispersive X-ray (EDX), Brunauer-Emmett-Teller (BET) surface area analysis and Thermogravimetric analysis-Mass spectroscopy (TGA-MS).

In order to get insights on the rate determining step and subsequently, the most probable reaction pathways followed, kinetic isotope effect (KIE) was studied. Furthermore, periodic density functional theory (DFT) calculations were employed to establish the energetics of the pathways of formic acid decomposition on Pd(001), Pd(011) and Pd(111) surfaces as the most common models as explained in the previous chapter and, this way, to support the results obtained by the kinetic isotope effect studies. Transition states and its frequencies were calculated as well.

3.2. Results and discussion

The effect of the reaction conditions and their optimisation for the liquid-phase decomposition of formic acid on the commercial 5 wt. % Pd/C was investigated. As previously

explained, a batch reactor was used for this purpose since it can accurately and reproducibly provide a set of kinetic data in a short period of time. The reactions were monitored by withdrawing samples and injecting in an HPLC as presented in the experimental chapter and analysing the concentration of formic acid (reagent) remaining in the reactor. A representative time-online plot of two reproducible reactions of liquid-phase formic acid decomposition is displayed in figure 55. In this graph, conversion is plotted against reaction time for two runs under the same reaction conditions.

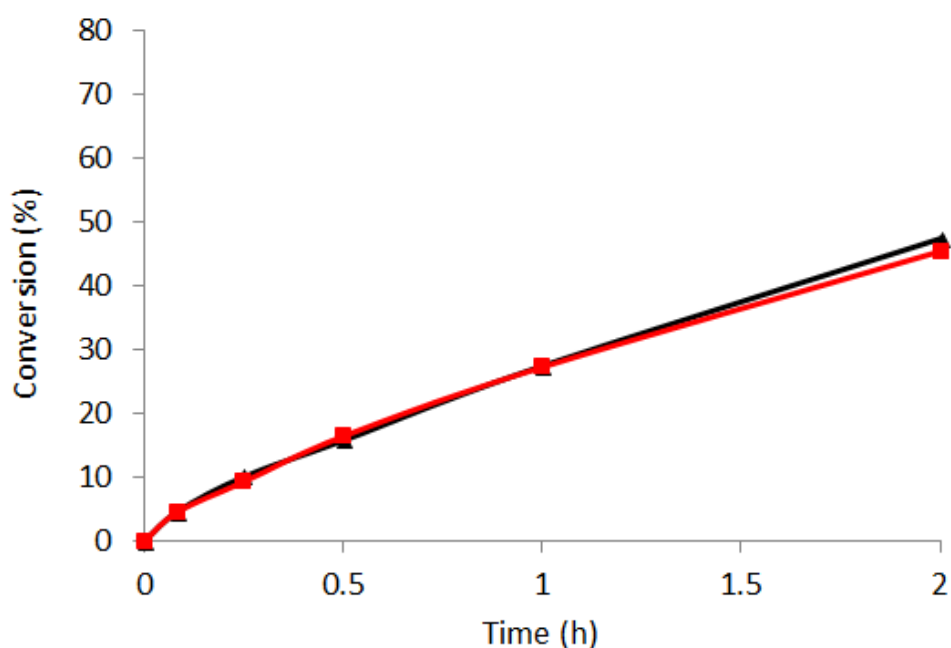


Figure 55. Conversion versus time plot for a representative liquid-phase formic acid decomposition. Reaction conditions: 30 °C, 5.3 mg of catalyst (substrate/metal molar ratio: 2000:1), 0.5 M HCOOH, 750 rpm, 2 h reaction time.

Note that the initial rate of reaction (conversion at $t = 5$ min divided by time) is for most of the experiments, the value required to compare catalysts and conditions, and needed for calculations as in kinetic isotope effect as will be shown in a subsequent section. During the first experiments, these were run until full conversion was obtained, however, since the initial rate is the quantity of interest, 2 hours of reaction was considered enough to obtain reproducible data and be able to discard data when it does not attach to a trend. Typically, an error of 5 % or less was accepted.

First, a blank reaction test, that is, a reaction without catalyst, with experimental conditions obtained from the literature, was performed to check that formic acid decomposition does not occur spontaneously at the conditions of the experiment. Once this was confirmed, a series of experiments were carried out as explained subsequently.

3.2.1. Reaction conditions optimisation for additive-free liquid-phase formic acid decomposition

A preliminary step in the evaluation of catalyst activity is to confirm that, at the conditions of the experiment, the reaction is kinetically limited, this means that the rate of reaction is not limited by diffusion or external/internal mass transfer. Two kinds of diffusion may be involved: external and internal. External diffusion is related to the transfer of the reactant from the solution to the surface of the particle while internal diffusion is related to the transfer of the reactant from the surface of the particle to its core through the pore channels. When diffusion is present, modifying the amount of catalyst, that is, the number of active sites, is not translated as a proportional change in the conversion, therefore, the conditions where the reaction is in kinetic regime are the first challenge to be solved.

To determine the regime of the reaction, as commented, the experiment to perform is to modify the amount of catalyst and observe how the conversion changes. In case the reaction is kinetically limited, the conversion will change proportionally with the amount of catalyst, however, when diffusion is the limiting step, the conversion will not change proportionally. For this purpose, the effect of formic acid/metal molar ratio was studied. As discussed in Chapter 2, formic acid concentration of 0.5 M and 30 °C were selected and 2 hours reaction time. Stirring rate was adjusted as a starting point to 750 rpm as previous preliminary experiments concluded it was an optimal value, however, a deeper explanation and study was performed afterwards. In this study, a formic acid/metal molar ratio in the range 125:1-6000:1, equivalent to 81-1.8 mg of catalyst respectively were studied. Two reaction regimes were identified as displayed in figure 56. Note that conversion was calculated for the initial rate. In the range of substrate/metal molar ratio between 2000:1-6000:1 (5.3-1.8 mg), the red dotted line, the initial conversion is proportionally dependant to the amount of catalyst, what means that the reaction is kinetically limited. An increment of the mass of catalyst above

5.3 mg does not produce a proportional increment in the conversion, thus, diffusion limitations were present.

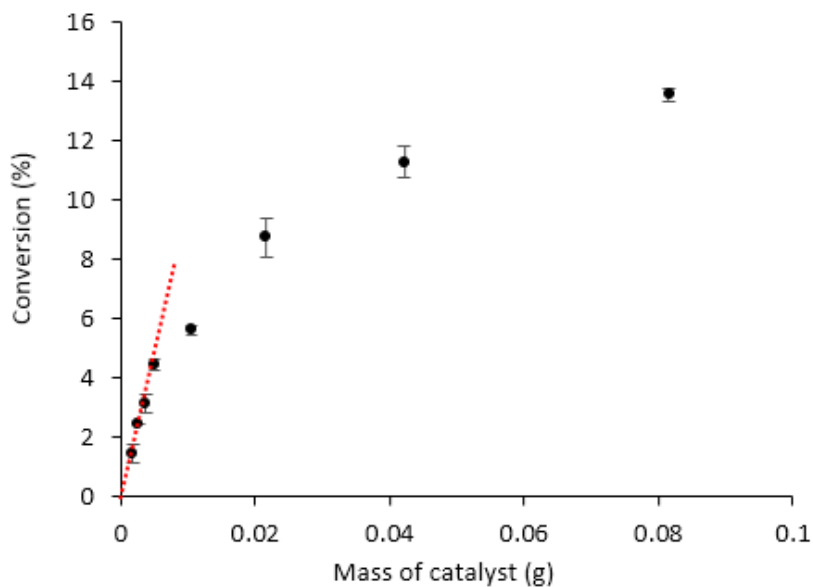


Figure 56. Effect of catalyst mass on conversion. Reaction conditions: 30 °C, 0.5 M HCOOH, 750 rpm, 2 h reaction time.

Figure 57 displays a magnification of the range where the reaction is kinetically limited.

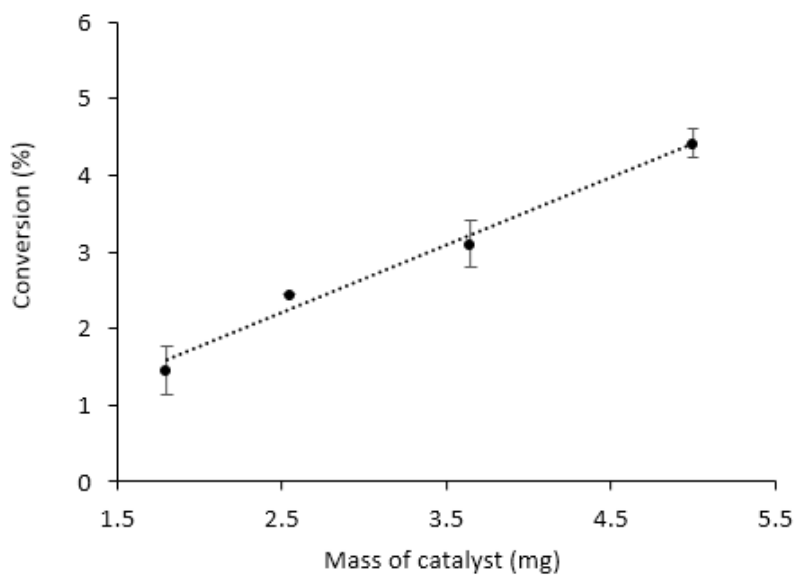


Figure 57. Effect of catalyst mass on conversion in a substrate/metal molar ratio range from 2000:1 to 6000:1. Reaction conditions: 30 °C, 0.5 M HCOOH, 750 rpm, 2 h reaction time.

Figure 58 shows that the TOF (turnover frequency) values are constant in that range, confirming that diffusion limitations are not present within this range. Above 5.3 mg, a decrease in TOF was observed, indicating that diffusion limitations were present, as obtained in previous results. Therefore, a catalyst mass of 5.3 mg was selected as the standard value for subsequent experiments since it presents the highest conversion while still in kinetic regime.

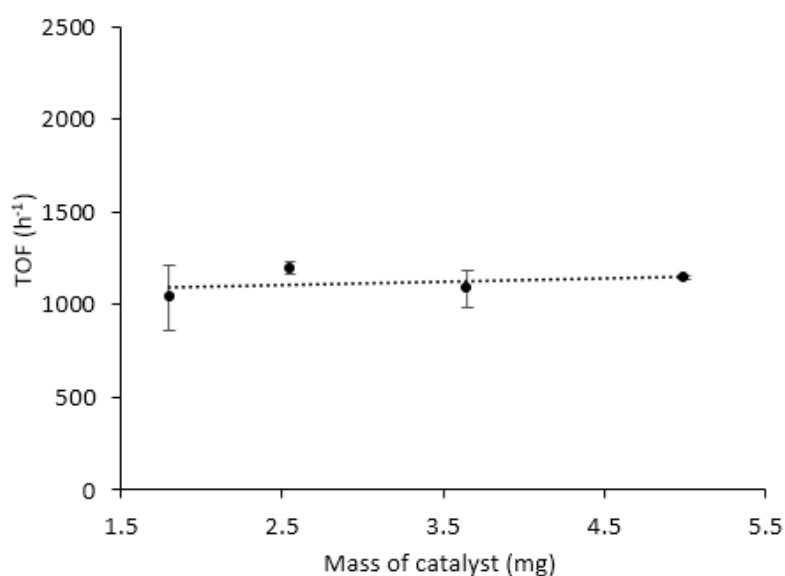


Figure 58. Effect of catalyst mass on TOF. Reaction conditions: 30 °C, 0.5 M HCOOH, 750 rpm, 2 h reaction time.

Stirring rate also plays an important role in mass transfer. This is due to the fact that increasing the stirring rate will increase the reactants collision with the solid catalyst and consequently, influence the rate of reaction. Therefore, a study in which stirring rate is modified can confirm if any external mass transfer limitation is present. If this is the case, an increment of stirring rate will increase the reaction rate and so, the conversion. On the contrary, the reaction rate will be independent of the stirring rate if no mass transfer limitations are present. For this purpose, stirring rate was varied in the range of 400-900 rpm at 30 °C and a substrate/metal molar ratio of 2000:1 (5.3 mg). Figure 59 shows the initial TOF compared with different stirring rates. As observed, from 600 to 750 rpm, the initial TOF values display a significant increment suggesting that the reaction is under diffusion regime, while in the range 750-900 rpm, TOF values increased very slightly, reaching a plateau, indicating that the stirring rate in this range

has a minor effect on the conversion and therefore, confirming the reaction is in kinetic regime. Working at a stirring rate of 900 rpm could assure total absence of an external mass transfer, although at this rate, the stability of the rotation axis of the stirrer represented a problem causing difficulties to reach enough reproducibility of data. Considering these results, a stirring rate of 750 rpm was selected as the optimum value for subsequent studies.

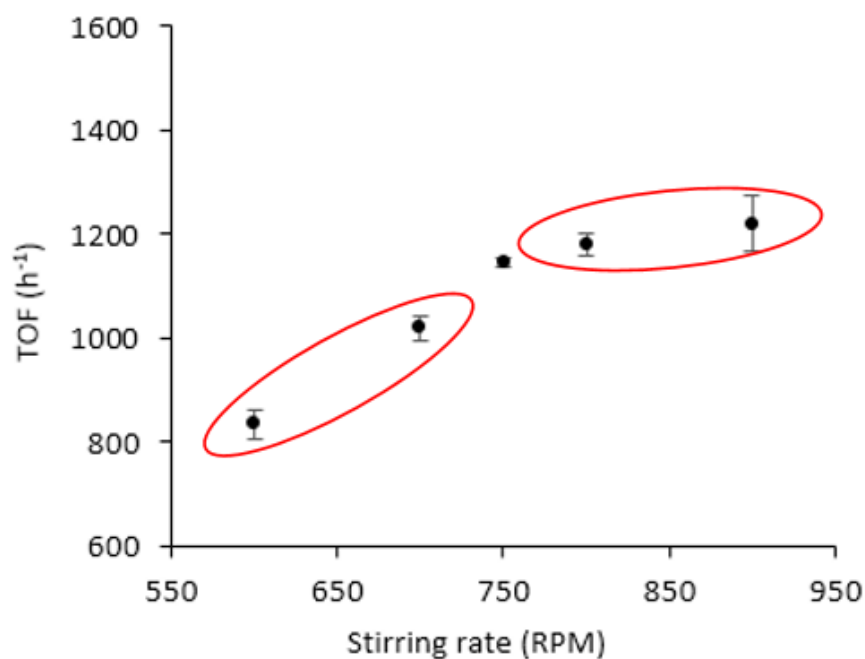


Figure 59. Effect of stirrer rate on TOF. Reaction conditions: 5.3 mg of catalyst (substrate/metal molar ratio: 2000:1), 30 °C, 0.5 M HCOOH, 2 h reaction time.

Once the conditions in which the reaction is kinetically limited are found, the next parameter to study was the effect of temperature and then, calculate the activation energy. Five reactions were performed in the range of temperature from 30 to 60 °C. The remaining conditions were the same as in previous experiments. Temperatures above 60 °C were not investigated since, as previously commented, one important requirement of portable devices employing formic acid fuel cells is the necessity of working under mild conditions and as previously reported, CO is evolved above 50 °C.¹ The results are displayed in figure 60. As expected, conversion of formic acid was enhanced when rising the temperature.

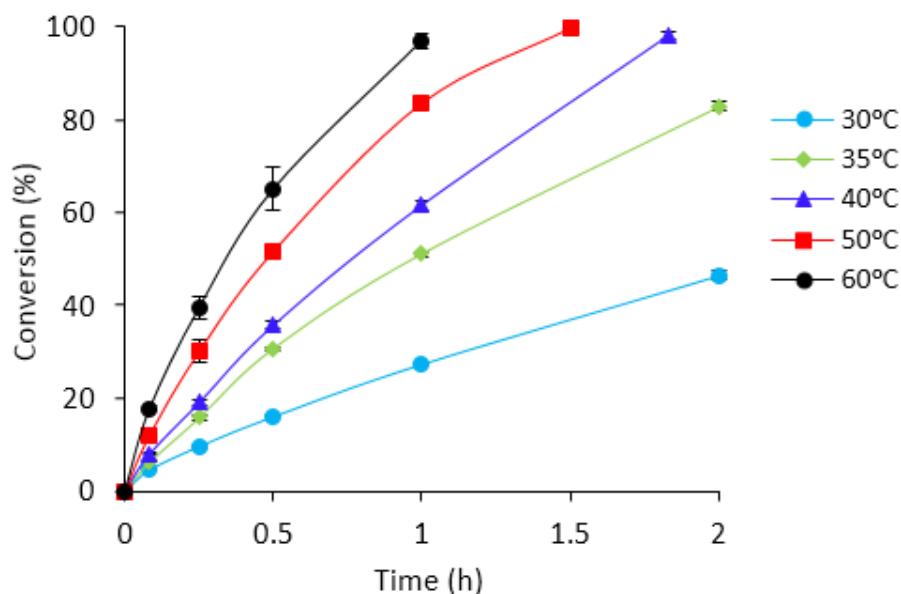


Figure 60. Effect of temperature on conversion. Range 30-60 °C. Reaction conditions: 5.3 mg of catalyst (substrate/metal molar ratio: 2000:1), 0.5 M HCOOH, 750 rpm, 2 h reaction time.

Activation energy (E_a^{app}) is a key parameter in catalysis. It is the minimum energy of the molecule to result in a chemical reaction. Arrhenius expressed it according to the following equation:

$$k = Ae^{\frac{-E_a}{RT}} \quad (\text{eq. 1})$$

Applying trivial logarithms, a linear equation is obtained, and, when plotted against $1/T$, the slope of the resulting line is the apparent activation energy (E_a^{app}) if pseudo first order is assumed. Note that T should be in Kelvin instead of Celsius in order to obtain activation energy in kJ/mol. Figure 61 displays the Arrhenius plot. Apparent activation energy (E_a^{app}) for the reaction was 39.0 kJ/mol which is among the best values reported for a monometallic Pd catalyst under kinetic regime².

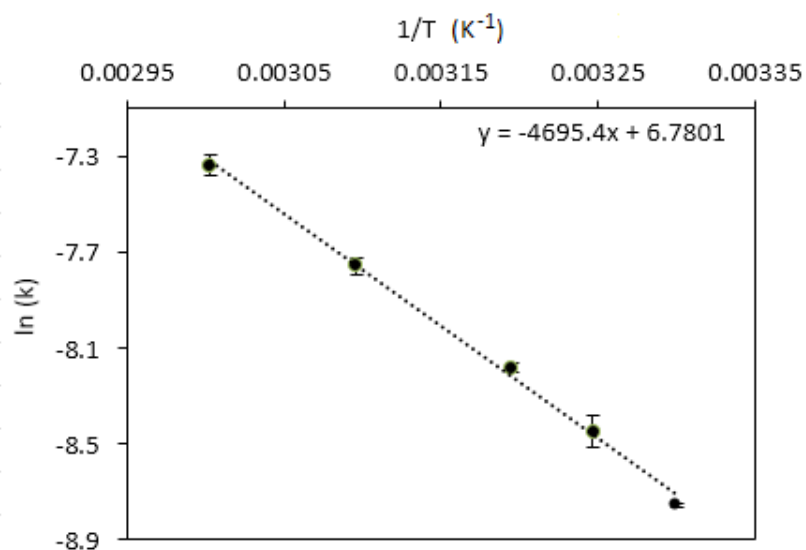


Figure 61. Arrhenius plot. Range 30-60 °C. Reaction conditions: 5.3 mg of catalyst (substrate/metal molar ratio: 2000:1), 0.5 M HCOOH, 750 rpm, 2 h reaction time.

As a final step in the investigation of reaction conditions and parameters, by studying the effect of formic acid concentration, it was possible to determine an approximate of the reaction order by using the power law equation as presented in Chapter 2. A set of experimental reactions with a concentration range of formic acid from 0.1 to 2 M at 30 °C and substrate/metal molar ratio of 2000 were performed (Figure 62).

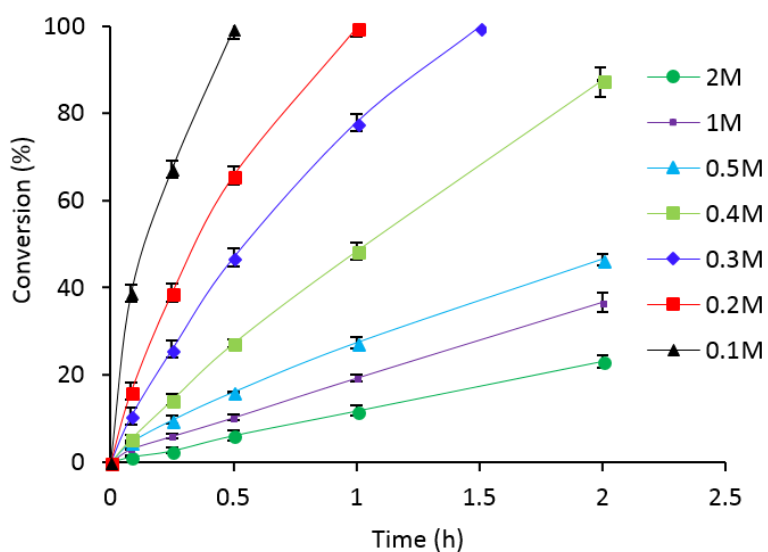


Figure 62. Effect of concentration of formic acid. Reaction conditions: 5.3 mg of catalyst (Substrate/metal molar ratio: 2000:1), 30 °C, 750 rpm, 2 h reaction time.

As explained in the experimental chapter, representing rate of reaction versus concentration as in figure 63, and fitting to a power-law equation model, an apparent reaction order of 0.2 with respect to formic acid was obtained.

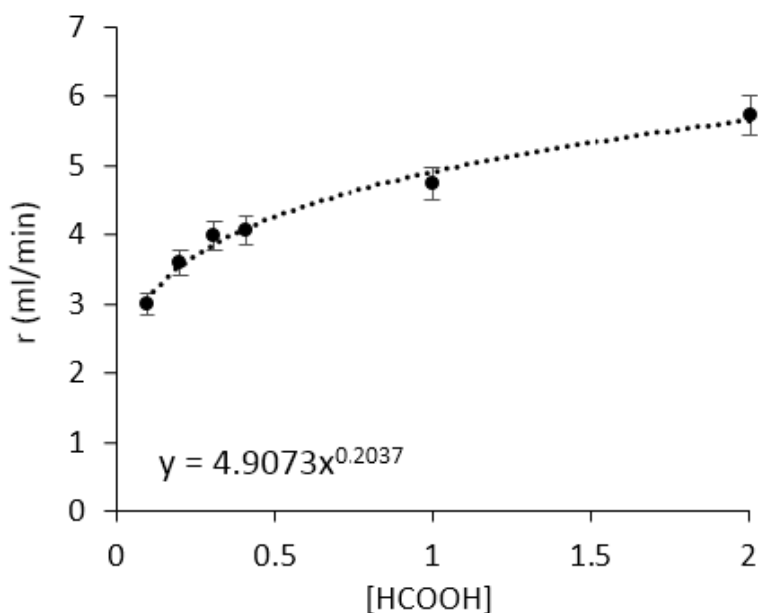


Figure 63. Rate versus concentration of formic acid. Reaction conditions: 5.3 mg of catalyst (Substrate/metal molar ratio: 2000:1), 30 °C, 750 rpm, 2 h reaction time.

At this point, the reaction conditions have been optimised in order to keep the reaction under kinetic regime, and apparent activation energy and reaction order have been calculated. An initial TOF of 1136 h^{-1} was calculated at the optimised conditions of substrate/metal molar ratio of 2000, 750 rpm, 30 °C and a concentration of formic acid of 0.5 M. Table 5 in Chapter 1 presented some of the most representative heterogeneous catalysts studied in liquid-phase formic acid dehydrogenation. As observed, the TOF obtained in this study is among the best catalysts to date in terms of activity.

3.2.2. Reusability tests of 5 wt. % Pd/C

Catalyst stability plays an important role in determining the economical point of view of the heterogeneous catalysts in large-scale industry, therefore, durability and recyclability of a catalyst are crucial for practical applications. The stability of the commercial 5 wt. % Pd/C catalyst was assessed at 30 °C for five subsequent catalytic cycles as explained in Chapter 2,

section 2.4. As displayed in figure 64, even after the fifth cycle of usage, the catalyst preserved 72 % of its original conversion, the conversion of the fresh catalyst. This slight decrease in the activity per run can be explained by several factors such as strong adsorption of either formic acid or an intermediate of the decomposition on the surface of the catalyst occupying active sites, poisoning from CO, Pd nanoparticles agglomeration, or decrease of Pd loading by leaching.

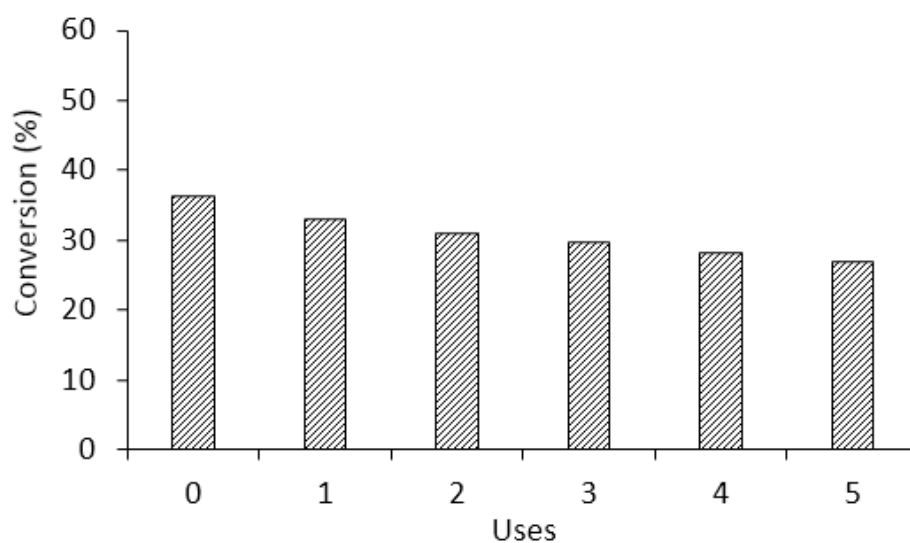


Figure 64. Reusability of 5 wt. % Pd/C after five cycles of reaction. Reaction conditions: 5.3 mg of catalyst (substrate/metal molar ratio: 2000:1), 30 °C, 750 rpm.

MP-AES analysis of the filtered liquid after each use of the reusability test presented negligible Pd concentration near the detectability limit of the instrument. The initial amount of Pd added into the reactor is approximately 26.5 ppm. As observed in table 10, the values obtained are on average 0.05 ppm. This analysis rejects the possibility of leaching of Pd from the catalyst.

Table 10. MP-AES analysis of the filtered solutions after reusability tests.

Cycle	Concentration of Pd (ppm)	% of initial Pd
Fresh	0.06	0.22
1	0.04	0.15
2	0.04	0.15

3	0.04	0.15
4	0.07	0.26
5	0.04	0.15

Analysis of the evolved gases will provide information about possible CO formation and thus, poisoning of the catalyst.

3.2.3. Analysis of evolved gases

As explained in the experimental chapter, by means of the water displacement method, gases evolved from formic acid decomposition were collected in a burette for subsequent analysis. Analysis of gases using the GC Varian 450 with a methanator showed that between 40000 and 50000 ppm were evolved from CO₂ while, 4 - 5 ppm were attributed to CO (Figure 65).

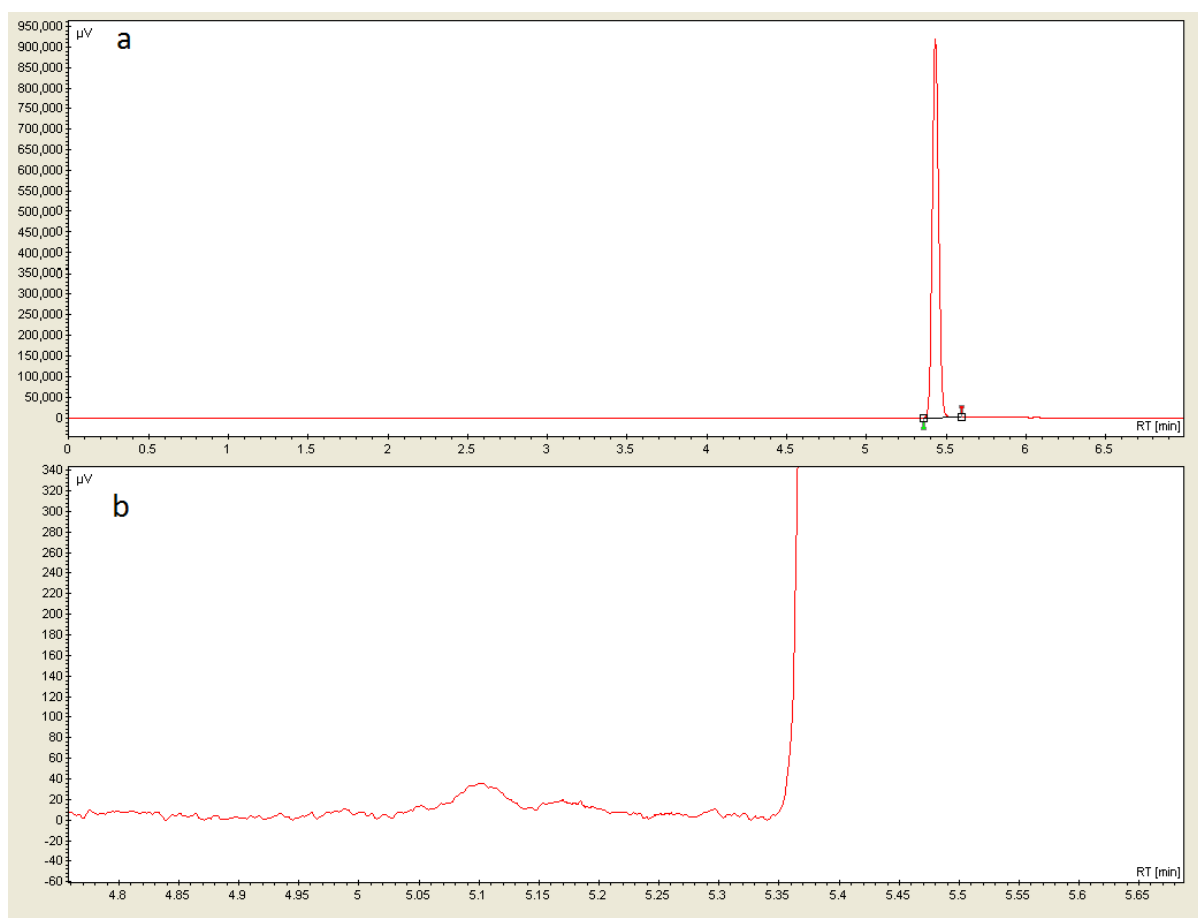


Figure 65. a) Chromatogram obtained using GC Varian 450. CO₂ at $t_r= 5.45\text{min}$, b) CO at $t_r= 5.1$.

This confirms that the reaction mainly follows the dehydrogenation route (to hydrogen and carbon dioxide).

As previously stated, Hiden QGA was used to analyse the concentration of hydrogen evolved and calculate the H_2/CO_2 ratio. Figure 66 displays a spectrum of the analysis of gases evolved from formic acid decomposition at the optimised conditions.

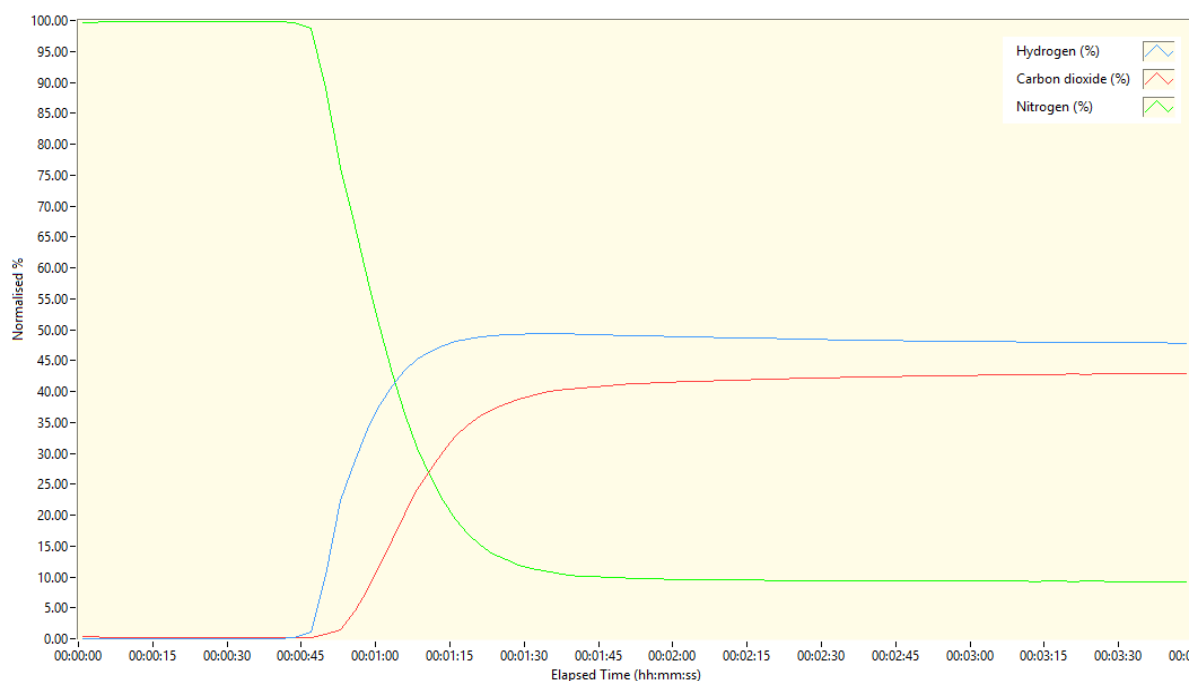


Figure 66. Analysis of the evolved gases with Hiden QGA selecting $m/z = 2$, 44 and 28 for hydrogen, carbon dioxide and nitrogen respectively.

Several reactions were performed in order to have reproducible data. H_2/CO_2 ratios were in the range from 1.06 to 1.13 confirming the proximity to the theoretical formula. Formic acid dehydrogenation should produce one molecule of hydrogen per molecule of carbon dioxide. The slight deviation obtained could be addressed to a difference in solubility of CO_2 and H_2 or a consumption and adsorption of hydrogen by PdO as previously reported².

After the second cycle of the reusability test, a sample of gases was collected to investigate how the recyclability affects the CO evolution. The gas analysis performed on the gas-phase products also showed a low CO evolution from 4 to 6 ppm, supporting the promising results obtained during the reusability tests.

As commented in Chapter 1 (section 1.1.5.1), 20 ppm of carbon monoxide is the general limit established for PEM fuel cells. In this experiment, carbon monoxide concentration was always

within the accepted values in order not to poison the catalyst to a large extent. Consequently, strong absorption of formic acid on the surface and agglomeration are the most probable explanation of the slight decrease in catalytic activity for subsequent cycles of reaction.

At this point in the research, further characterisation of the catalyst is needed to continue finding explanations and correlate activity of the catalyst with its structure. For this purpose, a series of characterisation techniques were employed.

3.2.4. Catalyst Characterisation

A full set of characterisation experiments have been performed on the commercial 5 wt. % Pd/C. These techniques were performed in both fresh and used catalyst after formic acid decomposition. The catalyst was characterised in detail using bulk and surface-specific techniques in order to establish a structure/activity relationship. Particle size distribution, surface area, leaching, poisoning and oxidation state of the metal are fundamental parameters to analyse to be able to understand the behaviour of a heterogeneous catalyst under a chemical reaction. With this objective in mind, X-ray diffraction, X-ray photoelectron spectroscopy, transmission and scanning electron microscopy, BET surface area and thermogravimetric analyses were performed.

3.2.4.1. X-ray Diffraction

X-ray diffraction analysis was performed on the fresh and used samples to determine the crystal structure and the mean crystallite size of the involved metal using the Scherrer equation as explained in Chapter 2, section 2.5.1, equation 8. Figure 67 displays the XRD patterns of the fresh and used catalysts. The broad diffraction peak or reflection appearing at 25° and the peaks at 57° and 62° are attributed to the carbon support, specifically, to the hkl planes (002), (004) and (103) of activated carbon respectively². The reflections at $2\theta = 40.4^\circ$, 46.8° and 68.3° are addressed to the (111), (200) and (220) characteristic planes of the face-centered cubic structure of Pd respectively. The peaks appearing at 35.8° and 43.8° are assigned to PdO (101) and (110) respectively³.

X-ray diffraction pattern of the used catalyst displays a reduction of the intensity of the diffraction peaks attributed to PdO at $2\theta = 35.8^\circ$ and 43.8° and an increase of the reflections

at $2\theta = 40.4^\circ$ ascribed to (111) plane of Pd suggesting a possible reduction of Pd^{II} to metallic Pd due to the *in-situ* generation of hydrogen during the reaction. This fact has been further investigated by means of XPS studies.

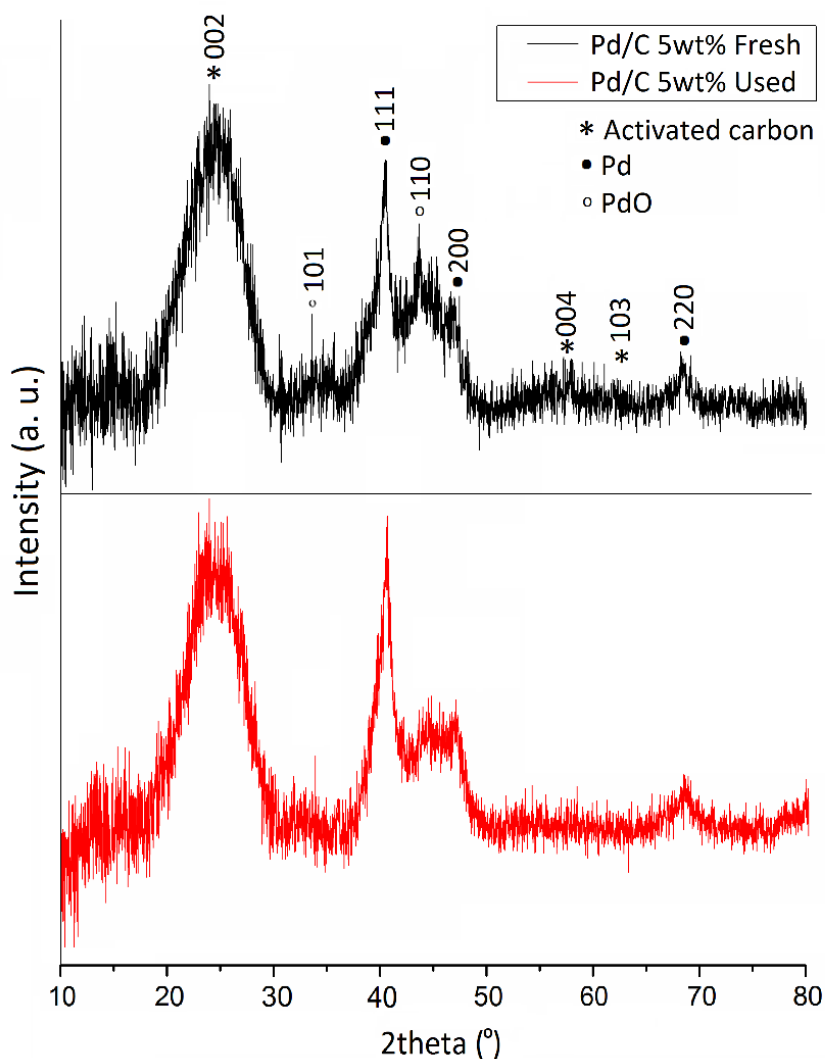


Figure 67. XRD patterns of fresh and used 5 wt. % Pd/C catalysts.

The Scherrer equation was employed to calculate the mean crystallite size of the Pd metal as explained in Chapter 2, section 2.5.1. This equation was applied to the diffraction peak at 40.4° corresponding to (111) reflection. Table 11 presents both the FWHM and crystallite size of the fresh and used catalysts.

Table 11. Crystallite size of Pd particles calculated using the Scherrer equation.

Sample	FWHM of (111) reflection at 40.4°	Crystallite size (nm)
Fresh	1.75	4.8
Used	1.30	6.5

An average crystallite size of 4.8 nm has been calculated for the fresh catalyst. At this point, the reader may note that, in the experimental chapter, it was stated that a crystallite size lower than 5 nm may not produce a reflection due to the small range structure. However, the result obtained is still close to the detectability limit of the instrument and furthermore, the relatively high loading of the catalyst, which possesses a nominal total metal loading of 5 wt. % (which will be subjected to analysis in following sections), has prevailed and produced a detectable XRD signal as observed. The results obtained by using Scherrer equation are generally matched by TEM micrographs as presented in a subsequent section.

The increment in the crystallite size for the used catalyst could be explained by the agglomeration of Pd particles during the reaction and consequently generate larger Pd crystallite size.

3.2.4.2. X-ray photoelectron spectroscopy

XPS is an analytical technique which provides quantitative information about the catalyst surface composition and the oxidation state of the metals which are of great importance and affect catalytic performance to a large extent. XPS analyses of the fresh and used catalyst were performed to determine the electronic states of the samples. XPS analysis of the Pd 3d region is presented in figure 68.

The constraints used for the deconvolution are given in Chapter 2, section 2.5.2. Each Pd species displays two doublets due to the Pd 3d_{5/2} transition, presenting a binding energy around 334 - 338 eV; and Pd 3d_{3/2} transition, with a characteristic binding energy around 339 - 343 eV. The peaks at 335.4 and 340.7 eV are assigned to the presence of metallic Pd⁰ while the peaks at approximately 337 - 338 eV and at 342 - 343 eV correspond to Pd^{II} being PdO the most probable species^{5,6}.

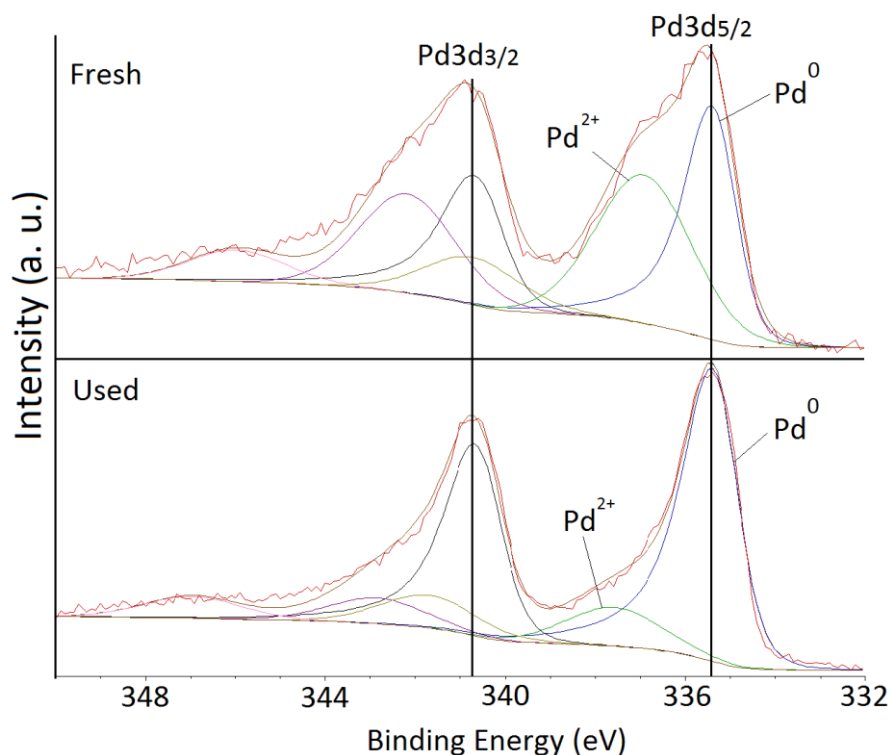


Figure 68. XPS spectra of fresh and used 5 wt. % Pd/C in the binding energy region of 232–350 eV corresponding to Pd 3d.

Detailed XPS binding energy of Pd, its oxidation states and relative content of each species are presented in table 12.

Table 12. XPS binding energies of Pd with respective oxidation state and relative content of each species.

Sample	3d _{5/2} (eV)		3d _{3/2} (eV)	
	Pd ⁰ (%)	Pd ^{II} (%)	Pd ⁰	Pd ^{II}
Fresh	335.4 (60)	337.0 (40)	340.7	342.2
Used	335.4 (83.9)	337.6 (16.1)	340.7	342.9

For the fresh catalyst, metallic Pd accounts for approximately 60 %, while for the used catalyst, it increased up to 83.9 %. The reduction of the intensity of the peaks assigned to Pd^{II} and the simultaneous increase of Pd⁰ for the used catalyst are consistent with the data obtained from XRD suggesting a reduction of Pd^{II} to metallic Pd while using the catalyst, due to the hydrogen evolution from formic acid decomposition.

Pd, O and Cl atomic percentages for both fresh and used catalysts are shown in table 13.

Table 13. Pd, Cl and O content on the surface from XPS.

Catalyst	Pd content (at. %)	Cl content (at. %)	O content (at. %)
Fresh	1.33	0.10	7.82
Used	1.82	0.05	9.07

A Pd content of 1.33 % is obtained for the fresh catalyst while 1.82 % is obtained for the used. Note that the nominal content of 5 wt. % comprises the bulk of the catalyst whilst XPS atomic percentages are calculated on the surface of the catalysts since this technique is surface sensitive providing information on the state of the surface at a depth of 25–30 Å.⁷ On the contrary, characterisation techniques such as EDX provide an average content for the bulk of the catalyst. Analysis by EDX will be provided later in this chapter. In case EDX confirms a Pd content of 5 wt. %, this means that, while the majority of nanoparticles are located outside the pores of the support, a significant amount of Pd is located inside the pores. The increment observed for the Pd surface atomic content in the used catalyst could be explained by a desorption of the nanoparticle, migration to the external surface and readsorption. Since surface tension of small nanoparticles is high, during the readsorption step, nanoparticles may agglomerate in order to relieve part of this energy. This could also explain the small increment in Pd crystallite size observed in the XRD pattern of the used catalyst.

Chlorine impurities have been studied too since these can promote catalyst sintering or act as catalysts poison by occupying active sites^{8,9}. A negligible Cl content of 0.1 and 0.05 % was found for the fresh and used catalysts respectively. The decrease for the Cl content for the used catalyst can be explained by formation and release of HCl.

XPS has been also used to measure the relative concentration of sp³ and sp² hybridisation type from the deconvolution of the C1s peak. The C1s XPS spectra of both fresh and used catalysts are present in figure 69.

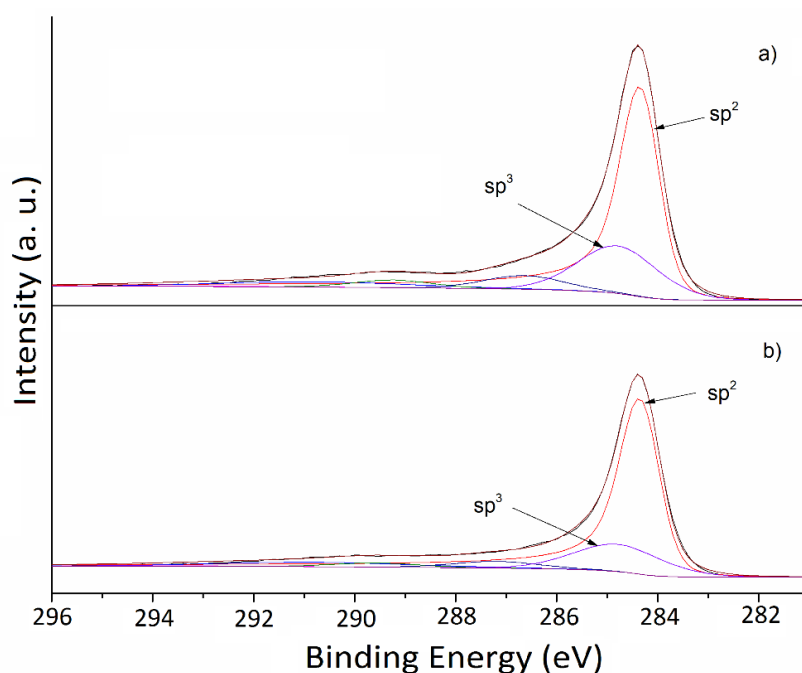


Figure 69. XPS spectra of (a) fresh and (b) used 5 wt. % Pd/C in the binding energy region of 281–296 eV corresponding to C1s.

Table 14 presents the relative concentrations of sp^2 and sp^3 hybridisations and its ratio (sp^2/sp^3) since it determines structure properties of carbon materials. The component appearing at approximately 284 eV is attributed to sp^2 carbon and the component at 285 eV, to sp^3 -hybridised carbon species¹⁰. As observed, for the used catalyst, sp^2 content increases while sp^3 content decreases. This change may be caused by the water washing away a certain amount of amorphous carbon from the surface of the catalyst during the reaction process.

Table 14. Atomic content of sp^2 and sp^3 carbon and ratio sp^2/sp^3 from XPS for the commercial 5 wt. % Pd/C.

Catalyst	C sp^2 (%)	C sp^3 (%)	sp^2/sp^3
Fresh 5 wt. % Pd/C	64.0	20.6	3.11
Used 5 wt. % Pd/C	69.9	16.8	4.17

Oxygen has been analysed by the O1s emission (Figure 70). O1s peaks are well described by a Gaussian-Lorentzian curve after subtraction of a Shirley background¹¹. The assignment of

the components in the O1s spectra is not straightforward although there is a certain degree of agreement in the position range of the peaks.

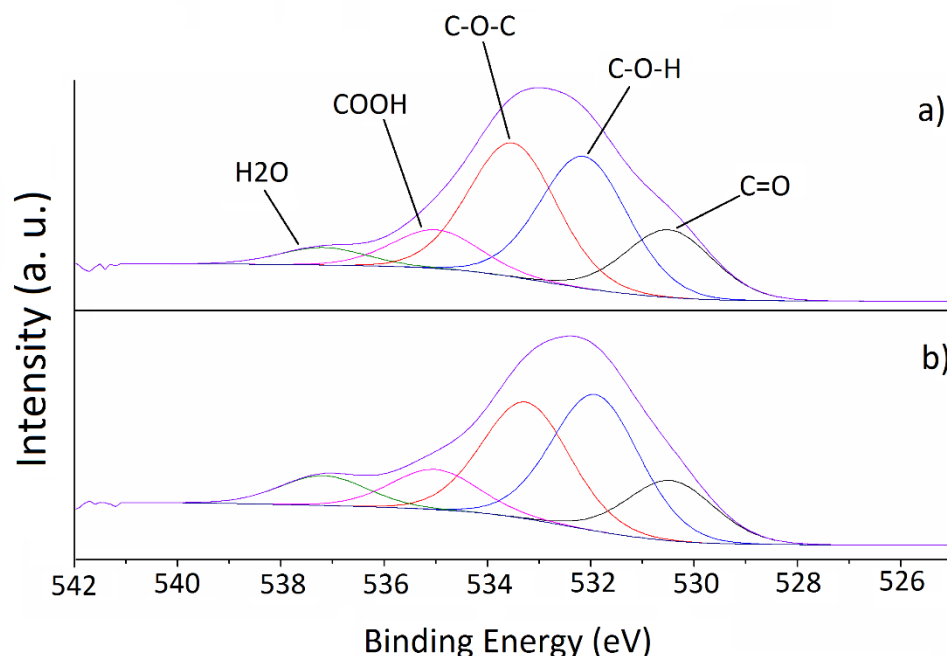


Figure 70. XPS spectra of (a) fresh and (b) used 5 wt. % Pd/C in the binding energy region of 525–542 eV corresponding to O1s.

Typically, carbon-oxygen double bond (C=O) falls in the range 530.0-531.5 eV; regarding the assignment of C-O-H and C-O-C, in the literature, several contrasting opinions have been expressed. However, since carbon is slightly more electronegative than hydrogen, carbon-oxygen single-bonds in hydroxyl groups should appear at a slightly lower energy, in the region: 531.5-531.9 eV and carbon-oxygen ether-like single bond at approximately 533.0-533.5 eV. Carboxylic groups (COOH) are usually located in the range 534.5-535.0 eV and even though a lot of debate is present in literature, the peak at 536.7-537.2 eV might be attributed to adsorbed water although the assignment is not entirely clear.¹²⁻¹⁴

Even though a significant change is not observed for the used catalyst in comparison with the fresh catalyst, it is possible to note a slight increment for the region ascribed to carbon-oxygen single-bonds in hydroxyl groups and the region attributed to water. As expected, adsorption of water up to a certain extent takes place during the reaction and as observed, the drying process at ambient temperature does not totally desorb this water which is expected as well.

A more significant change occurs since carbon-oxygen single-bonds in hydroxyl groups increase while carbon-oxygen ether-like single bond decreases indicating the creation of more hydroxyl groups.

3.2.4.3. Transmission Electron Microscopy (TEM)

Transmission electron microscopy is a key technique to study the metal/support interaction. Particle size distribution and mean particle size of the fresh and used Pd/C catalysts were analysed by means of TEM. Figure 71 displays the bright field TEM micrographs. These indicate a good dispersion of the Pd nanoparticles. Mean particle size distribution for both fresh and used catalysts were in the range 2–6 nm. While for the fresh catalyst, mean particle size of Pd was 3.3 ± 0.3 nm, for the used catalyst, it slightly increased to 3.7 ± 0.3 nm. This increase of particle size is small, even though, this could partially be an explanation for the reduction in catalyst activity observed in the reusability tests since, after the first cycle, conversion decreased approximately 10 %.

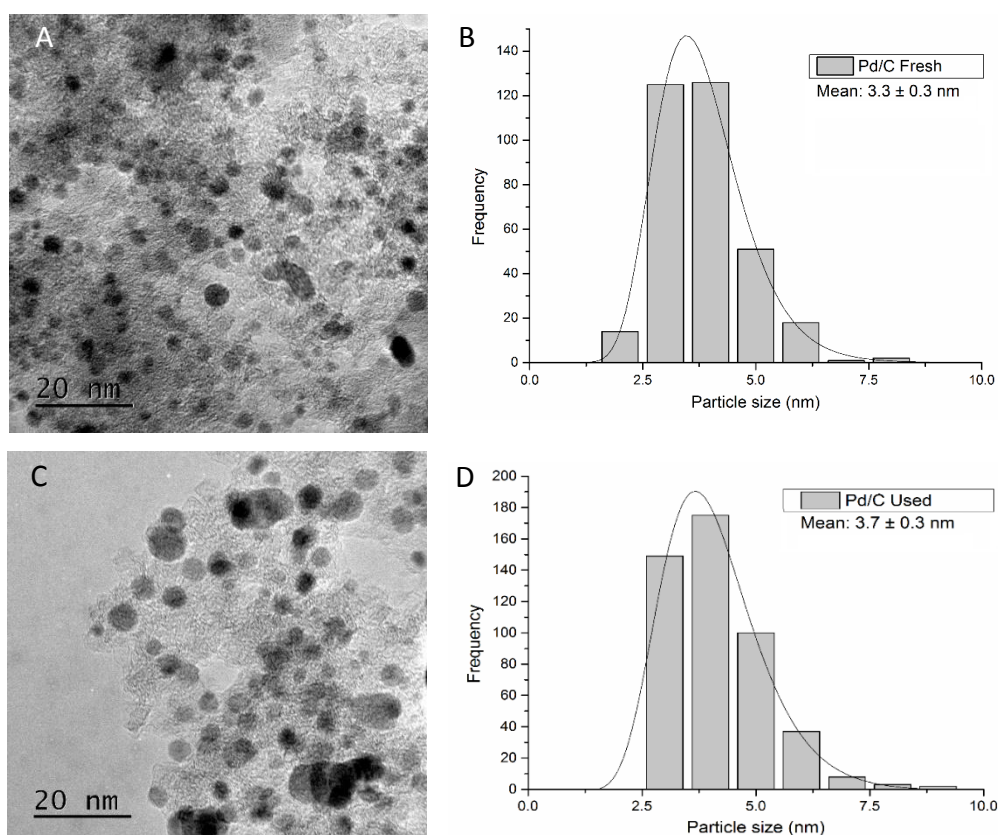


Figure 71. Bright field TEM micrographs and corresponding histograms of the particle size distributions for the commercial 5 wt. % Pd/C. (A, B) Fresh Pd/C, (C,D) Used Pd/C. Magnification: $\times 250k$.

Lattice fringes of Pd nanoparticles were studied by means of High-Resolution TEM (HRTEM). Figure 72 presents the micrograph for the fresh commercial 5 wt. % Pd/C. It displays discrete lattice-fringes of the face-centered cubic (fcc) Pd crystal with a d-spacing of 0.225 nm, which is in reasonable agreement with the lattice spacing of the (111) plane in our computational model (0.271 nm) taking into account the atomic radius of the element¹⁵.

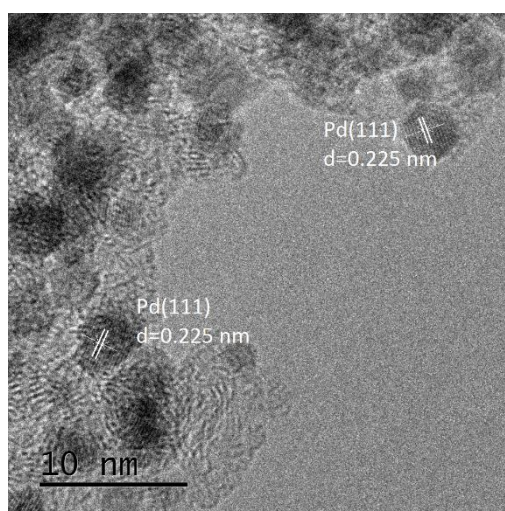


Figure 72. HRTEM image of the fresh 5 wt. % Pd/C. Magnification: $\times 600k$.

At this point, where CO evolution and Pd leaching were discarded, and TEM results do not provide a definitive reason for loss of catalyst activity, adsorption of intermediates such as formate or carboxylic acid seems the most probable reason for the decrease in activity observed. As a reminder, note that reusability of the catalyst provided a very promising result, even though, an answer for the slight decrease is being investigated.

3.2.4.4. Scanning Electron Microscopy-Energy Dispersive X-Ray spectroscopy

Even though a significant morphology change after using the catalyst was rejected by TEM observations, the morphology of the fresh and used catalysts was studied using SEM to confirm no macroscopic modification was produced. As previously commented, the nominal metal loading of the catalyst was investigated by means of EDX, therefore, during SEM observation, the composition of the Pd nanoparticles was analysed by means of EDX for the

fresh and used catalyst. A representative SEM image of the fresh and used 5 wt. % Pd/C is presented in figure 73.

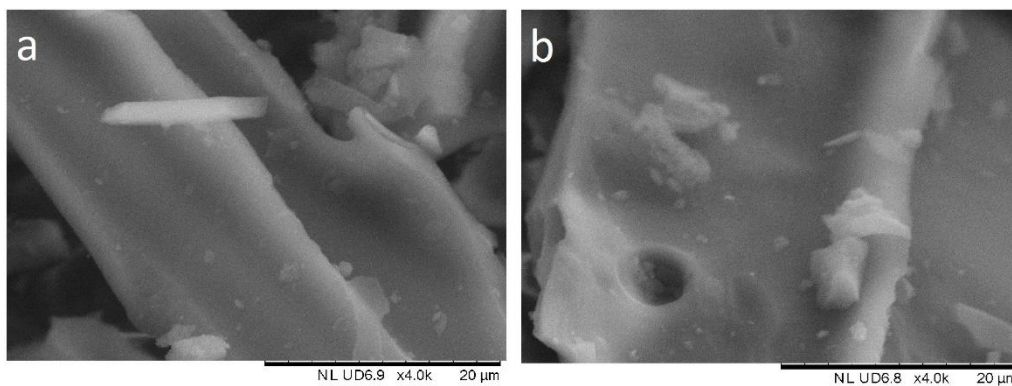


Figure 73. (a) SEM image of the fresh Pd/C and (b) SEM image of the used Pd/C.

EDX mapping during SEM observation was performed to elucidate possible agglomeration of nanoparticles and calculate total metal loading. Figure 74 presents representative EDX maps of the fresh and use catalysts.

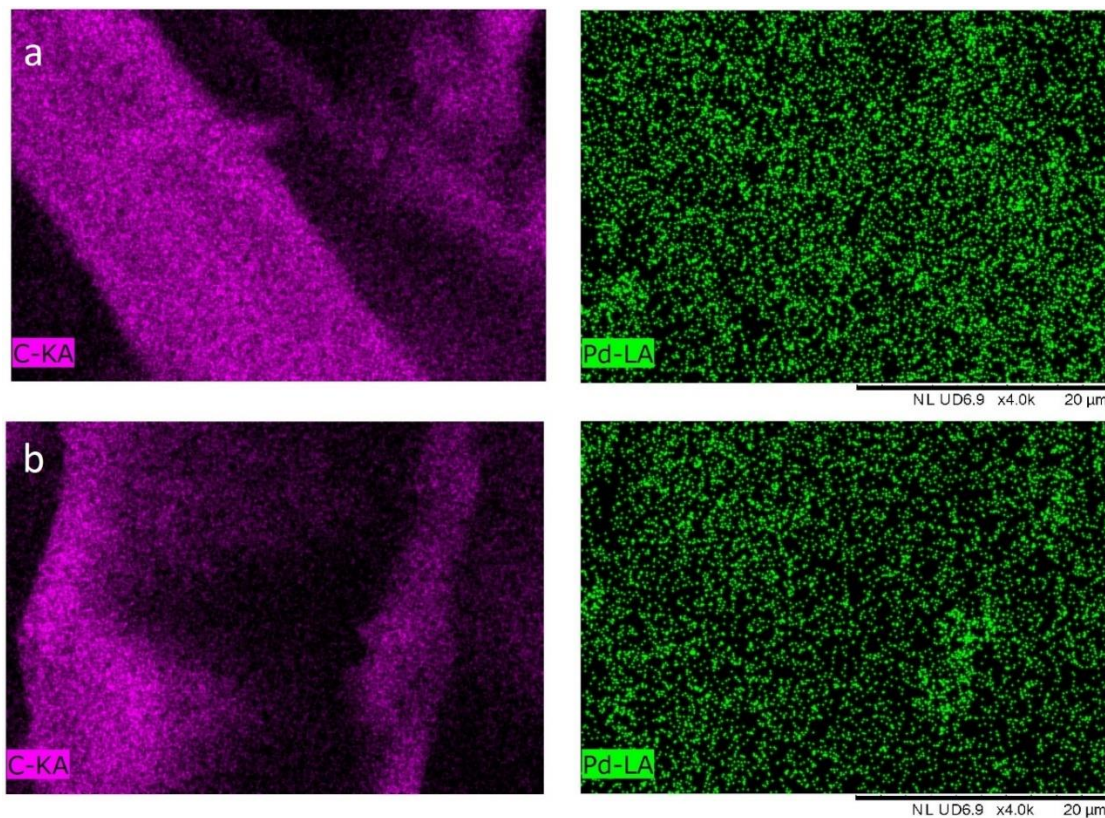


Figure 74. (a) Mapping image of the fresh Pd/C and (c) Mapping image of the used Pd/C.

No apparent variation of the morphology is observed for the used catalyst. EDX spectra confirm the nominal value of 5 wt. % guaranteed by Sigma Aldrich. Actually, the average total metal loading obtained by EDX was 5.1 and 5.0 wt. % for the fresh and used catalyst respectively which is in concordance with the results obtained by MP-AES after using the catalyst in which no leaching was detected. However, comparing the SEM-EDX mapping of fresh and used catalyst, a slightly lower degree of homogeneity is observed and the formation of agglomerated particles is evident in some areas, which will definitively have a negative impact on the catalyst activity during recycling tests.

Previously, XPS results presented a Pd atomic content on the surface lower than 2 %, however, now it is confirmed that the theoretical total metal loading was 5 wt. %. Thus, as previously suggested, a significant amount of Pd was located inside the pores of carbon. BET surface area was then used to analyse the pore characteristics and surface area.

3.2.4.5. Brunauer, Emmett and Teller (BET) method surface area

The surface area of catalysts is known to be of great importance in determining the catalytic performance of the catalyst. For the fresh Pd/C catalyst, BET surface area accounted for 820 m²/g with an average pore volume of 0.73 cc/g and pore size of 3.56 nm which, according to the IUPAC classification, is characteristic of solid with mesoporous (2–50 nm) structure¹⁶. For the used catalyst, a very similar BET surface area of 800 m²/g, pore volume of 0.77 cc/g and pore size of 3.86 nm respectively was obtained. As observed, surface area and porous structure of the catalyst is negligibly affected by formic acid decomposition.

3.2.4.6. Thermogravimetric Analysis - Mass spectrometry (TGA-MS)

As a summary, CO evolution and Pd leaching were discarded, TEM results were not conclusive although particle size increase with use could be a contributory factor, thus, adsorption of intermediates species needs to be investigated in order to find the reason for the slight decrease in activity of the reused catalyst. With this aim, thermogravimetric analysis coupled with a mass spectrometer was used to determine weight loss and chemical species evolved. Figure 75 displays the catalyst mass drop and the spectra obtained from the selected masses against temperature for the fresh and used catalysts.

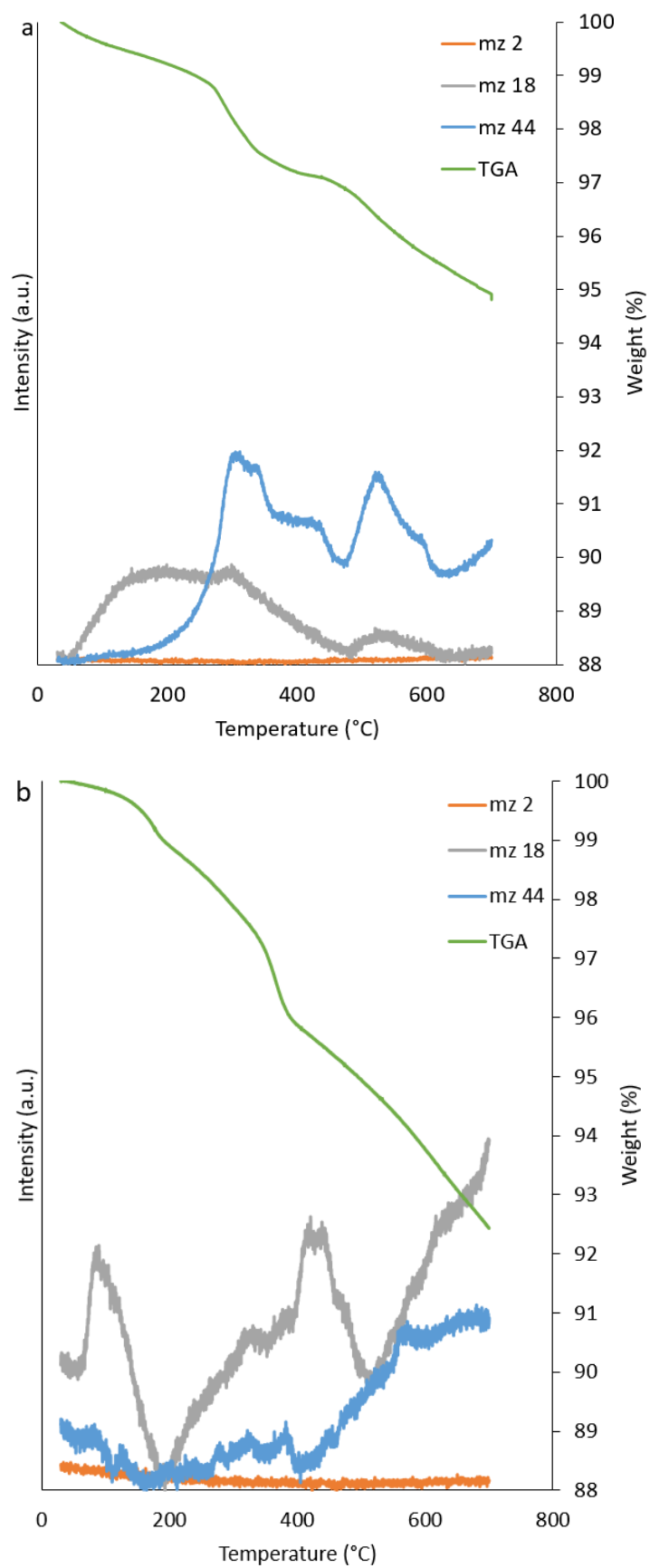


Figure 75. TGA of the (a) fresh, and (b) used catalyst with MS curves of selected m/z values.

The selected masses were $m/z = 2, 18, 44$ and 46 attributed to hydrogen, water, carbon dioxide and formic acid respectively. First, in terms of the catalysts mass drop in weight % with temperature, the trend in both cases is the gradual decrease along the temperature change with a steeper drop between $300 - 400$ °C. Comparing both catalysts, a deeper decrease is observed for the used catalyst, meaning that more adsorbed species were present. This is in concordance with the supposition that adsorbed species could be the most plausible explanation for the loss of activity after using the catalyst. The objective then was to identify the compound or compounds adsorbed.

Observing the mass spectra of the selected masses, in both catalysts, the compounds that more contribute towards weight loss were water and carbon dioxide. Formic acid $m/z = 46$ was analysed although, only a noise signal was obtained. And, in the used catalyst a small portion of hydrogen was desorbed during the first minutes of the analysis. This is clearly a negative aspect since it is the desired product of the reaction, however, the positive side is that the intensity of the signal is very low as well and therefore, the amount of adsorbed hydrogen could be negligible. In the case of the fresh catalyst, water is first desorbed in the moment temperature begins to increase due to residual moisture. Carbon dioxide is mainly desorbed between 200 and 300 °C although at 500 °C there is another peak. This was most likely due to palladium oxide being reduced and the released oxygen reacting with the carbon support producing carbon dioxide.¹⁷ In the case of the used catalyst, the peak of CO_2 is also attributed to palladium reduction and subsequent oxidation of the support. The main difference with the fresh catalyst is the amount of water desorbed. Note that the reaction is produced in aqueous media and moreover, formic acid decomposes mostly to carbon dioxide and hydrogen but there is also a very small portion of carbon monoxide and water. There is initially a similar peak as in the fresh catalyst due to residual moisture and a broad desorption profile at high temperature that can be explained by strong interactions of polar water molecules with the catalyst surface.¹⁸ Hence, water seems to be the species, or at least one of them, adsorbed onto the catalyst surface occupying active sites and affecting the catalyst reusability, in agreement with previous works.⁸

A batch reactor was previously used to study the catalyst activity due to the reproducibility and accuracy of the procedure. Nevertheless, a batch reactor might not be the most suitable method to study reusability since it requires stopping the reaction, filtering the catalyst

(accompanied by a logical loss of part of it which remains stuck into the filter paper), drying, weighing and starting the reaction again. In order to solve these inconveniences, a continuous flow set up was used instead of a batch set up.

3.2.5. Continuous flow set up

Continuous flow was used to try to enhance the reusability of the catalyst using an improved method. Since deactivation of the catalyst is intrinsic to the reaction in aqueous media, it could not be avoided in continuous flow. However, an easy method for the reactivation of the catalyst was developed. As previously presented, water was at least one of the species adsorbed on the catalyst surface preventing a better reusability, thus, facilitating the desorption of this species, could probably liberate active sites which would be then available to decompose formic acid in the next cycle of the reaction.

The reaction conditions were the same as in batch reactor with the exception that approximately 0.1 g of the commercial catalyst was packed by glass wool in the middle section of the reactor, and, since it is continuous flow, it needed a pump whose formic acid solution flow was adjusted to 0.05 ml/min. The gas produced was collected and the volume annotated every 1-2 minutes depending on the rate of reaction. Once the reaction rate decreased to 10-20 % of the original one, the pump was switched off and the temperature of the furnace increased to 180 °C for 1.5 hours. After this time, the oven was switched off, and once stabilised the temperature at 30 °C, the reaction was again started by switching on the pump. Figure 76 presents time online of the reusability experiment in continuous flow set up.

It is observed that after 10 reactivation processes the catalyst presents a similar catalytic behaviour to that of the fresh sample indicating that the species adsorbed on the active sites such as water or formate, was desorbed to a high extent, achieving a very promising degree of reactivation. Note that after the first cycle, there is a slight increase in gas production rate due probably to the reduction of Pd^{II} to Pd⁰ due to hydrogen evolution. The subsequent progressive decrease in catalyst activity for the next runs could probably be caused by two reasons: (i) agglomeration of nanoparticles due to the temperature treatment at 180 °C, and (ii) increase of the strength of the adsorbed species.

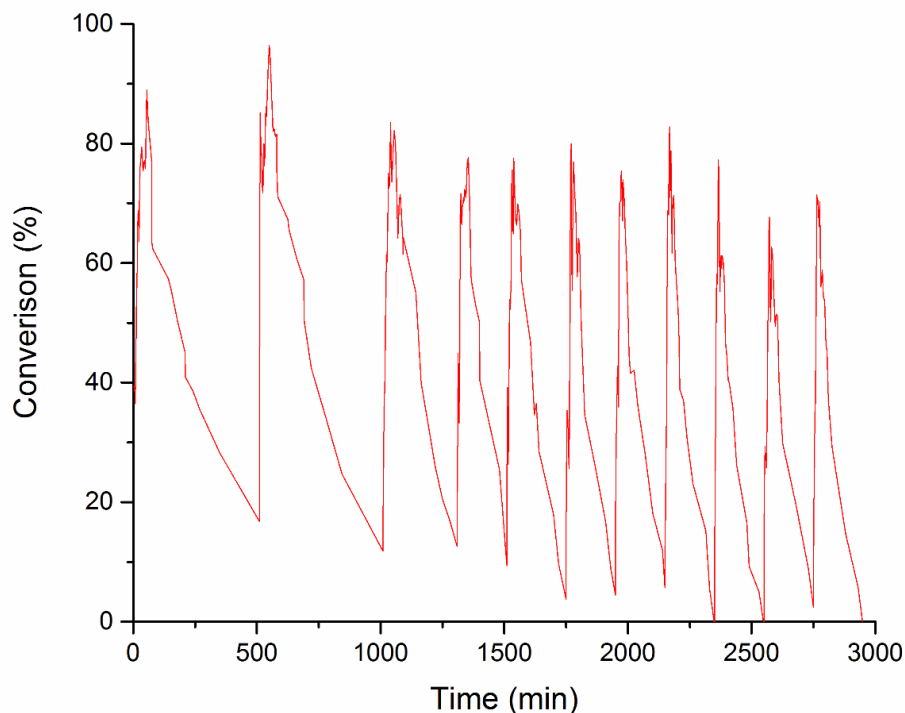


Figure 76. Conversion versus time plot for the reusability study performed in continuous flow. Reaction conditions: 30 °C, 0.1 g of catalyst, 0.5 M HCOOH, 0.05 ml/min.

From the one side, even though, 180 °C is not high enough to produce obvious changes in the catalyst structure, the combination of the cycling liquid-phase formic acid decomposition and subsequent temperature changes may then affect the surface, producing an increase of Pd particle size, reducing the very long-term reusability. 180 °C were selected according to preliminary experimental results that showed a significantly lower reactivation for lower temperatures, meaning that at least 180 °C was necessary to desorb the species without significantly affecting the morphology of the catalyst.

On the other side, this temperature was enough to produce the desorption of most of the adsorbed species although, according to the analysis with TGA-MS, water was desorbed at higher temperature probably, as previously explained, due to strong interactions of polar water molecules with the catalyst surface. This means that the longer the experiment, the higher the probability for water or another species to be strongly adsorbed onto the surface being those not desorbed at the temperature of the heat treatment and therefore, reducing catalyst reusability.

Nevertheless, these results are very promising and suggest that even after 10 regenerations, the initial activity of the catalyst was almost fully restored for a certain period of time,

indicating an excellent regenerability for liquid-phase formic acid dehydrogenation in continuous flow reactor.

At this point that liquid-phase formic acid decomposition was studied in batch and continuous flow setups, and the catalyst thoroughly characterised, the elemental steps of the reaction would shed some light in order to continue investigating the production of hydrogen from formic acid. For this purpose, Kinetic Isotope Effect (KIE) was studied.

3.2.6. Kinetic Isotope Effect (KIE)

Kinetic Isotope Effect studies were performed using HCOOH, DCOOH and DCOOD to gain additional insights into the rate-determining step of the reaction. In this study, decomposition of the isotopologue was performed under the optimised conditions of a typical liquid-phase formic acid dehydrogenation. In order to avoid effect of exchange of deuterons with protons from water, the reactions using HCOOH and DCOOD as reagents were performed in D₂O. Figure 77 displays the plot obtained of the time online of the reaction.

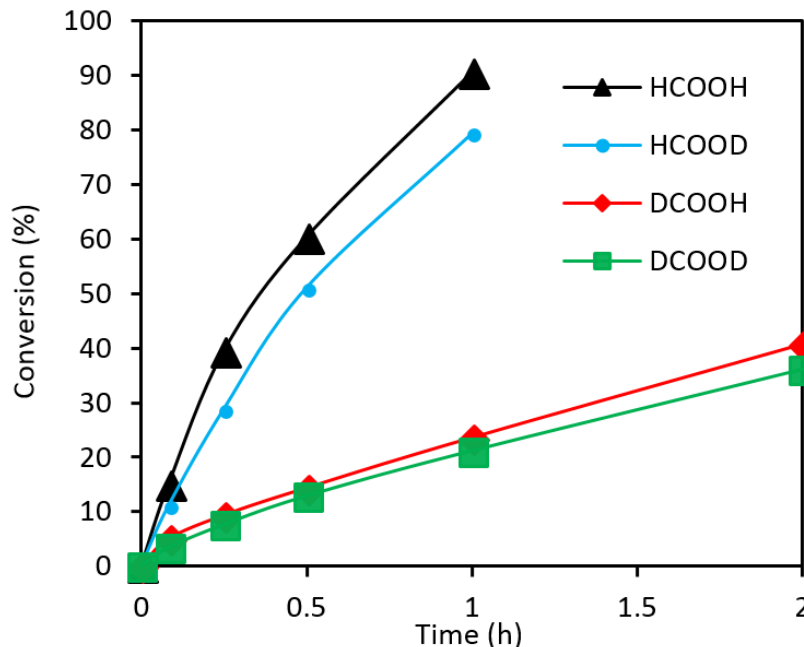


Figure 77. Conversion versus time plot for decomposition of formic acid and its isotopologues. Reaction conditions: 30 °C, 5.3 mg of catalyst (substrate/metal molar ratio: 2000:1), 0.5 M substrate, 750 rpm, 2 h reaction time.

KIE values are calculated as the ratio between the reaction rate when HCOOH is used and the reaction rate when an isotopologue is used. These values are presented in table 15. Depending on the values obtained, three possible options are presented:

- In case of KIE values for HCOOD are close to 1 but larger value for DCOOH, it means that HCOOH dissociation is kinetically relevant.
- On the contrary, KIE values close to 1 for DCOOH but not for HCOOD is due to limitation by the formate decomposition.
- Finally, in the case of KIE values of approximately 1 for both HCOOD and DCOOH, it can be explained by a limiting hydrogen desorption both from HCOOD and DCOOH.¹⁹

Table 15. Ratio of reaction rates during kinetic isotope effect.

Substrate	r_H/r_D
HCOOD	1.3
DCOOH	3.0
DCOOD	4.4

Reaction rate using HCOOD resulted in reaching a very similar conversion as in the standard reaction using HCOOH. This means that HCOOD presents the closest KIE value to unity, while, both DCOOH and DCOOD presented larger values. According to the previous statements, the cleavage of the bond O-D or O-H is not relevant to the rate of reaction while breaking C-H or C-D presents a significant difference. These results confirm that the rate determining step is the cleavage of the bond C–H/D. With this in mind, the most probable pathway followed by formic acid decomposition is the formation of formates instead of carboxylic species. Thus, hydrogen atoms formed after the O–H dissociation recombines with those hydrogen atoms formed after the formate decomposition producing hydrogen and carbon dioxide through the dehydrogenation pathway.

By using Density Functional Theory, the thermodynamic profile is going to be simulated in order to shed more light on the energetics of the pathways.

3.2.7. DFT studies

Kinetic isotope effect has presented the most probable pathway to decompose formic acid using Pd. DFT calculations were performed to support these results and calculate the potential energy of each elementary step. Furthermore, DFT calculations were also performed to provide insights about the decomposition of formic acid (dehydrogenation versus dehydration) on the most usual Pd(001), Pd(011) and Pd(111) surfaces present on a Pd structure with different particle size. This way, it is possible to elucidate the structure leading towards the highest hydrogen selectivity and identify the structure and/or pathway leading to the production of CO. (111), (011) and (001) surfaces were used to simulate each step of formic acid decomposition. Adsorbed species are presented in this text with the symbol *. From HRTEM micrographs it was observed that Pd(111) structure was the most abundant, therefore, even though the three surfaces have been studied to the same extent, an in-depth overview of each one of them would be out of the scope of this Thesis, thus, more emphasis will be given to the Pd(111) surface. For this purpose, for the decomposition of formic acid on Pd(111) surface, insights into each elementary step with its correspondent side and top views of the best initial state, transition state and best final state is given. E_f denotes the activation energy barrier calculated as the energy of the transition state – energy of the best initial state. Palladium, carbon, oxygen and hydrogen atoms are indicated in grey, brown, red and light grey respectively.

(111) Surface. The energy profile displayed in figure 78 shows the energy requirements of two different paths started by O-H (**1**: formate (HCOO) formation) and C-H (**2**: carboxylic (COOH) formation) dissociation for the Pd(111) surface.

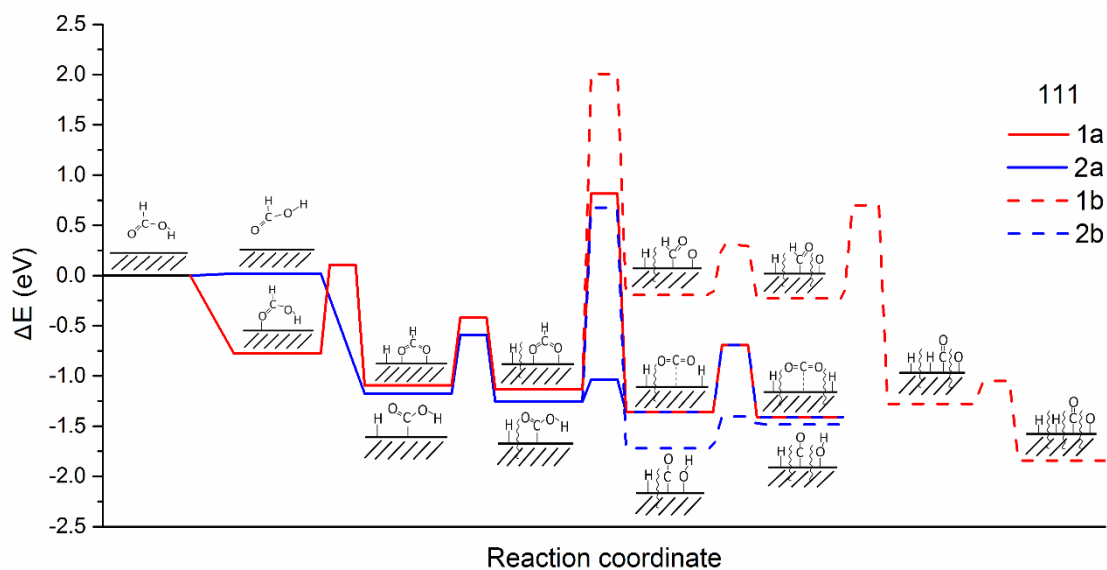


Figure 78. Potential energy surface for formic acid decomposition on Pd(111) surface. Red and blue lines indicate HCOO and COOH paths. Solid lines lead to CO₂ whereas dashed line, to CO.

Formate pathway (**1**) initiates with the adsorption of the most stable perpendicular trans-configuration of HCOOH* ($E_B = -0.77$ eV) and subsequent splitting of the O-H bond ($E_R = -0.32$ eV) which requires an activation energy of 0.88 eV (Figure 79).

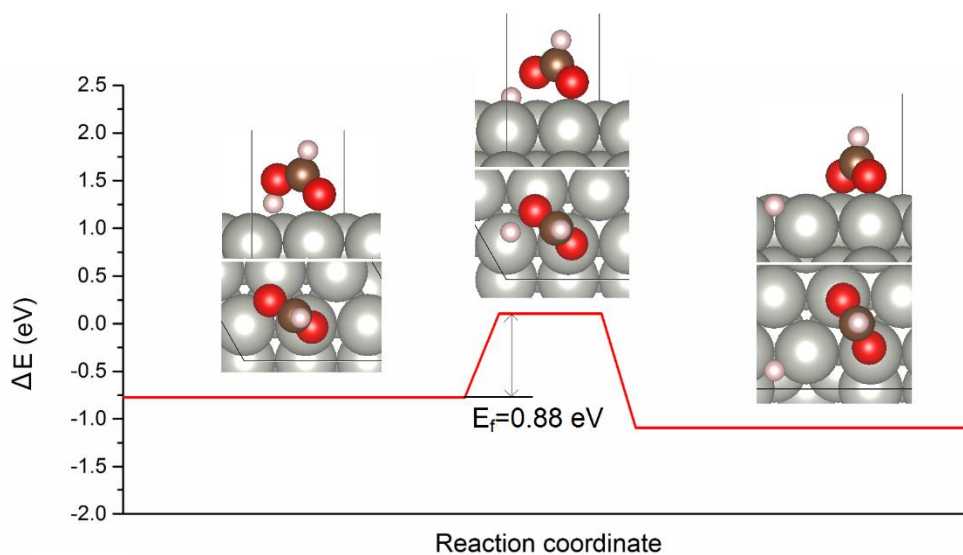


Figure 79. Reaction coordinate for HCOOH* + * → HCOO* + H* on Pd(111).

From this intermediate (HCOO*), pathway **1** either follows route **a** to produce CO₂ (cleavage of C-H) or route **b**, to CO (cleavage of C-O). HCOO* decomposition to CO₂* and H* (**1a**) has a

barrier of 1.95 eV and is exothermic by 0.23 eV (Figure 80), while HCOO* decomposition to HCO* and O* has an activation energy of 3.14 eV and is endothermic by 0.94 eV (Figure 81).

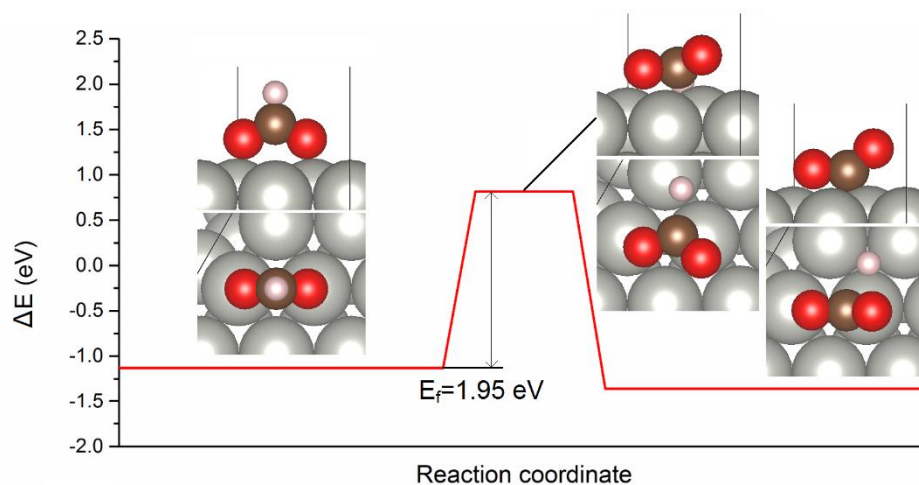


Figure 80. Reaction coordinate for $\text{HCOO}^* + * \rightarrow \text{CO}_2^* + \text{H}^*$ on Pd(111).

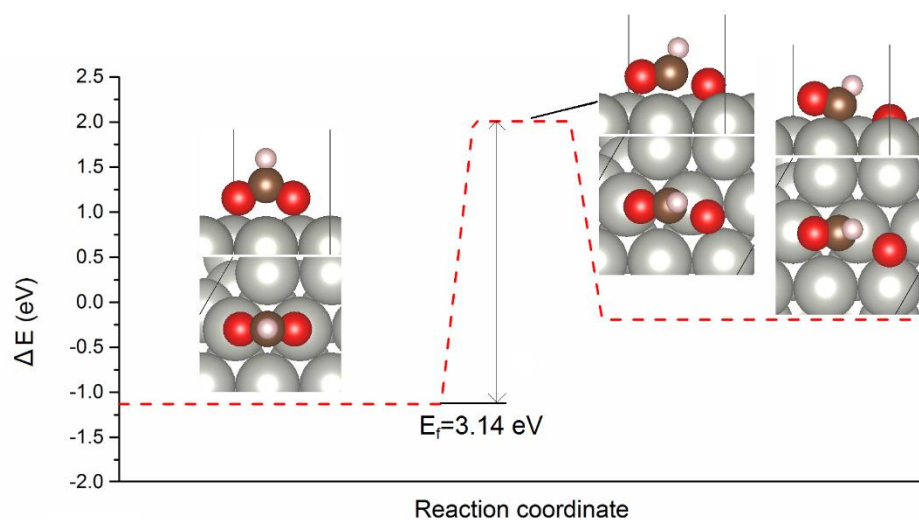


Figure 81. Reaction coordinate for $\text{HCOO}^* + * \rightarrow \text{HCO}^* + \text{O}^*$ on Pd(111).

The last step is the decomposition of HCO* to H* and CO*. It is exothermic by 1.05 eV and requires an activation energy of 0.93 eV (Figure 82).

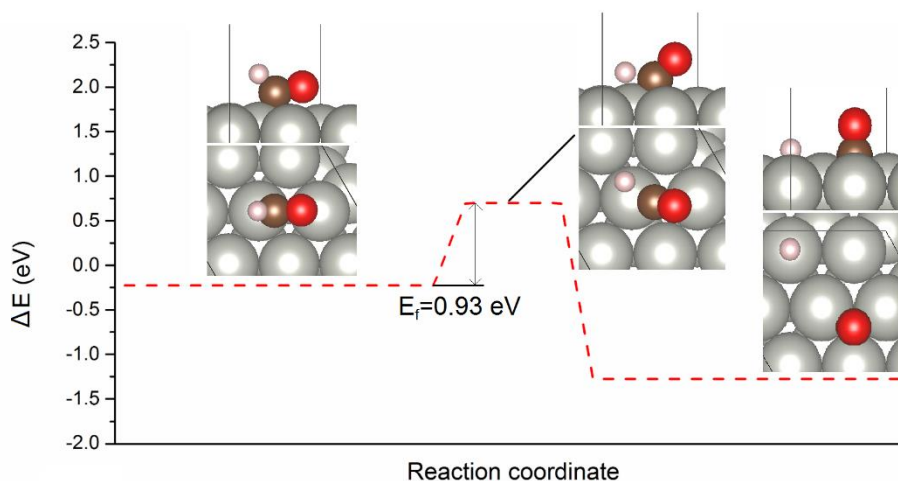


Figure 82. Reaction coordinate for $\text{HCO}^* \rightarrow \text{H}^* + \text{CO}^*$ on Pd(111).

On the other hand, COOH^* pathway (2) starts with a reorientation of HCOOH from trans to cis-configuration, which imposes a slight energy increment of 0.02 eV. After the adsorption, again two possibilities are shown: O-H cleavage to produce CO_2 , or C-O cleavage to produce CO.

O-H scission is exothermic by 0.10 eV and its activation energy is 0.22 eV (Figure 83).

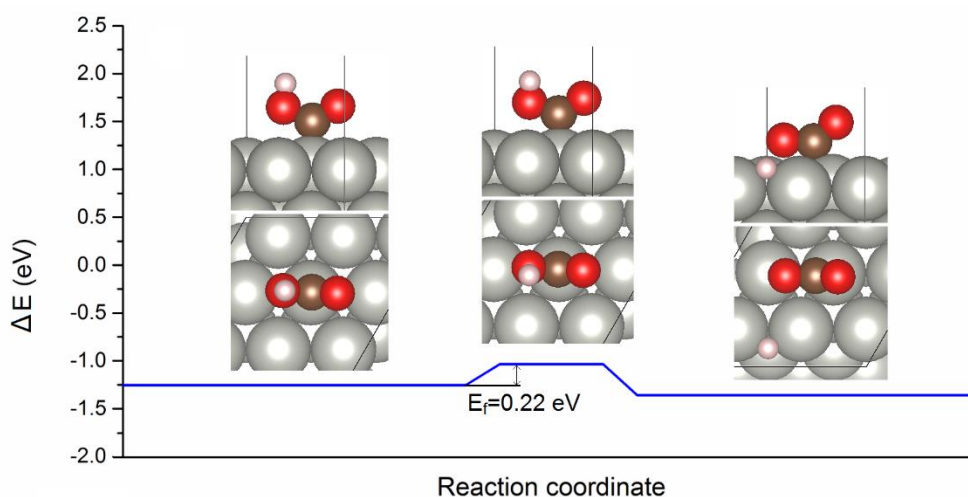


Figure 83. Reaction coordinate for $\text{COOH}^* + * \rightarrow \text{CO}_2^* + \text{H}^*$ on Pd(111).

COOH^* dissociation to CO^* and OH^* is exothermic by 0.46 eV and the barrier is 1.93 eV (Figure 84).

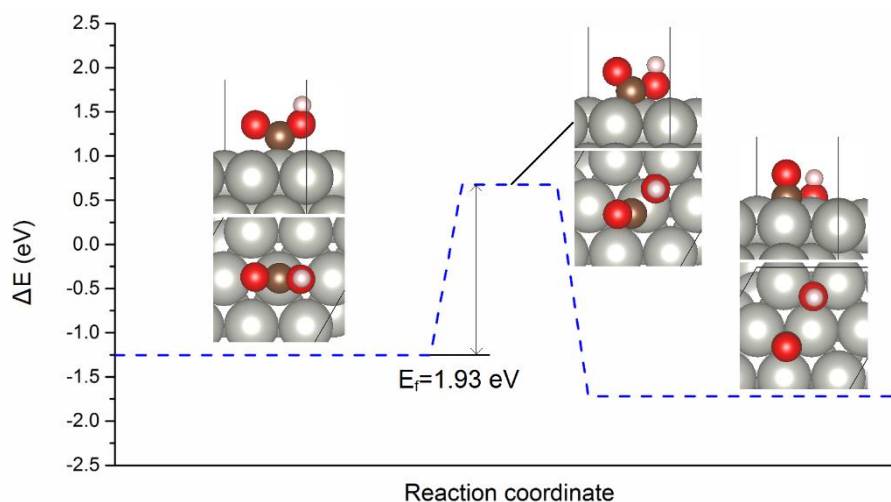


Figure 84. Reaction coordinate for $\text{COOH}^* \rightarrow \text{CO}^* + \text{OH}^*$ on Pd(111).

Before continuing providing results, a brief summary will help to tighten the information given so far:

- As reported in the previous Kinetic Isotope Effect study, HCOO^* is the preferable intermediate over COOH^* since C-H scission is largely unfavourable, even though both formate and carboxylic intermediates are very close in energy (-1.13 and -1.25 eV respectively).
- From the decomposition of HCOO^* , two possible pathways were available, however, since the C-O dissociation step (**1b**) was shown highly unfavourable ($E_f = 3.14$ eV), the main pathway followed was C-H cleavage ($E_f = 1.95$ eV) leading consequently to CO_2 and H_2 , in concordance with the experimental low ppm level of CO found during the gas analysis.
- Even though HCOO^* intermediate is more plausible, HCOOH may also decompose through COOH^* route. Moreover, in this case, the difference in energy barriers is significant, 0.22 eV to produce CO_2 , while 1.93 eV is necessary to lead to CO evolution, which also explains the low concentration of CO.

As previously explained, low CO ppm is a condition required for PEM fuel cells due to the poisoning of the catalyst. With this in mind, the experimental part in this Thesis was performed at 30 °C and the analysis of gases already presented, confirmed the low CO concentration evolved. As observed in the DFT results, formic acid decomposition leading to

CO evolution requires a supply of energy higher than to produce hydrogen and carbon dioxide. At this point, finding the temperature that increases the concentration of CO in the evolved gases, would be interesting. This experiment was performed with the catalysts supported on carbon nanofibers and the results will be provided in the next chapter.

Resuming with the DFT results, the transition states of Pd(111) have been presented. As previously commented, such an in-depth collection of results would be counter-productive for the purpose of this Thesis. Thus, a lighter overview of the Pd(011) and Pd(001) will be provided next and followed by a table with the energy of the reactions and its transition states for further comparison.

(011) Surface. The energy profile is displayed in figure 85.

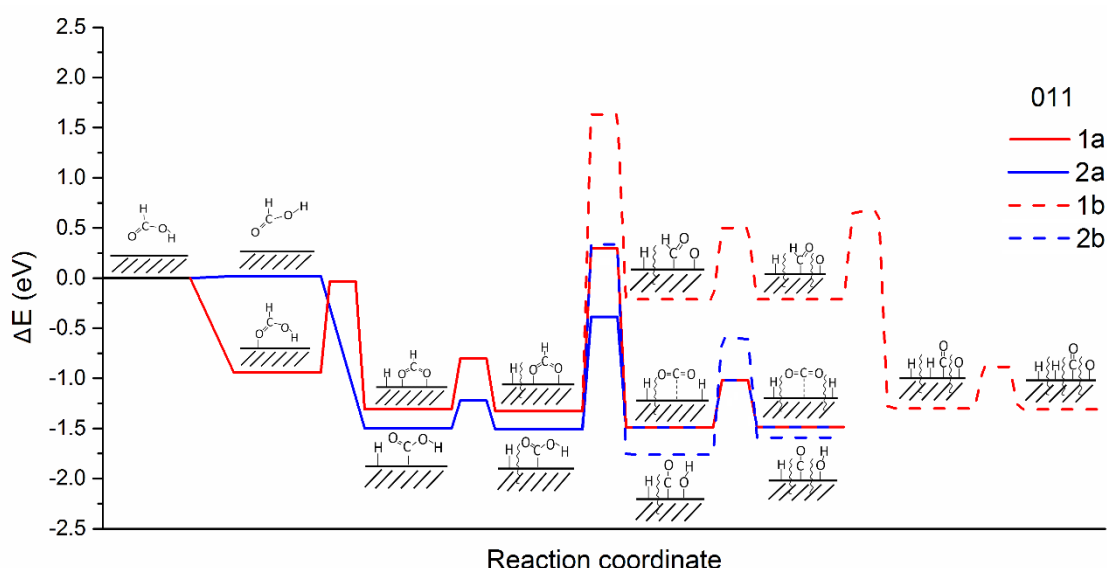


Figure 85. Potential energy surface for formic acid decomposition on Pd(011) surface. Red and blue lines indicate HCOO and COOH paths. Solid lines lead to CO₂ whereas dashed line, to CO.

(011) Surface. In this case, the adsorption of trans-configuration of HCOOH* supposes a relaxation of $E_B = -0.94$ eV and the splitting of O-H bond ($E_R = -0.37$ eV) requires an activation energy of 0.91 eV. As with the (111) surface, the pathway splits following the route **a** to CO₂ and the route **b** to CO. HCOO* decomposition to CO₂* and H* (**1a**) is exothermic by 0.16 eV and has a barrier of 1.62 eV. HCOO* decomposition to HCO* and O* has an activation energy

of 2.96 eV and is an endothermic process by 1.12 eV. The decomposition of HCO^* to H^* and CO^* is exothermic by 1.09 eV and requires an activation energy of 0.87 eV.

Since the reorientation of HCOOH occurs in gas phase, the requirement is the same, 0.02 eV. Once COOH^* is adsorbed on the Pd(011) surface, O-H scission is very slightly endothermic by 0.02 eV and its activation energy is 1.12 eV. COOH^* dissociation to CO^* and OH^* is exothermic by 0.25 eV and the barrier is 1.85 eV.

(001) Surface. The energy profile is displayed in figure 86.

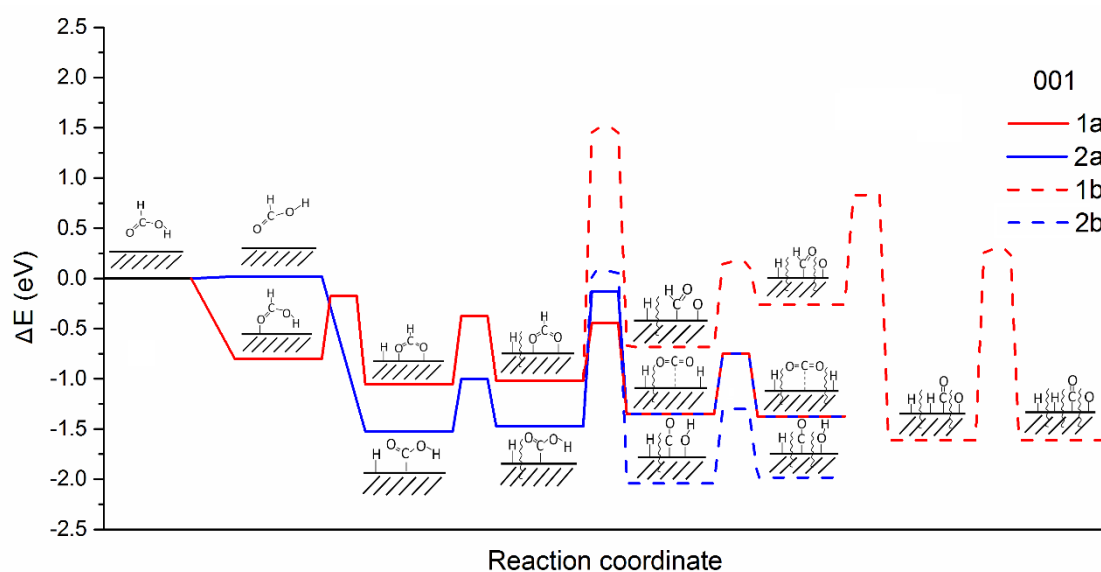


Figure 86. Potential energy surface for formic acid decomposition on Pd(001) surfaces. Red and blue lines indicate HCOO and COOH paths. Solid lines lead to CO_2 whereas dashed line, to CO.

(001) Surface. Adsorption of trans-configuration of HCOOH^* relaxes the system by 0.80 eV and the breakage of the O-H bond ($E_R = -0.25$ eV) which requires an activation energy of 0.63 eV. Pathway **1a** ($\text{HCOO}^* + * \rightarrow \text{CO}_2^* + \text{H}^*$) is exothermic by 0.33 eV and has a barrier of 0.57 eV while pathway **1b** ($\text{HCOO}^* + * \rightarrow \text{HCO}^* + \text{O}^*$) has an activation energy of 2.51 eV and is an endothermic process by 0.33 eV. The decomposition of HCO^* to H^* and CO^* is exothermic by 1.35 eV and requires an activation energy of 1.09 eV.

Pathway **2** initiates with the reorientation of HCOOH and adsorption of COOH . From this intermediate, O-H scission is endothermic by 0.12 eV and its activation energy is 1.35 eV. COOH^* dissociation to CO^* and OH^* is exothermic by 0.57 eV and the barrier is 1.55 eV.

Table 16 displays the activation energy (E_f) requirements for each transition state and its reaction energy (ΔE) calculated as energy of the best final state – energy of the best initial state.

Table 16. Activation energy barrier (E_f) and reaction energy (ΔE) for all transition states on Pd(111), Pd(011) and Pd(001).

Transition state	E_f (eV)			ΔE (eV)		
	(111)	(011)	(001)	(111)	(011)	(001)
$\text{HCOOH}^* + * \rightarrow \text{HCOO}^* + \text{H}^*$	0.88	0.91	0.63	-0.32	-0.37	-0.25
$\text{HCOO}^* + * \rightarrow \text{CO}_2^* + \text{H}^*$	1.95	1.62	0.57	-0.23	-0.16	-0.33
$\text{HCOO}^* + * \rightarrow \text{HCO}^* + \text{O}^*$	3.14	2.96	2.51	0.94	1.12	0.33
$\text{HCO}^* + * \rightarrow \text{H}^* + \text{CO}^*$	0.93	0.87	1.09	-1.05	-1.09	-1.35
$\text{COOH}^* + * \rightarrow \text{CO}_2^* + \text{H}^*$	0.22	1.12	1.35	-0.10	0.02	0.12
$\text{COOH}^* + * \rightarrow \text{CO}^* + \text{OH}^*$	1.93	1.85	1.55	-0.46	-0.25	-0.57

An explanation of the low carbon monoxide concentration evolved has been given for Pd(111) surface. Differences in terms of activation and reaction energies related with the structure Pd(111), Pd(011) and Pd (001), may shed some light on the composition of gases and more importantly, provide information that can lead to catalysts design with improved properties and 0 ppm CO evolution.

From the one side, Pd(011), having in mind that the most common pathway followed is the HCOO^* decomposition, even though the activation energy for the step $\text{HCOO}^* + * \rightarrow \text{HCO}^* + \text{O}^*$ is slightly lower than for Pd(111), the reaction energy is considerably higher [1.12 eV for (011) and 0.94 eV for (111)] therefore, carbon dioxide and hydrogen will be again the main products.

From the other side, Pd(001) presents the lowest activation energy for the process $\text{HCOO}^* + * \rightarrow \text{HCO}^* + \text{O}^*$ and furthermore the difference of the initial and final state is lower than for the two previous surfaces meaning that CO is produced by Pd(001) at a lower temperature compared with the other two surfaces since it requires less energy introduced into the system.

Although HCOO* decomposition is the main pathway, COOH* decomposition may take place as well. In this case, again Pd(111) is the surface leading to the lowest concentration of CO. Note how the activation energy increases in the order Pd(111)<Pd(011)<Pd(001) for the decomposition to hydrogen and carbon dioxide while the opposite trend is observed for the pathway leading to carbon monoxide. Moreover, the reaction energy changes from exothermic for Pd(111) to endothermic for Pd(001) for the production of CO₂ which means that an increase in temperature will facilitate CO evolution in Pd(001) as well.

All these results aim in the same direction. Even though Pd(111) and Pd(011) can produce CO under certain conditions, Pd(001) requires less supply of energy to produce CO, thus, at mild conditions, it may produce low ppm of CO, but will undoubtedly increase when increasing temperature. Hence, very small nanoparticles with large extensive area of (001) would be detrimental for CO evolution. In this research, mean particle size was between 3 and 4 nm. This diameter seems to be large enough to avoid (001) surface to a large extent since very low ppm of CO were evolved. Besides the presence of Pd(001), cis configuration, and therefore, COOH* decomposition is the main pathway leading to CO formation even at low temperature. As a conclusion, Pd(001) and COOH* decomposition are the structure and pathway that lead to a higher concentration of CO.

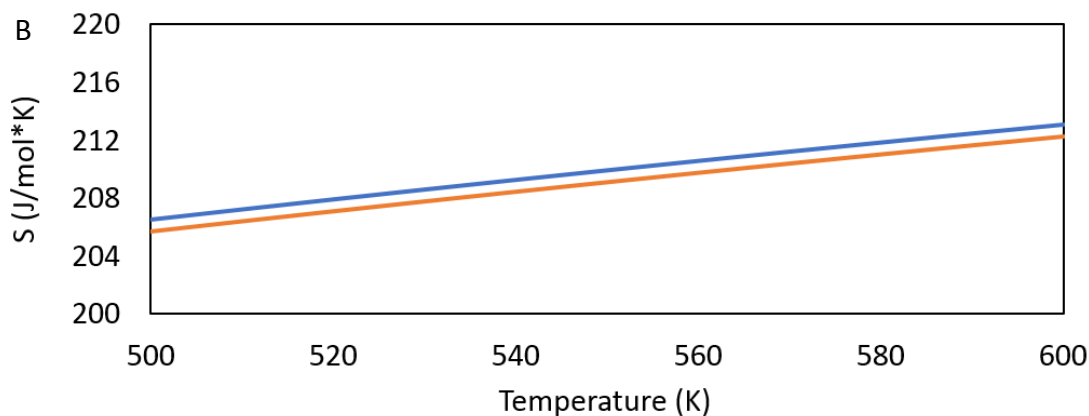
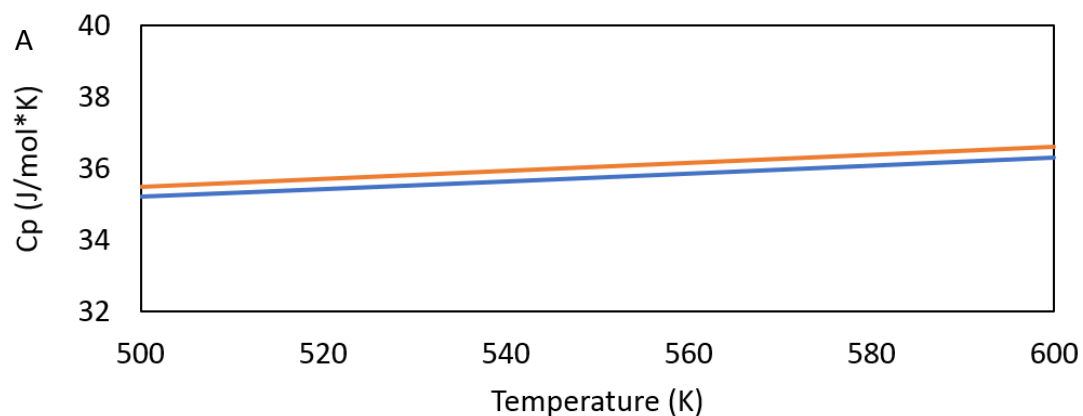
Vibrational frequencies were calculated merely to verify the transition states by identifying a single imaginary frequency. The computed vibrational frequencies of the main transition steps of HCOOH decomposition is presented in table 17.

Table 17. Vibrational imaginary frequencies of all transition states on Pd(111), Pd(011) and Pd(001).

Transition state	Frequency (cm ⁻¹)		
	(111)	(011)	(001)
HCOOH* + * → HCOO* + H*	433.3	1315.8	611.2
HCOO* + * → CO ₂ * + H*	1113.1	809.5	212.2
HCOO* + * → HCO* + O*	573.0	146.4	122.5
HCO* + * → H* + CO*	430.4	693.3	566.1
COOH* + * → CO ₂ * + H*	997.5	1343.7	1506.8
COOH* + * → CO* + OH*	521.9	502.3	332.3

By using DRIFT, experimental values obtained could be compared with the calculated values, however, since carbon is used as a support, Beer's equation is not followed and therefore, this technique could not be performed.²⁰

Once all the relevant processes involved in the reaction were investigated, a micro-kinetic simulation based on results from density functional theory (DFT) calculations was performed considering reaction, adsorption and desorption processes of reactants, intermediates and products, involved in the formic acid decomposition on Pd(001), Pd(011), and Pd(111) surfaces. This model was used to confirm the energy profile previously obtained by comparing the limitant reactions with the experimental results. First, the thermodynamic variables: heat capacity (C_p), Gibbs free energy (G), standard enthalpy (H) and standard entropy (S) obtained by DFT were compared with those obtained by the Shomate equation,²¹ (Figure 87) which confirmed the good accuracy of calculations in the range of temperatures considered. The range of temperature in the next graphs was selected according to the available references, although in the computational model, a broader range of temperature from 250 to 600 K was studied.



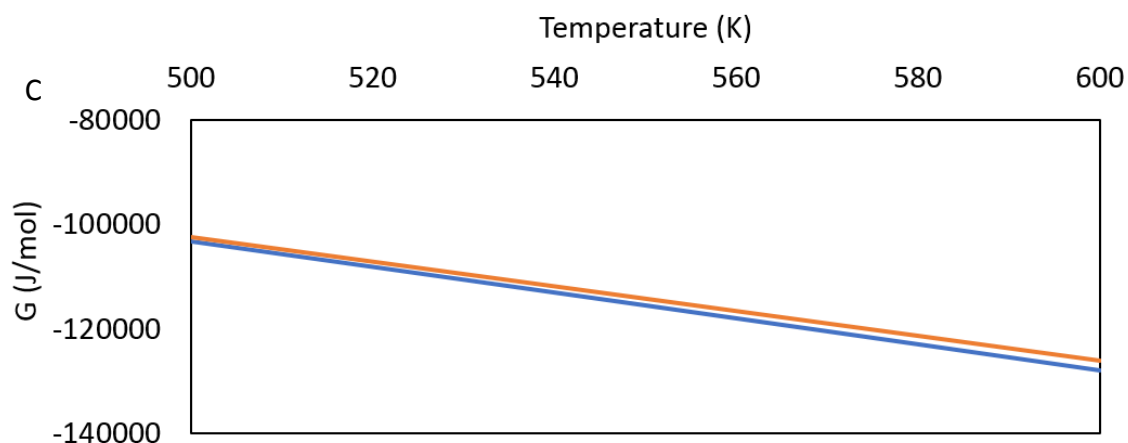


Figure 87. A) Heat capacity, B) standard entropy, and C) Gibbs free energy comparison of values calculated by Shomate equation (Blue) and values obtained using the micro-kinetics model (orange).

IR spectra obtained by the kinetic modelling and experimental²² are displayed in figure 88. Note that the band at approximately 1700 cm^{-1} is due to long-range interaction between molecules.

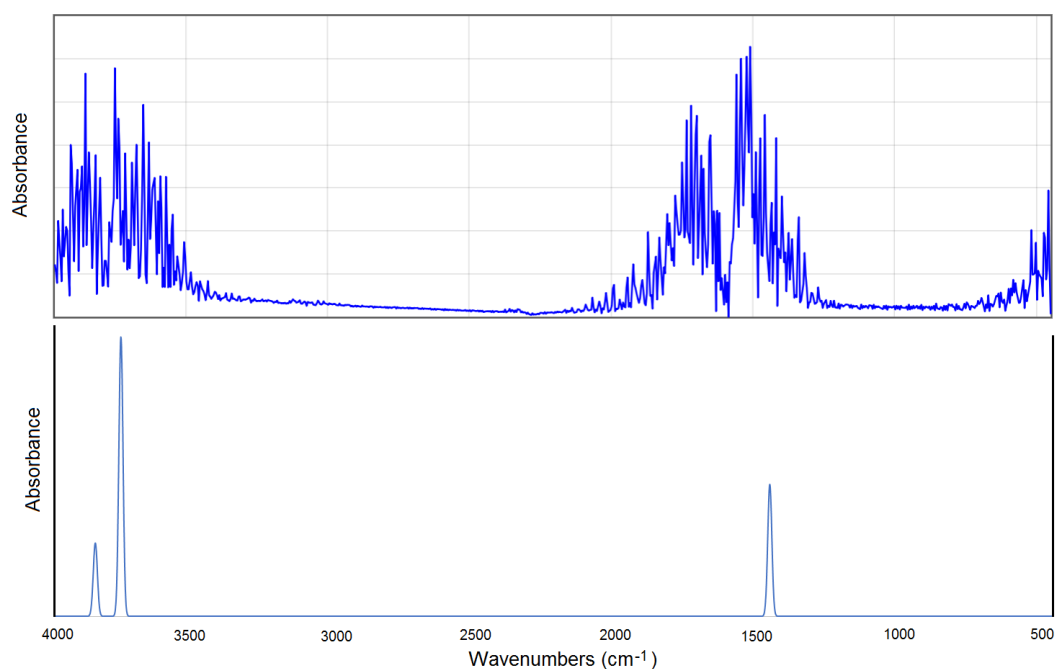


Figure 88. IR spectra of water. Experimental (top), kinetic simulation (bottom).

As observed, the computational model matches the experimental IR spectra of water, therefore, this validates the computational set up employed. By using this model, the reaction

constant (k_{rate}) can be calculated for each surface and by plotting $\text{Log}(k_{\text{rate}})$ against temperature, the limitant steps in formic acid decomposition can be identified (Figure 89).

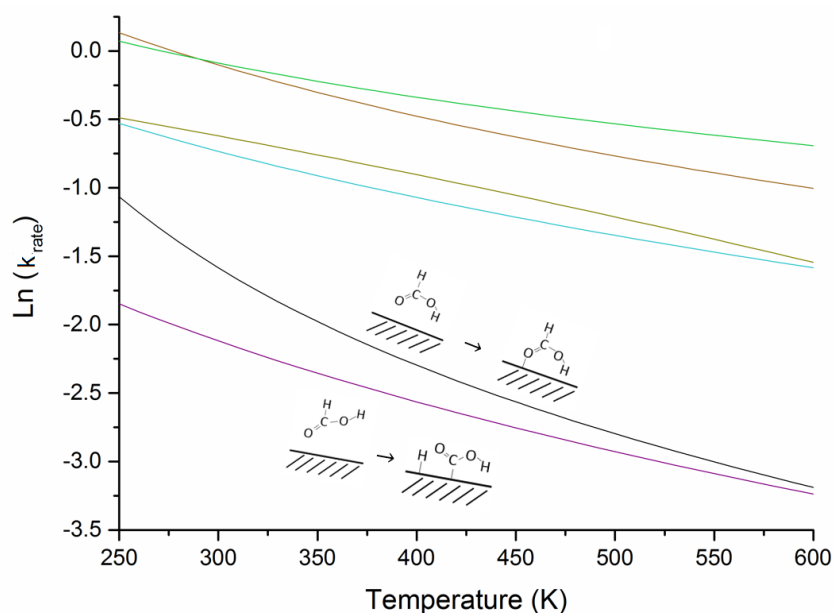


Figure 89. $\text{Log}(k_{\text{rate}})$ against temperature.

Consequently, adsorption of species is the limiting step since these present the lowest reaction constants. As observed, in the adsorption of formic acid *cis*, the C-H cleavage is involved which is in concordance with the previous results from KIE.

In summary, a commercial 5 wt. % Pd/C was used to decompose formic acid producing mainly hydrogen and carbon dioxide. The reaction was studied using the fresh catalyst as bought, without any further chemical or thermal treatment and a solution of additive-free formic acid. With these components, the optimum conditions were found and, the reusability test exposed a slight decrease in activity whose reason was also found through characterisation and analysis of the reaction products.

As shown in the literature, most of the catalysts preparation methods comprise a final calcination to stabilise the structure and remove impurities²³ however, it also affects particle size. Hence, this had to be investigated as well.

3.2.8. Effect of calcination on catalyst activity

To get insights into the effect of thermal treatment, the 5 wt. % Pd/C commercial catalyst was calcined at 200 and 250 °C in flowing air for 3 h. This range of temperature was selected to investigate the impact of heat treatment on the catalytic activity, oxidation state and particle size of Pd, and maintaining the thermal stability of the activated carbon support. Catalyst activity was studied at the optimised reaction conditions.

Figure 90 displays the time on-line plot of the comparison of the fresh and the calcined catalysts.

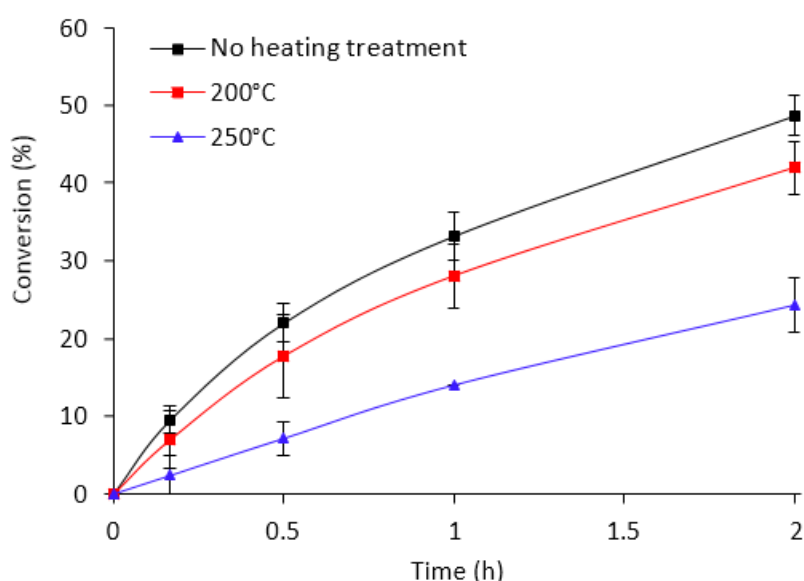


Figure 90. Conversion versus time plot for liquid-phase formic acid decomposition using the fresh and calcined catalysts. Reaction conditions: 30 °C, 5.3 mg of catalyst (substrate/metal molar ratio: 2000:1), 0.5 M substrate, 750 rpm, 2 h reaction time.

As observed, even at mild temperature, calcination significantly affected the catalytic performance in a negative way, making the drop in catalytic activity more noticeable for the catalyst treated at higher heat treatment temperature. Calcination at 200 °C reduced the conversion of the fresh catalyst from ~ 10 to 7 % while, at 250 °C it drastically decreased to 2.5 %.

Initial suppositions attribute this activity drop to particle aggregation decreasing metal surface area. In order to confirm this idea, characterisation of these catalysts was needed.

Figure 91 displays the XRD patterns of the calcined catalysts.

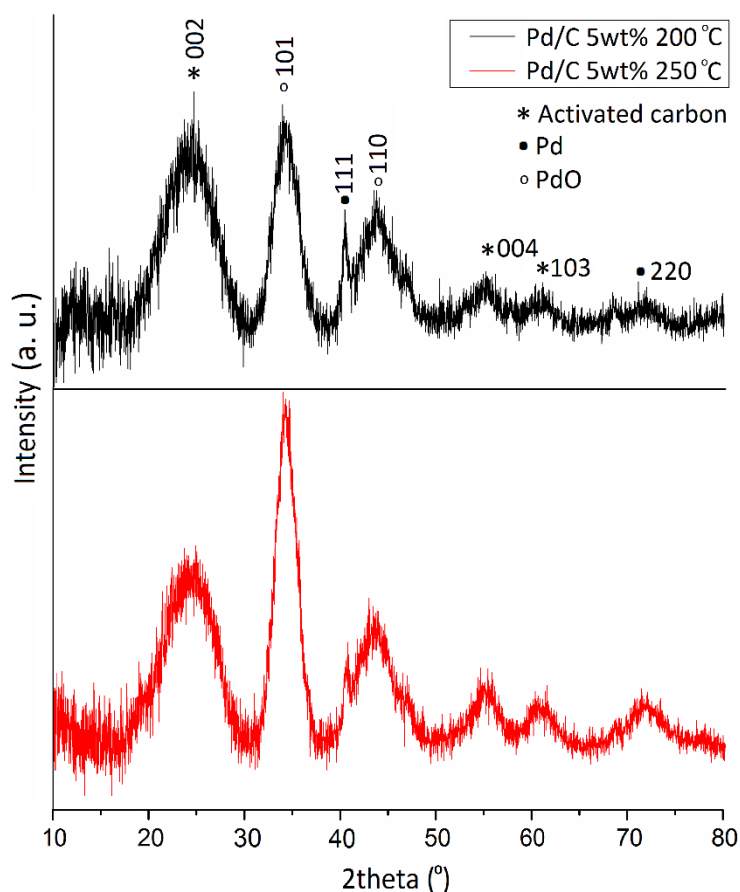


Figure 91. XRD patterns of calcined catalysts.

In comparison with the XRD pattern of the fresh catalyst presented in Chapter 3, section 3.2.4.1, on the one side, the diffraction peaks assigned to PdO significantly rose after the heat treatment and, on the other side, the diffraction peak corresponding to metallic Pd decreased significantly. It is known that metallic Pd tends to oxidise when exposed to air at high temperatures, which is confirmed by this experiment. Furthermore, the decrease of the intensity of the diffraction peak at $2\theta = 40.4^\circ$ supports this observation. For the catalyst calcined at 250 °C, the decrease of the intensity of the diffraction peak was more noteworthy due possibly to a lower presence of metallic Pd in the catalyst. XPS will be used to provide more information about the oxidation state of the metals.

The Scherrer equation was again employed to calculate the mean crystallite size of the Pd nanoparticles. The equation was applied to the diffraction peak at 40.4° corresponding to (111) reflection. Table 18 presents both the FWHM and crystallite size of the fresh and calcined catalysts 200 and 250 °C.

Table 18. Crystallite size of Pd particles calculated using the Scherrer equation.

Sample	FWHM of (111) reflection at 40.4°	Crystallite size (nm)
Fresh	1.75	4.8
Calcined at 200 °C	0.85	9.9
Calcined at 250 °C	0.80	10.5

There is a significant increase of the Pd crystallite size during calcination process. This is most probably due to a relatively weak interaction between Pd nanoparticles and the carbon support, facilitating then the agglomeration and sintering of particles. The decrease in activity could be related to both, the higher presence of PdO and the increase in crystallite size.

XPS analysis of the calcined samples is displayed in figure 92.

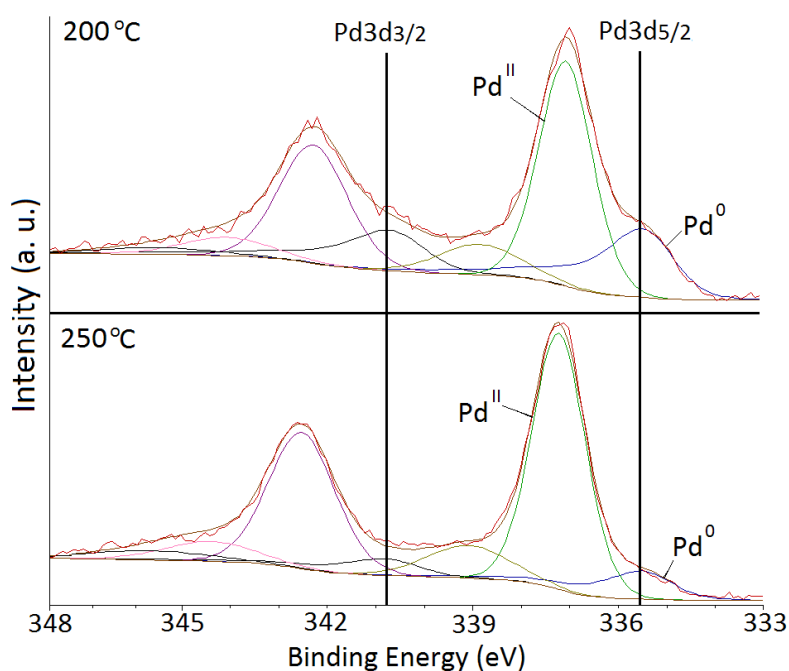


Figure 92. XPS spectra of fresh and calcined catalysts in the binding energy region of 233–348 eV corresponding to Pd 3d.

The constraints used for the deconvolution and identification of each region has been previously presented. XPS spectra confirmed the decrease of metallic Pd and its subsequent progressive oxidation to PdO as the temperature of the heat treatment increased.

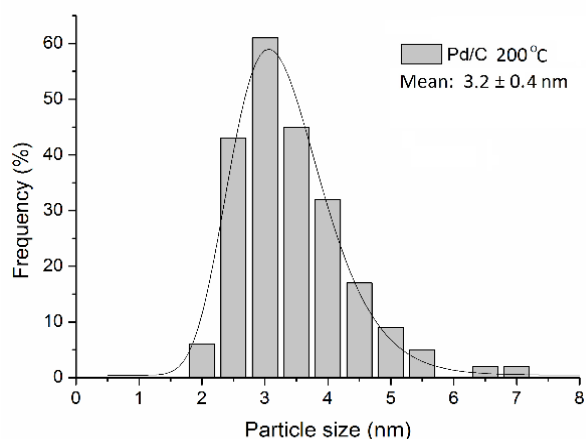
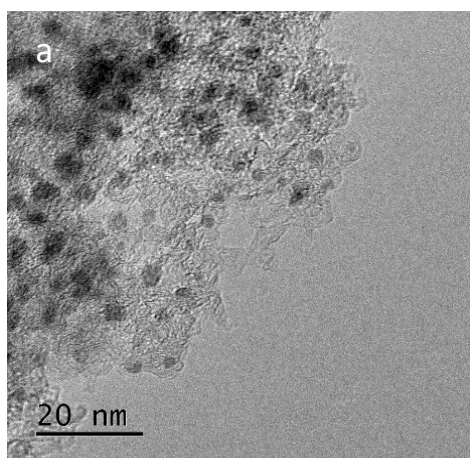
Detailed XPS binding energy of Pd, its oxidation states and relative content of each species are presented in table 19.

Table 19. XPS binding energies of Pd with respective oxidation state and relative content of each species.

Sample	3d _{5/2} (eV)		3d _{3/2} (eV)	
	Pd ⁰ (%)	Pd ^{II} (%)	Pd ⁰	Pd ^{II}
Fresh	335.4 (60)	337.0 (40)	340.7	342.2
Calcined at 200 °C	335.4 (32.8)	337.2 (67.2)	340.7	342.5
Calcined at 250 °C	335.4 (14.7)	337.2 (85.3)	340.7	342.6

While for the fresh catalyst, metallic Pd accounts for 60 %, for the calcined catalysts, it decreases to approximately half (32.8 %) for the catalyst calcined at a lower temperature, and for the catalyst calcined at 250 °C, it further decreases by half again (14.7 %). This result is in concordance with the XRD data, and the dramatic decrease of metallic Pd content is a plausible reason for the decrease in catalytic activity.

In order to find the average Pd particle size and its distribution, TEM was performed. The TEM micrographs and its respective size distribution of the calcined catalysts at 200 and 250 °C are displayed in figure 93. No apparent change of the mean particle size is shown for the catalyst calcined at 200 °C, while, at 250 °C mean particle size very slightly increased to 4.0 ± 0.3 nm due probably to sintering.



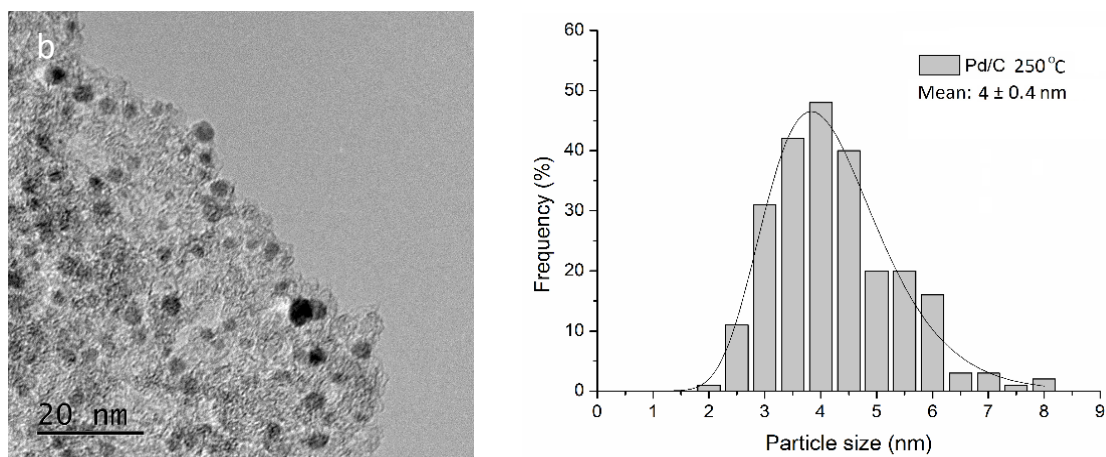


Figure 93. Bright field TEM micrographs and corresponding histograms of the particle size distributions for the calcined catalysts at (a) 200 °C, (b) 250 °C. Magnification: $\times 250k$.

Lattice fringe of Pd nanoparticles of the calcined catalysts was also studied by means of High-Resolution TEM (HRTEM). Figure 94 presents these micrographs.

For the catalyst calcined at the lowest temperature, it was only observed a discrete lattice-fringe of the face-centered cubic (fcc) Pd crystal with a d-spacing of 0.225 nm, while at 250 °C, a certain number of particles showed an additional lattice fringe with d-spacing of 0.26 nm assigned to the PdO (002) or PdO (101)^{24,25}.

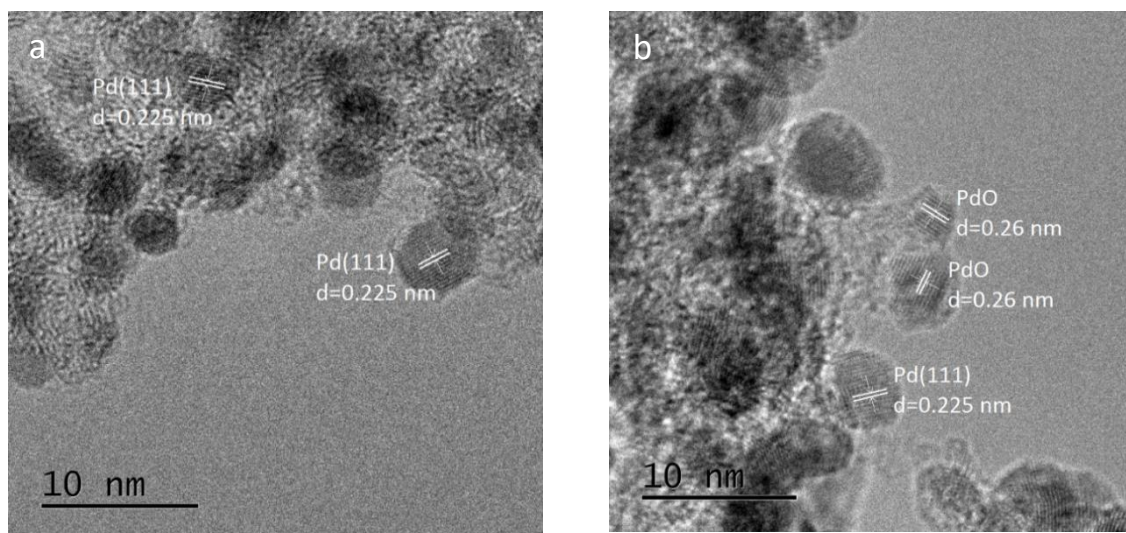


Figure 94. HRTEM image of the calcined catalysts at (a) 200, and (b) 250 C. Magnification: $\times 600k$.

Calcination is typically the last step of preparation methods to stabilise the material and remove impurities, however, for this catalyst, it negatively influenced the activity to a large

extent by slightly increasing the particle size and, without a doubt, oxidising the metal nanoparticles, which is seen as the main reason for the detrimental effect in activity. For the catalyst calcined at 250 °C, less than 15 % of the metal on the surface is in metallic state and the catalyst activity drops consequently. A conclusion from this is that metallic Pd is the active site for formic acid decomposition although it is still not totally clear if Pd^{II} is also an active site to some extent. Nevertheless, even if Pd^{II} plays an active role in formic acid decomposition, as observed in this last experiment, the activity drops dramatically therefore, only Pd⁰ will be treated as active site and the effect of Pd^{II} as the active site can be neglected.

3.3. Conclusions

In this chapter, a commercial Pd/C catalyst was used as a reference and starting point for the optimisation of reaction conditions of formic acid decomposition in aqueous solution as a model reaction for the production of hydrogen. The first part of the systematic study led to finding the optimal parameters which produce a kinetically limited reaction opposite to a reaction limited by mass transfer. A substrate/metal molar ratio of 2000:1 and 750 rpm stirring speed was found to be these optimised parameters. Under these conditions, a concentration of formic acid of 0.5 M, and 30 °C, an initial TOF of 1136 h⁻¹ was measured. Through the study of the effect of temperature, apparent activation energy was calculated to be 39.0 kJ/mol, being this, one of the lowest values reported for HCOOH decomposition on a heterogeneous catalyst.

Once the reaction was studied, a reusability test showed a slight decrease in catalyst activity. After the fifth consecutive run, 72 % of its original conversion was maintained. This result was promising but further analysis was required to find out the reason for this decrease. Leaching of Pd from the support was first rejected. Afterwards, gas analysis revealed that only 4-5 ppm of CO was released, which is within the permitted range and does not affect catalyst activity in a noticeable manner.

Characterisation of the fresh and used catalysts after liquid-phase formic acid decomposition was then performed in order to establish a structure/activity relationship and try to find the reason for the deactivation. XRD showed that both metallic and Pd^{II} were present on the catalyst and a crystallite size of 4.8 nm was obtained for the fresh catalyst. By means of XPS, the relative content of both species was measured and the reduction of Pd^{II} to metallic Pd

due to hydrogen evolution was quantified. The content of water was found to increase after using the catalyst. TEM showed a very small variation in particle size after using the catalyst (3.3 nm for the fresh and 3.7 nm for the used catalyst), therefore, the reduction in catalyst activity upon reaction with formic acid could not be addressed entirely to nanoparticles agglomeration. SEM-EDX confirmed the nominal loading of 5 wt. % Pd/C. BET surface area method showed the preservation of the pore structure and surface area for the used catalyst. TGA-MS was used to try to find the species or species adsorbed on the surface of the catalyst and its temperature of desorption. Water was found to be one of the possible species reducing the reusability of the catalyst since it remains adsorbed on the surface at temperatures higher than 100 °C probably due to the strong interactions of polar water molecules with the catalyst surface. The presence of water was in concordance with XPS results.

In order to improve reusability, an innovative method was developed using continuous flow set up. It was found that at 180 °C, most of the adsorbed species were desorbed and the active sites liberated. This way, the initial activity was almost completely restored. However, the long-term experiment showed that the catalyst was suffering either agglomeration or the stronger adsorption of species such as water, in concordance with TGA-MS; or a combination of both.

Kinetic Isotope Effect (KIE) was subsequently studied to investigate the elemental steps of the reaction and its main pathway. The results from KIE studies showed that the HCOOH dissociation follows two different paths: through carboxylic and formate intermediates, being the C–H bond cleavage the kinetically relevant step. Hence, formate decomposition seemed the most probable pathway.

Then, Density Functional Theory was performed to calculate the potential energy of each elementary step and its transition states on the most usual Pd(001), Pd(011) and Pd(111) surfaces. It was observed that the main causes of CO evolution even at low temperature are the presence of Pd(001), and cis configuration, and so, COOH* decomposition. These findings leave a door open to continue the investigation trying to design experimental methodologies that develop supported Pd nanoparticles exposed with more extent of (111) and (011) surfaces and whether possible, find experimental conditions that avoid COOH intermediate formation.

As a last experiment, a modification of the catalyst was performed to investigate the effect on formic acid decomposition. It was exposed to a calcination process and, even though the results did not enhance catalyst activity, it was confirmed that the most active species in the catalyst is Pd in metallic state rather than oxidised.

Liquid-phase formic acid decomposition has been studied and optimised with a commercial catalyst. Once a reference was established, preparation of new supported nanoparticles heterogeneous catalysts became the objective. The next chapter will be focused on the preparation and extensive study of Pd nanoparticles supported on carbon nanofibers for formic acid decomposition.

3.4. References

- 1 K. Tedsree, T. Li, S. Jones, C. W. A. Chan, K. M. K. Yu, P. a J. Bagot, E. a Marquis, G. D. W. Smith and S. C. E. Tsang, *Nat. Nanotechnol.*, 2011, **6**, 302–307.
- 2 C. Hu, J. K. Pulleri, S. W. Ting and K. Y. Chan, *Int. J. Hydrogen Energy*, 2014, **39**, 381–390.
- 3 A. K. Datye, J. Bravo, T. R. Nelson, P. Atanasova, M. Lyubovsky and L. Pfefferle, *Appl. Catal. A Gen.*, 2000, **198**, 179–196.
- 4 M. C. Militello and S. J. Simko, *Surf. Sci. Spectra*, 1994, **3**, 387–394.
- 5 M. C. Militello and S. J. Simko, *Surf. Sci. Spectra*, 1994, **3**, 395–401.
- 6 X. Wang, G. W. Qi, C. H. Tan, Y. P. Li, J. Guo, X. J. Pang and S. Y. Zhang, *Int. J. Hydrogen Energy*, 2014, **39**, 837–843.
- 7 K. Pattamakomsan, K. Suriye, S. Dokjampa and N. Mongkolsiri, *Catal. Commun.*, 2010, **11**, 311–316.
- 8 Y. Zhao, L. Jia, J. A. Medrano, J. R. H. Ross and L. Lefferts, *ACS Catal.*, 2013, **3**, 2341–2352.
- 9 R. F. Bueres, E. Asedegbega-Nieto, E. Diaz, S. Ordonez and F. V. Diez, *Catal. Today*, 2010, **150**, 16–21.
- 10 F. Y. Xie, W. G. Xie, L. Gong, W. H. Zhang, S. H. Chen, Q. Z. Zhang and J. Chen, *Surf. Interface Anal.*, 2010, **42**, 1514–1518.
- 11 D. A. Shirley, *Phys. Rev. B*, 1972, **5**, 4709–4714.
- 12 R. Arrigo, M. Havecker, S. Wrabetz, R. Blume, M. Lerch, J. McGregor, E. P. J. Parrott, J. A. Zeitler, L. F. Gladden, A. Knop-Gericke, R. Schlogl and D. S. Su, *J. Am. Chem. Soc.*, 2010, **132**, 9616–9630.
- 13 O. Baghriche, S. Rtimi, C. Pulgarin, C. Roussel and J. Kiwi, *Appl. Catal. B Environ.*, 2013, **130–131**, 65–72.
- 14 B. P. Payne, M. C. Biesinger and N. S. McIntyre, *J. Electron Spectros. Relat. Phenomena*, 2009, **175**, 55–65.
- 15 L. R. S. Lara, A. D. Zottis, W. C. Elias, D. Faggion, C. E. Maduro de Campos, J. J. S. Acuña and J. B. Domingos, *RSC Adv.*, 2015, **5**, 8289–8296.
- 16 J. Germain, J. M. J. Fréchet and F. Svec, *J. Mater. Chem.*, 2007, **17**, 4989–4997.
- 17 M. J. Thornton and G. S. Walker, *Xinxing Tan Cailiao/ New Carbon Mater.*, 2009, **24**, 251–259.
- 18 W. Suprun, M. Lutecki and H. Papp, *Chem. Eng. Technol.*, 2011, **34**, 134–139.
- 19 M. Ojeda and E. Iglesia, *Angew. Chemie - Int. Ed.*, 2009, **48**, 4800–4803.
- 20 G. V. A. Martins, G. Berlier, C. Bisio, S. Coluccia, H. O. Pastore and L. Marchese, *J. Phys. Chem.*

- C, 2008, **112**, 7193–7200.
- 21 U.S. Secretary of Commerce, NIST - Gas Phase Heat Capacity (Shomate Equation), <https://webbook.nist.gov/cgi/cbook.cgi?ID=C7732185&Type=JANAFG&Plot=on>.
- 22 U.S. Secretary of Commerce, NIST - IR spectra, <https://webbook.nist.gov/cgi/cbook.cgi?ID=C7732185&Type=IR-SPEC&Index=0#IR-SPEC>.
- 23 L. Prati and A. Villa, *Catalysts*, 2012, **2**, 24–37.
- 24 C. J. Huang, F. M. Pan, T. C. Tzeng, C. Li and J. T. Sheu, *J. Electrochem. Soc.*, 2009, **156**, J28–J31.
- 25 S. Penner, D. Wang, B. Jenewein, H. Gabasch, B. Klötzer, A. Knop-Gericke, R. Schlögl and K. Hayek, *J. Chem. Phys.*, 2006, **125**, 094703.

4. CATALYTIC INVESTIGATION OF SUPPORTED PD NANOPARTICLES ON FUNCTIONALISED CARBON NANOFIBERS: EFFECT OF FUNCTIONALISATION, HEAT TREATMENT AND PREPARATION METHOD

4.1. Introduction

Liquid-phase formic acid decomposition has already been evaluated using a commercial catalyst as a reference to optimise the reaction conditions in batch. Its reusability in continuous flow reactor showed a very promising result. The most probable pathway followed by the reaction was found and, Density Functional Theory calculations provided more information about the energetics of each elementary step. The commercial catalyst was thoroughly characterised using a series of bulk and surface-specific techniques and a structure/activity relationship was established.

As previously commented, even slight modifications on the catalyst surface or bulk, have a crucial impact on the catalyst activity, therefore, understanding how these changes affect the activity is paramount in order to design an active, efficient, reusable and economically profitable catalyst. These four parameters will become the focus of attention in the next chapters of this Thesis.

In Chapter 2, section 2.1.2, carbon nanofibers (CNFs) were introduced and the advantages of these supports against other materials were given. This chapter presents the effect on the catalytic activity of Pd nanoparticles supported on different types of CNFs in the catalytic aqueous formic acid decomposition. A variety of CNFs was used as previously introduced:

- (1) Pyrolytically stripped (PS-CNF)
- (2) Low heat treated (LHT-CNF)
- (3) High heat treated (HHT-CNF)
- (4) N-functionalised (N-PS-CNF)
- (5) O-functionalised (O-PS-CNF)

Within this series of supports, there are three different graphitisation degrees (PS, LHT and HHT) and two different functionalisation: oxygen and nitrogen. From the one side, the

purpose of the graphitisation treatment is the induction of a gradual regularisation of the carbon structure.¹ From the other side, the purpose of the functionalisation with oxygen and nitrogen is to modify the electrostatic interactions with the support and stabilise the supported metal nanoparticles. The addition of oxygen-containing surface groups oxidises the catalyst surface and creates reactive carboxylic acid and ether-type acid sites.² Further functionalisation with ammonia, as explained in Chapter 2, produces the exchange of most of the oxygen-containing groups to nitrogen-containing surface groups which enhance the basic strength of the active sites. Furthermore, functionalisation of carbon nanofibers makes possible the control of the surface chemistry by modifying wettability. Surface oxygen groups can exhibit some degree of hydrophilic character while nitro groups enhance the hydrophobic nature of the carbon nanofibers.²

The goals were, therefore, to study the effect of the carbon nanofibers graphitisation degree and the effect of the oxygen and nitrogen functionalities in terms of catalytic performance.

The influence of two preparation methods for each of those catalysts was investigated as well. The synthesis techniques selected were sol immobilisation (using polyvinyl alcohol (PVA) as stabiliser and NaBH_4 as reducing agent) and impregnation, following the guidelines presented in Chapter 2, section 2.1.2.

In summary, five types of nanofibers and two preparation methods make up to a total of ten different catalysts to be studied in this chapter.

In the previous chapter, 5 wt. % Pd/C catalyst was used as a reference to find the optimised conditions of liquid-phase formic acid decomposition. Those conditions were used as a starting point in this chapter to evaluate the activity of each catalyst. The next natural step would be to optimise the conditions of liquid-phase formic acid decomposition using these catalysts, however, since performing this series of experiments in a batch of ten catalysts in a timely manner would be prohibitive, the two most active catalysts were chosen for an extensive study of the reaction conditions. The procedure followed to optimise the reaction conditions was identical to that used in the previous chapter: a set of reaction parameters such as substrate/metal molar ratio, stirrer speed, temperature and concentration of formic acid were varied in order to find the conditions where the reaction is kinetically limited and find the apparent activation energy and order of reaction.

Fresh and used catalysts were thoroughly characterised by means of X-ray diffraction (XRD), X-ray photoelectron spectroscopy (XPS), transmission electron microscopy (TEM), scanning electron microscopy (SEM) with energy dispersive X-ray (EDX), Brunauer-Emmett-Teller (BET) surface area analysis and, in the case of the functionalised carbon nanofibers, Ammonia - Temperature Programmed Desorption (NH₃-TPD).

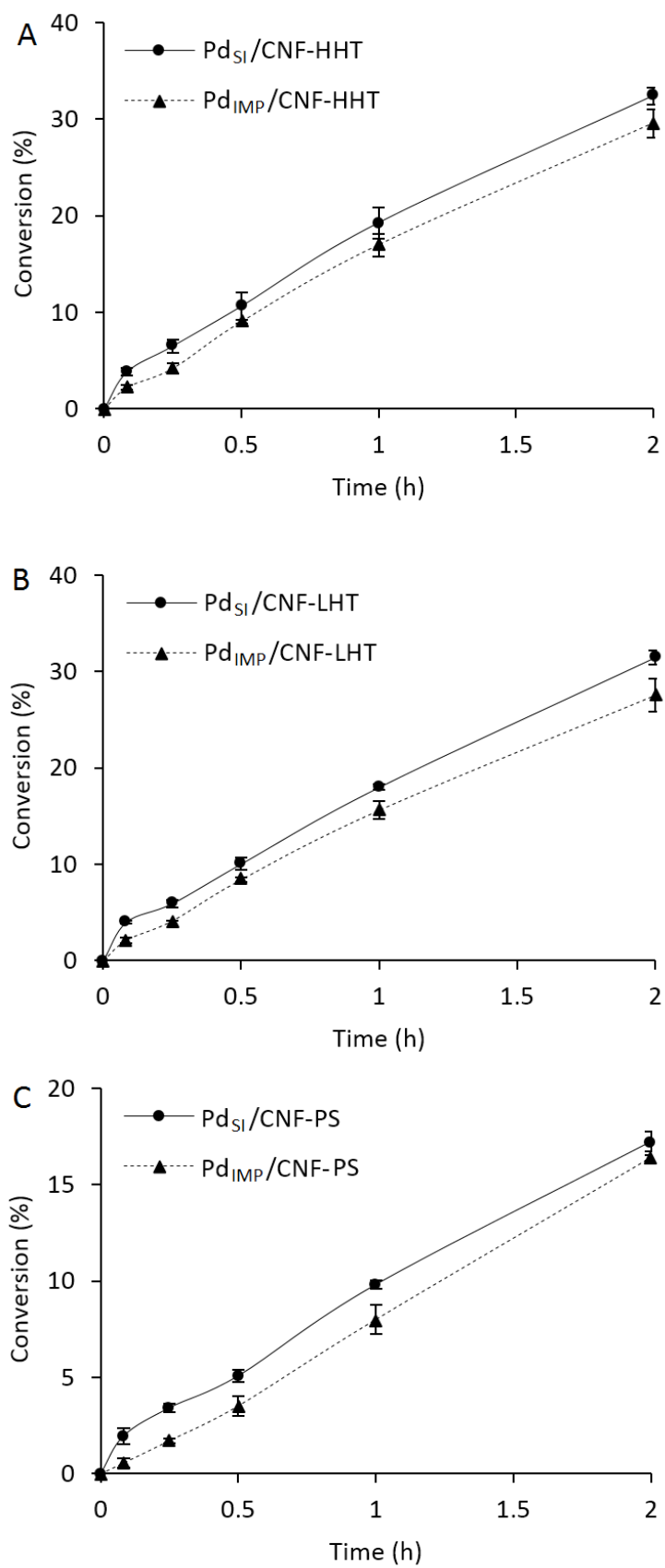
4.2. Results and discussion

Every initial comment introduced in Chapter 3 regarding the experimental procedure is applied here as well: same experimental protocol in terms of analytical techniques and experimental conditions are used. As a brief summary, samples were withdrawn periodically as per the procedure presented in the experimental chapter and HPLC was used to analyse the concentration of formic acid remaining in solution. The initial rate of reaction is considered as the conversion at $t = 5$ min divided by time. Reactions were run for 2 hours.

4.2.1. Initial catalytic activity screening of the Pd/CNF series catalysts for liquid-phase formic acid decomposition

The first step in this study was a preliminary activity screening under the optimised conditions found in Chapter 3: substrate/metal molar ratio 2000:1, 750 rpm, 30 °C and 0.5 M formic acid. This way, an initial structure/activity relationship could be presented and subsequently confirmed or rejected according to the characterisation results. Due to the nature of the experiment and the catalysts selected, three different parameters have been evaluated: preparation method, degree of graphitisation and functionalisation.

Figure 95 displays the comparison of the effect of the preparation methods (sol-immobilisation and impregnation as presented in Chapter 2, section 2.1.2) in the catalytic performance of 1 wt. % Pd/CNFs with different graphitisation degree (A to C) and functionalisation (D and E).



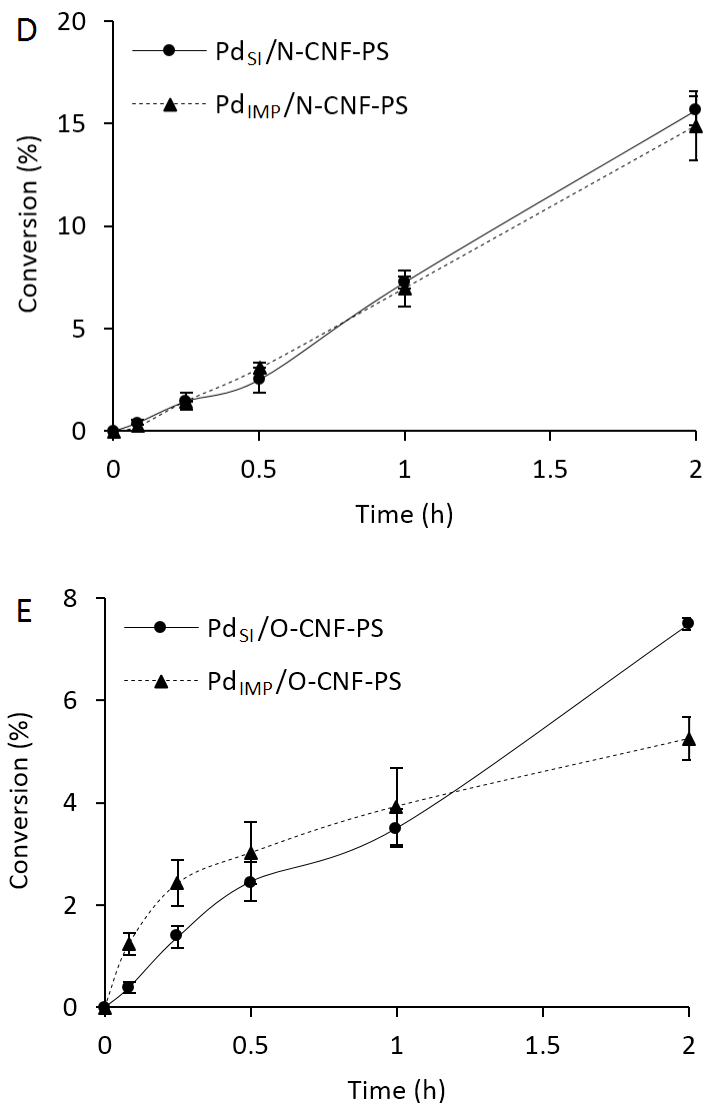


Figure 95. Conversion versus time plot for the comparison of preparation method for Pd/CNFs with different graphitisation degree (A, B and C) and functionalisation (D and E). Reaction conditions: 30 °C, 26.5 mg of catalyst (substrate/metal molar ratio: 2000:1), 0.5 M HCOOH, 750 rpm, 2 h reaction time.

Besides the graphical comparison, the TOFs obtained for the whole series are presented in table 20.

As observed in the conversion versus time plots, a slightly higher conversion was generally achieved by the catalysts prepared by sol-immobilisation method compared with the catalysts prepared by the impregnation method. The out-of-trend result observed on the catalyst supported on O-CNF-PS will be commented in the next paragraph. TOFs presented in table 20 indicated a significant difference between the two preparation methods for each group of catalysts, although, after 2 hours of reaction, as observed in figure 95, the four pairs of catalysts (excluding O-CNF-PS) led to similar final conversion.

Table 20. Catalytic activity of the Pd/CNFs catalysts series for the liquid-phase formic acid decomposition.

Catalyst	TOF (h ⁻¹)
Pd _{IMP} /CNF-HHT	563.2
Pd _{IMP} /CNF-LHT	527.5
Pd _{IMP} /CNF-PS	136.3
Pd _{IMP} /N-CNF-PS	53.5
Pd _{IMP} /O-CNF-PS	279.4
Pd _{SI} /CNF-HHT	979.1
Pd _{SI} /CNF-LHT	965.2
Pd _{SI} /CNF-PS	484.4
Pd _{SI} /N-CNF-PS	99.8
Pd _{SI} /O-CNF-PS	90.2

Prior to further characterisation of the catalysts, this trend can be explained due to the presence of polyvinyl alcohol (PVA) during the preparation method by sol-immobilisation: PVA may bond to the carbon surface creating hydroxyl groups (C-O-H) that might occupy active sites and lead to a slightly faster deactivation than the catalysts prepared by impregnation method. This idea was analysed using characterisation techniques as presented next in this chapter.

The inversion observed on the O-CNF-PS supported materials in which during the first hour of reaction impregnated samples reached a slightly higher conversion, can be explained because during the preparation of 1 wt. % Pd_{SI}/O-CNF-PS catalyst, especially entangled nanofibers were formed causing the creation of flakes which took several minutes to homogeneously distribute the nanofibers within the reactor, producing, therefore, a mass transfer limitation and so, the induction time-like trend observed during the reaction. Once the flakes were broken down and the nanoparticles distributed along the reactor, catalyst activity rapidly increased. However, every effort to manually break the flakes before the reaction was unsuccessful due to the strong electrostatic interaction between the nanofibers.

Figure 96 presents the catalytic activities of the catalysts series by impregnation (A) and sol-immobilisation (B).

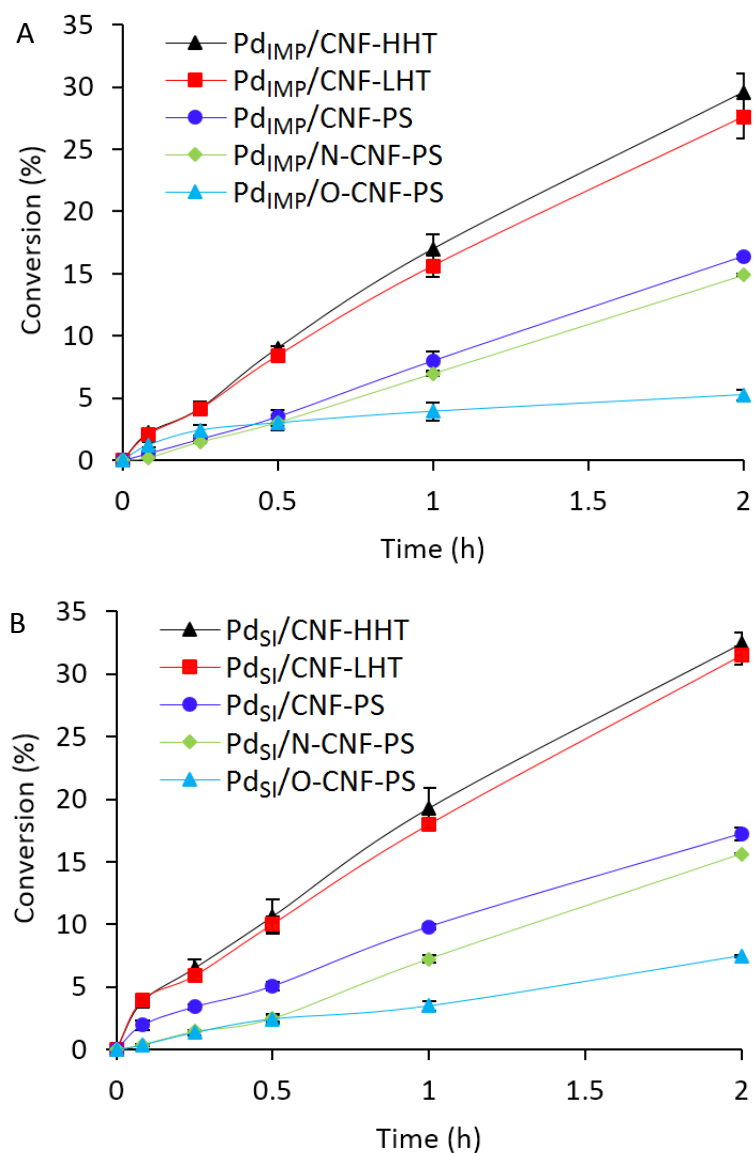


Figure 96. Conversion versus time plot for the comparison of support graphitisation degree and functionalisation. Reaction conditions: 30 °C, 26.5 mg of catalyst (substrate/metal molar ratio: 2000:1), 0.5 M HCOOH, 750 rpm, 2 h reaction time.

As observed, catalytic activities were strongly dependent on the support. Among the three grades tested (different graphitisation degree), in terms of TOF, CNF-HHT was the most effective support while CNF-PS was the least effective, being CNF-LHT very close to CNF-HHT. Hence, the catalytic performance of the samples significantly increased with annealing temperature. In order to find a scientific reason for this result, it is necessary to state that, even though carbon graphitises at approximately 2000 °C, structural order already increases at 1500 °C.³ Oberlin and co-workers observed that graphitic domains appear at 1000-2000 °C, forming graphene layers when increasing the temperature.⁴ It means that in CNF-LHT the

order of the outer layer improves compared with CNF-PS. This structural rearrangement affects catalyst activity. The higher activity was correlated then, to a lower number of structural defects. This might lead to Pd particles anchoring more strongly to the more ordered graphite edges.

On the other hand, when comparing the functionalisation, for the impregnated samples, the catalyst supported on oxygen-functionalised CNF showed higher activity (279.4 h^{-1}) than both pristine CNF-PS (136.3 h^{-1}) and nitrogen-functionalised catalyst (53.5 h^{-1}), whereas for the sol-immobilisation procedure, both pristine CNF-PS (484.4 h^{-1}) and nitrogen-functionalised catalyst (99.8 h^{-1}) presented higher activity than oxygen-functionalised CNF (90.2 h^{-1}) since the big flakes formed during the sol-immobilisation caused a mass transfer limitation as previously commented. Consequently, TOF of $\text{Pd}_{\text{SI}}/\text{O-CNF-PS}$ catalyst should not be compared with the remaining TOFs of the catalyst series.

For the impregnated samples, the increase of TOF for the oxygen-containing CNF could be addressed to a favoured deprotonation step during formic acid decomposition due to the presence of O^- on the surface, which can lead to an easier dehydrogenation of formic acid. However, as observed in figure 95E, deactivation of the catalyst was occurring after 30 minutes of reaction. Oxygen on the catalyst surface from the functionalisation may react with the carbon surface producing concomitant CO as a result, thus, offering a possible explanation for the quick deactivation of the catalyst.

Introducing basic functionalities as nitrogen in the support did not enhance the catalytic activity of the catalyst.

The reason for the observed trends and subsequent structure/activity relationship will be provided by means of extensive catalyst characterisation of the whole series in a following section. Nevertheless, before performing the characterisation techniques, as previously stated, the two most active catalysts in this preliminary screening ($\text{Pd}_{\text{SI}}/\text{CNF-HHT}$ and $\text{Pd}_{\text{IMP}}/\text{CNF-HHT}$) were used for an in-depth study of the reaction conditions similar to the study presented in Chapter 3.

4.2.2. Reaction conditions optimisation for additive-free liquid-phase formic acid decomposition

Even though the previous screening was performed at the optimised conditions provided by the commercial 5 wt. % Pd/C, it was also necessary to perform these studies using Pd_{SI}/CNF-HHT and Pd_{IMP}/CNF-HHT in order to find any possible changes in the experimental conditions due to different metal/support interactions. For this purpose, the optimisation of the reaction conditions followed the same procedure as in the previous chapter. A set of reaction parameters were varied in order to find the conditions at which the reaction is kinetically limited and find the apparent activation energy and order of reaction.

The first step was to confirm that, at the conditions of the experiment, the reaction is kinetically limited, then, the effect of catalyst mass (substrate/metal molar ratio) was investigated at 30 °C, stirring rate of 750 rpm and 2 h reaction time. Figure 97 displays the effect of the mass of catalyst on conversion and TOF.

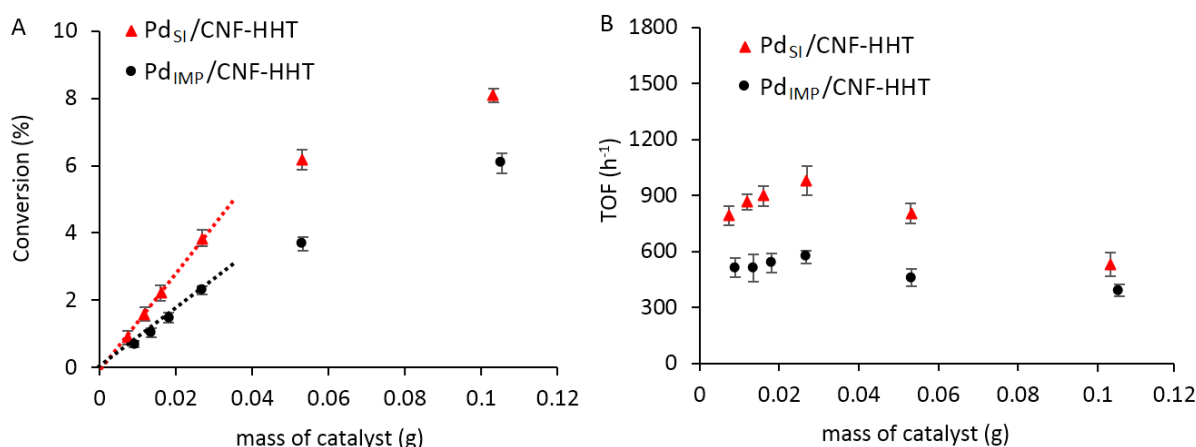


Figure 97. Effect of catalyst mass on (A) Conversion of formic acid dehydrogenation, (B) TOF. Reaction conditions: 30 °C, 0.5 M HCOOH, 750 rpm, 2 h reaction time.

In this study, a formic acid/metal molar ratio in the range 500:1-6000:1, equivalent to 106-9 mg of catalyst respectively, was studied. As observed, two reaction regimes were identified for each catalyst. As with the commercial catalyst, in the range of substrate/metal molar ratio between 2000:1-6000:1 (26.5-9 mg), dotted lines, the initial conversion was proportionally dependant to the amount of catalyst, and so, the reaction was kinetically limited. Turnover frequency (TOF) remained constant in that range confirming that the reaction was kinetically

limited. By increasing the catalyst mass above 26.5 mg, a decrease in TOF was observed, indicating that diffusion limitations were present. Hence, a catalyst mass of 26.5 mg was selected as the standard value in subsequent experiments.

Stirring rate was also investigated to find the optimal value which avoids diffusion limitations without compromising reproducibility. Figure 98 displays the initial TOF compared against different stirring rates.

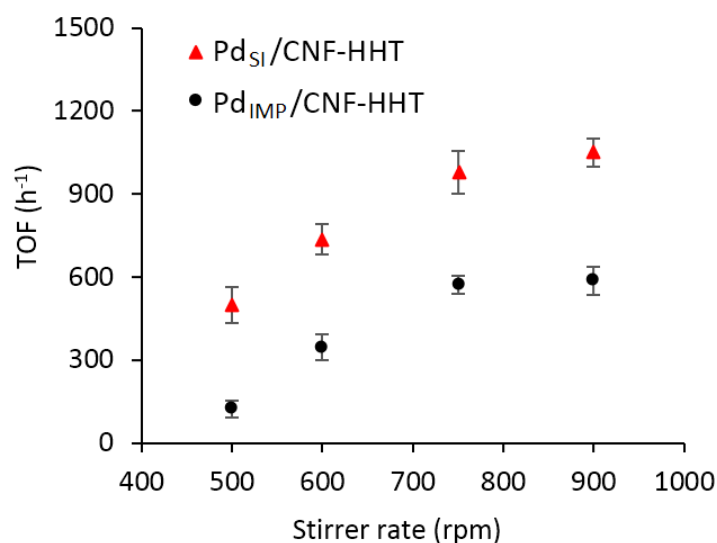


Figure 98. Effect of stirrer rate on TOF. Reaction conditions: 26.5 mg of catalyst (substrate/metal molar ratio: 2000:1), 30 °C, 0.5 M HCOOH, 2 h reaction time.

A range between 500 and 900 rpm was studied. As observed, increasing the stirring rate from 500 rpm (TOF 123 h⁻¹ for Pd_{IMP}/CNF-HHT and TOF 500 h⁻¹ for Pd_{SI}/CNF-HHT) to 750 rpm (TOF 572 h⁻¹ for Pd_{IMP}/CNF-HHT and TOF 979 h⁻¹ for Pd_{SI}/CNF-HHT), a substantial increment was observed in TOF due to the enhancement of the contact and collision between the reactant and the solid catalyst, therefore, it means that mass transfer was limiting the reaction. Above 750 rpm, TOF values increased very slightly indicating that the stirrer rate had a minor effect, and thus, confirming the reaction was in kinetic regime. For the same reason explained in the previous chapter, 750 rpm was selected as the optimised value for the subsequent studies. As presented, the conditions in which the reaction was kinetically limited were identical to those found for the commercial catalyst in the previous chapter. Extrapolating to the whole series of catalysts, this means that the initial screening was in kinetic conditions and therefore, the activity values obtained were reliable.

The next parameter to investigate was the effect of temperature and activation energy. Five reactions were performed in the range of temperature from 30 to 60 °C and also, further increase of temperature was not investigated since, besides the necessity of fuel cells in portable devices to operate at mild conditions, CO was reported to evolve above 50 °C.⁵ As expected, conversion of formic acid was enhanced when rising the temperature, however, the important information from this study is the activation energy. It was calculated by the slope of the Arrhenius plot presented in figure 99 and by proceeding as explained in Chapter 3, the values were 27.5 kJ mol⁻¹ and 26.2 kJ mol⁻¹ for Pd_{IMP}/CNF-HHT and Pd_{SI}/CNF-HHT respectively which is an improvement compared with the commercial catalyst.

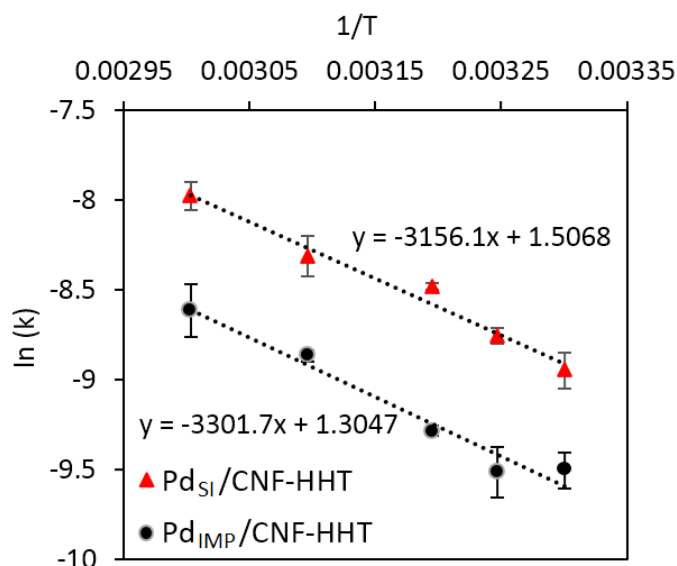


Figure 99. Arrhenius plot. Range 30-60 °C. Reaction conditions: 26.5 mg of catalyst (substrate/metal molar ratio: 2000:1), 0.5 M HCOOH, 750 rpm, 2 h reaction time.

The effect of formic acid concentration and therefore, the apparent kinetic order of the reaction was the last step in this study. Figure 100 presents the plot of reaction rate versus concentration of formic acid in the range 0.1-1 M.

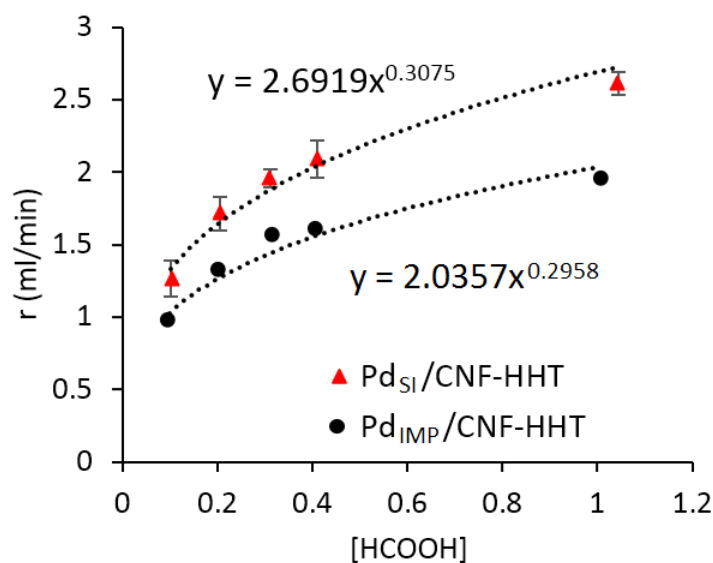


Figure 100. Rate versus concentration of formic acid. Reaction conditions: 26.5 mg of catalyst (Substrate/metal molar ratio: 2000:1), 30 °C, 750 rpm, 2 h reaction time.

By fitting to the power-law equation model, apparent reaction orders of 0.30 and 0.31 with respect to formic acid for Pd_{IMP}/CNF-HHT and Pd_{SI}/CNF-HHT respectively were obtained.

In summary, at the optimised reaction conditions of substrate/metal molar ratio of 2000:1 and 750 rpm, formic acid concentration of 0.5 M and 30 °C, initial TOFs of 979 h⁻¹ for Pd_{SI}/CNF-HHT, and 572 h⁻¹ for Pd_{IMP}/CNF-HHT were obtained. Remarkably, 1 wt. % Pd_{SI}/CNF-HHT showed a high catalytic activity very close to the commercial catalyst. These values were significantly promising for supported Pd nanoparticles on carbon nanofibers. Moreover, in comparison with other representative heterogeneous catalysts studied in liquid-phase formic acid dehydrogenation (Chapter 1, table 5), this as-synthesised catalyst was among the best catalysts up to date in terms of activity.

4.2.3. Reusability tests

Catalyst stability was also studied with the two most active catalysts (Pd_{IMP}/CNF-HHT and Pd_{SI}/CNF-HHT) for five subsequent catalytic cycles as explained in Chapter 2, section 2.4. The method used with these catalysts differs from the technique used with the commercial catalyst since then the amount of catalyst required was not a challenge. As a summary, in this case, after 2 hours of reaction, a liquid sample was analysed by HPLC to quantify the remaining

formic acid, and the necessary amount of pure formic acid to reach the initial concentration of 0.5 M was calculated and added into the reactor. As shown in figure 101, the as-synthesised catalysts exhibit a certain loss of activity within every use, more significant for Pd_{IMP}/CNF-HHT. This decrease in catalytic activity may be attributed to the same possible factors as in Chapter 3: (i) decrease of percentage of atomic Pd on the surface by leaching or migration from the outer wall to the inner wall of the nanofiber, (ii) poisoning from CO, (iii) agglomeration of Pd nanoparticles, (iv) adsorption of species (reactant/products) on the surface of the catalyst occupying active sites.

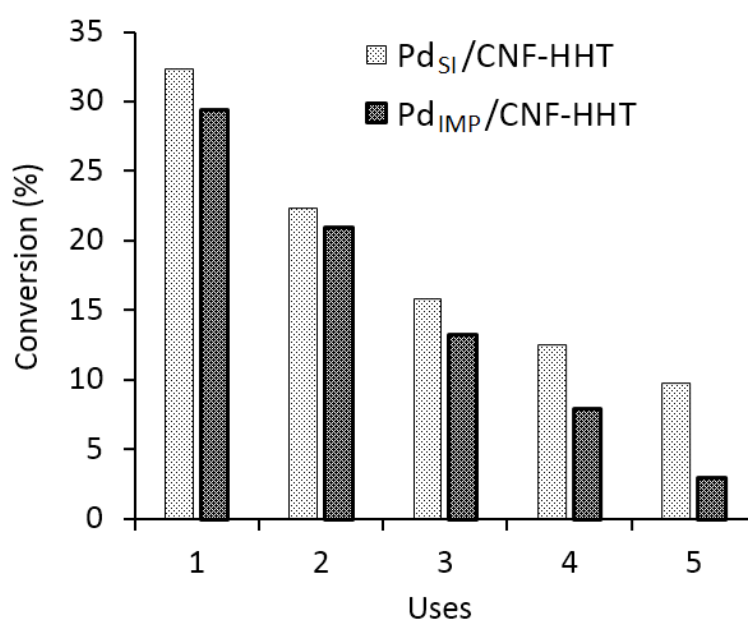


Figure 101. Reusability Pd/CNF-HHT catalysts prepared by sol-immobilisation and impregnation after five cycles of reaction. Formic acid was added after 2 h of reaction. Reaction conditions: 26.5 mg of catalyst (substrate/metal molar ratio: 2000:1), 30 °C, 750 rpm.

In order to quantify the leaching of Pd from the catalysts, previously, MP-AES was performed on the liquid samples after reusability. It is a quick and inexpensive method, however, the quantification of Pd did not present the best accuracy. Considering this, ICP-MS (Inductively Coupled Plasma Mass Spectrometry) was selected instead. ICP-MS of the filtered solution after the five cycles of the reusability test was performed. For Pd_{IMP}/CNF-HHT, 0.034 ppm (0.12 % of initial Pd amount) of Pd were detected while, for Pd_{SI}/CNF-HHT, 0.014 ppm (0.05 % of initial Pd amount) were found. Thus, leaching of Pd from the catalyst is negligible.

Similarly, the evolved gases were analysed to provide information about possible concomitant CO formation and thus, poisoning of the catalyst.

4.2.4. Analysis of evolved gases

By using the water displacement method, gases evolved from liquid-phase formic acid decomposition were quantified by GC with methanator for carbon monoxide and carbon dioxide; and MS for hydrogen and carbon dioxide.

CO₂ concentration was in the range between 50000 and 60000 ppm for both Pd_{IMP}/CNF-HHT and Pd_{SI}/CNF-HHT while, 15 and 11 ppm of CO were obtained for Pd_{IMP}/CNF-HHT and Pd_{SI}/CNF-HHT respectively (selectivity > 99.95 %). As observed, very low CO concentration was produced by both preparation methods, with the lowest level of CO production being observed for the catalyst prepared by the colloidal method. Therefore, CO evolution was within the limit of 20 ppm established for PEM fuel cells. Selectivity toward hydrogen was higher than 99.99 %, confirming that the reaction mainly followed the dehydrogenation route. H₂/CO₂ ratios were calculated to be between 0.94 and 1.09.

A further step was given in the analysis of gases. Quantification of CO was also performed to reactions carried out at different temperatures in order to elucidate the effect of this parameter on CO evolution and confirm the data reported by Tsang *et al.*⁵ In that article, a substantial increment of CO concentration was produced when increasing reaction temperature. Table 21 presents the results obtained in this study.

Table 21. CO concentration evolved from liquid-phase formic acid decomposition performed at different temperatures.

Temperature	Catalyst	CO (ppm)	CO/CO ₂ ratio
30	Pd _{IMP} /CNF-HHT	15	0.00026
	Pd _{SI} / CNF-HHT	11	0.00018
40	Pd _{IMP} /CNF-HHT	29	0.00074
	Pd _{SI} / CNF-HHT	48	0.00068
70	Pd _{IMP} /CNF-HHT	876	0.00362
	Pd _{SI} / CNF-HHT	415	0.00619

As expected, CO concentration is intimately related to reaction temperature. An increment of 10 °C from the standard experimental conditions made these catalysts not suitable for PEM fuel cells and, further increment to 70 °C, reached dangerous limits for human beings. Typically, 50 ppm is the maximum permissible exposure in the workplace, and 1000 ppm can produce loss of consciousness after 1 hour of exposure.⁶ These values cannot be compared with the values experimentally obtained since the gas was collected in a closed system, although it is an important guide to follow and consider when this technology is implemented. From the DFT results, it was observed that carboxylic pathway was the pathway leading to CO evolution and mainly in the Pd(001) surface. More research is then needed in this topic to try to maximise the Pd(011) and Pd(111) surfaces to reduce the impact of temperature on CO evolution. Additional information for future steps will be provided in Chapter 6.

At 30 °C however, CO poisoning can be neglected (< 20 ppm) and thus, absorption of formic acid or intermediates on the surface, migration of Pd nanoparticles to the inner wall, and/or agglomeration seemed to be the most probable reasons for the drop in catalytic activity during the reusability test.

The reason for the differences in catalytic activity was studied by means of characterisation techniques in order to find structure/activity relationship.

4.2.5. Catalyst Characterisation

An extensive characterisation of the series of fresh and used catalysts was performed. As previously commented, particle size distribution, surface area and oxidation state of the metal were the main focus of this characterisation. With this objective in mind, X-ray diffraction, X-ray photoelectron spectroscopy, transmission and scanning electron microscopy, BET surface area and ammonia temperature-programmed desorption analyses were performed.

4.2.5.1. X-ray Diffraction

XRD patterns of the fresh series of catalysts in displayed in figure 102.

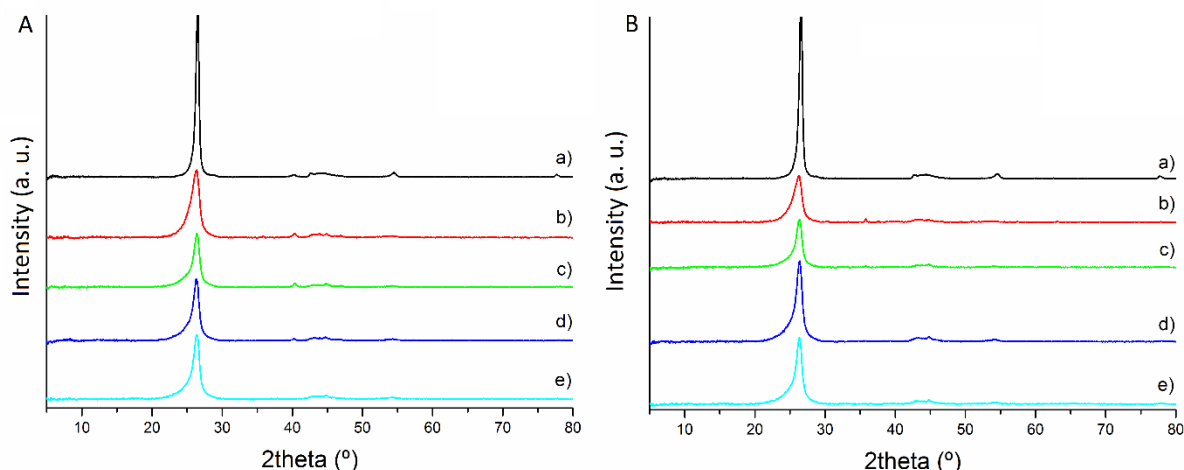


Figure 102. XRD patterns of fresh Pd/CNF (A) Catalyst synthesised by impregnation: (a) Pd_{IMP}/CNF-HHT, (b) Pd_{IMP}/CNF-LHT, (c) Pd_{IMP}/CNF-PS, (d) Pd_{IMP}/N-CNF-PS, (e) Pd_{IMP}/O-CNF-PS. (B) Catalysts synthesised by sol-immobilisation: (a) Pd_{SI}/CNF-HHT, (b) Pd_{SI}/CNF-LHT, (c) Pd_{SI}/CNF-PS, (d) Pd_{SI}/N-CNF-HHT, (e) Pd_{SI}/O-CNF-HHT.

At approximately 26° appears the most visible feature which is the diffraction peak assigned to the (002) plane, of graphitic carbon,³ being this peak more evident in the CNF-HHT samples. The intensity of this peak increases, probably due to the heat treatment applied to the support since high-temperature post-treatment remarkably enhances the graphitic character of carbon materials and so, the increase of the diffraction peak of graphitic carbon. This is in concordance with the initial idea that the order degree of the carbon layer present in CNF-PS increases when increasing the temperature.³ A more in-depth description for graphitisation degree will be given when explaining XPS and Raman results in a subsequent section.

In figure 103, the XRD patterns of the fresh series of catalysts are presented in more detail. The reflections at $2\theta = 40.4^\circ$, 44.9° and 68.3° (grey lines) are assigned to the characteristic planes (111), (200) and (220) of the face-centered cubic structure of Pd^{7,8} and are present only in the catalysts prepared by impregnation as it is evident from the XRD patterns. As explained in Chapter 3, a crystallite size of approximately 5 nm is the limit of XRD technique.⁹ In the previous chapter, crystallite size was slightly below the limit, however, the loading was high. In this case, with a nominal loading of 1 wt. %, no or very weak and broad diffraction peaks are present for the catalysts synthesised by the sol-immobilisation method. This suggests a crystallite size below 5 nm for these catalysts. Analysis by TEM was performed to confirm this hypothesis.

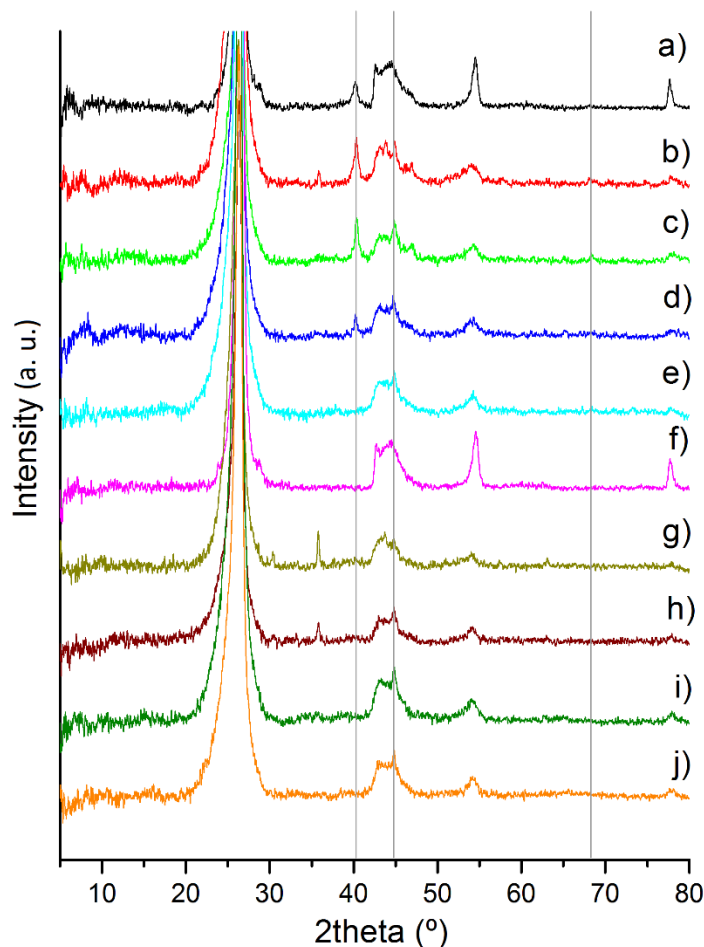


Figure 103. XRD patterns of fresh Pd/CNF materials (a) Pd_{IMP}/CNF-HHT, (b) Pd_{IMP}/CNF-LHT, (c) Pd_{IMP}/CNF-PS, (d) Pd_{IMP}/N-CNF-PS, (e) Pd_{IMP}/O-CNF-PS, (f) Pd_{SI}/CNF-HHT, (g) Pd_{SI}/CNF-LHT, (h) Pd_{SI}/CNF-PS, (i) Pd_{SI}/N-CNF-HHT, (j) Pd_{SI}/O-CNF-HHT. Grey lines: characteristic planes of face-centered cubic structure of Pd.

Between 42° and 46°, a broad band is observed. It is attributed to either (100) or (101) planes of C, however, since both hexagonal and rhombohedral graphite present diffraction peaks in this region, the attribution of each peak to its corresponding species is not straightforward.³ Two intense and sharp diffraction peaks at 54° and 78° are observed for both catalysts supported on CNF-HHT. The diffraction peak at 78° is assigned to the graphite (110) plane, therefore, the presence of rhombohedral graphite is confirmed.³ The attribution of the diffraction peak at 54° present some more difficulty since both graphite (004) and PdO (112) planes could be assigned to the same diffraction peak.^{3,7} XRD patterns of the bare supports were analysed in order to clarify this. Figure 104 presents the XRD patterns.

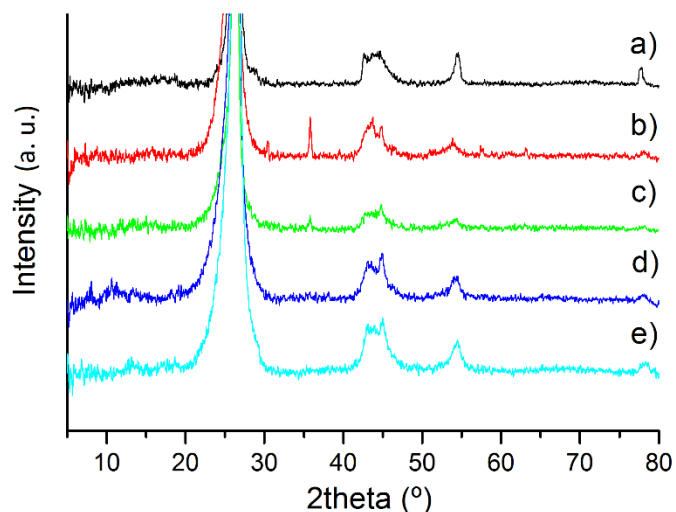


Figure 104. XRD patterns of the supports: (a) CNF-HHT, (b) CNF-LHT, (c) CNF-PS, (d) N-CNF-HHT, and (e) O-CNF-LHT.

A diffraction peak appears at 54° confirming, thus, the presence of graphite (004) plane since no Pd can be present in the sample, however, this peak shows a lower intensity compared with the XRD pattern of the catalysts. In that case, PdO (112) plane might be also present and overlaid by graphite (004) plane, therefore, indicating the presence of both.

XRD analysis of the used catalysts was performed as well. Figure 105 presents the XRD patterns. The main change observed is the appearance and increment of the reflections at $2\theta = 40.4^\circ$ and 44.9° assigned to (111) and (200) planes of Pd. As with the commercial catalyst, this change indicates the reduction of Pd^{II} to metallic Pd due to the hydrogen generation and subsequent reduction of Pd^{II} to Pd.

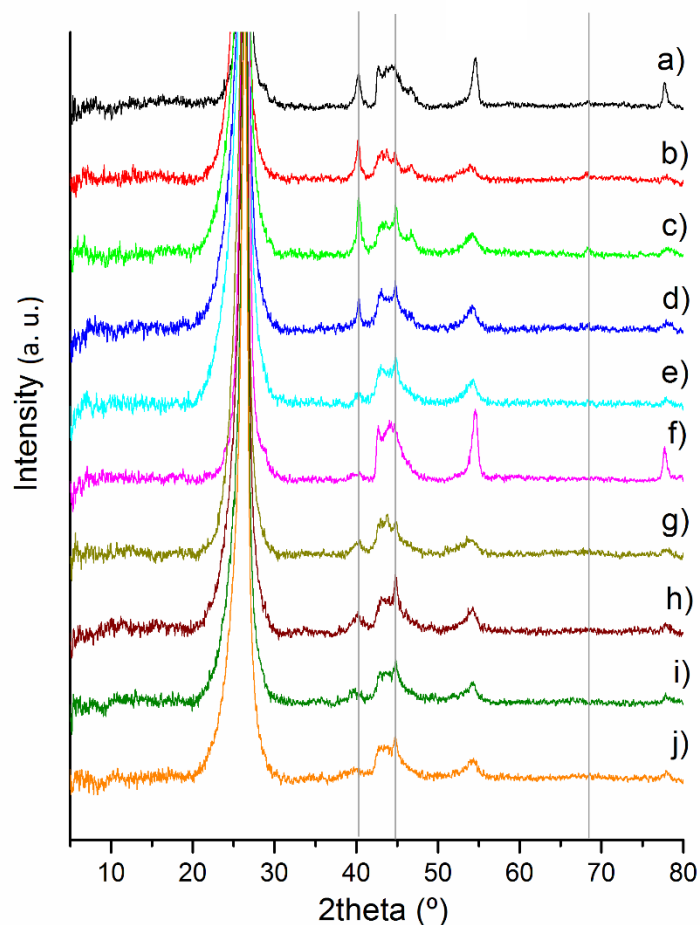


Figure 105. XRD patterns of used Pd/CNF (a) Pd_{IMP}/CNF-HHT, (b) Pd_{IMP}/CNF-LHT, (c) Pd_{IMP}/CNF-PS, (d) Pd_{IMP}/N-CNF-PS, (e) Pd_{IMP}/O-CNF-PS, (f) Pd_{SI}/CNF-HHT, (g) Pd_{SI}/CNF-LHT, (h) Pd_{SI}/CNF-PS, (i) Pd_{SI}/N-CNF-HHT, (j) Pd_{SI}/O-CNF-HHT.

As a summary, both Pd and, highly probable, PdO species were present in the fresh and used catalysts. Since the percentage of Pd on the surface and its composition are crucial, XPS was performed to confirm the presence and percentage of metallic Pd.

4.2.5.2. X-ray photoelectron spectroscopy (XPS)

XPS spectra of Pd 3d of the as-synthesised fresh catalysts for impregnation and sol-immobilisation methods are presented in figure 106.

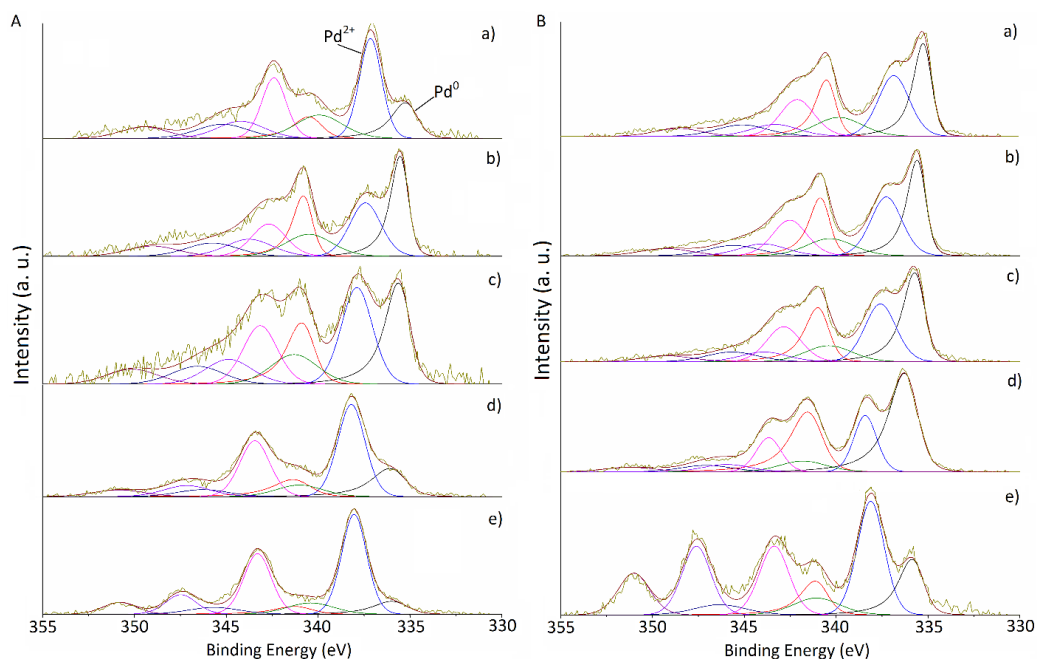


Figure 106. XPS spectra of fresh Pd/CNF (A) Catalyst synthesised by impregnation: (a) Pd_{IMP}/CNF-HHT, (b) Pd_{IMP}/CNF-LHT, (c) Pd_{IMP}/CNF-PS, (d) Pd_{IMP}/N-CNF-PS, (e) Pd_{IMP}/O-CNF-PS. (B) Catalysts synthesised by sol-immobilisation: (a) Pd_{SI}/CNF-HHT, (b) Pd_{SI}/CNF-LHT, (c) Pd_{SI}/CNF-PS, (d) Pd_{SI}/N-CNF-HHT, (e) Pd_{SI}/O-CNF-HHT.

Pd, N, O and Cl content and surface percentage of metallic Pd for both fresh and used series derived from XPS data are shown in table 22.

Table 22. Palladium content, (%) metallic Pd on the surface, N, O and Cl content from XPS

Catalyst	Pd content		(% Pd ⁰ on the surface)		N content		O content		Cl content	
	Fresh	Used	Fresh	Used	Fresh	Used	Fresh	Used	Fresh	Used
Pd _{IMP} /CNF-HHT	0.71	0.52	30.1	74.1	-	-	0.94	1.40	-	-
Pd _{IMP} /CNF-LHT	0.57	0.49	55.0	73.7	0.10	-	2.60	2.94	0.04	-
Pd _{IMP} /CNF-PS	0.40	0.23	45.1	61.2	0.71	0.19	2.94	6.34	0.06	-
Pd _{IMP} /N-CNF-PS	0.82	0.66	30.8	34.4	2.04	1.68	8.67	8.72	0.04	-
Pd _{IMP} /O-CNF-PS	0.75	0.59	15.0	33.0	0.91	0.78	12.05	11.93	0.04	-
Pd _{SI} /CNF-HHT	0.93	0.72	51.9	73.1	-	-	2.72	4.05	0.06	-
Pd _{SI} /CNF-LHT	1.44	0.98	53.1	69.8	0.12	-	4.49	3.49	0.05	-
Pd _{SI} /CNF-PS	0.90	0.04	53.7	84.9	0.66	-	5.07	18.23	0.05	-
Pd _{SI} /N-CNF-PS	1.27	0.81	70.0	67.7	2.06	1.48	10.53	8.91	0.07	-
Pd _{SI} /O-CNF-PS	0.69	0.45	32.1	51.4	0.76	0.95	14.36	15.57	0.07	-

The Pd $3d_{5/2}$ component at 335 eV approximately was attributed to metallic Pd and the component at approximately 337 eV, to Pd^{II} mainly present as PdO.^{10,11}

The catalysts prepared by impregnation method displayed in general a lower surface Pd atomic percentage than the samples prepared by sol-immobilisation. This feature is also seen in figure 106 in which the impregnated samples presented lower spectral intensities and a noisier signal. As previously commented, these atomic percentages are calculated on the surface of the catalysts, existing differences with those percentages calculated by EDX.¹² It was also observed that most of the catalysts prepared by sol-immobilisation presented a higher percentage of Pd⁰ species. This suggests that the presence of PVA ligand by partly covering Pd nanoparticles could inhibit the oxidation of the Pd surface due to ambient air. The higher atomic Pd percentage on the surface and higher content of metallic Pd could explain the higher activity observed for the catalysts synthesised by the colloidal method.

No trend was deduced for the variation of Pd content or percentage of metallic Pd due to modifications in morphology through heat treatment. Hence, the increment of the reaction rates with increasing the heat treatment is not directly related to modifications on the Pd content on the surface or composition of Pd.

As previously reported,¹³ functionalisation plays an important role in both the Pd⁰/Pd^{II} molar ratio and the metal content. Thus, nitrogen-functionalised CNF presents a higher Pd content when compared with oxygen-functionalised CNF. This increase in the Pd content can be possibly related to the higher degree of hydrophobic character in N-CNF-PS due to the amination process in contrast to the predominantly hydrophilic character in O-CNF-PS¹⁴. The oxygen-functionalised catalysts predominantly exhibited Pd²⁺ species as could be expected due to the treatment of pristine CNF with HNO₃. Furthermore, by using the colloidal method, a significant increase of Pd⁰ species by a factor of 2 was accomplished.

Analysis of the used samples was performed to identify any possible change in Pd content and composition. XPS analyses of used catalysts are presented in figure 107.

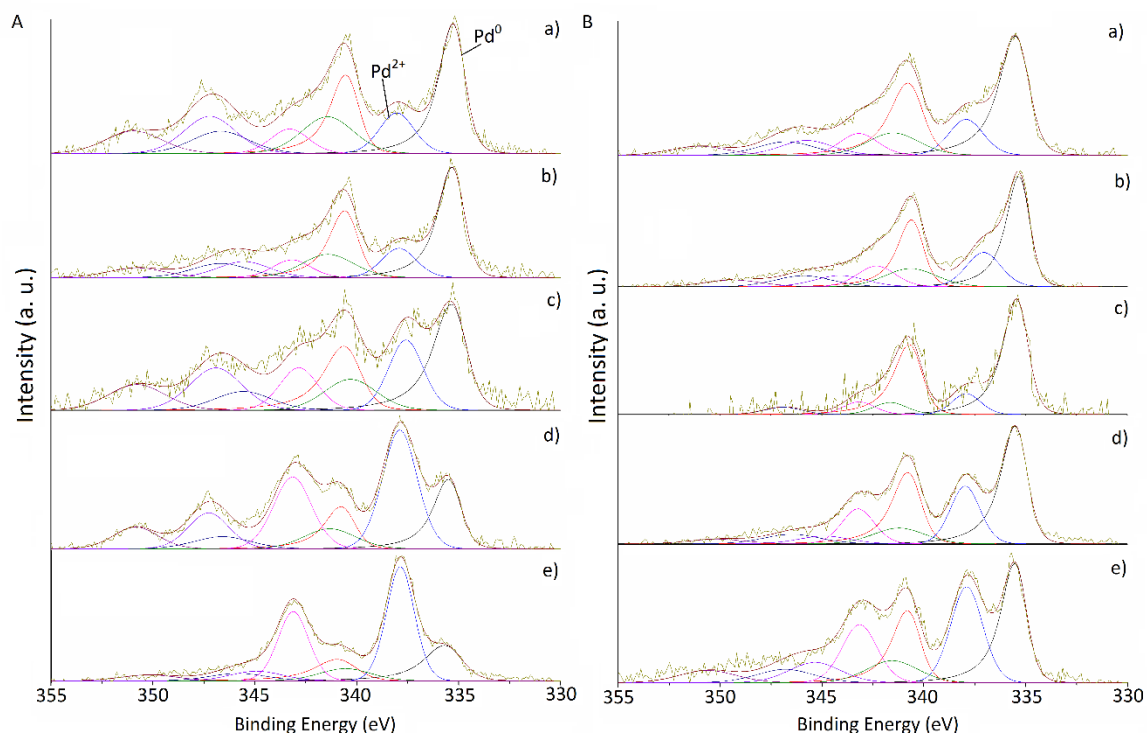


Figure 107. XPS spectra of used Pd/CNF (A) Catalyst synthesised by impregnation: (a) Pd_{IMP}/CNF-HHT, (b) Pd_{IMP}/CNF-LHT, (c) Pd_{IMP}/CNF-PS, (d) Pd_{IMP}/N-CNF-PS, (e) Pd_{IMP}/O-CNF-PS. (B) Catalysts synthesised by sol-immobilisation: (a) Pd_{SI}/CNF-HHT, (b) Pd_{SI}/CNF-LHT, (c) Pd_{SI}/CNF-PS, (d) Pd_{SI}/N-CNF-HHT, (e) Pd_{SI}/O-CNF-HHT.

Table 22 and figure 107 display the increase of the percentage of metallic Pd after the reaction, confirming again that the hydrogen released during the liquid-phase decomposition of HCOOH can reduce Pd^{II} to Pd⁰ species in concordance with XRD.

It was also observed a reduction in the atomic Pd content on the surface of the used catalyst. Since XPS is surface sensitive, and Pd leaching from the reaction was discarded, the decrease of Pd content for the used catalyst could be explained by:

- (i) migration (leaching and re-adsorption) of the nanoparticles to the inner wall of the nanofiber,
- (ii) increase of Pd particle size by agglomeration.

Further study by TEM will provide information to approve or disapprove the hypothesis of agglomeration of Pd nanoparticles.

XPS was also used to quantify the relative concentration of sp^2 and sp^3 hybridisation type from the deconvolution of C1s. XPS spectra in the C1s region of the fresh and used series of catalysts is presented in figure 108. Table 23 presents the concentrations of sp^2 and sp^3 hybridisation and its ratio (sp^2/sp^3) since it determines structure properties of carbon materials. The component appearing at approximately 285 eV is attributed to sp^3 -hybridised carbon species, while the component at 284 eV, to sp^2 carbon¹⁵. As observed, both sp^2 content and ratio sp^2/sp^3 increase with increasing annealing temperature, confirming thus the graphitisation of the surface. The catalysts supported on CNF-PS presents a ratio 2.85-2.98; for the catalysts supported on CNF-LHT, is 3.70-4.13; and for the catalysts supported on CNF-HHT, 10.10-10.95; indicating in this last case that sp^2 bond is primary. Subsequently, the content of sp^3 -hybridised carbon species decreased as expected with increasing annealing temperature.

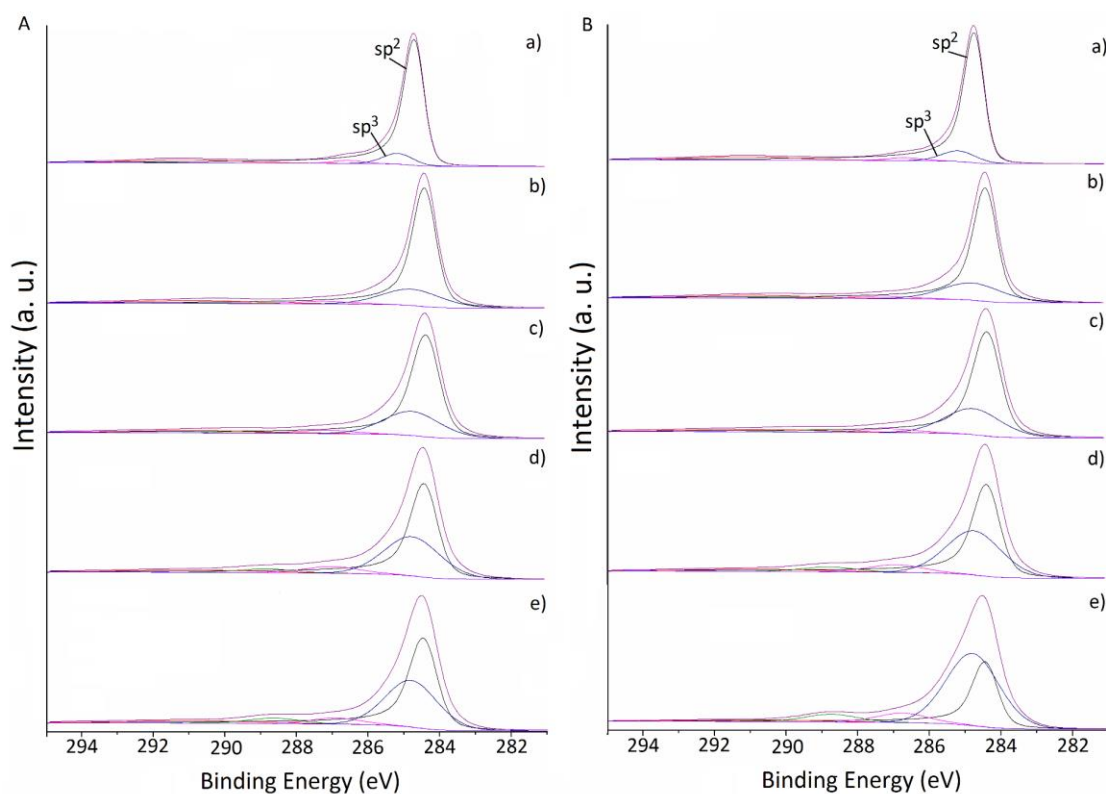


Figure 108. XPS spectra of fresh Pd/CNF in the binding energy region of 281–295 eV corresponding to C1s. (A) Catalyst synthesised by impregnation: (a) Pd_{IMP}/CNF-HHT, (b) Pd_{IMP}/CNF-LHT, (c) Pd_{IMP}/CNF-PS, (d) Pd_{IMP}/N-CNF-PS, (e) Pd_{IMP}/O-CNF-PS. (B) Catalysts synthesised by sol-immobilisation: (a) Pd_{SI}/CNF-HHT, (b) Pd_{SI}/CNF-LHT, (c) Pd_{SI}/CNF-PS, (d) Pd_{SI}/N-CNF-HHT, (e) Pd_{SI}/O-CNF-HHT.

Table 23. Atomic content of sp² and sp³ carbon and ratio sp²/sp³ from XPS for the bare supports and the catalysts subjected to different temperature treatments.

Catalyst	C sp ² (%)	C sp ³ (%)	sp ² /sp ³
CNF-HHT	-	-	-
CNF-LHT	-	-	-
CNF-PS	-	-	-
Pd _{IMP} /CNF-HHT	82.10	7.50	10.95
Pd _{IMP} /CNF-LHT	72.01	17.43	4.13
Pd _{IMP} /CNF-PS	66.73	22.37	2.98
Pd _{SI} /CNF-HHT	81.87	8.11	10.09
Pd _{SI} /CNF-LHT	70.44	19.05	3.70
Pd _{SI} /CNF-PS	65.80	23.12	2.85

Chlorine impurities must receive special attention since these can promote catalyst sintering or poisoning by occupying active sites^{16,17}. Figure 109 displays the spectra of the fresh and used catalysts in the binding energy region of 198–199 eV corresponding to Cl 2p_{3/2}. Cl relative atomic content of the series of catalysts was previously presented in table 22.

As observed, negligible chlorine from Pd precursor was found corresponding to inorganic chlorine Cl 2p_{3/2} peak either as chloride anions or chlorine covalently bonded to carbon atoms. Nevertheless, certain amounts of PdCl₂ may have remained in some catalysts as evidenced by the 339–340 eV shoulders in figure 106. In contrast to previous work¹⁸, the catalysts prepared by sol-immobilisation showed slightly larger amount of chlorine impurities on the surface, however, this could be addressed to slight differences on the amount of water used during the filtration process and washing or differences of the setup used.

The total disappearance of chlorine in the surface for all the used catalysts is displayed in figure 109 and table 22. This could be explained by the generation and release of HCl during the reaction, and thus, this assures that chlorine impurities were not relevant in the deactivation of these catalysts and did not present any influence after the first cycle of reaction.

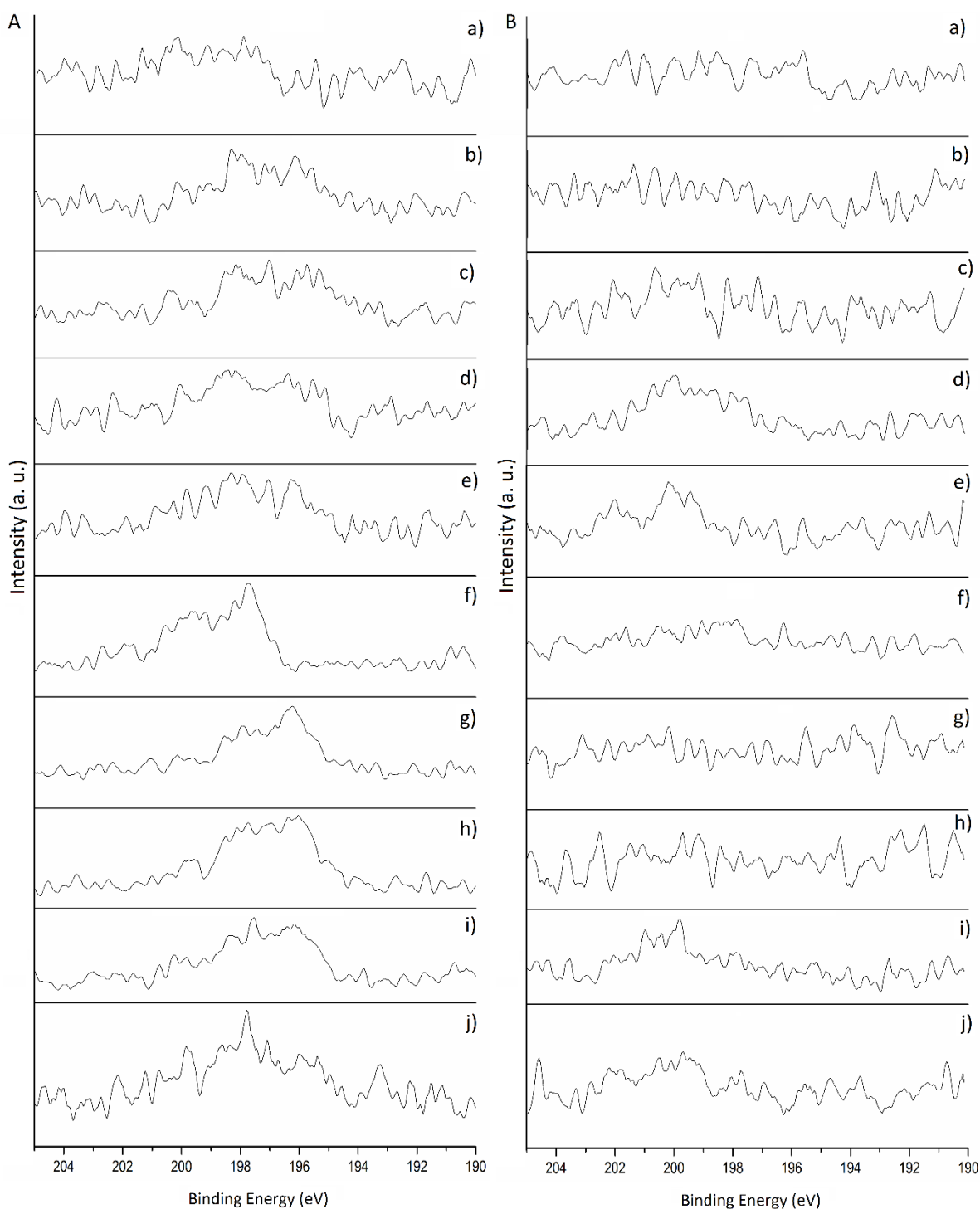


Figure 109. XPS spectra of the fresh (A) and used (B) catalysts in the binding energy region of 190–205 eV corresponding to Cl 2p_{3/2}. (a) Pd_{IMP}/CNF-HHT, (b) Pd_{IMP}/CNF-LHT, (c) Pd_{IMP}/CNF-PS, (d) Pd_{IMP}/N-CNF-PS, (e) Pd_{IMP}/O-CNF-PS, (f) Pd_{SI}/CNF-HHT, (g) Pd_{SI}/CNF-LHT, (h) Pd_{SI}/CNF-PS, (i) Pd_{SI}/N-CNF-HHT, (j) Pd_{SI}/O-CNF-HHT.

Table 22 presented the nitrogen and oxygen relative atomic content of the series of catalysts. There is a small presence of N- and O-containing groups in some of those catalysts which have not been functionalised. This could be explained by their exposure to atmosphere: oxygen

easily reacts with the dangling bonds of incomplete graphitic layers at room temperature and this also explains the decrease in the relative atomic content of O and N elements with increasing annealing temperature due to the reduction in the number of dangling bonds and subsequent graphitisation of the surface¹⁹. Furthermore, a slightly higher functionalisation degree was reached by sol-immobilisation method compared with the impregnation method. Figure 110 presents the XPS spectra in the region of O1s in order to analyse oxygen composition.

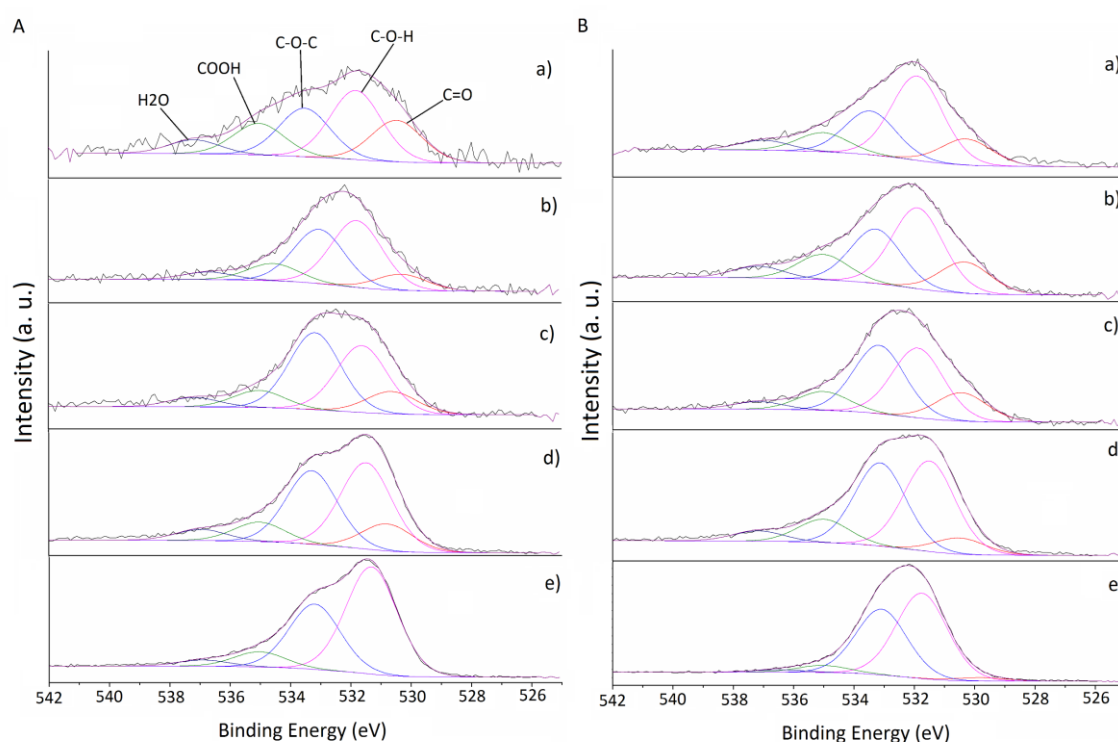


Figure 110. XPS spectra of fresh Pd/CNF in the binding energy region of 525-542 eV corresponding to O1s. (A) Catalyst synthesised by impregnation: (a) Pd_{IMP}/CNF-HHT, (b) Pd_{IMP}/CNF-LHT, (c) Pd_{IMP}/CNF-PS, (d) Pd_{IMP}/N-CNF-PS, (e) Pd_{IMP}/O-CNF-PS. (B) Catalysts synthesised by sol-immobilisation: (a) Pd_{SI}/CNF-HHT, (b) Pd_{SI}/CNF-LHT, (c) Pd_{SI}/CNF-PS, (d) Pd_{SI}/N-CNF-HHT, (e) Pd_{SI}/O-CNF-HHT.

O1s peaks are well described by a Gaussian-Lorentzian curve after Shirley background subtraction. The same procedure explained in Chapter 3 for the assignment of the components in the O1s spectrum was followed here.

For the comparison of preparation method, a clear trend was observed for the intensity of the peak attributed to the carbon-oxygen single-bonds in hydroxyl groups (C-O-H). Due to the presence of PVA and its hydroxyl groups, a higher ratio of C-O-H is produced in the sol-

immobilisation method. As expected, carbon-oxygen ether-like single bonds decrease when increasing the annealing temperature due to the graphitisation of the surface as previously presented. Regarding the oxygen-functionalised carbon nanofibers, very low presence of carbon-oxygen double bonds is found.

Furthermore, for the commercial catalyst, a significant increment of the region attributed to water was observed for the used catalyst. This is not the case for the Pd nanoparticles supported on CNFs.

As a summary, XPS analysis presented two types of Pd species in the fresh and used samples as expected. The catalysts prepared by sol-immobilisation technique exhibited a higher atomic Pd percentage and, since PVA ligands tend to inhibit the oxidation of the Pd surface, a higher percentage of Pd⁰. Increasing annealing temperature, concentration of sp² hybridisation type increases as a result of the graphitisation of the surface.

4.2.5.3. Raman

Raman spectroscopy was performed to analyse the structure and graphitisation degree of the carbon nanofibers. Raman spectra was measured in the range of 900–1900 cm⁻¹. Figures 111, 112 and 113 display respectively the Raman spectra of the bare supports, fresh and used catalysts exposed to different temperature treatments.

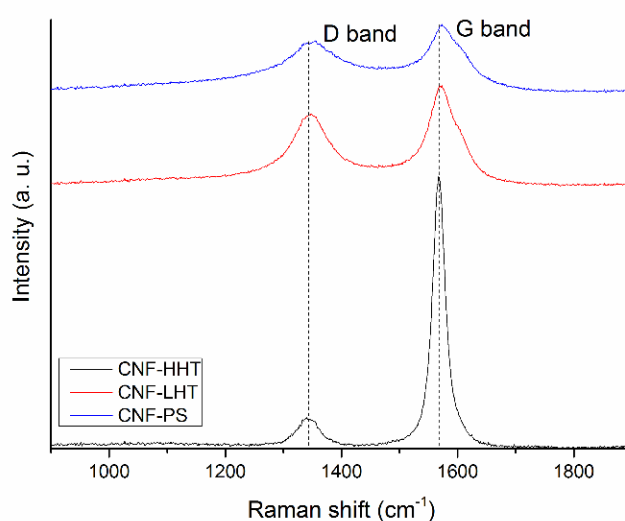


Figure 111. Raman spectra of the bare supports: CNF-HHT (black curve), CNF-LHT (red curve) and CNF-PS (blue curve).

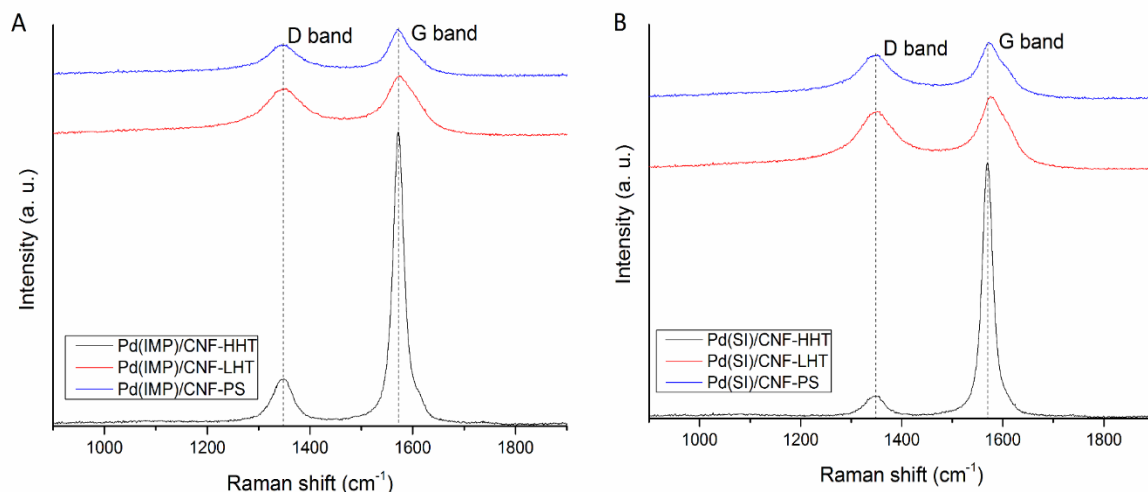


Figure 112. Raman spectra of the fresh samples. (A) Catalyst synthesised by impregnation: (a) Pd_{IMP}/CNF-HHT (black curve), (b) Pd_{IMP}/CNF-LHT (red curve), (c) Pd_{IMP}/CNF-PS (blue curve). (B) Catalysts synthesised by sol-immobilisation: (a) Pd_{SI}/CNF-HHT (black curve), (b) Pd_{SI}/CNF-LHT (red curve), (c) Pd_{SI}/CNF-PS (blue curve).

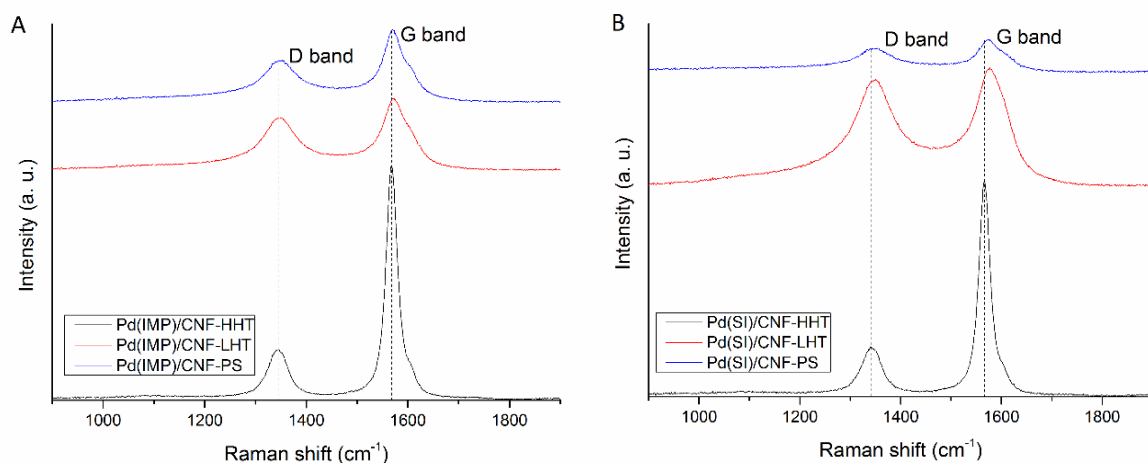


Figure 113. Raman spectra of the used samples. (A) Catalyst synthesised by impregnation: (a) Pd_{IMP}/CNF-HHT (black curve), (b) Pd_{IMP}/CNF-LHT (red curve), (c) Pd_{IMP}/CNF-PS (blue curve). (B) Catalysts synthesised by sol-immobilisation: (a) Pd_{SI}/CNF-HHT (black curve), (b) Pd_{SI}/CNF-LHT (red curve), (c) Pd_{SI}/CNF-PS (blue curve).

The main peaks at 1348 and 1572 cm^{-1} and are attributed to the D and G bands for sp^2 clusters respectively. D band is caused by the presence of disorder in sp^2 -hybridised carbon and G band is due to the stretching of the C-C bonds in sp^2 systems providing evidence of graphitisation. The relative intensity between these two bands (I_D/I_G) is related with the structural disorder and subsequently with the size of graphitic domains.²⁰

Table 24 shows the intensity of the peaks and ratios I_D/I_G .

Table 24. ID/IG ratio from Raman for the bare supports and the catalysts exposed to different temperature treatments.

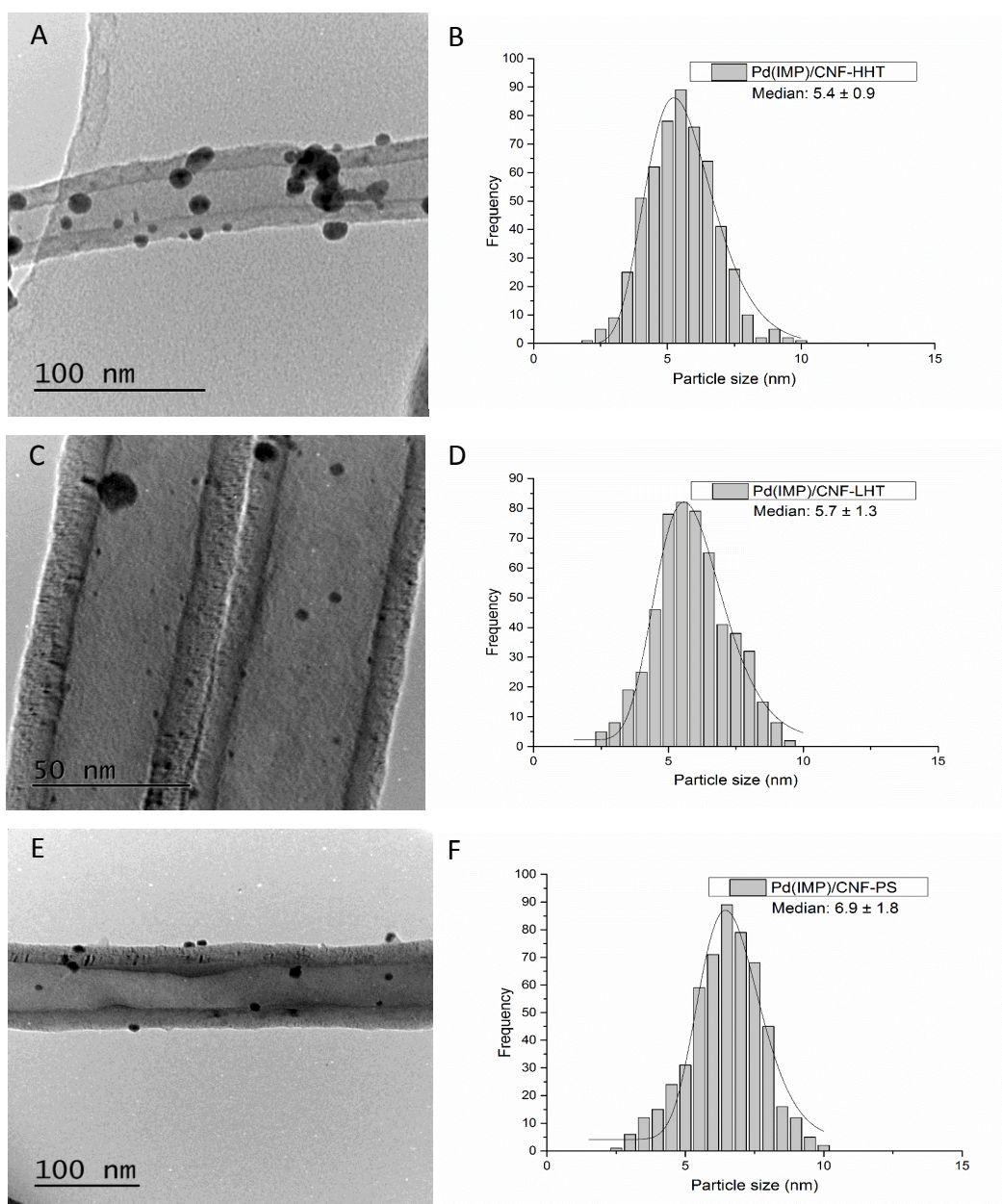
Catalyst	I _D /I _G	
	Fresh	Used
CNF-HHT	0.11	-
CNF-LHT	0.71	-
CNF-PS	0.75	-
Pd _{IMP} /CNF-HHT	0.26	0.21
Pd _{IMP} /CNF-LHT	0.78	0.73
Pd _{IMP} /CNF-PS	0.67	0.57
Pd _{SI} /CNF-HHT	0.08	0.23
Pd _{SI} /CNF-LHT	0.80	0.90
Pd _{SI} /CNF-PS	0.78	0.71

Both D and G Raman bands are present in all the catalysts in this group. Analysing the bare supports, the ratio I_D/I_G decreases with increasing annealing temperature, as expected, presenting a deeper drop when the support is treated at the highest temperature. However, for the synthesised catalysts, both fresh and used, and mainly during impregnation, the opposite trend is observed for the PS samples (pyrolytically stripped at 700 °C): I_D/I_G ratio decreases. This variation may be explained because during the preparation method, the catalyst was washed to remove the remaining of stabiliser or precursor and this could be affecting the amorphous phase of the carbon, being this amorphous phase washed away to some extent and subsequently showing this low I_D/I_G ratio. This experiment produced a further decrease in the I_D/I_G: 0.61 for Pd_{IMP}/CNF-PS and 0.67 for Pd_{SI}/CNF-PS. Confirming that the amorphous carbon was removed to a certain extent from the surface when preparing the catalyst.

The results obtained in Raman are in agreement with the difference observed in XPS between the concentrations of sp² and sp³; the catalysts annealed at 3000 °C presented the highest graphitisation and, a certain difference with LHT samples (annealed at 1500 °C) as observable in the ratio sp²/sp³. A small difference was observed between LHT and PS samples, confirmed by both concentrations of sp² and sp³ and I_D/I_G ratio.

4.2.5.4. Transmission Electron Microscopy (TEM)

Particle size of metal nanoparticles plays a key role in the catalytic activity. Particle size distributions of the catalysts series for both impregnated and sol-immobilised samples were assessed from analysis of bright field TEM micrographs. Figure 114 presents a representative micrograph and its particle size distribution for the samples synthesised via impregnation route while figure 115, presents the homologue for the sol-immobilisation route.



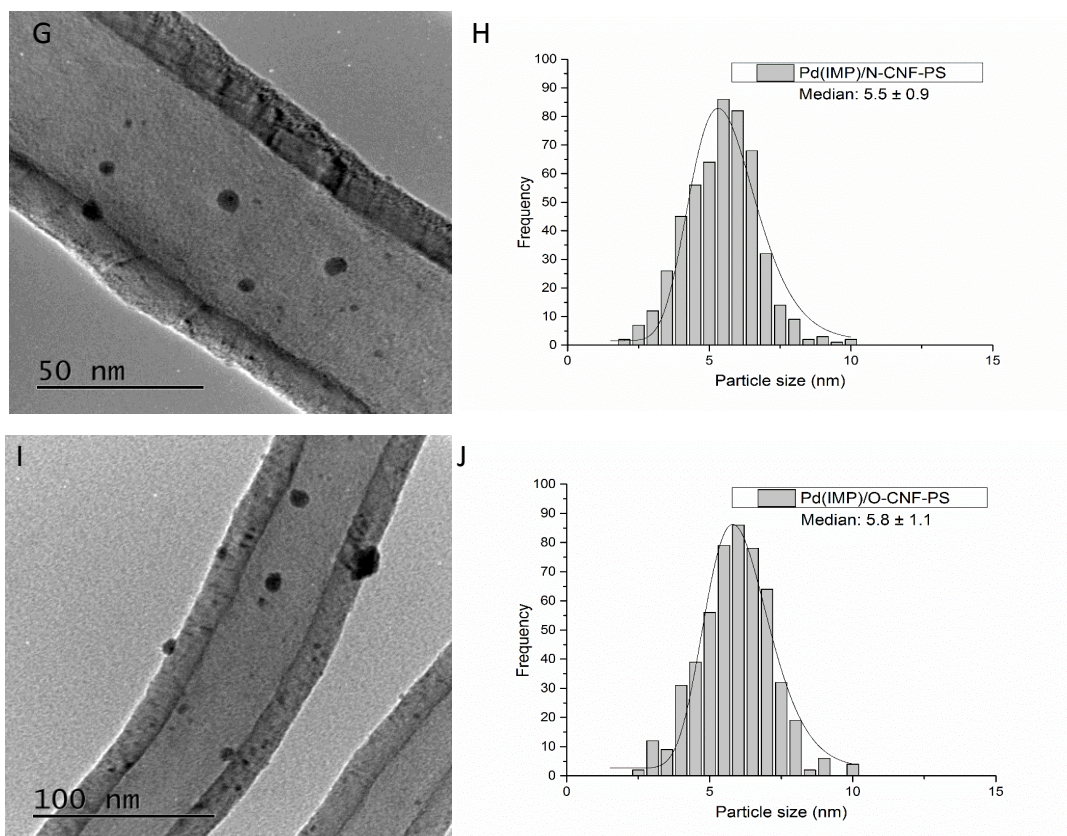
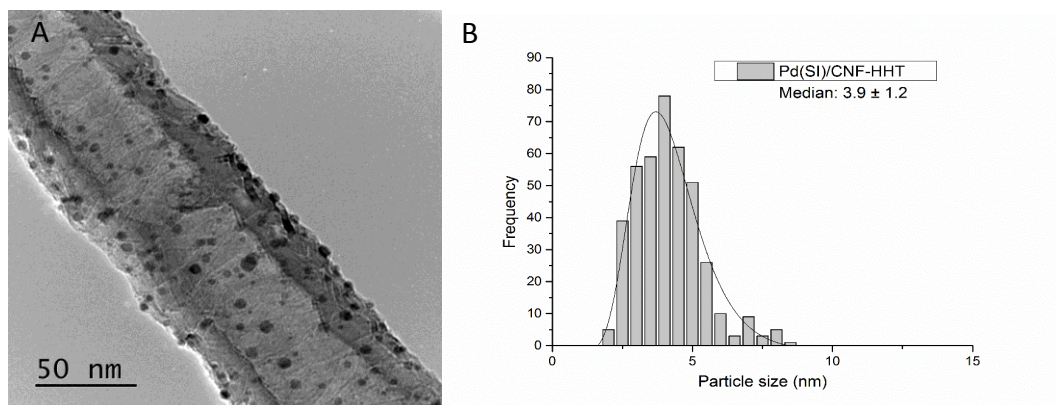


Figure 114. Bright field TEM micrographs and corresponding histograms of the particle size distributions for the fresh catalysts prepared by impregnation. (A,B) Pd_{IMP}/CNF-HHT, (C,D) Pd_{IMP}/CNF-LHT, (E,F) Pd_{IMP}/CNF-PS, (G,H) Pd_{IMP}/N-CNF-PS, (I,J) Pd_{IMP}/O-CNF-PS.



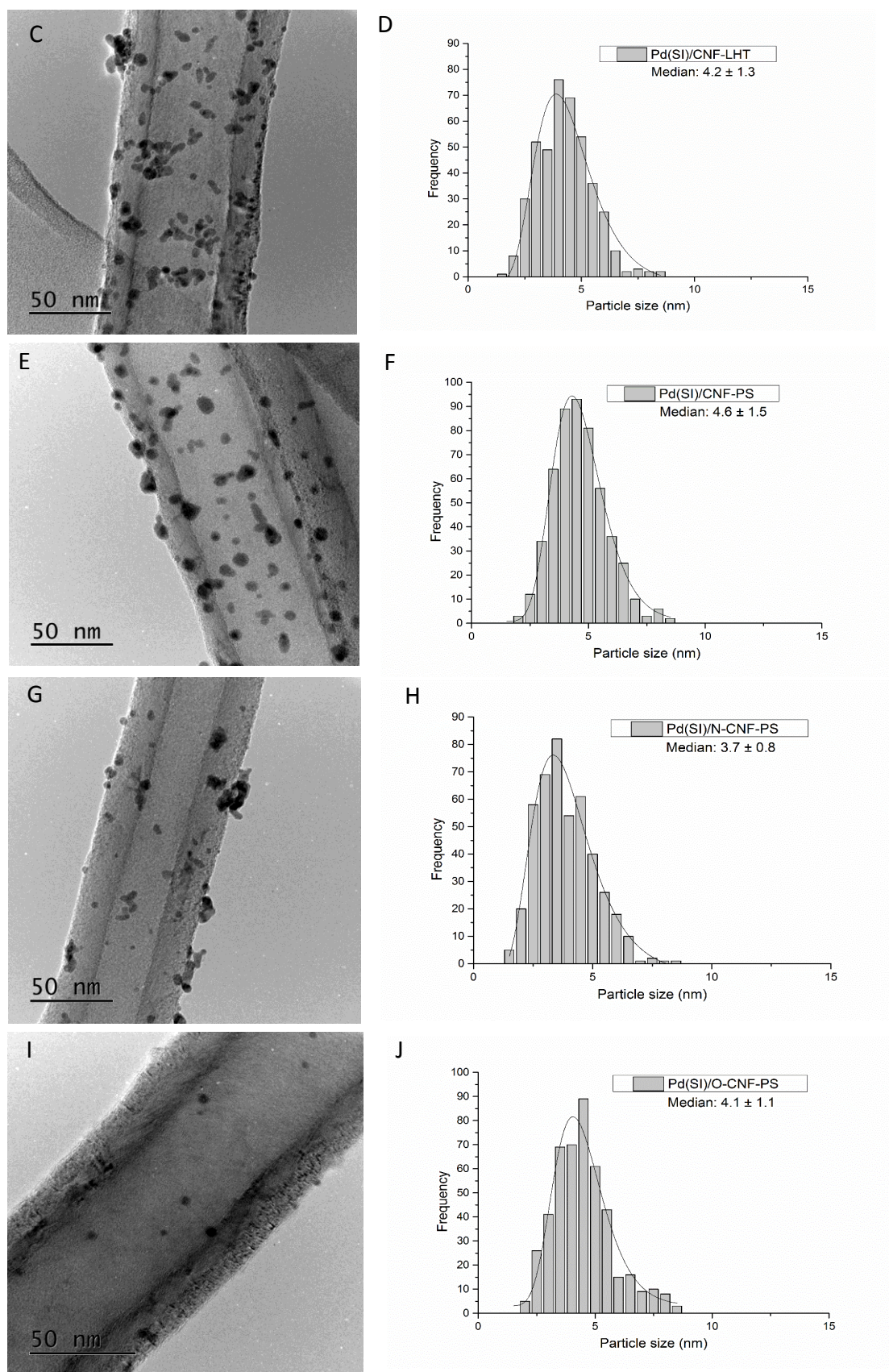


Figure 115. Bright field TEM micrographs and corresponding histograms of the particle size distributions for the fresh catalysts prepared by sol-immobilisation. (A,B) Pd_{SI}/CNF-HHT, (C,D) Pd_{SI}/CNF-LHT, (E,F) Pd_{SI}/CNF-PS, (G,H) Pd_{SI}/N-CNF-PS, (I,J) Pd_{SI}/O-CNF-PS.

Table 25 shows the mean particle size of the as-synthesised fresh and used catalysts.

Table 25. Statistical mean and standard deviation of particle size analysis.

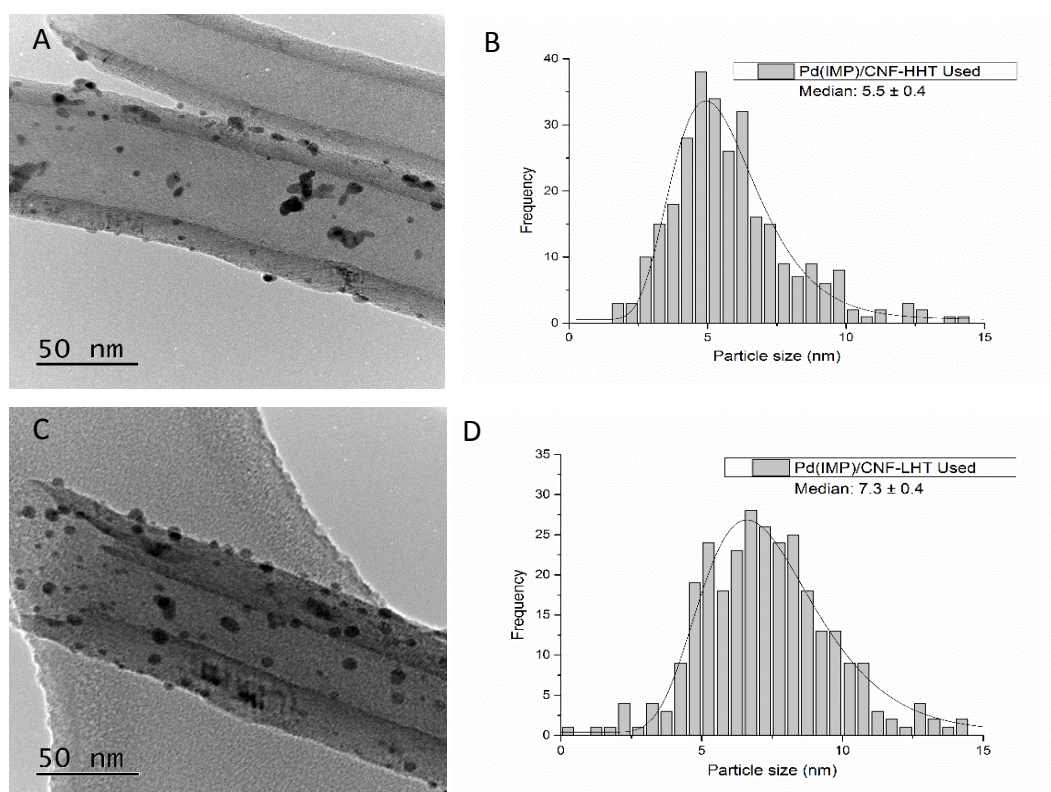
Catalyst	Fresh		Used	
	Mean particle size (nm)	Standard deviation	Mean particle size (nm)	Standard deviation
Pd _{IMP} /CNF-HHT	5.4	0.9	5.5	0.4
Pd _{IMP} /CNF-LHT	5.7	1.3	7.3	0.4
Pd _{IMP} /CNF-PS	6.9	1.8	6.8	0.3
Pd _{IMP} /N-CNF-PS	5.5	0.9	5.7	0.3
Pd _{IMP} /O-CNF-PS	5.8	1.1	5.7	0.5
Pd _{SI} /CNF-HHT	3.9	1.2	4.5	0.3
Pd _{SI} /CNF-LHT	4.2	1.3	6.2	0.4
Pd _{SI} /CNF-PS	4.6	1.5	5.4	0.4
Pd _{SI} /N-CNF-PS	3.7	0.8	4.5	0.4
Pd _{SI} /O-CNF-PS	4.1	1.1	4.8	0.3

Generally, the samples synthesised via impregnation route present a particle size distribution in the 2.5 - 10 nm range, while the catalysts prepared by sol-immobilisation method present a narrower particle size distribution of 2 - 8 nm. A lower Pd mean particle size is observed for the samples prepared by the colloidal method. Then, the higher catalytic activity observed could be attributed to the smaller Pd mean particle size. Furthermore, TEM analyses provided evidence that the Pd nanoparticles were more evenly dispersed on the catalysts prepared by sol-immobilisation in comparison with the impregnated samples. 3D tomography was performed in selected catalysts to confirm this hypothesis.

Regarding graphitisation, particle size tended to decrease for increasing annealing temperature of the support, being this change more evident for the impregnated samples. The concentration of sp² and sp³ carbon previously calculated could explain this behaviour. Carbon with sp² hybridisation is less reactive than carbon with sp³. The catalysts supported on CNF-HHT present a high percentage of sp², this means that less reactive sites on the carbon

surface are present. During the preparation method, when the Pd nanoparticle approximates the carbon surface in sol-immobilisation method or when the Pd agglomerates forming the nanoparticle in impregnation technique, it binds to it preferentially with the most reactive sites of carbon, what could facilitate a smaller particle size for HHT CNFs since sp^3 sites are more spatially distributed within the nanofiber.

Figures 116 and 117 present representative TEM micrographs and particle size distribution for the used catalysts by impregnation and sol-immobilisation respectively. As displayed in table 25, no remarkable increment in the average Pd particle size has been observed for the used catalysts except for the catalysts supported on CNF-LHT. The heat treatment applied to this support was observed to slightly modify the surface creating graphitic domains but to a low extent. This could have created tensions on the catalyst surface possibly affecting the metal/support interaction and therefore, leading to a certain increase in particle size.



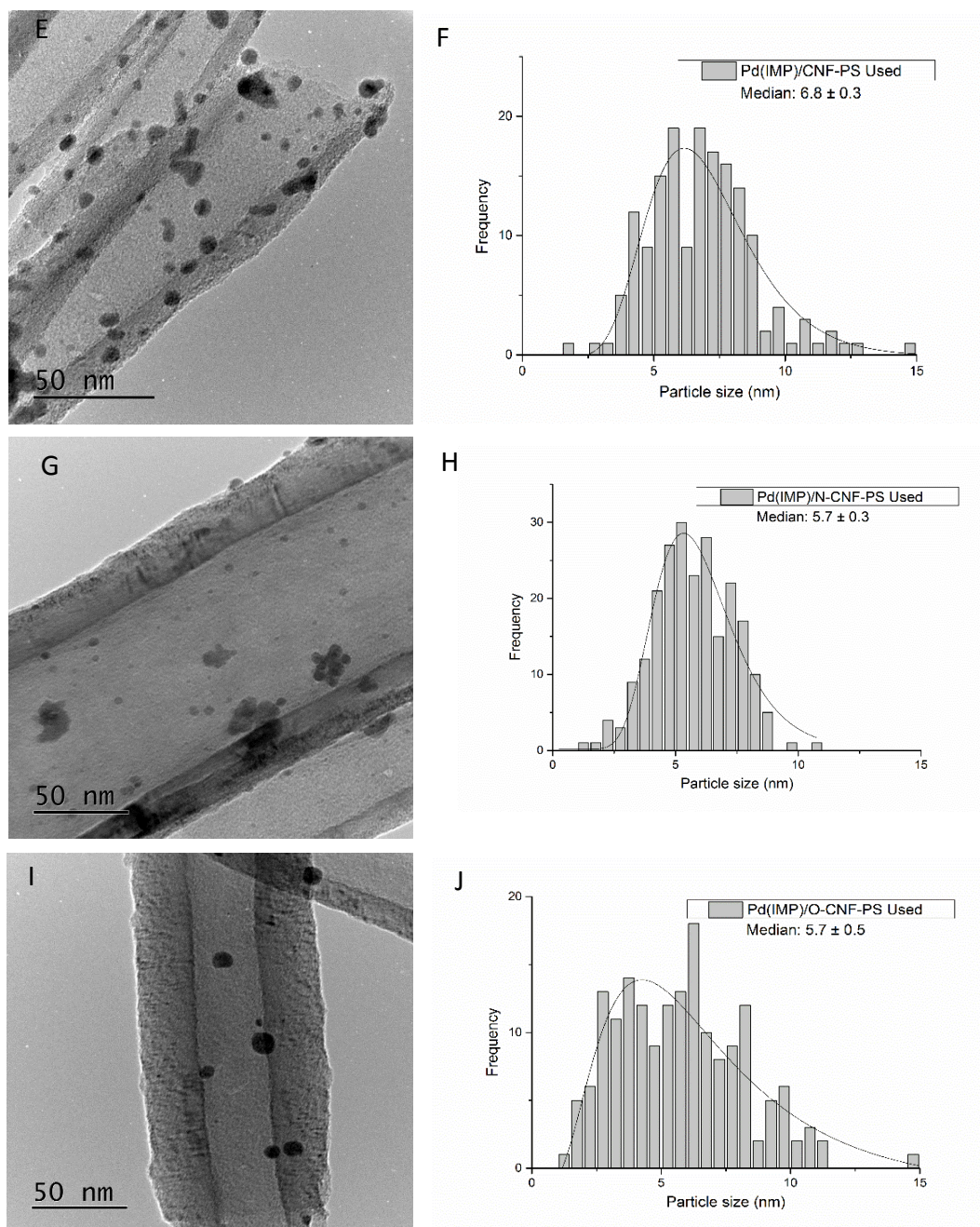
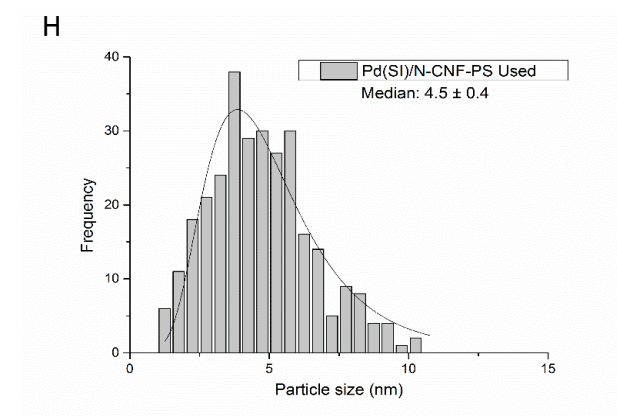
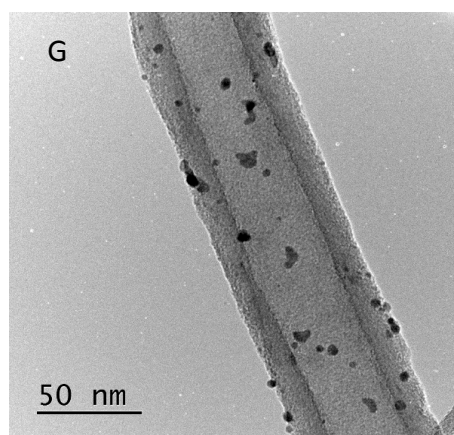
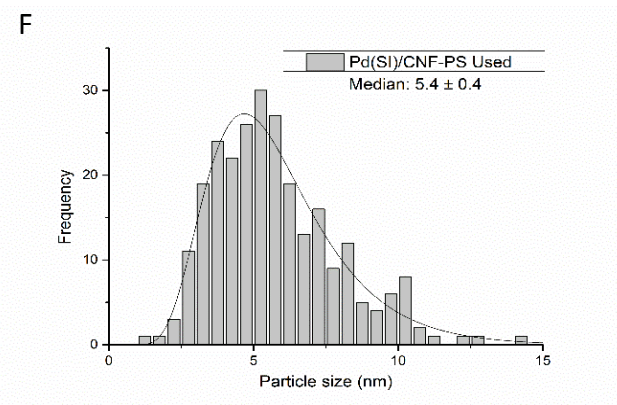
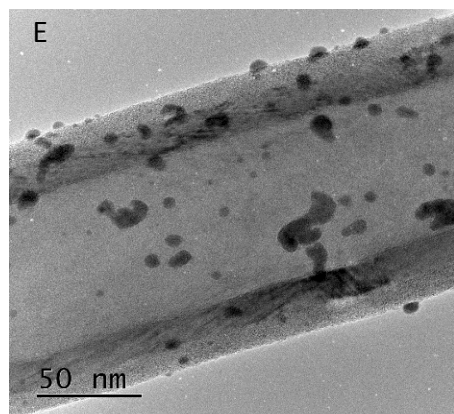
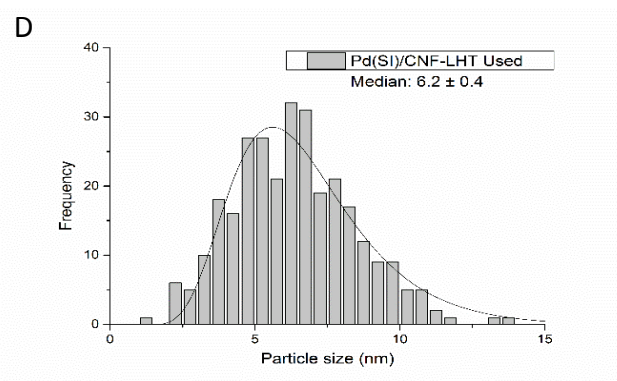
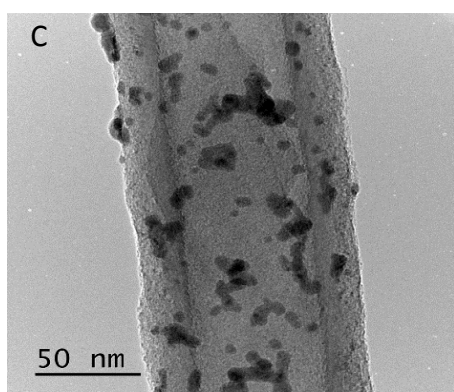
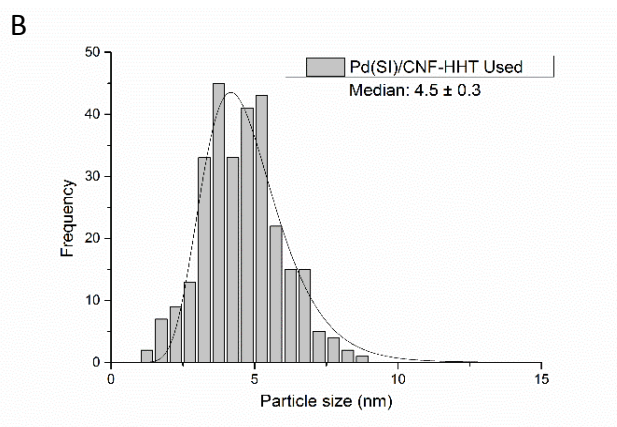
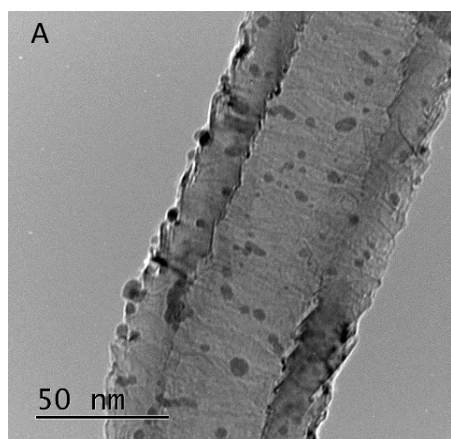


Figure 116. Bright field TEM micrographs and corresponding histograms of the particle size distributions for the used catalysts prepared by impregnation. (A,B) Pd_{IMP}/CNF-HHT, (C,D) Pd_{IMP}/CNF-LHT, (E,F) Pd_{IMP}/CNF-PS, (G,H) Pd_{IMP}/N-CNF-PS, (I,J) Pd_{IMP}/O-CNF-PS.



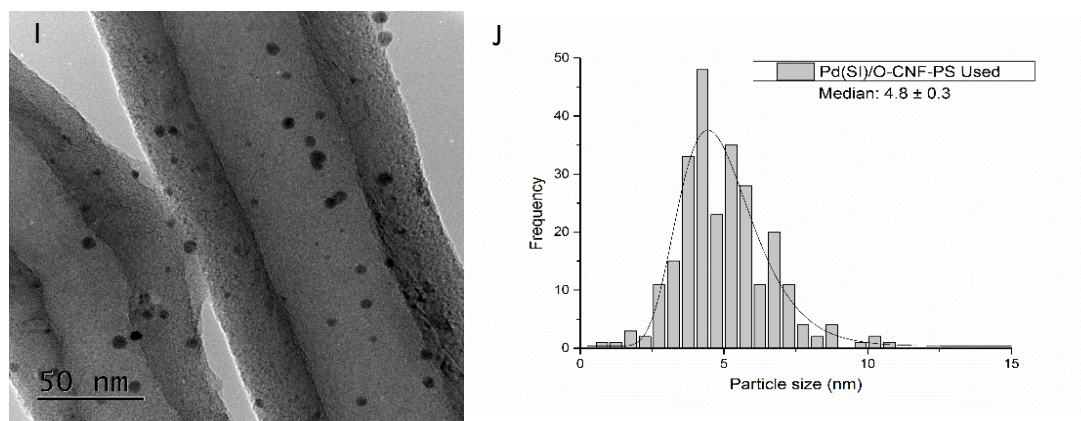


Figure 117. Bright field TEM micrographs and corresponding histograms of the particle size distributions for the used catalysts prepared by sol-immobilisation. (A,B) Pd_{Si}/CNF-HHT, (C,D) Pd_{Si}/CNF-LHT, (E,F) Pd_{Si}/CNF-PS, (G,H) Pd_{Si}/N-CNF-PS, (I,J) Pd_{Si}/O-CNF-PS.

The previous study by means of XPS exposed a decrease in Pd content on the surface. This was addressed to a possible agglomeration of the nanoparticles or leaching and re-adsorption. This study discards the agglomeration since it only occurs in two catalysts, consequently, leaching and re-adsorption of Pd nanoparticles from the surface of the nanofibers to the inner wall is the most plausible explanation for the decrease in atomic Pd percentage and therefore, difficulties could arise for formic acid to access these active sites inside the nanofibers, providing this a plausible explanation for the low reusability capacity. In comparison, the 5 wt. % Pd/C studied in the previous chapter, increased the Pd content on the surface after using the catalyst whilst, for this series of catalysts, it is reduced. From this result, a weak metal-support interaction for this kind of support can be assumed.

Besides migration of nanoparticles, adsorption of reaction intermediates, as concluded in Chapter 3, plays an important role in the long-term stability of the catalyst. For this purpose, TGA-MS was performed in the whole series of catalysts, however, nanofibers possess such a low density that the cuvette available in the instrument could only hold approximately 2 mg of sample which eventually rendered no conclusive results. In conclusion, without the possibility of obtaining definitive data by means of TGA-MS for these catalysts, adsorption of intermediate species including water and migration to the inner wall of the nanofiber seems the most probable reasons for the low reusability capacity of these catalysts.

4.2.5.5. Scanning Electron Microscopy-Energy Dispersive X-Ray spectroscopy

The distribution and dispersion of Pd within the CNFs was evaluated with SEM-EDX. Figure 118 displays a representative SEM image of the fresh and used Pd_{IMP}/CNF-HHT respectively. As observed, no significant variation is apparent between the samples. EDX analysis from a wide area during SEM observation was performed confirming the presence of Pd. Total metal loading both fresh and used catalysts series derived from EDX analysis is presented in table 26.

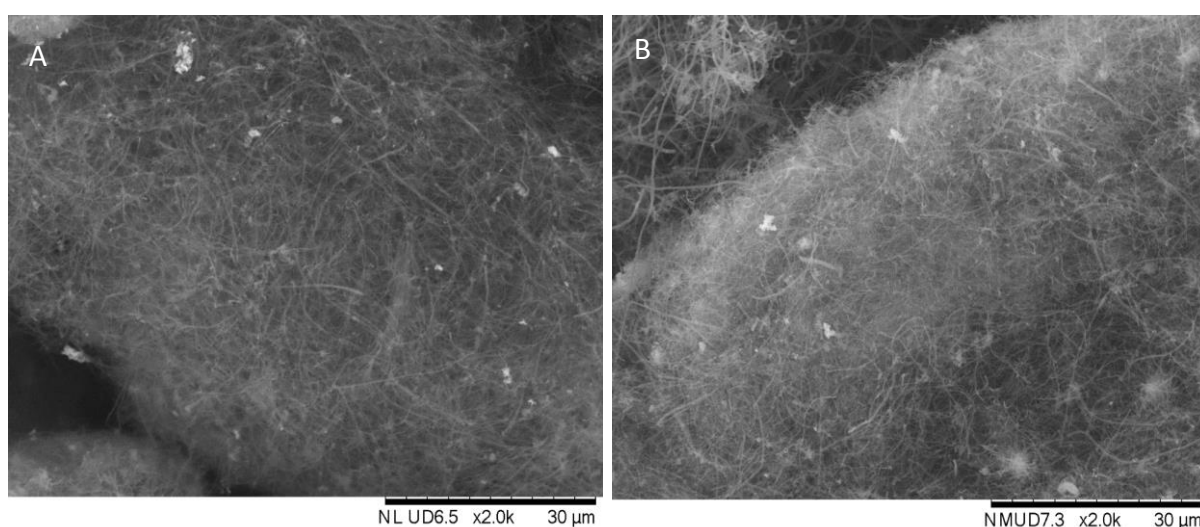


Figure 118. (A) SEM image of fresh Pd_{IMP}/CNF-HHT, (B) SEM image of used Pd_{IMP}/CNF-HHT.

Table 26. Palladium loading from EDX data for the different catalysts studied.

Catalyst	Pd loading EDX (wt. %)	
	Fresh	Used
Pd _{IMP} /CNF-HHT	1.03	1.01
Pd _{IMP} /CNF-LHT	1.03	0.99
Pd _{IMP} /CNF-PS	1.04	0.95
Pd _{IMP} /N-CNF-PS	0.99	0.97
Pd _{IMP} /O-CNF-PS	1	1
Pd _{SI} /CNF-HHT	0.91	1.01
Pd _{SI} /CNF-LHT	1.09	0.96

Pd _{SI} /CNF-PS	1.05	1.05
Pd _{SI} /N-CNF-PS	0.97	1.05
Pd _{SI} /O-CNF-PS	1.05	0.93

Total metal loading of the as-prepared catalysts is close to the theoretical 1 wt. % and it is not considerably affected by the preparation method used. Comparing fresh and used catalysts, no change was observed in the metal loading during the reaction, however, SEM-EDX mapping in figure 119 exposes that whereas for the fresh catalyst, Pd is homogeneously distributed in the catalyst, areas with high particles density and agglomeration is observed in the used catalysts as reported in Chapter 3 as well.

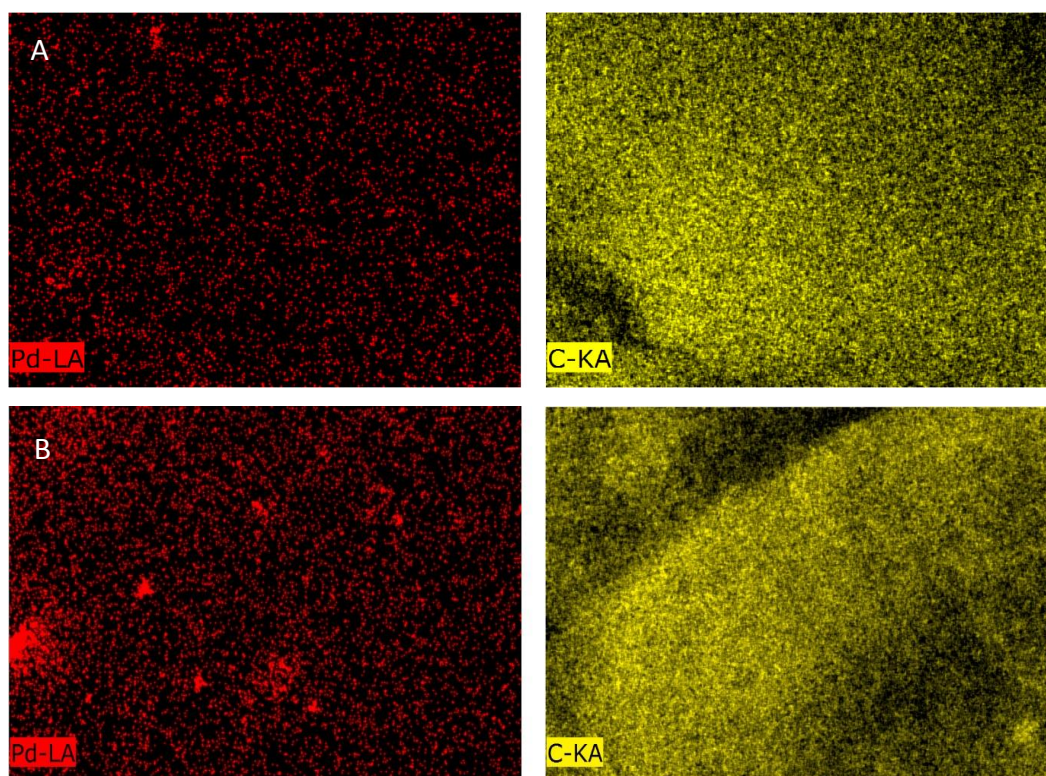


Figure 119. (A) Mapping images of fresh Pd_{IMP}/CNF-HHT, (B) mapping images of used Pd_{IMP}/CNF-HHT.

From XPS data in table 22, a higher Pd atomic percentage on the surface was obtained for the sol-immobilised samples, however, EDX, which is a bulk-sensitive technique, displayed a metal loading for all the catalysts series near 1 wt. %. Hence, it is clear that, with the sol-immobilisation method, Pd nanoparticles were preferentially distributed on the surface of the nanofibers, while the impregnation method might lead to a certain portion of the formed Pd

nanoparticles to be located and distributed in the inner walls of CNFs, besides deposited on the external surface. For this purpose, 3D tomography was performed in order to identify the location of the particles within the nanofiber.

4.2.5.6. 3D Tomography

This analysis was carried out for two representative catalysts of sol-immobilisation and impregnation. Figures 120 and 121 present a sequence of TEM micrographs showing the position of the nanoparticles in the nanofiber.

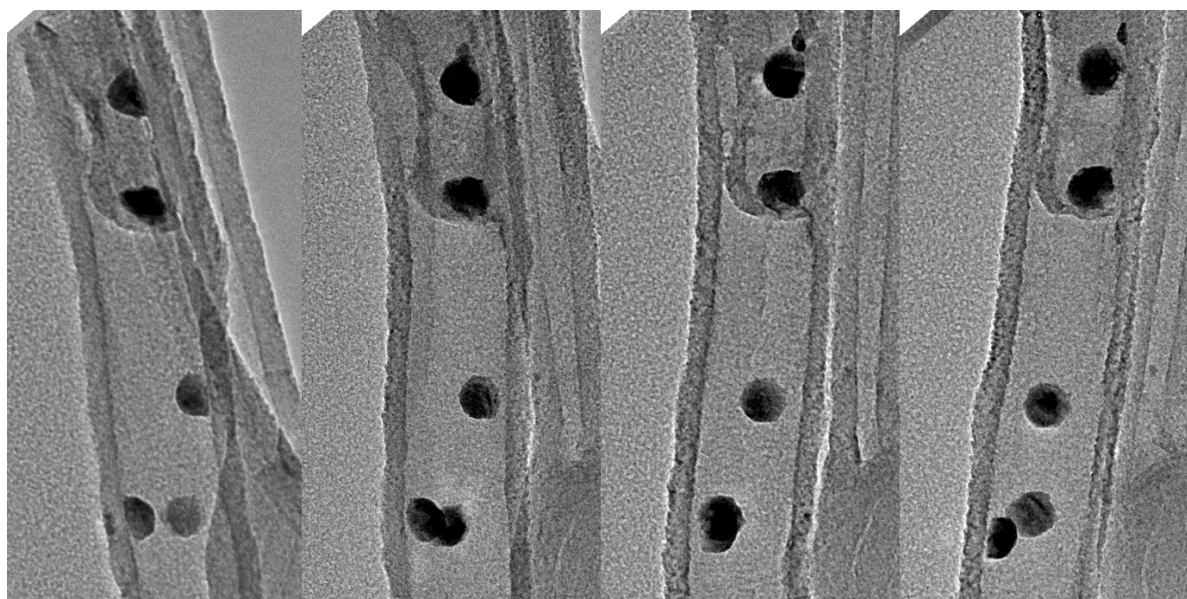


Figure 120. 3D tomography of Pd_{IMP}/CNF-LHT.

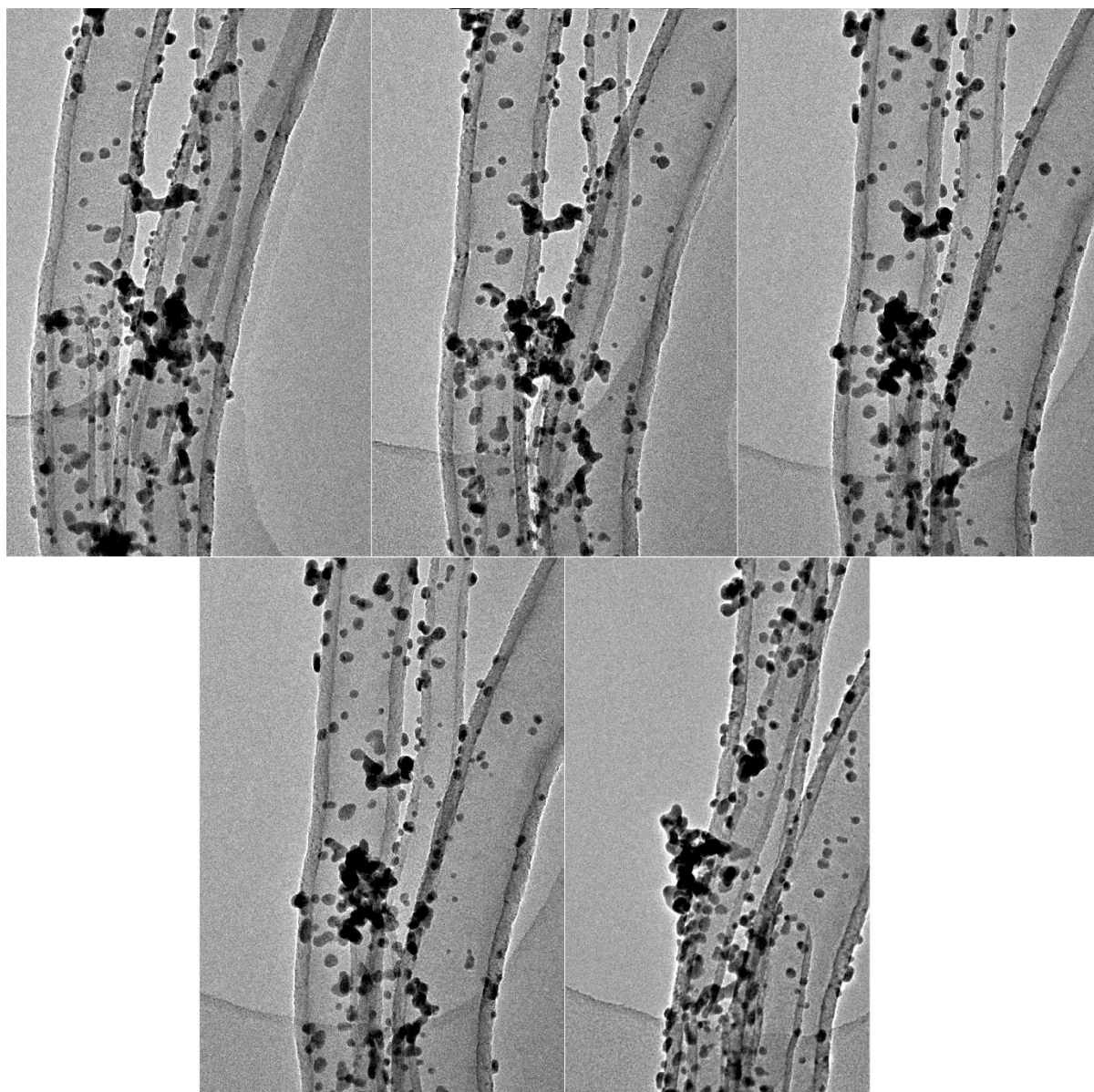


Figure 121. 3D tomography of Pd_{Si}/CNF-HHT.

As expected, Pd nanoparticles tend to distribute on the outer wall of the nanofiber for the sol-immobilisation technique while, for impregnation technique, remarkably, a certain number of Pd nanoparticles were allocated inside the inner wall as shown in figure 120. Note that, as in the colloidal method, most of the nanoparticles were deposited outside the nanofiber, however, a bigger number of nanoparticles were observed inside the nanofiber than for sol-immobilisation. The only purpose of the image chosen in figure 120 is to show without a doubt the location of some nanoparticles, although a representative image would be closer to figure 121. Since 3D tomography is by far the most laborious and expensive

technique used in this Thesis, no quantitative analysis could be performed. Nevertheless, as a rough and personal opinion, for the impregnated samples, approximately 95 % of the nanoparticles were located in the outer wall and the remaining 5 %, inside the inner channel. However, no scientific evidence could be extracted.

4.2.5.7. Ammonia -Temperature Programmed Desorption (NH₃-TPD)

Acidity of the nitrogen and oxygen functionalised CNFs was measured by temperature programmed desorption of ammonia. This technique allows getting a qualitative overview of the acidic strength of the active sites. This strength is estimated according to the intensity and temperature of the ammonia desorption peaks. The acid strength can be classified as weak (150–250 °C), medium (250–420 °C) and strong (420–750 °C).²¹ Figures 122 and 123 show the NH₃-TPD desorption profiles obtained.

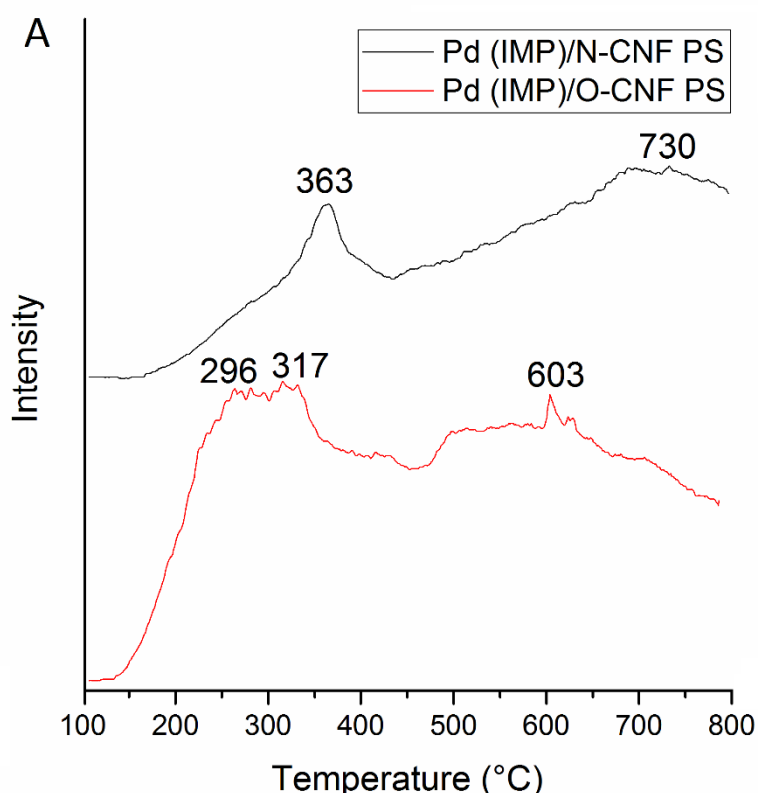


Figure 122. NH₃-TPD desorption profile of Pd_{IMP}/N-CNF-PS and Pd_{IMP}/O-CNF-PS.

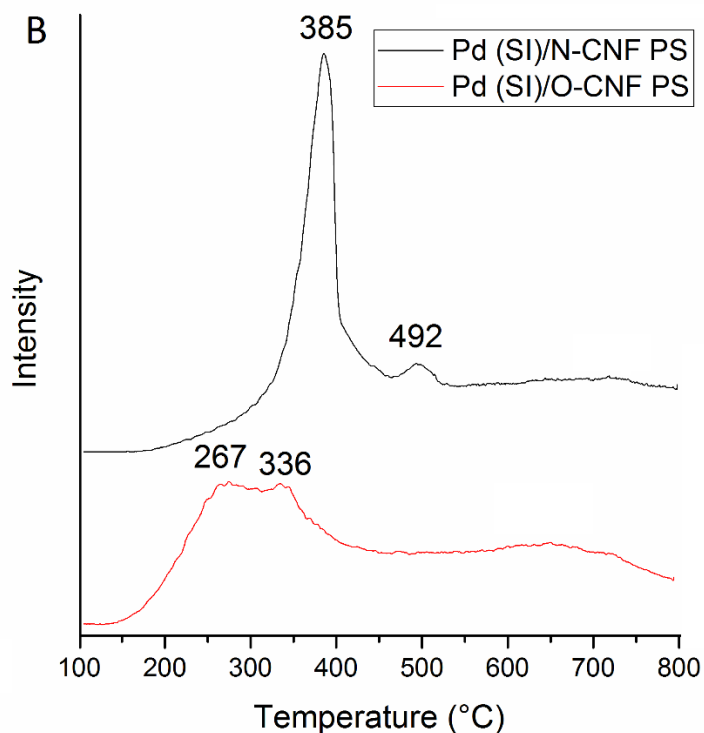


Figure 123. NH₃-TPD desorption profile of Pd_{SI}/N-CNF-PS and Pd_{SI}/O-CNF-PS.

For impregnated samples, the oxygen functionalised CNF present mainly three desorption peaks at 296, 317 and 603 °C while, for the sol-immobilisation method, only 267 and 336 °C, indicating thus the presence of medium strength acid sites in both catalysts, and strong acid sites only in the sample prepared by impregnation.

Regarding the nitrogen functionalised CNF, these peaks shift to a relatively higher temperature, appearing for sol-immobilisation at 385 and 492 °C, and for impregnation, there is just one medium strength acid sites peak at 363 and one strong acid peak at 730 °C.

As commented in the experimental chapter, a more in-depth study using pyridine FT-IR would provide more information about the types of acid since Bronsted or Lewis acids could not be distinguished using NH₃-TPD. However, due to the presence of carbon as support, FT-IR is not suitable due to the fact that Beer's equation would not be followed.²²

4.2.5.8. Brunauer, Emmett and Teller (BET) method surface area

Table 27 presents the total surface area determined from the BET equation.

Table 27. BET surface areas for the as-synthesised catalysts and supports.

Catalyst	Support	Impregnation	Sol-immobilisation
Pd/CNF-HHT	34	37	36
Pd/CNF-LHT	32	41	36
Pd/CNF-PS	43	50	47
Pd/N-CNF-PS	45	51	37
Pd/O-CNF-PS	48	52	47

It ranges from approximately 32 m²/g to 52 m²/g. This low surface area compared with carbon nanotubes (up to 1200 m²/g) is caused by the thickness of the walls (ca. 45 nm). By comparing preparation method, impregnation leads to slightly higher surface area, however, since BET surface area instruments have a certain error, in some cases up to 10 %, no conclusion can be extracted for the apparent variations in the surface area of these samples.

4.3. Conclusions

In this study, a series of monometallic Pd nanoparticles supported on carbon nanofibers (CNFs) were synthesised. Five different types of carbon nanofibers were used: three graphitisation grades and two functionalisation, oxygen and nitrogen. The objective was to study the effect on the catalyst activity of graphitisation, and subsequently structural order from one side, and, from the other side, of the modifications of the electrostatic interactions with the support. Sol-immobilisation and impregnation techniques were selected as model preparation methods widely used for the deposition of Pd nanoparticles.

An initial screening of the full series of catalysts established that catalysts synthesised by sol-immobilisation method exhibit higher initial activity when compared with catalysts prepared by impregnation method, although after 2 hours of reaction, similar conversion was achieved by these pairs of catalysts probably due to the presence of PVA which may occupy active sites and thus, leading to a faster deactivation. Characterisation techniques showed that the catalysts synthesised by sol-immobilisation present a higher surface atomic Pd percentage, and a higher percentage of Pd⁰ due to the presence of PVA ligand that tends to inhibit the oxidation of the Pd surface. Through TEM analysis it was found that these catalysts present

smaller Pd particle size as well. These are the most probable reasons for the enhancement of activity. Furthermore, an initial analysis by means of 3D tomography showed a slightly higher presence of nanoparticles inside the inner wall for the catalysts prepared by impregnation method.

The study of catalyst activity with different graphitisation degree showed that the catalytic performance significantly increased with the increase of annealing temperature and so, structural order. It was observed that catalyst activity was greatly enhanced by the samples supported on the carbon nanofibers treated at 1500 °C, even though the surface was only slightly modified. A further increment of the heat treatment up to 3000 °C, significantly rearranged the structure by improving the structural order, however, the increment in activity was not proportional. Besides the structural order improvement, smaller Pd nanoparticles were formed, and with improved dispersion, as the annealing temperature increased, explaining the enhancement in activity.

Regarding functionalisation, the lack of enough variety of samples rendered impossible the obtention of a conclusive result. Nevertheless, for the impregnated samples, an increment in activity was observed for the catalyst using oxygen functionalised carbon nanofibers. This was explained by a favoured deprotonation step due to the presence of O⁻ on the surface although deactivation of the catalyst was occurring soon after the start of the reaction most probably due to concomitant CO formation on the catalyst surface paradoxically also caused by the presence of oxygen from the functionalisation.

Optimisation of the reaction conditions with the two most active catalysts confirmed that the initial screening of the series of catalysts was performed under kinetic regime and therefore, making the data valid and reproducible. Under the optimised conditions, a remarkable initial TOF of 979 h⁻¹ was achieved by Pd₅₁/CNF-HHT, the most active catalyst in this series, with high selectivity for hydrogen (>99.9 %) at 30 °C.

Reusability studies for the two most active catalysts exhibited a certain loss of activity for each run. Once leaching, agglomeration of nanoparticles, and CO poisoning (at 30 °C) were rejected, the remaining possible reasons for the deactivation were adsorption of reaction intermediates on the catalyst surface, as confirmed in the previous chapter, and migration during the reaction to the inner wall of nanoparticles with less metal/support interaction.

The next chapter will make use of the results obtained so far. It will be focused on the preparation of Pd nanoparticles by the sol-immobilisation method. This preparation method will be extensively studied by varying a set of parameters in order to investigate the effects it has on the structure and morphology of the synthesised catalysts.

4.4. References

- 1 A. Lazzarini, A. Piovano, R. Pellegrini, G. Agostini, S. Rudić, C. Lamberti and E. Groppo, *Phys. Procedia*, 2016, **85**, 20–26.
- 2 K. L. Klein, A. V. Melechko, T. E. McKnight, S. T. Retterer, P. D. Rack, J. D. Fowlkes, D. C. Joy and M. L. Simpson, *J. Appl. Phys.*, , DOI:10.1063/1.2840049.
- 3 J.-P. Tessonnier, D. Rosenthal, T. W. Hansen, C. Hess, M. E. Schuster, R. Blume, F. Girgsdies, N. Pfänder, O. Timpe, D. S. Su and R. Schlögl, *Carbon N. Y.*, 2009, **47**, 1779–1798.
- 4 A. Oberlin, *Carbon N. Y.*, 1984, **22**, 521–541.
- 5 K. Tedsree, T. Li, S. Jones, C. W. A. Chan, K. M. K. Yu, P. a J. Bagot, E. a Marquis, G. D. W. Smith and S. C. E. Tsang, *Nat. Nanotechnol.*, 2011, **6**, 302–307.
- 6 S. T. Omaye, *Toxicology*, 2002, **180**, 139–150.
- 7 C. J. Huang, F. M. Pan, T. C. Tzeng, C. Li and J. T. Sheu, *J. Electrochem. Soc.*, 2009, **156**, J28–J31.
- 8 Z.-L. Wang, J.-M. Yan, H.-L. Wang, Y. Ping and Q. Jiang, *Sci. Rep.*, 2012, **2**, 598–604.
- 9 M. P. Lazaro, E. Garcia-Bordeje, D. Sebastian, M. J. Lazaro and R. Moliner, *Catal. Today*, 2008, **138**, 203–209.
- 10 M. C. Militello and S. J. Simko, *Surf. Sci. Spectra*, 1994, **3**, 387–394.
- 11 M. C. Militello and S. J. Simko, *Surf. Sci. Spectra*, 1994, **3**, 395–401.
- 12 K. Pattamakomsan, K. Suriye, S. Dokjampa and N. Mongkolsiri, *Catal. Commun.*, 2010, **11**, 311–316.
- 13 R. Arrigo, S. Wrabetz, M. E. Schuster, D. Wang, A. Villa, D. Rosenthal, F. Girsgdies, G. Weinberg, L. Prati, R. Schlögl and D. S. Su, *Phys. Chem. Chem. Phys.*, 2012, **14**, 10523–10532.
- 14 R. Arrigo, M. Havecker, S. Wrabetz, R. Blume, M. Lerch, J. McGregor, E. P. J. Parrott, J. A. Zeitler, L. F. Gladden, A. Knop-Gericke, R. Schlogl and D. S. Su, *J. Am. Chem. Soc.*, 2010, **132**, 9616–9630.
- 15 F. Y. Xie, W. G. Xie, L. Gong, W. H. Zhang, S. H. Chen, Q. Z. Zhang and J. Chen, *Surf. Interface Anal.*, 2010, **42**, 1514–1518.
- 16 Y. Zhao, L. Jia, J. A. Medrano, J. R. H. Ross and L. Lefferts, *ACS Catal.*, 2013, **3**, 2341–2352.
- 17 R. F. Bueres, E. Asedegbega-Nieto, E. Diaz, S. Ordonez and F. V. Diez, *Catal. Today*, 2010, **150**, 16–21.
- 18 H. Bahruji, M. Bowker, G. Hutchings, N. Dimitratos, P. Wells, E. Gibson, W. Jones, C. Brookes, D. Morgan and G. Lalev, *J. Catal.*, , DOI:10.1016/j.jcat.2016.03.017.
- 19 Y. V. Butenko, S. Krishnamurthy, A. K. Chakraborty, V. L. Kuznetsov, V. R. Dhanak, M. R. C. Hunt and L. Šiller, *Phys. Rev. B - Condens. Matter Mater. Phys.*, 2005, **71**, 1–10.
- 20 F. Tuinstra and J. L. Koenig, *J. Chem. Phys.*, 1970, **53**, 1126–1130.
- 21 M. Zhou, P. Liu, K. Wang, J. Xu and J. Jiang, *Catal. Sci. Technol.*, 2016, **6**, 7783–7792.
- 22 G. V. A. Martins, G. Berlier, C. Bisio, S. Coluccia, H. O. Pastore and L. Marchese, *J. Phys. Chem. C*, 2008, **112**, 7193–7200.

5. INVESTIGATION OF SUPPORTED Pd-BASED COLLOIDAL NANOPARTICLES IN THE LIQUID PHASE DECOMPOSITION OF FORMIC ACID: EFFECT OF STABILISER, METAL LOADING, SUPPORT, AND BIMETALLICS RATIO

5.1. Introduction

This Thesis started with the evaluation of liquid-phase formic acid decomposition using a commercial catalyst to optimise the reaction conditions. In Chapter 4, a series of Pd nanoparticles supported on carbon nanofibers with different graphitisation degree and functionalisation, prepared by two preparation methods and the catalytic performance of the synthesised materials was evaluated for the liquid phase decomposition of formic acid and thoroughly characterised.

In previous works, it was found that final morphology and structure of synthesised colloidal metal nanoparticles can be affected by the selection of ligand and its amount, variations of concentration of metal precursor, reducing agent, temperature of colloidal reduction, and nature of ligand and reducing agent.¹⁻³ For this purpose, the present chapter reports the synthesis of Pd nanoparticles using colloidal methodology varying the amount of stabiliser (polyvinyl alcohol), Pd loading, support (activated charcoal and TiO₂) and Au-Pd atomic ratio, with the objective of tuning the morphology of the catalysts and so affecting catalytic performance. Subsequently, reusability studies of the most active monometallic Pd catalyst were performed.

The catalyst activity was evaluated as usually, using liquid phase formic acid decomposition as the model reaction for hydrogen production at mild conditions.

5.2. Results and discussion

As for Chapter 4, a similar experimental procedure was followed in this chapter. However, a slight variation in the experimental conditions was performed since preliminary tests displayed a generally lower activity for this series of catalysts compared with previous chapters. For this reason, initial conversion after 5 minutes of reaction did not provide with enough difference in the activity so as to extrapolate a trend and be able to elucidate how

activity is affected by structural changes. Hence, the temperature at which the reaction was performed was increased from 30 °C to 50 °C since it would increment activity and thus, emphasise the differences. Furthermore, the reactions were also kept running for 4 hours instead of 2 in order to find a more accurate behaviour trend.

5.2.1. Catalytic activity screening of the as synthesised Pd catalysts for liquid-phase formic acid decomposition: effect of PVA

Catalytic performance of the Pd catalysts prepared by sol-immobilisation was evaluated under the optimised conditions of substrate/metal molar ratio of 2000:1 and 750 rpm, and at 50 °C and 0.5 M initial HCOOH concentration. As introduced in Chapter 1, polyvinyl alcohol (PVA) was used during the preparation method as a steric stabiliser to prevent agglomeration. Figure 124 displays the catalytic activity of the catalysts synthesised by varying the PVA/Pd weight ratio.

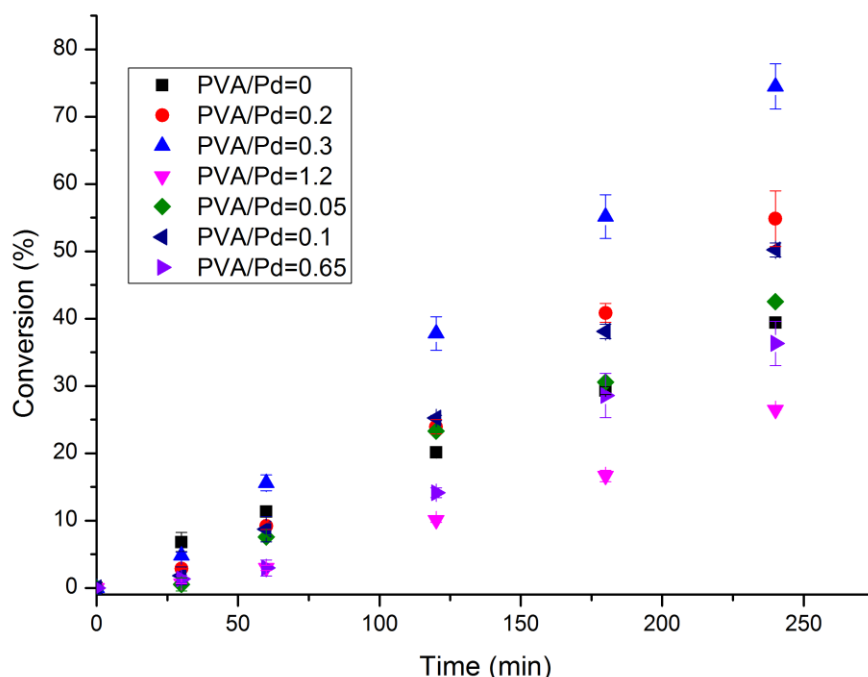


Figure 124. Conversion vs. time plot for the effect of stabiliser. Reaction conditions: 50 °C, 26.5 mg of catalyst (substrate/metal molar ratio: 2000:1), 0.5 M HCOOH, 750 rpm, 4 h reaction time.

In terms of conversion, the highest catalytic performance was obtained for the catalyst Pd/AC-0.3 (PVA/Pd weight ratio = 0.3, initial TOF 366 h⁻¹). Nevertheless, the highest initial

activity is achieved by the catalyst Pd/AC-0 (PVA/Pd weight ratio = 0) with an initial TOF of 560 h^{-1} (note that TOF was calculated for the first 5 minutes of reaction even though the graph does not show the points for clarity of results), however, after the first hour of reaction, a steep decrease in catalytic activity is observed only for this last catalyst. This result is interesting since it indicates that, from one side, PVA may occupy active sites and therefore, in the sample in which PVA was not used a higher percentage of active sites are available at the beginning of the reaction although, on the other side, samples with PVA tend to maintain a higher degree of stability. Since the role of the stabiliser is to prevent agglomeration, this could explain the result obtained in this study: even though a higher initial activity is achieved by the sample without PVA, without the effect of a stabiliser, metal nanoparticles tend to agglomerate to relax the electronic structure and consequently, the long-term use of this catalyst may be prevented due to a higher increment of Pd particle size.

By plotting final conversion against PVA/Pd weight ratio, figure 125 is obtained.

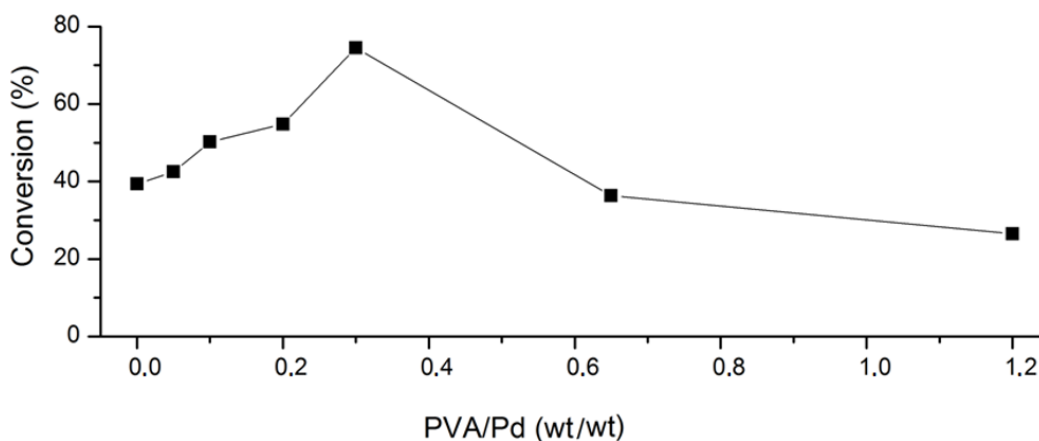


Figure 125. Effect of PVA/Pd weight ratio on catalytic performance. Reaction conditions: $50 \text{ }^\circ\text{C}$, 26.5 mg of catalyst (substrate/metal molar ratio: 2000:1), 0.5 M HCOOH, 750 rpm, 4 h reaction time.

A volcano plot is observed in which the catalyst synthesised with PVA/Pd weight ratio = 0.3 reached the highest final conversion. This means that an equilibrium is necessary probably due to blockage of active sites to a large extent when PVA/Pd weight ratio increases beyond 0.3. As usual, through catalyst characterisation techniques, this effect will be explained and the structure and morphology of this series of catalysts will be studied to find the structure/activity relationship when possible.

5.2.1.1. Catalyst Characterisation

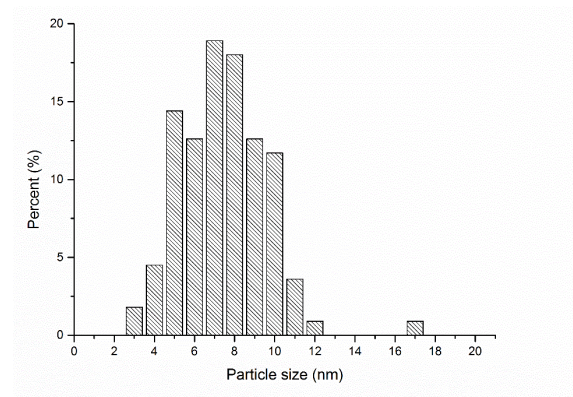
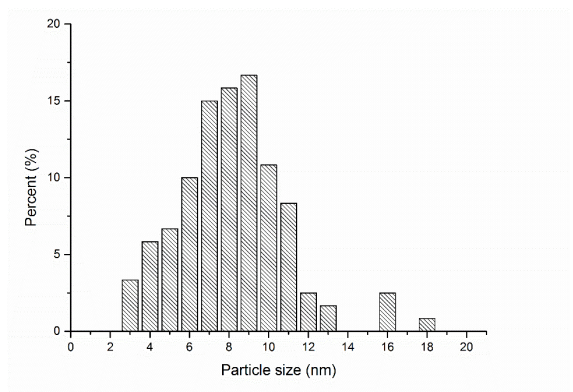
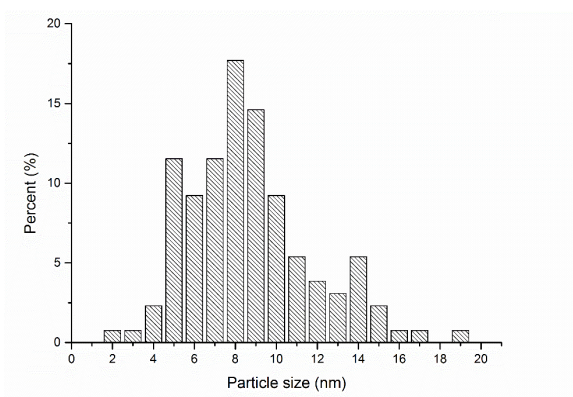
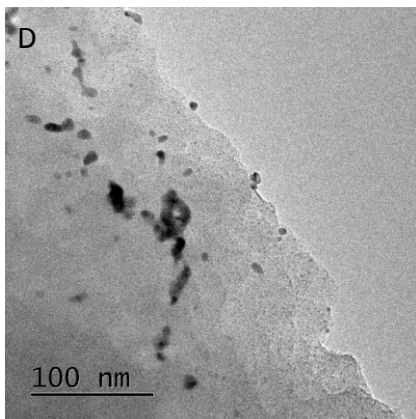
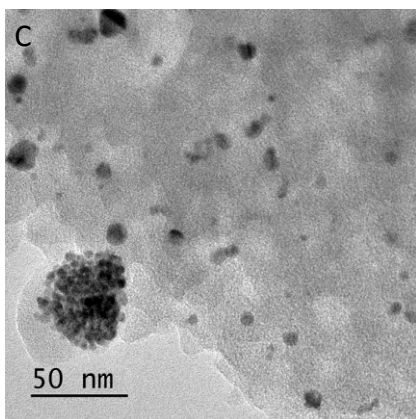
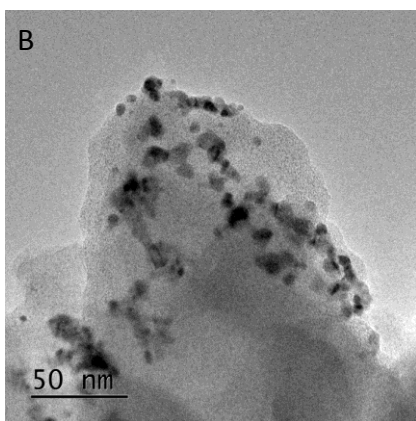
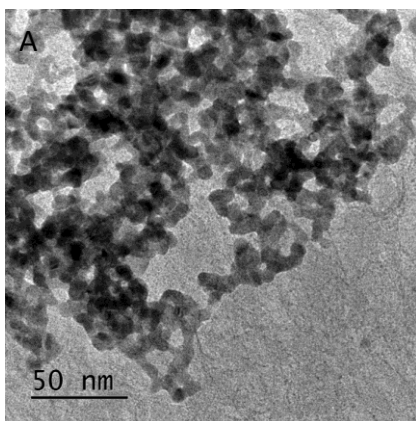
Characterisation of the series of catalysts was performed by means of transmission and scanning electron microscopy, X-ray photoelectron spectroscopy and BET surface area. First, SEM-EDX analysis was performed to confirm the presence of Pd and quantify the Pd loading. Subsequently, by TEM, Pd particle size distribution was calculated, and BET surface area was performed to identify possible changes in the morphology. XPS was used to correlate Pd content on the surface and presence of metallic Pd with changes in the PVA/Pd weight ratio. Table 28 presents elemental chemical composition, mean Pd particle size and surface area analysis of the catalysts studied during the optimisation of the colloidal preparation method.

Table 28. Pd elemental chemical composition, mean Pd particle size and surface area analysis of the catalysts studied during optimisation of the sol-immobilisation method.

Catalyst	PVA/Pd weight ratio	Pd (wt. %) by EDX	Surface area (m ² /g)	Mean particle size (nm)
Pd/AC-0	0	1.03	62	-
Pd/AC-0.05	0.05	1.03	64	8.2 ± 3.0
Pd/AC-0.1	0.1	1.17	62	7.7 ± 2.7
Pd/AC-0.2	0.2	1.11	81	6.9 ± 2.2
Pd/AC-0.3	0.3	1.07	56	4.8 ± 2.0
Pd/AC-0.65	0.65	1.15	57	3.0 ± 0.9
Pd/AC-1.2	1.2	1.25	54	3.1 ± 1.1

SEM-EDX confirmed that Pd metal loading of the as-synthesised Pd catalysts is in concordance with the nominal value of 1 wt. %. Activated charcoal possesses a specific surface area of 64 m²/g approximately, therefore, as in previous chapters, no significant modification of the surface area is produced after the immobilisation process.

Pd mean particle size and particle size distributions of the catalysts were analysed by TEM (Table 28) and representative bright field TEM micrographs are shown in figure 126 for this series of catalysts.



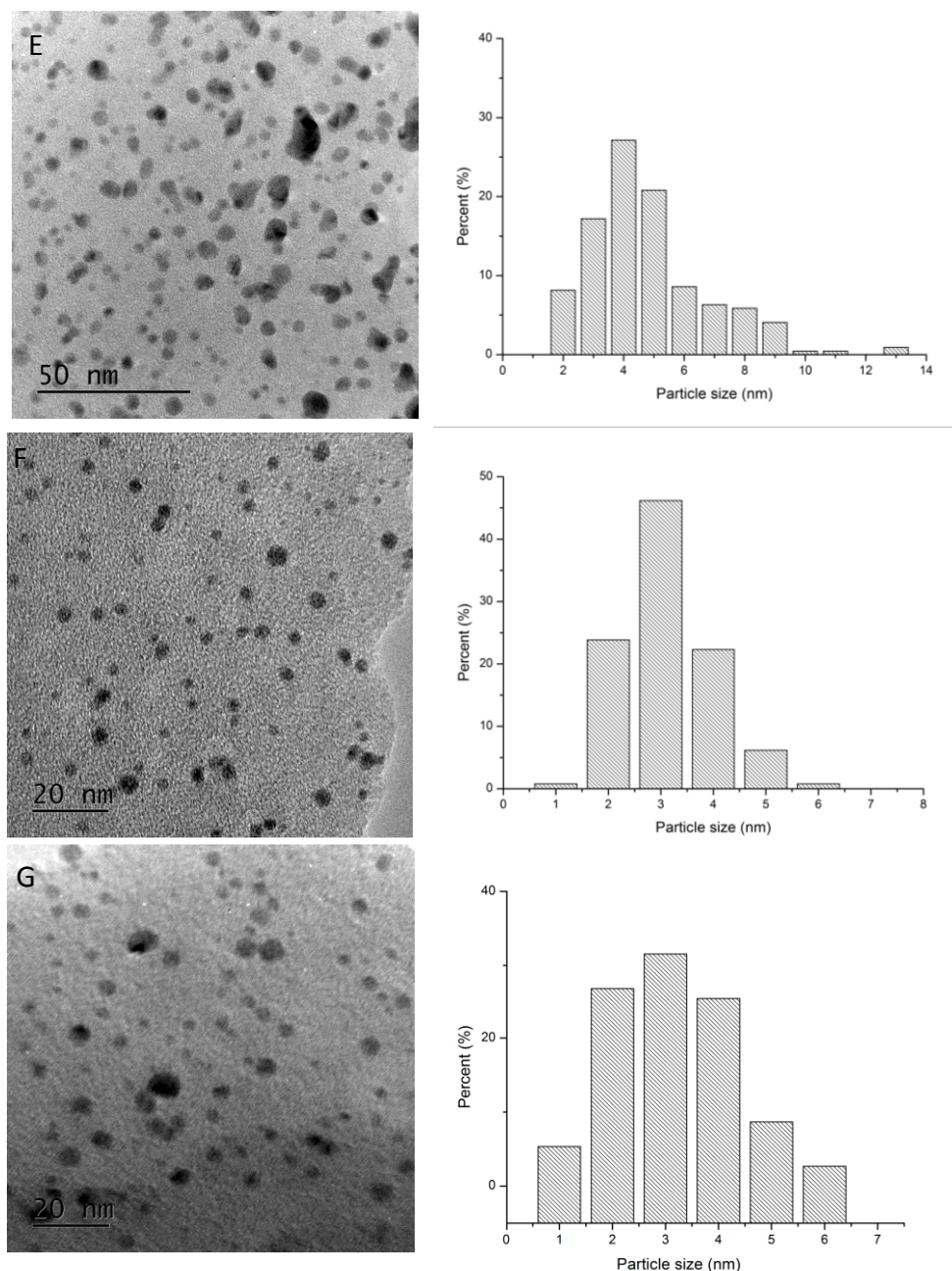


Figure 126. Bright field TEM micrographs and corresponding histograms of the particle size distributions of the catalysts. A: Pd/AC-0, B: Pd/AC-0.05, C: Pd/AC-0.1, D: Pd/AC-0.2, E: Pd/AC-0.3, F: Pd/AC-0.65, G: Pd/AC-1.2.

A significant variation in terms of Pd mean particle size, particle size distribution, and agglomeration of Pd particles on the surface was observed when modifying the PVA amount used during the synthesis of the catalysts. At the lowest PVA/Pd weight ratio (PVA/Pd=0, 0.05, 0.1) agglomeration of Pd nanoparticles and the presence of larger Pd nanoparticles were evident. An inverse relationship was observed in table 28 between PVA/Pd weight ratio and mean particle size: as PVA/Pd weight ratio increased (up to PVA/Pd weight ratio = 1.2), mean Pd particle size decreased, and a steep drop in Pd particle agglomeration was observed up to

PVA/Pd weight ratio = 0.3. Further increment of PVA/Pd weight ratio from 0.65 to 1.2 led to very similar mean Pd particle size (3.0 and 3.1 nm, respectively). In summary, by using a PVA/Pd weight ratio of 0.3, small Pd nanoparticles with narrow particle size distribution was achieved. Although a higher amount of PVA produced smaller Pd nanoparticles, figure 125 shows a decrease in catalytic activity due probably to blockage of Pd active sites due to the high concentration of PVA. Furthermore, at the temperature of the reaction, PVA is soluble in water and so, during the reaction it can slowly solubilise.

XPS analysis of the as-synthesised catalysts was performed to quantify the surface Pd atomic content and identify the Pd electronic states and its percentages. Pd atomic content and percentage of Pd⁰ are shown in table 29.

Table 29. Palladium atomic content and % Pd⁰ on the surface from XPS.

Catalyst	PVA/Pd weight ratio	Atomic % of Pd	% Pd ⁰
Pd/AC-0	0	2.2	44
Pd/AC-0.05	0.05	2.8	72
Pd/AC-0.1	0.1	3.6	64
Pd/AC-0.2	0.2	7.2	38
Pd/AC-0.3	0.3	7.8	39
Pd/AC-0.65	0.65	3.7	62
Pd/AC-1.2	1.2	2.4	30

As in previous chapters, the presence of two peaks corresponding to the Pd 3d_{5/2} and 3d_{3/2} transitions were observed. The peak at 335 eV was assigned to the presence of metallic Pd⁰ and the peak at approximately 337 eV, to the presence of Pd^{II} species, mainly present as PdO nanoparticles.⁵

It has been shown from previous catalytic studies that the amount of metal on the surface can significantly influence catalytic performance.^{6,7} As displayed in table 29, atomic Pd content on the surface increased up to 7.8 % for the catalyst synthesised using PVA/Pd weight

ratio = 0.3. Plotting the Pd content on the surface against PVA/Pd weight ratio, a similar volcano plot to figure 125 was obtained. This result confirms the influence of PVA/Pd weight ratio on the exposure of Pd on the surface and subsequently, on the activity of the catalyst. Figure 127 compares figure 125 with the effect of PVA/Pd weight ratio on Pd content on the surface.

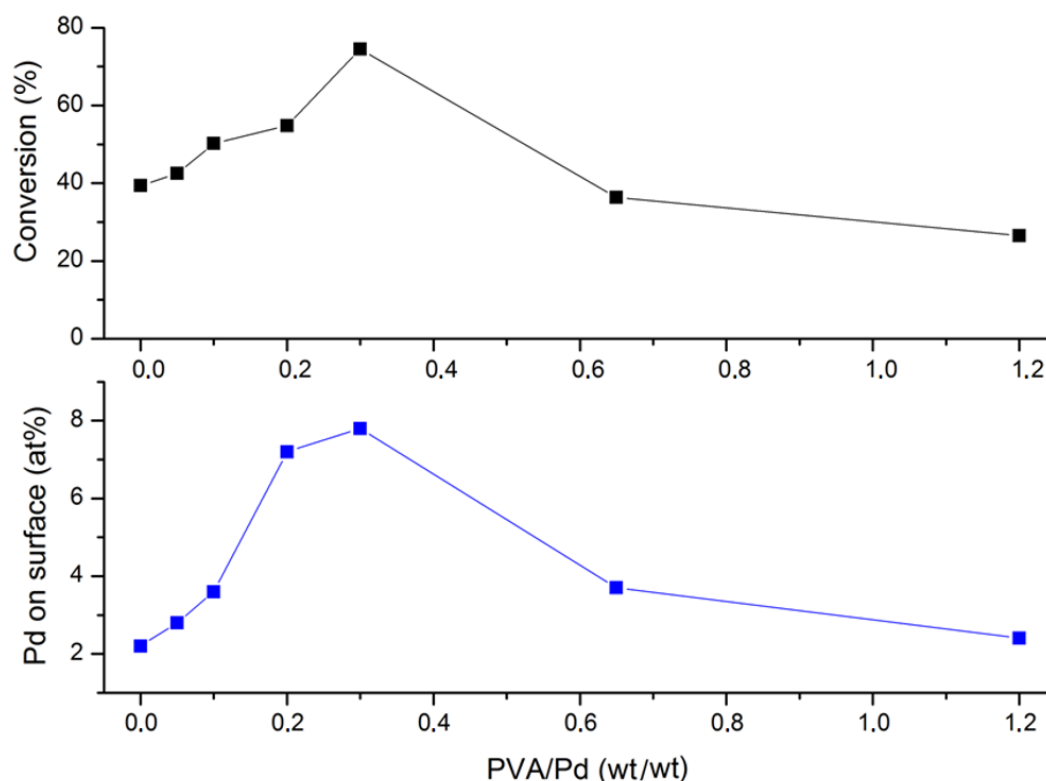


Figure 127. Effect of PVA/Pd weight ratio on catalytic performance and on Pd content on the surface. Reaction conditions: 50 °C, 26.5 mg of catalyst (substrate/metal molar ratio: 2000:1), 0.5 M HCOOH, 750 rpm, 4 h reaction time.

As previously commented, the catalyst synthesised using PVA/Pd weight ratio = 0.3 presents the highest atomic content of Pd on the surface, increasing this the probability for formic acid to reach the active sites and explaining the increment in catalyst activity.

Atomic surface Pd content was observed to increase up to a PVA/Pd weight ratio of 0.3. Further increment above 0.3, produced a sequential decrease. It is expected, as it has been shown from previous studies that the content of Pd on the surface may be affected by (i) particle size of Pd, (ii) amount and presence of PVA and (iii) porosity of the support.⁸

For a PVA/Pd ratio lower than 0.3, it is expected that the dominant factor for Pd exposure on the surface is influenced by particle size effects. This means that large Pd particle size leads to lower surface Pd exposure and therefore, low number of active sites and subsequently, low catalyst activity in terms of corner, edge and flat sites.

Catalysts synthesised using a PVA/Pd weight ratio above 0.3 presented a mean Pd particle size of approximately 3 nm. The pore diameter of active charcoal is around 3.7 nm. This means that smaller Pd nanoparticles than 3.7 nm could lay deeper in the internal surface of the activated charcoal support, and thus, rendering not observable through XPS technique which is surface sensitive. Formic acid molecules would encounter more difficulties reaching the Pd active sites when Pd nanoparticles are supported deep inside the pores and therefore, negatively affecting conversion as observed in figure 127. As previously commented, conversion would also be affected by the blockage of Pd active sites by the presence of PVA. In summary, a delicate balance must be reached. A low PVA/Pd weight ratio produced catalysts with high agglomeration of Pd particles and high mean Pd particle size. Above PVA/Pd weight ratio of 0.3, even though the Pd particle size is small, the blockage of active sites and the presence of nanoparticles inside the pores reduces catalyst activity.

5.2.2. Reusability tests

Reusability of the most active catalysts, 1 wt. % Pd/AC-0.3 was studied at 50 °C and 0.5 M formic acid for 5 subsequent catalytic cycles. Reusability test was carried out by filtrating the catalyst at ambient temperature without further washing and using it for a new reaction under the same reaction conditions. Figure 128 displays the results obtained.

There was a certain loss of catalytic activity for the first three runs. Afterwards, activity reached stabilisation and preserved approximately 69 % conversion of its initial value after the fifth use. As previously commented, this decrease may be attributed to (i) increment in particle size or agglomeration, (ii) decrease of Pd loading by leaching, (iii) poisoning from CO, (iv) strong adsorption of reaction intermediates and/or water.

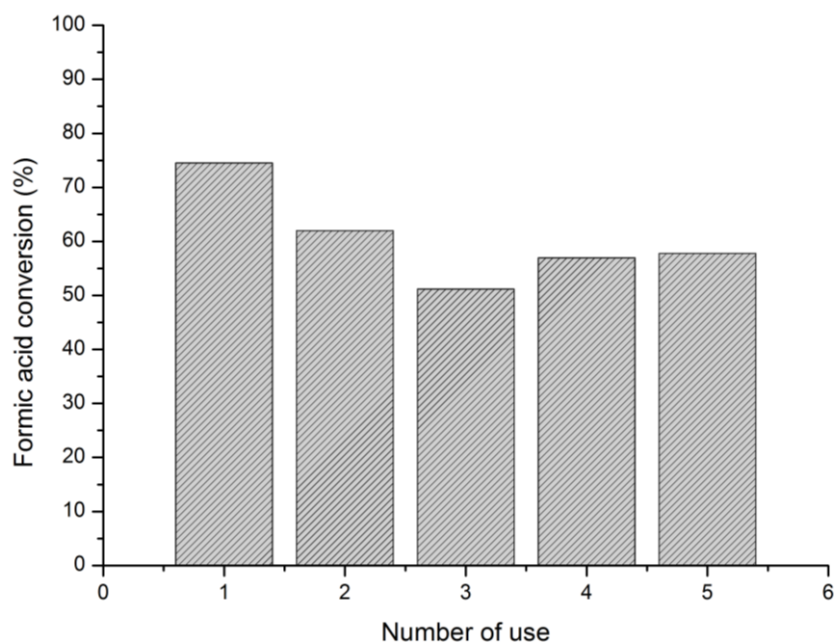


Figure 128. Reusability of Pd/AC-0.3. Reaction conditions: substrate/metal molar ratio: 2000:1, 50 °C, 0.5 M HCOOH, 750 rpm, 4 h reaction time.

Representative images of the used catalyst after five runs and particle size distribution are reported in figure 129.

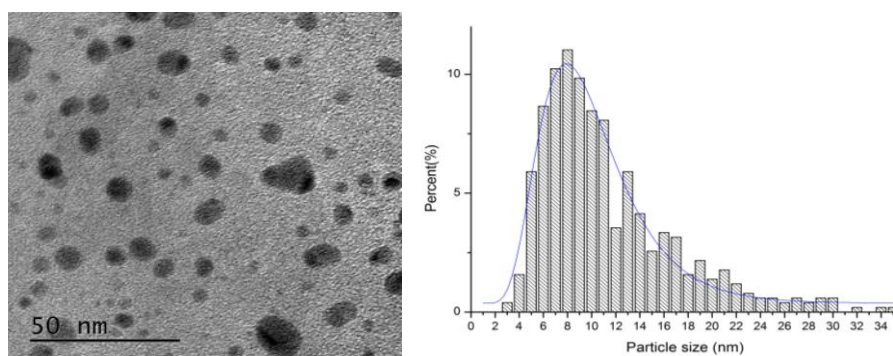


Figure 129. Bright field TEM micrograph and corresponding histogram of the particle size distribution of the Pd/AC-0.3 after 5 cycles of use.

While for the fresh catalyst, mean Pd particle size was 4.8 ± 2.0 nm, after the fifth run, it increased to 6.9 ± 3.1 nm and the particle size distribution was broader: 50 % of the particles were in the range 6 - 11 nm. Sintering phenomena is visible from the snapshot presented. XPS analysis was performed to quantify Pd content on the surface and identified signs of Pd leaching or migration to the inner pores. In this case, Pd surface exposure dropped from 7.8 % for the fresh catalyst to 2.3 % after the fifth use. Since XPS is surface sensitive, the main

reasons for the reduction of Pd metal content are (i) leaching, (ii) migration of the Pd nanoparticles from the external surface to the pores, (iii) increase in Pd mean particle size. In previous chapters, Pd was found to present a relatively good interaction with the support, preventing leaching. Agglomeration was confirmed and could be the main reason but, migration of Pd nanoparticles to the pores may take place to a certain extent as well, however, mean Pd particle size was reasonably higher than mean pore size.

From previous chapters, the most probable reason for the decrease in reusability was attributed to adsorption of reaction intermediates and water on Pd active sites. Due to the slightly low activity of this series of catalysts, enough volume of gas evolved from the reaction could not be collected rendering impossible the analysis of gases, however, in previous chapters CO was found to be in acceptable range also at 50 °C. Sintering phenomena is observed and Pd particle size increased approximately 30 % after the fifth use. Therefore, a sum of several factors seems plausible to explain the decrease in activity.

Once the effect of PVA/Pd on catalyst activity was studied and the preparation method optimised, several catalysts with different Pd loading were synthesised to investigate how this parameter affected catalyst activity and find the optimal value.

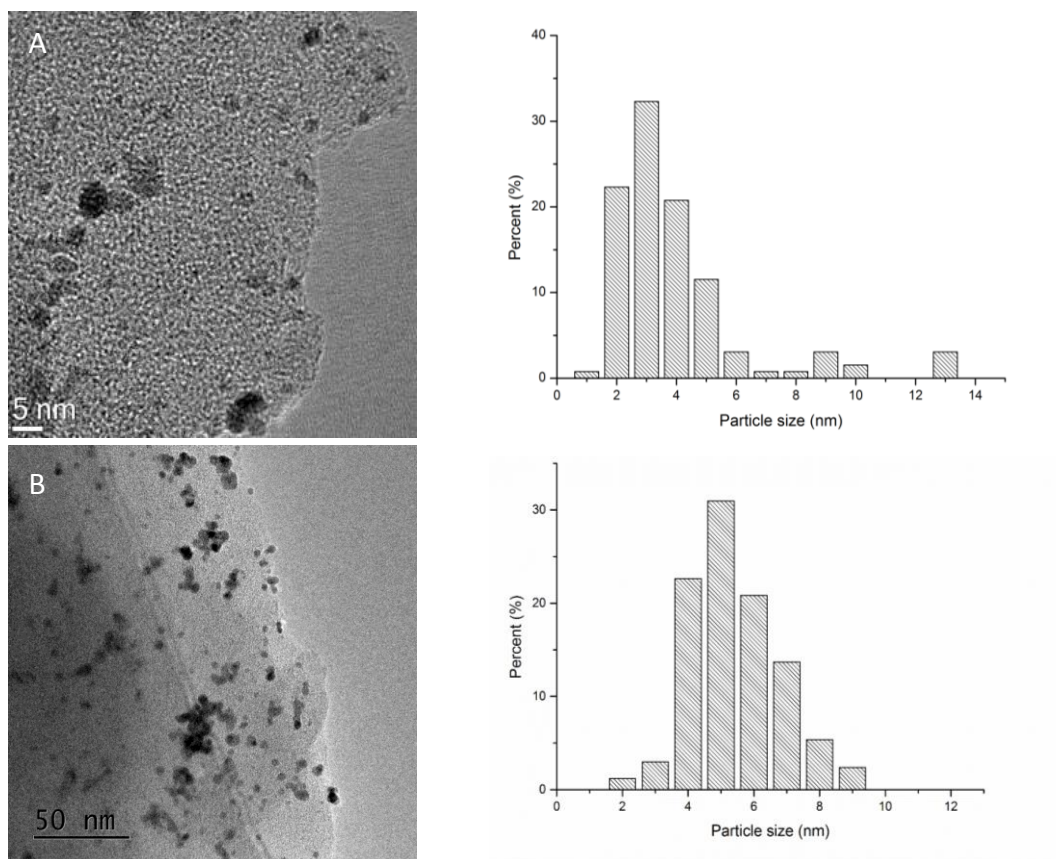
5.2.3. Effect of Pd loading on Pd/AC catalysts

Loading plays an important role in catalyst activity since, among other effects, it can influence nanoparticles dispersion and particle size. Besides 1 wt. % Pd/AC-0.3 already prepared, four more catalysts were prepared by sol-immobilisation using the optimised value PVA/Pd of 0.3. Table 30 displays the initial TOFs achieved and characterisation results obtained of the as-synthesised samples.

Table 30. Structural and chemical composition of the catalysts studied during effect of loading investigation.

Catalyst	TOF (h ⁻¹)	Pd loading (%) EDX	Mean particle size	Surface Area (m ² /g)	% Pd ⁰	At. % Pd
0.2 wt. %-Pd/AC-0.3	278	0.20	3.9 ± 2.3	71	55	1.9
0.5 wt. %-Pd/AC-0.3	272	0.48	4.9 ± 1.3	60	50	4.6
0.7 wt. %-Pd/AC-0.3	239	0.68	4.9 ± 1.4	71	50	4.8
1 wt. %-Pd/AC-0.3	366	1.07	4.8 ± 2.0	56	55	7.9
1.2 wt. %-Pd/AC-0.3	326	1.25	3.8 ± 1.1	35	44	6.9

A loading of 1 wt. % produced the highest catalyst activity of this series of catalysts. First, the theoretical amount of metal was confirmed experimentally by EDX analyses and then the samples were characterised by means of TEM. Figure 130 displays the TEM micrographs and particle size distributions of these catalysts.



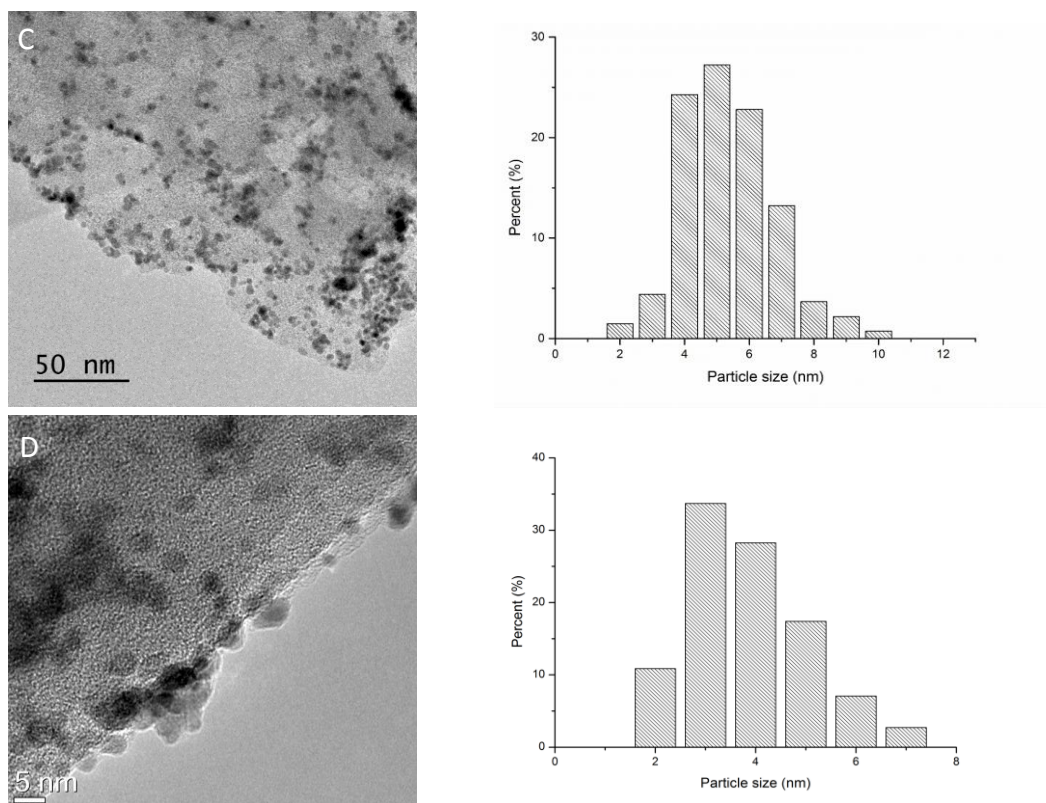


Figure 130. Bright field TEM micrographs and corresponding histograms of the particle size distributions of the Pd/AC catalysts as a function of Pd loading. A: 0.2 wt. % Pd/AC-0.3, B: 0.5 wt. % Pd/AC-0.3, C: 0.7 wt. % Pd/AC-0.3 and D: 1.2 wt. % Pd/AC-0.3.

As observed, even though the catalyst with the highest loading had the lower mean particle size and narrower distribution, effects of agglomeration were observable (as presented in the EDX mapping in figure 131), explaining the decrease in catalytic activity.

XPS analysis revealed the most probable explanation for the behaviour of the observed catalyst activity: the presence of Pd on the surface showed, also in this case, a volcano plot where the amount of Pd on the surface reached the maximum for the 1 wt. % loading, providing a plausible explanation for the maximum of activity produced by this catalyst as shown in table 30.

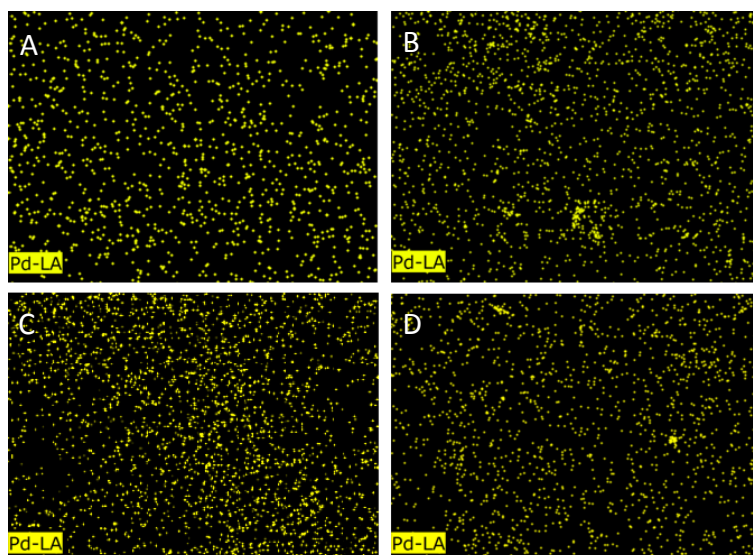


Figure 131. EDX mapping of Pd/AC catalysts as a function of Pd loading. A: loading 0.2 wt. %, B: loading 0.7 wt. %, C: loading 1 wt. %, D: loading 1.2 wt. %.

5.2.4. Characterisation and catalytic performance of $\text{Au}_x\text{Pd}_y/\text{TiO}_2$ for liquid-phase formic acid decomposition

In previous studies, it was reported by many research groups that the combination of Pd with Au may significantly enhance catalytic activity in several catalytic reactions, including oxidation of alkanes, alcohols and polyols, hydrogenation of aldehydes and in situ hydrogen peroxide synthesis.^{9,10} With this aim, the catalytic activity of Au_xPd_y ratio for TiO_2 -supported nanoparticles for the liquid phase decomposition of formic acid was investigated. These catalysts were prepared using the optimised synthesis procedure reported for the supported monometallic Pd catalysts (PVA/M weight ratio = 0.3). Instead of activated charcoal, titania was used as support. This way, a possible comparison with activated charcoal can be performed and spectroscopic characterisation in terms of CO-DRIFTS and FTIR could be carried out. Furthermore, TiO_2 enhances an electronic effect where hypo-d-electronic Ti^{3+} promotes electrocatalytic features of hyper-d-electronic noble catalyst surface atoms which have been related to a decrease in the adsorption energy of CO intermediates and consequently enhancing the mobility of CO groups.¹¹ This could lead to higher resistance against CO poisoning and therefore, result in an improvement of durability of the heterogeneous catalyst.

During the preparation of the catalysts, as explained in Chapter 2, section 2.1.3, UV-vis spectra (200-900 nm) of the colloidal solutions were recorded to follow the reduction of the metal precursors. The UV-vis spectra are presented in figure 132.

In the case of Au, when the AuCl_4^- anion is reduced to Au^0 , the peak at $\lambda_{\text{max}} = 220 \text{ nm}$ disappeared and the plasmon resonance band appeared at approximately 505 nm.¹² It is known that particle size lower than 9 nm produces a plasmon resonance peak below 517 nm.¹³ In the case of Pd, the peak of the metal precursor at 235 nm¹⁴ disappeared after the reduction. Pd^0 plasmon peak was not observable in the UV spectra. Metals for which the imaginary part of the dielectric constant is small, such as Au or Ag, present the strongest, narrowest resonances. Nevertheless, most of the metals possess inter- and intraband transitions that enhances the imaginary part of their dielectric constants. For this reason, Pd among other metals such as Cr, Ru, Pt, and W have weaker, broader plasmonic resonances rendering not visible in the UV spectra.

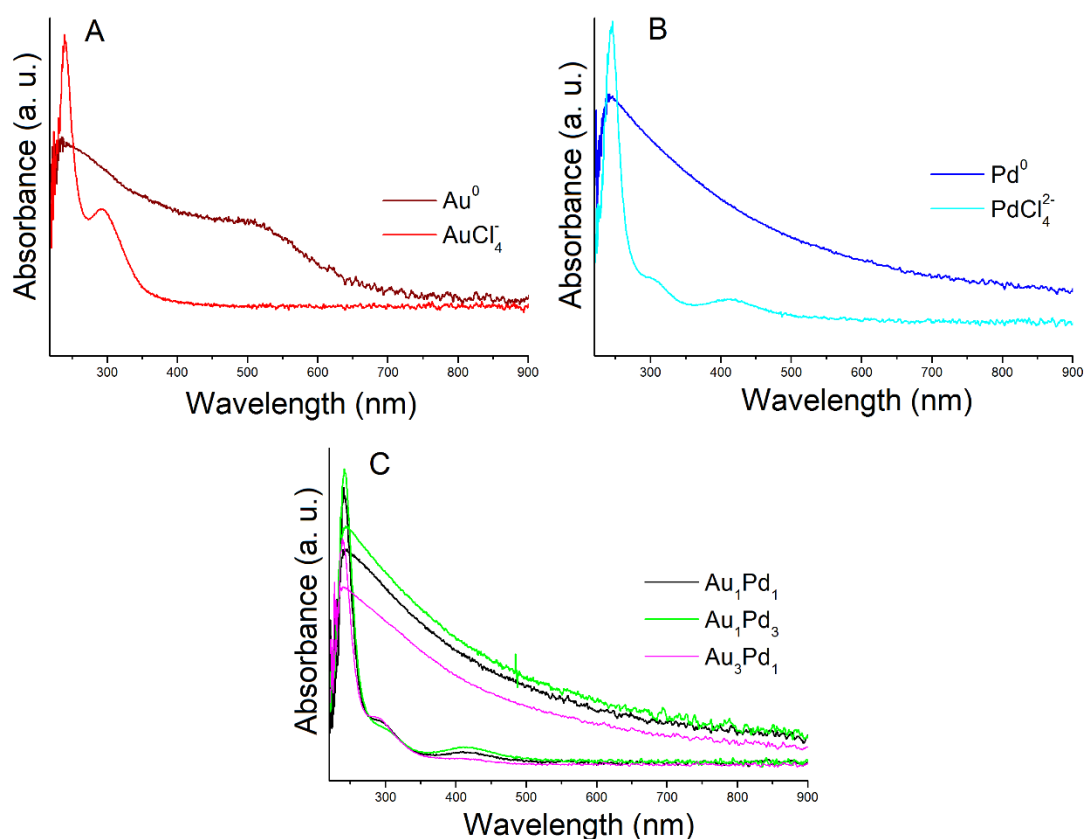


Figure 132. UV-visible spectra: A) reduction of Au; B) reduction of Pd; C) reduction of the alloy Au-Pd.

For bimetallic Au_xPd_y systems, no plasmon resonance band for Au was apparent in the spectra. This behaviour is typical among the bimetallic systems when one of the metals does not present plasmon band. Several examples can be found in literature such as in the formation of Ag-Pd nanoparticles,¹⁵ or Ag-Rh.¹⁶ Specifically for Au-Pd, Deki *et al.* demonstrated that due to the formation of the alloy the plasmon peak of gold disappeared.¹⁷ Same conclusion was reached by Dimitratos *et al.* during the studies about the effect of bimetallic Au-Pd systems on the oxidation of glycerol.¹⁸

Once the formation of the alloys was confirmed and the preparation finished, catalyst activity was evaluated. Figure 133 displays the catalytic performance of the $Au_xPd_y-TiO_2$ catalysts for the liquid-phase formic acid decomposition at 50 °C.

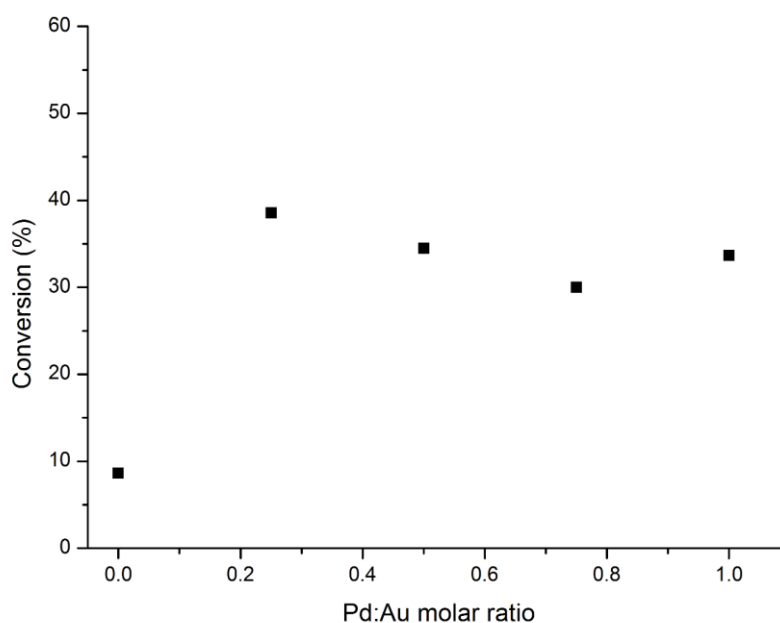


Figure 133. Conversion of formic acid as a function of Pd:Au molar ratio. Reaction conditions: 30 °C, 26.5 mg of catalyst (substrate/metal molar ratio: 2000:1), 0.5 M HCOOH, 750 rpm, 4 h reaction time.

As observed, Au presented very low catalytic activity towards liquid-phase decomposition of formic acid. On the other hand, a small amount of Pd with Au (Au_3Pd_1/TiO_2) produced a synergistic effect exhibiting a high catalytic activity with a TOF of $627h^{-1}$ at 50 °C after 5 min indicating that the presence of a small amount of Pd is essential to significantly promote Au activity for the liquid phase decomposition of formic acid. The observed catalytic behaviour has been already extensively studied elsewhere.^{19,20}

Furthermore, the monometallic Pd catalyst can be compared with the previously presented 1 wt. % Pd/AC-0.3. Table 31 compares both initial TOF and conversion after 4 hours of reaction.

Table 31. Theoretical composition and characterisation data of the monometallic study.

Sample	Initial TOF (h ⁻¹)	Conversion after 4 h (%)
Pd/TiO ₂	71	33
Pd/AC-0.3	366	77

Clearly, for this type of catalysts, using TiO₂ as catalyst support negatively affects catalyst activity. Activated charcoal typically presents a pore size of approximately 3.6 - 3.8 nm, while pore size of titania is about 28 nm. This could prevent nanoparticles from entering the pores and, since pore size is large in the case of titania, allow nanoparticles to be immobilised inside the pores increasing the difficulty for formic acid to find the active sites and consequently, reducing catalyst activity. Furthermore, nanoparticles supported on TiO₂ present typically a hemispherical shape due to the wetting effect of the metal nanoparticle onto metal oxide, reducing so the active metal surface area and thus decreasing catalyst activity.

5.2.4.1. Catalyst Characterisation

Characterisation of the series of catalysts was performed to identify the structure/activity relationship. Techniques used were transmission and scanning electron microscopy, X-ray photoelectron spectroscopy and BET surface area. As previously explained, the first step was the quantification of loading by means of SEM-EDX analysis. TEM was used to calculate the metal particle size distribution and BET surface area was performed to identify possible changes in the morphology. XPS was used to find possible binding energy shifts when alloying the Au and Pd metals.

Table 32 summarises the theoretical composition and characterisation data of the as-prepared catalysts.

Table 32. Theoretical composition and characterisation data of the monometallic-bimetallic study.

Sample	% mol [Pd ²⁺]	% mol [Au ³⁺]	Loading Pd (wt. %) from EDX	Loading Au (wt. %) from EDX	Mean particle size (nm)	Surface Area (m ² /g)	% Pd ⁰
Pd/TiO ₂	1	-	0.96	-	3.6 ± 1.9	51	54
Au ₁ Pd ₃ /TiO ₂	0.75	0.25	0.80	0.13	3.2 ± 2.2	51	56
Au ₁ Pd ₁ /TiO ₂	0.50	0.50	0.70	0.40	3.4 ± 1.1	45	58
Au ₃ Pd ₁ /TiO ₂	0.25	0.75	0.30	0.70	3.0 ± 1.0	50	56
Au/TiO ₂	-	1	-	1.00	4.0 ± 0.9	47	-

First, SEM-EDX mapping was performed to confirm the loading of Pd and provide information in terms of metal dispersion. SEM-EDX mapping presented in figure 134 shows that Au-Pd nanoparticles were well dispersed in the as-synthesised catalysts without areas of high nanoparticle density/agglomeration; and the calculated metal loading and theoretical values were within the experimental error.

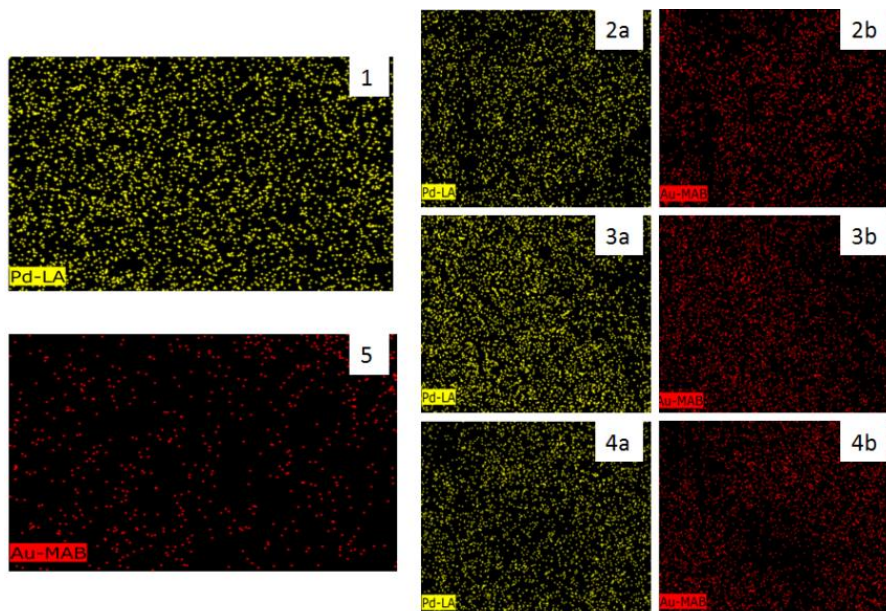
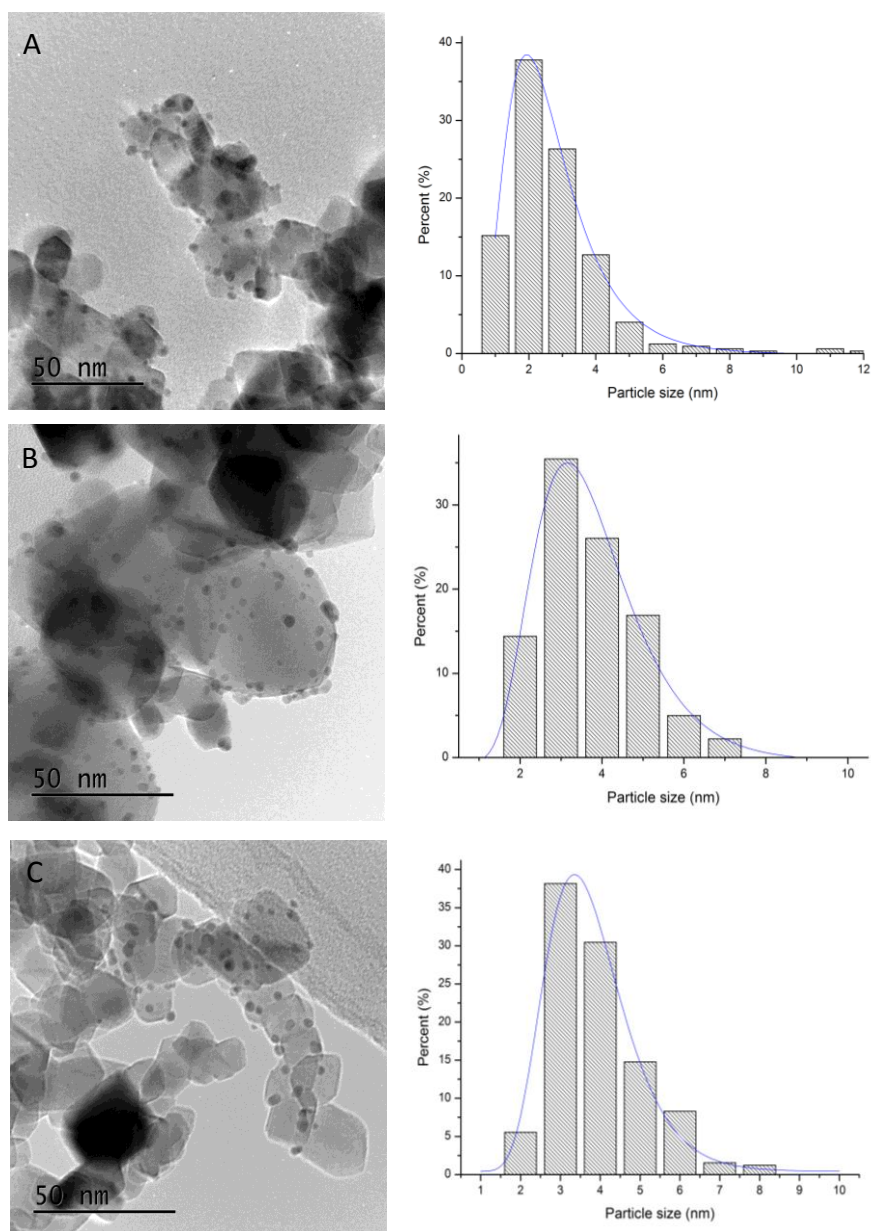


Figure 134. SEM-EDX mapping. 1) Pd/TiO₂, 2a) Pd in Au₁Pd₃/TiO₂, 2b) Au in Au₁Pd₃/TiO₂, 3a) Pd in Au₁Pd₁/TiO₂, 3b) Au in Au₁Pd₁/TiO₂, 4a) Pd in Au₃Pd₁/TiO₂, 4b) Au in Au₃Pd₁/TiO₂, 5) Au/TiO₂.

Mean particle size and particle size distribution were calculated by TEM analysis. Figure 135 displays representative TEM images and particle size distribution of the as-synthesised catalysts.



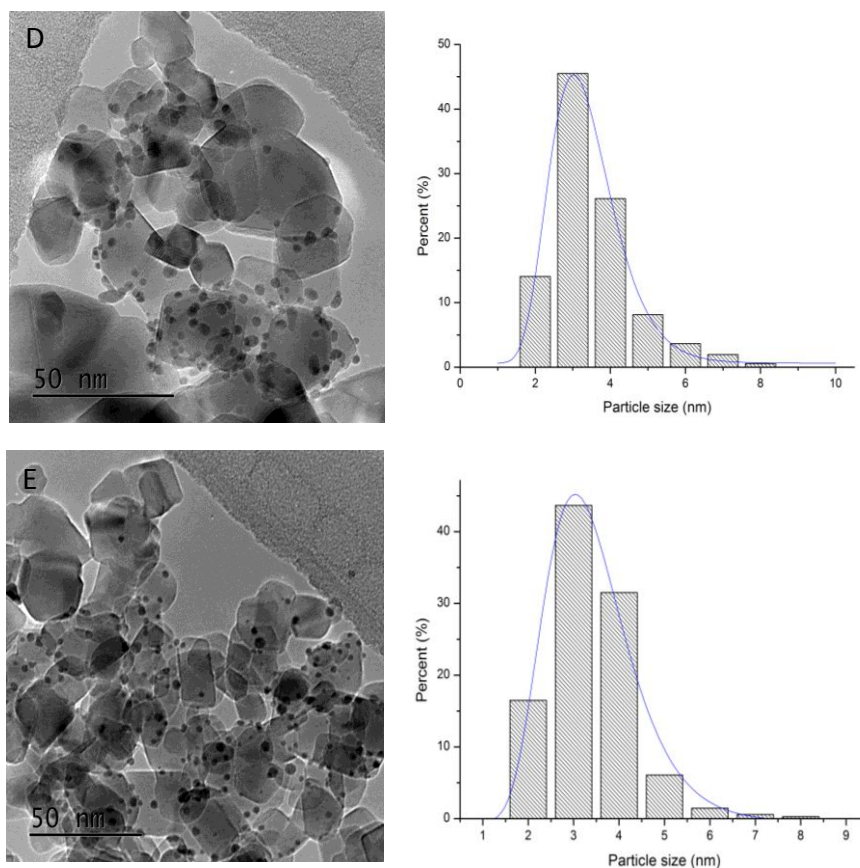


Figure 135. Bright field TEM micrographs and corresponding histograms of the particle size distributions of the catalysts. A: Pd/TiO₂, B: Au₁Pd₃/TiO₂ C: Au₁Pd₁/TiO₂ D: Au₃Pd₁/TiO₂ and E: Au/TiO₂.

TEM analysis presented a good level of dispersion of the supported metal nanoparticles in agreement with SEM-EDX mapping. As already presented in this and in previous studies, a decrease of mean particle size produced a positive catalytic influence for the effective liquid-phase decomposition of formic acid.^{21–24} In this work, the monometallic Pd/TiO₂ and Au/TiO₂ catalysts presented very slightly larger mean particle size (3.6–4 nm range) (Table 32) than the bimetallic counterparts Au_xPd_y/TiO₂ (3–3.4 nm range). This suggests that the co-reduction of Au and Pd enhances the synthesis of slightly smaller mean particle size. Although this difference is almost negligible, so is the difference in activity of the bimetallic catalysts according to figure 133. Hence, confirming that activity and particle size are intimately related.

Furthermore, average pore size of titania P25 is approximately 28 nm, subsequently, a significant number of nanoparticles could be immobilised inside the pores as previously hypothesised, explaining the low activity compared with Pd nanoparticles supported on active

charcoal in which average pore size is 3.7 nm and therefore, preventing the nanoparticles to be immobilised inside the pores since average particle size is typically the same or larger.

Regarding XPS analyses, Au(4f) and Au(4d) + Pd(3d) spectra are shown in figures 136 and 137.

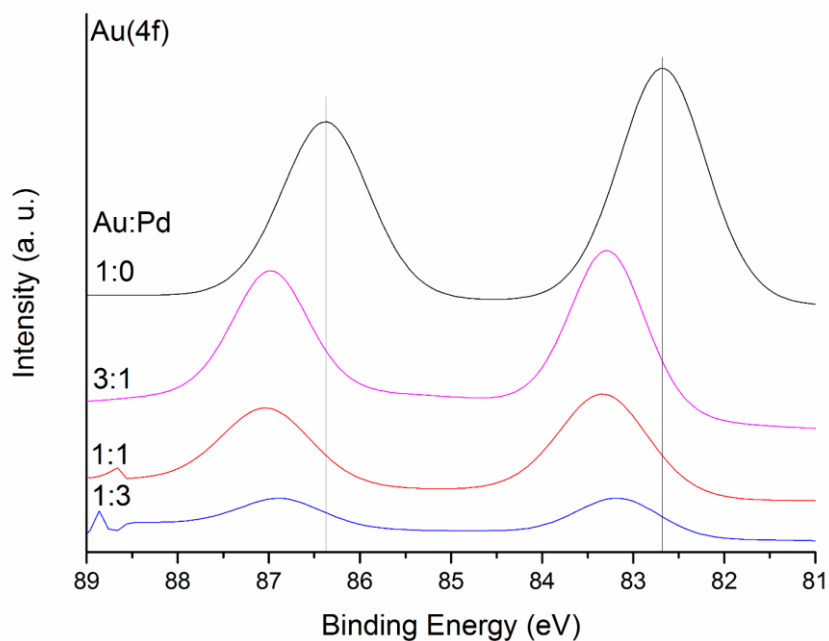


Figure 136. Au(4f) spectra for the series of Au_xPd_y/TiO₂ catalysts.

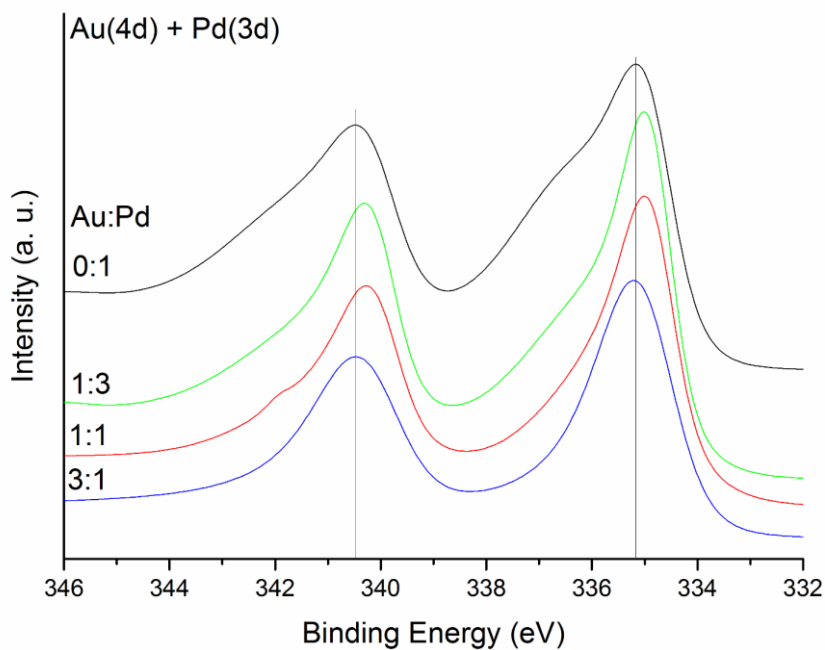


Figure 137. Au(4d) + Pd(3d) spectra for the series of Au_xPd_y/TiO₂ catalysts.

The peaks at 83-84 eV and 87 eV associated to Au4f_{7/2} and Au4f_{5/2} respectively are related to Au foil. The shifts observed in the binding energy of the peaks have been previously studied.²⁵ Table 33 presents the binding energy shifts when forming the alloy. Note % mol are showed as theoretical values.

Table 33. Binding energy and binding energy shifts of the monometallic-bimetallic study.

Sample	% mol	% mol	B.E. (eV)	B.E. (eV)	Δ B.E. (eV)	Δ B.E. (eV)
	[Pd ²⁺]	[Au ³⁺]	Pd3d _{3/2}	Au4f _{7/2}	Pd3d _{3/2}	Au4f _{7/2}
Pd/TiO ₂	1	-	340.459			
Au ₁ Pd ₃ /TiO ₂	0.75	0.25	340.274	83.148	-0.1849	0.4731
Au ₁ Pd ₁ /TiO ₂	0.50	0.50	340.295	83.318	-0.1642	0.6428
Au ₃ Pd ₁ /TiO ₂	0.25	0.75	340.470	83.281	0.0108	0.6061
Au/TiO ₂	-	1		82.675		

For Pd, only the Pd3d_{3/2} peak will be used to analyse the binding energy shifts since in the bimetallic catalysts there is an overlap of the peak Au4d_{5/2} with the Pd3d_{5/2} peak.²⁶⁻²⁸ As demonstrated by Radnik *et al.*,²⁹ the relative binding energy of Au4f_{7/2} shifts at 83 eV, therefore, Au in the as synthesised catalysts is in the metallic state. XPS provides information about the net electron transfer during bimetallic alloying, however, due to the complicated combination of initial and final state effects, caution has to be taken.³⁰ In terms of Pauling electronegativities of Au (2.54) and Pd (2.20), this suggests that a slight electron transfer may occur from Pd to Au. Regarding previous studies, when forming the alloy, binding energy of both Pd and Au tends to decrease. Moreover, particle size was found to have also an effect on the binding energy of metals.^{26,31,32} Regarding figure 136, opposite to the previous studies referenced, the peaks attributed to Au4f_{7/2} shifted to a higher binding energy (82.765 eV for Au monometallic, and between 83.148 and 83.318 eV for the alloys). This shift can be explained if particle size variations are considered. In the case of pure Au, mean particle size was 4 nm, while, for the alloys, it decreased to a range between 3 and 3.4 nm. Even though this is not a significant change, the electronic structure of the atoms may be modified to a certain extent and lead the shift to higher energy.

The same explanation applies for Pd. Regarding the mean particle size presented in table 32 and binding energy shifts from table 33 and figure 137, a shift to lower binding energies was observed when forming the alloy (it decreases from 340.459 eV for monometallic Pd, to approximately 340.3 eV) however, for Au:Pd ratio of 3:1, binding energy shifted to a higher value (340.470 eV), explained once again with the reduction of mean particle size of this catalyst to 3 nm.

Regarding oxidation state of Pd, negligible differences were observed when modifying Au content. Pd⁰ species very slightly increased until Au:Pd ratio of 1:1 and decreased for higher Au content, however, these variations were within the experimental error, consequently, no conclusive data can be extrapolated.

In terms of surface area, for TiO₂ P25 it is approximately 63 m²/g, while for the as-synthesised catalysts, it decreased approximately 20 % possibly due to factors such as coverage of PVA; nanoparticles immobilised in the mouth of the pores, blocking them; or intrinsic error of the system.

Due again to the low activity of this series of catalysts, reproducible analysis of gases could not be performed.

5.3. Conclusions

This chapter started with the study of the effect of stabiliser (PVA), synthesising Pd colloidal nanoparticles by varying the amount of stabiliser (PVA/Pd weight ratio) and supporting them on activated charcoal. This study related the amount of stabiliser with the final morphology of the supported nanoparticle (Pd particle size, particle size distribution, Pd oxidation state and surface exposure of Pd). A progressive decrease in the mean Pd particle size was observed when increasing PVA/Pd weight ratio up to 0.3. Further increment of PVA/Pd ratio from 0.65 to 1.2 did not present an effect on particle size. When modifying Pd/PVA weight ratio, two matching volcano plots were observed: catalytic activity and Pd atomic surface content presented the same trend. Below Pd/PVA weight ratio of 0.3 high agglomeration was observed and above 0.3, the blockage of active sites and presence of nanoparticles inside the pores reduces catalyst activity. Therefore, the observed catalytic activity could be attributed to (i) surface Pd exposure, (ii) Pd sites accessibility (coverage of the active sites) and (iii) mean Pd particle size.

Reusability test was performed for the most active monometallic Pd catalyst (Pd/PVA= 0.3) showing after 5 uses a drop of 31 % of the initial activity, probably caused by the growth of Pd nanoparticles besides the usual adsorption of intermediates or water on the active sites as observed throughout this Thesis.

In terms of Pd loading, it was investigated from 0.2 wt. % to 1.2 wt. %, showing the highest activity for the catalysts with 1 wt. % Pd loading. Presence of Pd on the surface was found to be the most probable reason for the changes in activity due to Pd loading rather than mean Pd particle size which was in the range 3.9 - 4.8 nm and was not altered at different Pd loadings.

In the case of TiO₂, and using the optimised experimental conditions, a similar particle size was observed with a higher percentage of metallic Pd species than the analogous Pd/AC sample, however, activated charcoal-supported Pd nanoparticles showed higher catalytic performance. This difference was attributed to (i) the higher surface percentage of metallic Pd for the Pd nanoparticles supported on activated charcoal and (ii) to the shape of the supported Pd nanoparticles: on activated charcoal Pd nanoparticles were spherical whereas hemispherical Pd nanoparticles were observed on titania, hence, decreasing the accessible active surface area exposed and subsequently, the observed catalytic activity.

A range of bimetallic Au-Pd catalysts were synthesized and the catalytic performance was evaluated. The highest catalytic activity was found to be with an optimum ratio of Au/Pd=1:3 suggesting that the addition of a small amount of Pd to Au produces a synergistic effect that enhances catalytic activity.

5.4. References

- 1 N. Dimitratos, A. Villa, L. Prati, C. Hammond, C. E. Chan-Thaw, J. Cookson and P. T. Bishop, *Appl. Catal. A Gen.*, 2016, **514**, 267–275.
- 2 S. M. Rogers, C. R. A. Catlow, C. E. Chan-Thaw, D. Gianolio, E. K. Gibson, A. L. Gould, N. Jian, A. J. Logsdail, R. E. Palmer, L. Prati, N. Dimitratos, A. Villa and P. P. Wells, *ACS Catal.*, 2015, **5**, 4377–4384.
- 3 S. M. Rogers, C. R. A. Catlow, C. E. Chan-Thaw, A. Chutia, N. Jian, R. E. Palmer, M. Perdjon, A. Thetford, N. Dimitratos, A. Villa and P. P. Wells, *ACS Catal.*, 2017, **7**, 2266–2274.
- 4 M. C. Militello and S. J. Simko, *Surf. Sci. Spectra*, 1994, **3**, 387–394.

- 5 M. C. Militello and S. J. Simko, *Surf. Sci. Spectra*, 1994, **3**, 395–401.
- 6 C. Bianchi, F. Porta, L. Prati and M. Rossi, *Top. Catal.*, 2000, **13**, 231–236.
- 7 F. Porta and L. Prati, *J. Catal.*, 2004, **224**, 397–403.
- 8 C. L. Bianchi, S. Biella, A. Gervasini, L. Prati and M. Rossi, *Catal. Letters*, 2003, **85**, 91–96.
- 9 N. Dimitratos, J. A. Lopez-Sanchez, D. Morgan, A. F. Carley, R. Tiruvalam, C. J. Kiely, D. Bethell and G. J. Hutchings, *Phys. Chem. Chem. Phys.*, 2009, **11**, 5142–5153.
- 10 J. Pritchard, L. Kesavan, M. Piccinini, Q. He, R. Tiruvalam, N. Dimitratos, J. A. Lopez-Sanchez, A. F. Carley, J. K. Edwards, C. J. Kiely and G. J. Hutchings, *Langmuir*, 2010, **26**, 16568–16577.
- 11 S. Bagheri, N. Muhd Julkapli and S. Bee Abd Hamid, *Sci. World J.*, 2014, **2014**, 21.
- 12 J. A. Lopez-Sanchez, N. Dimitratos, P. Miedziak, E. Ntainjua, J. K. Edwards, D. Morgan, A. F. Carley, R. Tiruvalam, C. J. Kiely and G. J. Hutchings, *Pccp*, 2008, **10**, 1921–30.
- 13 S. Link and M. A. El-Sayed, *J. Phys. Chem. B*, 1999, **103**, 4212.
- 14 Q.-L. Zhu, N. Tsumori and Q. Xu, *Chem. Sci.*, 2014, **5**, 195–199.
- 15 K. Tedsree, T. Li, S. Jones, C. W. A. Chan, K. M. K. Yu, P. a J. Bagot, E. a Marquis, G. D. W. Smith and S. C. E. Tsang, *Nat. Nanotechnol.*, 2011, **6**, 302–307.
- 16 K. Hirakawa and N. Toshima, *Chem. Lett.*, 2003, **32**, 78–79.
- 17 S. Deki, K. Akamatsu, Y. Hatakenaka, M. Mizuhata and A. Kajinami, *Nanostructured Mater.*, 1999, **11**, 59–65.
- 18 N. Dimitratos, J. A. Lopez-sanchez, D. Lennon, F. Porta, L. Prati and A. Villa, *Catal. Letters*, 2006, **108**, 147–153.
- 19 X. Gu, Z. Lu, H. Jiang, T. Akita and Q. Xu, *J. Am. Chem. Soc.*, 2011, 11822–11825.
- 20 M. S. Chen, K. Luo, T. Wei, Z. Yan, D. Kumar, C. Yi and D. W. Goodman, *Catal. Today*, 2006, **117**, 37–45.
- 21 L. I. Songju, Z. Xin and T. Weiquan, *J. Phys. Chem. A*, 2012, **116**, 11745–11752.
- 22 N. Wang, Q. Sun, R. Bai, X. Li, G. Guo and J. Yu, *J. Am. Chem. Soc.*, 2016, **138**, 7484–7487.
- 23 D. Liu, Z. Y. Gao, X. C. Wang, J. Zeng and Y. M. Li, *Appl. Surf. Sci.*, 2017, **426**, 194–205.
- 24 D. A. Bulushev, L. G. Bulusheva, S. Beloshapkin, T. O'Connor, A. V. Okotrub and K. M. Ryan, *ACS Appl. Mater. Interfaces*, 2015, **7**, 8719–8726.
- 25 A. Villa, N. Dimitratos, C. E. Chan-Thaw, C. Hammond, G. M. Veith, D. Wang, M. Manzoli, L. Prati and G. J. Hutchings, *Chem. Soc. Rev.*, 2016, **45**, 4953–4994.
- 26 Y. Lee and Y. Jeon, *J. Korean Phys. Soc.*, 2000, **37**, 451–455.
- 27 M. B. Griffin, A. A. Rodriguez, M. M. Montemore, J. R. Monnier, C. T. Williams and J. W. Medlin, *J. Catal.*, 2013, **307**, 111–120.
- 28 M. O. Nutt, K. N. Heck, P. Alvarez and M. S. Wong, *Appl. Catal. B Environ.*, 2006, **69**, 115–125.
- 29 J. Radnik, C. Mohr and P. Claus, *Phys. Chem. Chem. Phys.*, 2003, **5**, 172–177.
- 30 W. F. Egelhoff, *Surf. Sci. Rep.*, 1987, **6**, 253–415.
- 31 Z. Li, F. Gao, Y. Wang, F. Calaza, L. Burkholder and W. T. Tysoe, *Surf. Sci.*, 2007, **601**, 1898–1908.
- 32 C. W. Yi, K. Luo, T. Wei and D. W. Goodman, *J. Phys. Chem. B*, 2005, **109**, 18535–18540.

6. CONCLUSIONS AND RECOMMENDED FUTURE WORK

6.1. Conclusions

The ability to deliberately and successfully transform unusable energy into usable one has been undoubtedly one of the key aspects of human being's success. At this point in humankind History, energy has become a bottleneck in the research of new technologies and progress. For this purpose, new sources of energy are being investigated and the sustainable production of this energy is nowadays a key requirement. Hydrogen has become one of the most promising energy vectors in the last few years due to several advantages compared with conventional sources of energy: it can be generated, transported to the locations where needed and stored until being used. Fuel cells represent one of the most promising energy-related uses for hydrogen. Specifically, for proton exchange membranes, these generate electricity with the only by-product being water, which ticks all the boxes related to environmental safety and worldwide sustainability. Nevertheless, the hydrogen fuel used in most cases utilises the consumption of fossil fuels. Consequently, the development of effective sustainable energy production processes is required. For this reason, formic acid presents itself as one of the most suitable compounds to be used in a hydrogen economy due to its properties and furthermore, if considering that it is a major product formed during biomass processing, it completes the "green circle".

This Thesis evaluates the catalytic liquid-phase formic acid decomposition as a model reaction for hydrogen generation. **Chapter 3** started this investigation using a commercial Pd/C catalyst as a reference point. One of the fundamental studies performed was the optimisation of the reaction conditions to identify a kinetically limited reaction. Under these conditions, and 30 °C, an initial TOF of 1136 h⁻¹ was measured.

Reusability tests were carried out and, as a result, 72 % of its original conversion after the fifth cycle was obtained. Leaching, CO evolution and agglomeration of Pd nanoparticles were found to be negligible at the conditions of the experiment. By means of TGA-MS, water and formic acid intermediates such as CO₂ were found adsorbed on the used catalyst surface at temperatures higher than 100 °C probably due to strong interactions of polar water molecules with the surface. Therefore, water and possibly other intermediates (CO₂) to a lesser extent

are occupying active sites on the catalyst surface and rendering a less active catalyst in subsequent runs.

Reusability was improved using a continuous flow set up. An innovative method, never seen before in literature for this only purpose, was developed. In this technique, both reaction and heat treatment take place in the same oven. At 180 °C, a significant portion of the water and reaction intermediates adsorbed into the catalyst surface were desorbed and the active sites liberated. Initial activity was almost completely recovered.

HCOOH dissociation is known to follow two paths: through carboxylic (COOH) and formate (OOCH) intermediates depending on which hydrogen bond is broken first. By the study of the Kinetic Isotope Effect (KIE) it was found that C–H bond cleavage was the kinetically relevant step and so, formate decomposition represents the most probable pathway. Furthermore, in order to support the experimental data observed and expand the knowledge obtained from this reaction, Density Functional Theory was performed to identify reaction pathways and break them down to study the kinetics of each elementary step. By calculating the potential energy of elementary steps and its transition states, it was found that the main causes for CO evolution are the presence of Pd(001), and cis configuration, and therefore, COOH* decomposition explaining the low concentration of CO evolved since the formate intermediate is the main pathway.

Once liquid-phase formic acid decomposition was studied using the commercial catalyst and computational methods, in **Chapter 4**, a series of catalysts with different properties in terms of particle size, ox. State, dispersion and metal surface coverage were synthesised by two preparation methods. To start, it was found that sol-immobilisation technique presented catalysts with higher initial activity than the catalysts prepared by impregnation since PVA ligand inhibits the oxidation of the Pd surface and also the colloidal method leads to smaller mean particle size. The location of the nanoparticles was evaluated by means of 3D tomography. A certainly higher presence of nanoparticles was found inside the inner wall for the catalysts prepared by impregnation method in comparison with the colloidal method. Nevertheless, a similar final conversion was reached by the nanoparticles supported in the same type of carbon nanofiber due to the presence of PVA occupying active sites.

In terms of graphitisation degree, catalytic performance increased when the annealing temperature was higher and therefore, structural order. Through catalyst characterisation

results, it was observed that the increment from 700 to 1500 °C produced a smaller change in the graphitisation degree than the increment from 1500 to 3000 °C, however, catalyst activity was greatly enhanced by the samples supported on carbon nanofibers treated at 1500 °C. At 3000 °C structural order was significantly improved, although the increment in activity was not proportional. This means that starting from amorphous carbon, small rearrangements in structural order have a remarkable impact in catalyst activity but above a certain level, this relationship between order and activity becomes less noticeable. At this point of the research, economical balances are put aside, however, as a brief note, the slight difference in activities observed for the catalysts supported on CNF-HHT and CNF-LHT will not justify the energy cost required to increase in 1500 °C to fully graphitise the nanofiber. As said, this statement focusses only in activity and no other parameters are being considered. In terms of functionalisation, even though the results were not undoubtedly conclusive, an increment in catalytic activity was observed for the catalyst using oxygen functionalised carbon nanofibers due most probably to a favoured deprotonation step because of the presence of O⁻ on the surface which accelerates dehydrogenation of formic acid. Nevertheless, this presence of O⁻ led to early deactivation of the catalyst due to CO formation. Once the most active catalysts were identified and the reaction conditions optimised, initial TOF was calculated to be 979 h⁻¹ achieved by Pd₅₁/CNF-HHT, the most active catalyst in this series. This is a very remarkable result in comparison with the commercial Pd/C catalyst. Reusability studies exhibited again a certain depletion in activity for each run. Leaching, agglomeration of nanoparticles, and CO poisoning (at 30 °C) were also negligible, hence, the deactivation was attributed to adsorption of reaction intermediates or water on the catalyst surface, as previously confirmed, and possibly, migration of nanoparticles during the reaction from the outer wall of the nanofiber to the inner wall. Once the best preparation method was identified, a set of parameters were modified in **Chapter 5** to investigate the effects it had on the structure and morphology of the catalysts using colloidal methods. The amount of stabiliser was found to have a crucial importance on the final morphology of the supported nanoparticle and therefore, in catalyst activity. It was found that without any PVA, the catalyst presents a remarkably high activity, however, the surface suffers from deactivation due to the agglomeration of nanoparticles. When adding different amounts of PVA, a volcano plot is observed producing a PVA/Pd ratio of 0.3 the most

active catalyst. Below 0.3, agglomeration limited catalyst activity and above 0.3, active sites are presumably blocked by PVA, and nanoparticles are small enough to penetrate the pores which render impracticable for formic acid molecules and thus, reduces catalyst activity.

As in previous chapters, reusability test exposed a decrease of catalyst activity, in this case of approximately 30 % of its initial value in its third run, however, in this catalyst, activity keeps stable during the third fourth and fifth runs probably due to a stabilisation of particles growth. Pd loading was investigated and the catalyst with 1 wt. % Pd loading reached the highest catalytic activity most probably due to the higher presence of Pd on the surface.

Titania (TiO_2) was used as an alternative support to carbon or carbon nanofibers since they are expected to produce less CO sensitive catalysts, however, catalytic activity was very low compared with its carbonaceous analogues due mainly to the lower presence of metallic Pd on the surface due to the bigger pore size; and possibly also to the hemispherical shape of the nanoparticles due to the wetting effect.

Once formic acid decomposition was studied to a large extent with a monometallic Pd catalyst, an initial introduction to bimetallic Au-Pd catalysts (varying Au:Pd molar ratio) was performed in order to identify more possible pathways to continue in this research. An Au/Pd molar ratio of 1:3 was observed to produce the highest catalyst activity suggesting that even though Au is not active in monometallic state, the addition of Pd to Au produces a synergistic effect enhancing catalytic activity. A net electron transfer during bimetallic alloying takes place affecting binding energies, although this could not be quantified. In the next section, a method to shed some light on this synergistic effect is explained.

6.2. Recommended future work

This work has tackled some challenges and sheds some light on the combination of experimental and computational studies, however, new research pathways have been opened.

Continuous flow set up was only used as an introductory study. Very promising results were obtained in which useful life of the catalyst was greatly extended in comparison with batch configuration. From this starting point, a set of parameters can be tuned to identify the existence of intraphase mass transfer limitations and therefore find the conditions where the reaction is under chemical kinetic control.¹ Nevertheless, for this purpose, stabilisation of

conversion for a certain amount of time is required. In this work, continuous flow set up produced a peak of activity and subsequent drop of conversion after a short period. The reason for this deactivation was most probably due to the adsorption of water and reaction intermediates since, by increasing the temperature after the reaction, these adsorbed species were desorbed to a great extent. For this reason, trying to avoid the adsorption of species onto the active sites has become the most important objective for future research in this field. To try to overcome water adsorption and formate or other intermediate species on the catalyst surface, one possible solution may lie on the bimetallic alloying of Pd with Au since gold is known to form very weak Au-O bonds and generally thermally unstable.² In this work, Au-Pd alloys were studied as a starting point as well, however, the reason for the synergistic effect observed between Au and Pd could not be addressed. By performing X-ray absorption near-edge structure (XANES), and with the XPS results obtained, it would be possible to calculate the net charge redistribution at the Au and Pd sites according to the procedure explained by Jeon *et al.*³ This way, the binding energy shifts would be normalised taking into account the work function, relaxation states and d and non-d charge transfers. By calculating the net charge redistribution, it would allow a conclusive comparison between samples. XANES, however, was not available, but would shed light into the interaction between Pd and Au when forming the alloy and subsequently relate Au:Pd ratio with the two types of charge transfer (d and non-d) and so, probably unveil the reason for the synergistic effect observed in the performance study.

Another possible solution for water adsorption could possibly lie on pH variations of the aqueous media. In this work, only additive-free liquid-phase formic acid decomposition was performed, although additives have been reported to enhance catalyst activity in formic acid decomposition under a slightly basic environment. For this purpose, the use of NaCOOH has been demonstrated to be beneficial for catalyst activity since it is believed to increase contact probabilities of formate ions with metal catalytic sites,⁴⁻⁷ however, the stability of the catalyst still needs to be extensively studied. Since formate competes with other ions (including water and reaction intermediates) in adsorbing onto the active site, this surely is beneficial in decreasing the number of active sites occupied by water and other reaction intermediates which will not lead to hydrogen, and probably increase catalyst stability and activity as well.

When trying to improve reusability results, besides water, CO, as a reaction by-product, plays a crucial role. Even though CO evolution throughout this work has been always within the established limits for PEM fuel cells usage under mild conditions, very high CO concentration was found at 70 °C. PEM fuel cells are known to produce heat that, depending on the ambient temperature, may be difficult to exchange. For this purpose, a possible commercial catalyst used to decompose formic acid to hydrogen for PEM fuel cells usage should keep CO concentration below the limit of 20 ppm up to 90-100 °C. By means of DFT it was found that Pd(001) surface leads to the highest concentration of CO. As expected, the most common morphology in a catalyst exposes the lowest surface energy facets, which, in the case of Pd is the (111). On the contrary, Pd(001) surface is the most energetically unstable of the three representative surfaces. It is known that the synthetic protocols determine the facets exposed to the reaction media.^{8,9} For this purpose, it is of high importance to identify the preparation technique that grows the particles in solution with fewer constraints and focusing not only on size but also on shape control. In particular, in this work, sol-immobilisation was demonstrated to be preferred over impregnation due to the epitaxial growth in the latter method, which implies more constraints and therefore may lead to a higher proportion of Pd(001) surface.

Besides the surface, formic acid decomposition through carboxylic pathway was associated also with higher CO concentration than formate pathway. Hence, it would be interesting to find a way to avoid or reduce carboxylic pathway. A possible solution may lay on the formate additive as well. By adding formate ions into the media, this will definitively have an effect on the pathway that formic acid decomposition follows, favouring formate over carboxylic pathway.

These findings undoubtedly leave an open door to continue the investigation trying to design experimental methodologies that develop supported Pd nanoparticles exposed with more extension of (111) and (011) surfaces and whether possible, find experimental conditions that avoid carboxylic pathway.

On the other hand, the support plays an important role as explained throughout this Thesis. Using commercial titania (P25) as a support has a theoretically positive effect on producing catalysts more resistant against CO poisoning as presented in Chapter 5, section 5.2.4. However, the lower catalyst activity, compared with carbon and carbon nanofibers, may lead

to titania being crossed out from the possible commercial catalyst supports. This drop of activity was mainly attributed to the larger pore size of approximately 28 nm while the average particle size of the Pd nanoparticles is 3.7 nm, meaning that a certain portion of them could be immobilised inside the pores and subsequently, formic acid molecules facing fewer probabilities to find an empty active site. The literature on how to tune the pore size has been extensively written.^{10,11} From the one side, a decrease of pore size to 3-4 nm could prevent the nanoparticles from entering them and, on the other hand, an increase of pore size to several hundreds of nm would greatly reduce the difficulty for formic acid to find an active site.¹²

In regard to acidity or basicity of the carbon nanofibers, some results were presented however, the lack of enough variety of samples prevented the release of conclusive data. For this purpose, immobilisation of Pd nanoparticles on carbon nanofibers with different functionalisations could shed some light on the effect that acidity and basicity have on the metal/support interaction. Besides oxygen and nitrogen-doped carbon nanofibers, phosphorus has become an object of study in several fields.^{13,14} P has been reported to modify the electronic properties of Pd due to the transfer of electrons from carbon atoms to phosphorus atoms, favouring the formation of stable electron-rich Pd–P species. The functionalisation of the carbon/carbon nanofiber supports open a broad field of new experiments never reported before for formic acid decomposition. The interactions between metal and supports may be greatly modified by this method and so, activity, stability, selectivity, etc.

To conclude, this work has combined experimental methods with computational studies supporting each other. Joint works of experimental and computational studies are not common. It undoubtedly facilitates and, in some cases, gives possible solutions or new directions of research to specific scientific questions, which cannot be answered by using each characterisation technique separately. For this purpose, in order to continue this research, this combination of methodologies is strongly encouraged.

6.3. References

- 1 C. Perego and S. Peratello, *Catal. Today*, 1999, **52**, 133–145.
- 2 D. A. Roşca, J. A. Wright, D. L. Hughes and M. Bochmann, *Nat. Commun.*, 2013, **4**, 1–7.
- 3 Y. Lee and Y. Jeon, *J. Korean Phys. Soc.*, 2000, **37**, 451–455.

-
- 4 C. Feng, Y. Wang, S. Gao, N. Shang and C. Wang, *Catal. Commun.*, 2016, **78**, 17–21.
 - 5 X. Wang, G. W. Qi, C. H. Tan, Y. P. Li, J. Guo, X. J. Pang and S. Y. Zhang, *Int. J. Hydrogen Energy*, 2014, **39**, 837–843.
 - 6 Y. Ping, J.-M. Yan, Z.-L. Wang, H.-L. Wang and Q. Jiang, *J. Mater. Chem. A*, 2013, **1**, 12188.
 - 7 Z.-L. Wang, J.-M. Yan, H.-L. Wang, Y. Ping and Q. Jiang, *Sci. Rep.*, 2012, **2**, 598–604.
 - 8 R. Van Den Berg, G. Prieto, G. Korpershoek, L. I. Van Der Wal, A. J. Van Bunningen, S. Lægsgaard-Jørgensen, P. E. De Jongh and K. P. De Jong, *Nat. Commun.*, 2016, **7**, 20457–20465.
 - 9 J. C. Frost, *Nature*, 1988, **334**, 577–580.
 - 10 K. J. A. Raj, A. V. Ramaswamy and B. Viswanathan, *J. Phys. Chem. C*, 2009, **113**, 13750–13757.
 - 11 S. Sokolov, E. Ortel and R. Kraehnert, *Mater. Res. Bull.*, 2009, **44**, 2222–2227.
 - 12 L. Cao, D. Chen, W. Q. Wu, J. Z. Y. Tan and R. A. Caruso, *J. Mater. Chem. A*, 2017, **5**, 3645–3654.
 - 13 S. Campisi, S. Capelli, D. Motta, F. Sanchez Trujillo, T. E. Davies, L. P. Id, N. Dimitratos and A. Villa, *Carbon N. Y.*, 2018, **4**, 17.
 - 14 S. Campisi, F. Sanchez Trujillo, D. Motta, T. Davies, N. Dimitratos and A. Villa, *C*, 2018, **4**, 9.

PUBLICATIONS

Catalytic decomposition of carbon-based liquid-phase chemical hydrogen storage materials for hydrogen generation under mild conditions

F. Sánchez, D. Motta, and N. Dimitratos, *Appl. Petrochemical Res.*, vol. 6, no. 3, pp. 269–277, 2016.

Investigation of the Catalytic Performance of Pd/CNFs for Hydrogen Evolution from Additive-Free Formic Acid Decomposition

F. Sanchez, D. Motta, L. Bocelli, S. Albonetti, A. Roldan, C. Hammond, A. Villa and N. Dimitratos, *C*, vol. 4, no. 26, pp. 1–17, 2018.

Hydrogen Generation from Additive-Free Formic Acid Decomposition Under Mild Conditions by Pd/C: Experimental and DFT Studies

F. Sanchez, D. Motta, A. Roldan, C. Hammond, A. Villa, and N. Dimitratos, *Top. Catal.*, vol. 61, no. 3, pp. 254–266, 2018.

Hydrogen production from formic acid decomposition in the liquid phase using Pd nanoparticles supported on CNFs with different surface properties

F. Sanchez, M. H. Alotaibi, D. Motta, C. E. Chan-Thaw, A. Rakotomahevitra, T. Tabanelli, A. Roldan, C. Hammond, Q. He, T. Davies, A. Villa and N. Dimitratos, *Sustain. Energy Fuels*, vol. 2, pp. 2705-2716, 2018.

An investigation on AuPt and AuPt-Bi on granular carbon as catalysts for the oxidation of glycerol under continuous flow conditions

D. Motta, F. Sanchez, N. Dimitratos, A. Villa, and L. Prati, *Catal. Today*, vol 308, pp. 50-57, 2017.

Enhanced activity of Au/NiO nanohybrids for the reductive amination of benzyl alcohol

C. E. Chan-Thaw, L. E. Chinchilla, F. Sanchez, N. Dimitratos, G. A. Botton, L. Prati and A. Villa, *Materials (Basel)*., vol. 10, no. 12, pp. 1–11, 2017.

Exploring the Effect of Au/Pt Ratio on Glycerol Oxidation in Presence and Absence of a Base

A. Villa, A. Jouve, F. Sanchez, D. Motta, L. Prati, and N. Dimitratos, *Catalysts*, vol. 8, no. 2, pp. 54, 2018.

Controlling the Incorporation of Phosphorus Functionalities on Carbon Nanofibers: Effects on the Catalytic Performance of Fructose Dehydration

S. Campisi, F. Sanchez, D. Motta, T. Davies, N. Dimitratos, and A. Villa, *C*, vol. 4, no. 1, pp. 9, 2018.

Phosphorous Functionalized Carbon Nanofibers towards HMF Oxidation

S. Campisi, S. Capelli, D. Motta, F. Sanchez, T. E. Davies, L. P. Id, N. Dimitratos and A. Villa, *Carbon N. Y.*, vol. 4, no. 48, pp. 17, 2018.

ACKNOWLEDGEMENTS

First, I would like to thank Nikos for his guidance and support and for giving me the opportunity to perform this work in his group. His extensive experience and knowledge greatly helped me during the research. Also, the conversations about food. I hope we can have a proper octopus and *espeto* on the beaches of Málaga.

Special thanks must go to Ceri, even though he has a questionable hairstyle, he has been a very good co-supervisor.

I also appreciate the help and support of Alberto Villa. Sorry, Milan is too warm for me.

I would also like to thank Alberto Roldán and its invaluable help during the 5 minutes meetings (3 hours, actually).

Thanks also to all the people I have been working with and, let us say, bearing with at some moments.

I am thankful to my close friends, family and special people.

Finally, you, Reader, I hope you enjoyed or, at least, found useful information.